UAB

Universitat Autònoma de Barcelona

Fabrication methods for functional nanoparticles and interdigitated nanoelectrodes

Nerea Alayo Bueno

Tesi Doctoral
Programa Ciència de Materials

Director:
Francesc Pérez Murano

Tutor:
Manel del Valle Zafra

Departament de Química
Facultat de Ciències

2013

CnM Centre Nacional de Microelectrònica IMB

CSIC Consejo Superior de Investigaciones Científicas

Memòria presentada per aspirar al Grau de Doctor per Nerea Alayo Bueno
Vist i plau del Director Dr. Francesc Pérez Murano *i tutor* Dr. Manel del Valle Zafra*.*

Autor,   *Director,*   *Tutor,*
Nerea Alayo Bueno   Francesc Pérez Murano   Manel del Valle Zafra

Bellaterra, 25 de setembre de 2013

This is the version of the thesis presented for the official defense.

The author recommends looking for a final version of the thesis, including the comments of the jury, in the group's webpage
nanonems.imb-cnm.csic.es

The document can be downloaded from the following address:

http://nanonems.imb-cnm.csic.es/images/Thesis/alayo.pdf

Index

Introduction

Nanoscience studies the properties of matter at the nanometer scale (1 – 100 nm). This definition in terms of dimensions reflects its implication in diverse fields of science like physics, chemistry or biology.   Although nanoscience might seem to be a new research field, almost science fiction, it has been existed from ever, it is everywhere around us. Whereas, it obtain its fame acclaimed to the fact that the most relevant molecules in nature are in the nanoregion, such as DNA, proteins, enzymes… they are the pillars of the life. When researchers started to study nanoelements they realized that not everything was about size. At the nanoscale some properties not seen on a macroscopic scale become important, such as quantum mechanical and thermodynamic properties. A clear example of this is the special properties of nanoparticles.

In order to manipulate nanoscale objects, we would need to get to their size. Our natural condition does not allow us to *see* and *touch* at this scale but, during the last decades, several tools and techniques have been developed to reach the nanoscale. The term *nanotechnology* is used to call the different techniques that allow the manipulation, fabrication and characterization of nanoelements. Nanotechnology is a multidisciplinary field, it involves the production and application of physical, chemical and biological systems at scales ranging from individual atoms or molecules to about 100 nanometers, as well as the integration of the resulting nanostructures into larger systems.

Nanotechnology concept was inspired by the famous lecture "There is plenty Room at the Bottom" that Richard Feynman gave in 1956 at the American Physical Society meeting. He presented a technological vision of extreme miniaturization and he talked about the problem of manipulating and controlling things on a small scale. Since then, immense advances have been performed in this field. Science and engineering research in nanotechnology promises breakthroughs in areas such as materials, manufacturing, electronics, medicine and healthcare, energy, environment, biotechnology, information technology and national security. It is believed that nanotechnology will lead to the next industrial revolution.

Fabrication of nanostructures involves a number of new challenges. Nature is a good example to follow in nanofabrication issues. There are many nano-objects and nanomaterial in the world built by self-assembling of smaller molecules, such us multidomain proteins. The group of processes that follow this approach is named *bottom-up* nanofabrication. To compare with macroscopic scale, it would be like the growth of a plant from a seed.

On the contrary, when the fabrication is performed from the fracture of larger material, it is called *top-down* approach. A simile would be the sculpting of a stone. The most common top-down processes assortment is *nanolithography*. Lithography is the technique used to transfer arbitrary patterns onto a substrate. These patterns are normally used as mask in subsequent post-processing.

Although photolithography, i. e. the lithography using a UV light source, is by far the most widely used lithography technique in microelectronic fabrication, it cannot be directly used to create nanopatterns, since the wavelength of the light, 193 nm, limits the dimension of the patterns to several hundreds nanometers. The mostly used nanolithography alternatives at lab-level are the electron beam, X-ray, nanoimprint and stencil lithographies. All of them have a great potential to create nanopatterns down to few nanometers on a substrate.

However, most of these techniques require very high cost and slow tools. For instance, electron beam lithography is a extremely precise technique and high-resolution structures can be achieved with it. Nevertheless, it is a slow equipment, since a single beam has to sweep the entire surface. Moreover, due to the huge power needed and the high cost of the equipment (up to several million dollars) nowadays is not a viable option for large-scale production in industry. For this reason it is frequently used to make prototypes but not final products.

It is extremely relevant the investigation related to nanofabrication done at the lab, it becomes nanotechnology a live science that is impressively growing everyday. Whereas, the option to reproduce these findings at medium or large scale must exist to have utility in the real word, what frequently means Industry. In order that, high throughput technique able to reproduce the fundamental research done at the lab must be developed. Nanoimprint lithography is one of the most appropriate candidates to accomplish this goal. Nanoimprint lithography is a technique used to transfer nanopatterns from a stamp to a substrate.

Nanoimprint lithography and other techniques used for the large production of nanodevices and nanoparticles have been developed during this thesis. The results obtained from the performed work and feasibility of each process have been discussed in this document.

This thesis has been divided in three sections and six chapters:

Section I presents the introduction to nanoimprint lithography. The main notions of the technique and the state of the art are summarized **in Chapter 1**. In addition, the nanostructuration of novel polymers performed during this thesis as well as their characterization is explained in this section.

Section II describes two different approaches related to nanoparticle fabrication and characterization.

Nanoparticles are single nanometric elements with their own characteristics, different to the correspondent bulk material [1]. A bulk material should have constant physical properties regardless of its size, but at the nano-scale this is often not the case. Size-dependent properties are observed such as quantum confinement in semiconductor particles, surface plasmon resonance in some metal particles and superparamagnetism in magnetic materials [2]. Nanoparticles often have unexpected visible properties because they are small enough to confine their electrons and produce quantum effects [3]. For example gold nanoparticles appear deep red to black in solution [4,5]. Moreover, nanoparticles have a very high surface area to volume ratio. This provides a tremendous driving force for diffusion, especially at elevated temperatures.

When nanoparticles have crystalline structures, they are called nanocrystals. The high interest in nanocrystals principally comes from the electron confinement provided by them, which is a robust instrument to manipulate the electronic, optical and magnetic properties of a solid material. These characteristics make them interesting to be used in nano/microelectronics, especially for memory storage [6].

However, the exceptional properties of single nanoparticles are often difficult to characterize. In **Chapter 2**, a novel method to contact single nanocrystals with potential for high throughput has been developed. There have been some previous works were contact of single nanocrystals was reported. Nevertheless, nowadays there is a lack of feasible methods to achieve it. The design and optimization of the method, as well as the preliminary electrical results have been exposed.

On the other hand, in recent years the utility of metallic nanoparticles arrays to be used as sensor, for instance Localized Surface Plasmon Resonance (LSPR) sensors, have been demonstrated. Traditionally the fabrication of nanoparticles was done following chemical methods. However, it is complicated to obtain ordered arrays of nanoparticles needed for such applications, using chemically synthesized nanoparticles. Moreover, with the improvement of lithography techniques, the option to fabricate them by top-down approaches has taken prominence.

Chapter 3 presents a novel technique to fabricate metallic nanoparticles arrays by nanoimprint lithography. This technique is a step forward in the nanoimprint lithography's state of the art, since allows the fabrication of high aspect ratio nanostructures, facilitates the lift-off, provide alternative to obtain nanoparticles of different shapes and materials, and even combination of them. Plasmonic resonance behavior of the particles has also been demonstrated.

Section III relates to the fabrication and characterization of interdigitated nanoelectrodes to be used as (bio)sensors.

Interdigitated electrodes have been widely used in electrochemistry, with especial interest to perform voltammetry. When the size of the digits and the gaps are reduced to the diffusion layer dimensions, it contributes to the improvement of the sensitivity. Moreover, when the width of the digits and gaps are diminished to the nanoscale, the suitability of the sensors to be used for redox cycling selective detection in importantly enhanced.

In this section fabrication of interdigitated nanoelectrodes has been developed by different methods. In **Chapter 4,** fabrication of the sensors by thermal and UV nanoimprint lithography is described. The novel method used to improve the fabrication of interdigitated electrodes by nanoimprint lithography at large-scale, was based on the process explained in Chapter 3. Thermal nanoimprint process was developed at the CNM, while UV Step and Repeat process at The Molecular Foundry's clean room.

Chapter 5 presents the fabrication of interdigitated nanoelectrodes by e-beam lithography at wafer scale, combined with photolithography to define micrometer scale areas. In this chapter, two packaging designs used for the encapsulation of the devices are explained. The first one is a standard PCB, frequently used for the packaging of micro/nanodevices. The second packaging was developed during this thesis to satisfy the specific requirement of the devices and the experiments. It consists of a methacrylate holder with electrical and fluidic connections. An improvement in the results due to the new packaging is demonstrated.

Finally, in **Chapter 6** the electrochemical behavior of the interdigitated nanoelectrodes is discussed. An improvement on the selective detection of dopamine in presence of ascorbic acid was evidenced with the miniaturization of the devices. The experimental results are correlated with finite element simulations.

The thesis finalizes with the general conclusions of the performed work.

References in the Introduction

1. Josep Saldaña, V. P. *Nanoparticles before nanotechnology*. Vol. ebook series 3 (2013).

2. Saison-Francioso, O. *et al.* Plasmonic Nanoparticles Array for High-Sensitivity Sensing: A Theoretical Investigation. *The Journal of Physical Chemistry C* 116, 17819-17827(2012).

3. Sanvicens, N. & Marco, M. P. Multifunctional nanoparticles – properties and prospects for their use in human medicine. *Trends in Biotechnology* 26, 425-433 (2008).

4. Eustis, S. & El-Sayed, M. A. Why gold nanoparticles are more precious than pretty gold: Noble metal surface plasmon resonance and its enhancement of the radiative and nonradiative properties of nanocrystals of different shapes. *Chemical Society Reviews* 35, 209-217, (2006).

5. Jain, P., Huang, X., El-Sayed, I. & El-Sayed, M. Review of Some Interesting Surface Plasmon Resonance-enhanced Properties of Noble Metal Nanoparticles and Their Applications to Biosystems. *Plasmonics* 2, 107-118, (2007).

6. Kittelson, D. B. Engines and nanoparticles: a review. *Journal of Aerosol Science* 29, 575-588, (1998).

SECTION I

Nanoimprint lithography

1. ■ Nanoimprint Lithography, introduction and applications

Nanofabrication performed at research laboratory level is usually dedicated to the discovery of new material properties, understanding physical phenomena or device development to the limits of the state-of-the-art technologies. In contrast, the processes that are needed by the industry give more importance to parameters such as low-cost, short lead time or scalability. Therefore, if researchers want to see their developments become real products, they must consider the most reliable method to reproduce them. In this sense, Nanoimprint Lithography (NIL) arises as an extraordinary method to achieve this task. It is a mechanical process, which makes it a cheap and simple technique. For this reason, in 2011 the International Roadmap for Semiconductors (ITRS) accepted NIL as a candidate for "next generation lithography" (NGL), as depicted in Figure 1.1 [7].
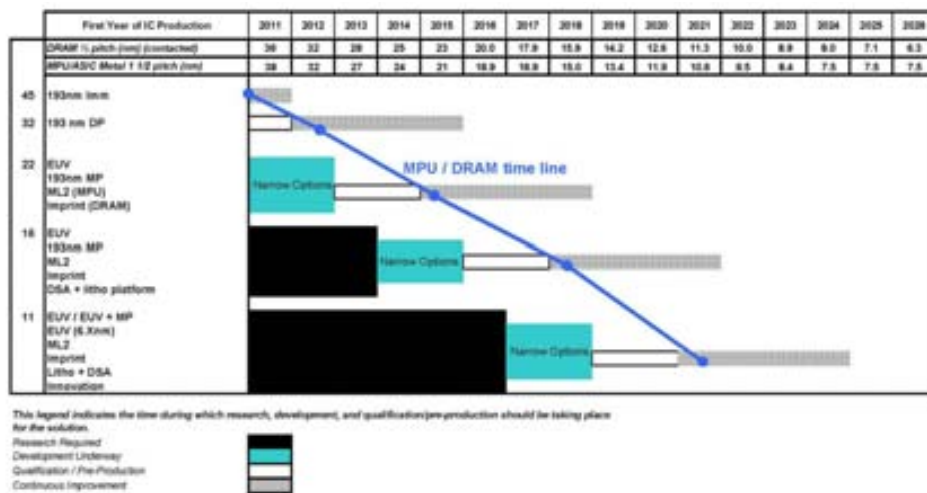
Figure 1.1. 2011 ITRS potential solutions roadmap.

Unlike other lithography methods, nanoimprint lithography resolution is not dependent on the wavelength, being able to replicate even molecular-scale patterns, as Hue et al. [8] demonstrated when they replicated a single-wall nanotube of 2.4 nm, Figure 1.2. The resolution limit of the nanoimprint lithography totally depends on the patterns on the stamp, consequently the

dimension of the replica will be related to our capability to fabricate the template.
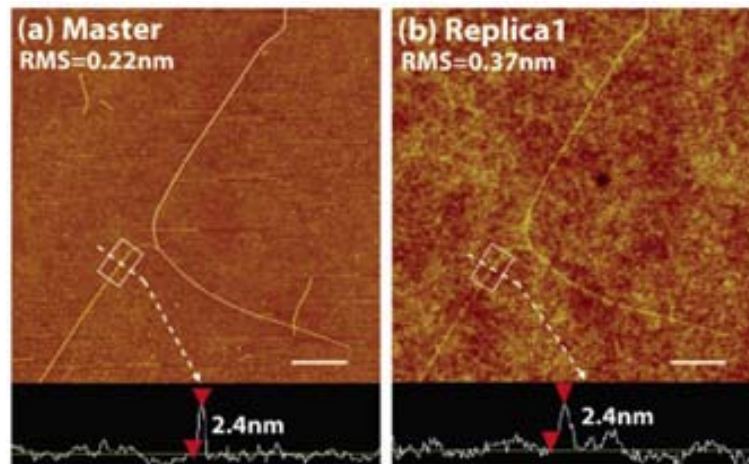
Figure 1.2. AFM image of nanoimprint stamp with nanotubes (left) and its replica (right) obtained by Hue et al. **[8]** in 2004.

Moreover, NIL is an attractive technique for a large range of applications, aside from semiconductor chip fabrication, but also for the "More than Moore" applications, such as the patterned of non-photocurable materials for microsystem technology [9,10]. Furthermore, nanoimprint has the unique capability to achieve 3D structures in a single imprint, while other techniques require several steps [11-13], Figure 1.3.
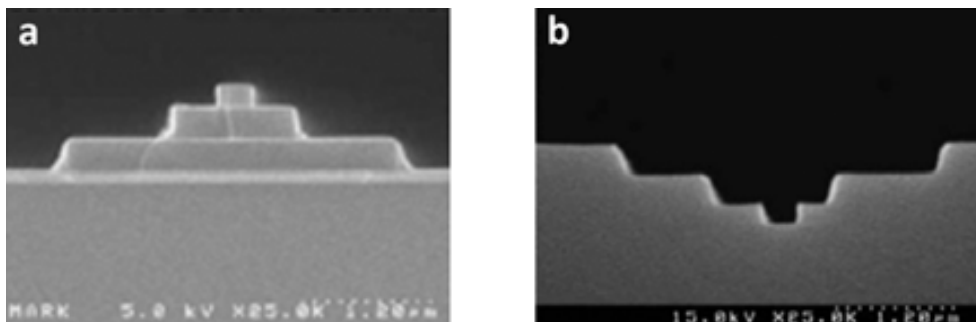
Figure 1.3. SEM image of 3D stamp (a) and replica (b) obtained in [12]

On contrast, the high sensitivity of nanoimprint to defects is an important challenge to overcome. The principal defect is the dirtiness, the minimum particle in the stamp or substrate could spoil the hole imprint. The defects not only affect to the imprinting area, but also to the surrounding areas. Moreover, the defect on the stamp will affect the subsequent imprints.

This thesis takes advantage of the benefits of nanoimprint lithography for different approaches.

10

On the one hand, it has been used to fabricate 3D metallic nanoparticles (Chapter 3). NIL has been used to fabricate a hard mask that subsequently was used to obtain high aspect ratio nanoparticles. In this case it has been taken advantage of, not only reproducibility of NIL, but also a novel technology has been developed, which could not be performed with other types of lithography.

Also fabrication of interdigitated nanoelectrodes by thermal and UV nanoimprint lithographies has been studied (Chapter 4). The results and conclusions obtained from this work can be extended to the fabrication of other nanodevices.

There are thousands of good articles, books and theses describing nanoimprint lithography technique and all the science around, some of them referenced along this thesis. Nevertheless, this chapter is destined to make a brief review of the nanoimprint lithography, which will facilitate the discussion of the performed investigation and the obtained results. There will be explained the main nanoimprint methods, how to fabricate stamps, imprintable materials, post processing and finally a discussion about how viable is nowadays nanoimprint lithography in the industry.

In this chapter it has been also included the research made about semicrystalline polymers. Structuration of semicrystalline polymers (i.e. PTT, PET, P(VDF-TrFE) and PBAC) by thermal nanoimprint lithography has been developed. These polymers can be used in different applications, such as soft lithography stamps or non-volatile memories. The study of fundamental characteristic of these polymers has been developed in collaboration with a research group expert in structured material science.

1.1 NANOIMPRINT MODES

Nanoimprint lithography is the technique where the patterns in a stamp are transferred to a substrate by means of different sources of energy. Several parameters can be modified to obtain variety of NIL processes, such as the stamp material (quartz, silicon, PDMS, etc), transfer method (thermal, UV) or the transfer layer (thermoplastic materials, UV-curable resists, Si-containing etch barriers).

Within the large number of NIL based works developed during the last years, the most relevant processes have been performed by thermal NIL, Step & Flash (S&F) UV-NIL and soft imprint lithography. Being the first two the most popular in nanodevice fabrication and the ones developed in this thesis.

Thermal NIL: a hard stamp (usually silicon) is used to pattern a thermoplastic material above the glass transition temperature and fix the patterns by cooling

down the polymer before raising the template [14-16] Figure 1.4a shows the steps of thermal NIL process.

UV-NIL: As Figure 1.4b shows, UV-sensible resist is patterned by means of a transparent stamp (normally quartz) when applying UV-light. The most used sort of UV-NIL is the Step and Flash (S&F), where several imprints are performed in a wafer using the same stamp [17,18].

Soft lithography: a liquid is molded in a patterned master and then cured into a soft stamp that is used to transfer the desired pattern [19-24], see Figure 1.4c.
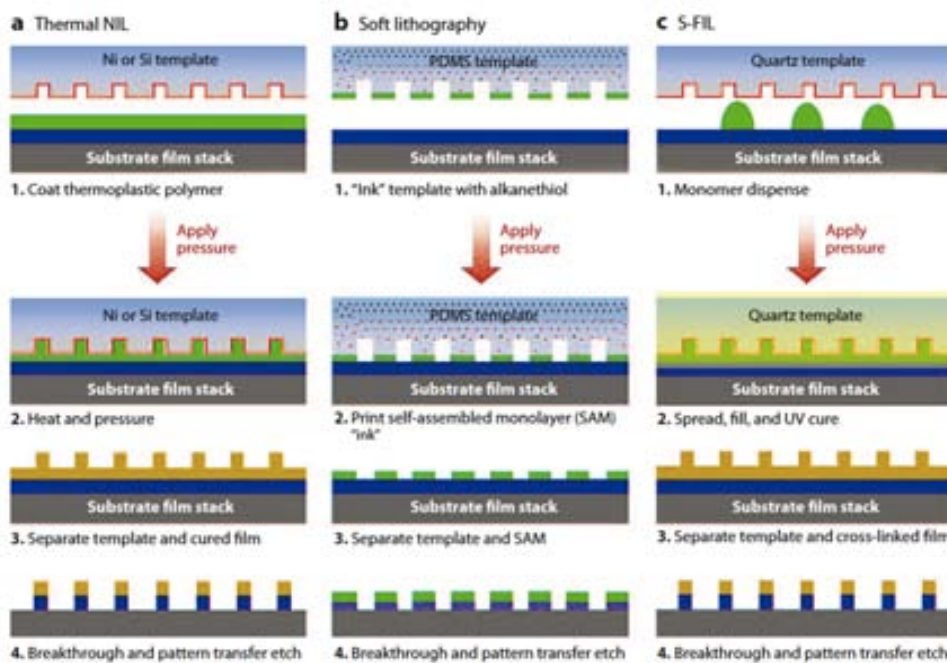
Figure 1.4. Description of the three main nanoimprint modes: a) Thermal NIL, b) Soft lithography and c) Step & Flash lithography. Extracted from **[17]**.

Other unusual nanoimprint methods have also been developed during the last decades. Some examples of these are the "millipede" where a heated AFM tips are used as stamps [25], room temperature imprint of thermoplastic polymers [26,27], solvent assisted NIL [28], reverse-nanoimprint [29]. All of them and more are named in the NaPANIL Library of Processes [30].

There are several variations of nanoimprint such as wafer-size stamp, Step and Repeat (S&R) or Step and Flash (S&F) [17,31] and roll-to-roll [32-34]. The first one is the parallel imprint of the template on the sample. Roll-to-roll is the modality when the substrate is a polymer-roll and the imprint is mass-produced by a roll stamp [33]. Finally S&R or S&F is the variant where a small stamp is replicated several times along the substrate, this modality can be used for the three modalities of NIL presented. It is called S&R for thermal NIL and S&F for UV-NIL. During the last years, S&F UV-NIL has obtained especial emphasis

from the industry and researchers to bring this technique to the semiconductor manufacturing industry.
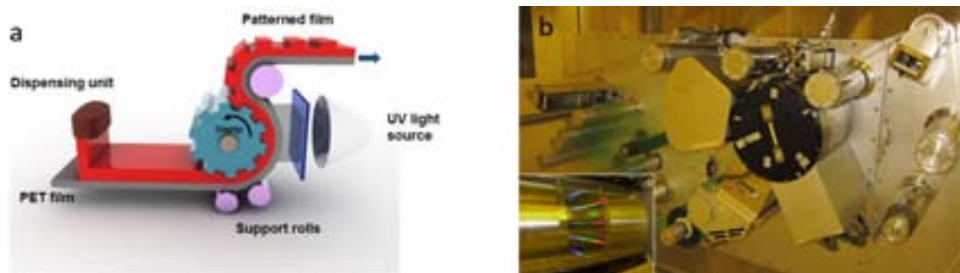
Figure 1.5. Sketch of the roll to roll nanoimprint process [35]. Image of a roll to roll equipment [36].

1.1.1 Thermal nanoimprint process

Thermal nanoimprint was the earliest NIL process presented in 1995 by S. Chou et al. [37]. This process uses a silicon stamp to pattern a thermoplastic polymer above glass transition temperature at high pressure. First the thermoplastic resist is spincoated on the substrate and the template is placed on top of it. Then the resist is heated up above glass transition temperature (T_g) and pressure is applied. The pressure is applied meanwhile $T_{imprint}$ is maintained. Then the resist is cooled down below T_g, the pressure is maintained until the suitable temperature is reached. When the resist cools down, the stamp is raised and as result the patterns are transferred into the resist. The complete process is explained in Figure 1.6.
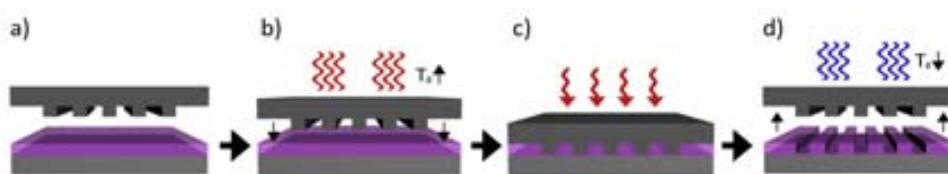
Figure 1.6. Thermal nanoimprint process: a) Thermoplastic polymer is spincoated on the substrate, the substrate and the template are aligned. b) The polymer and the template are heated up above the T_g of the polymer. c) Pressure is applied to the system. d) The system is cooled down below the T_g.

It is relatively easy to obtain desirable imprints finding the optimize trade-off between the applied pressure, imprinting/demolding temperature and time. Being the range of each one pretty wide. These parameters depend on the chosen imprinting resist and geometry of the patterns.

Between 10^3 and 10^7 Pa is usually the pressure that must be applied. At this range the viscosity of the polymer is enough low to push the polymer flow and fill the cavities of the stamp. At the same time it is enough high to allow the use of high pressures and compensate the waviness of the stamp. In order to trade-off the ripples of the substrate and template, it is also useful to place a soft material on top of the template, such as aluminum or polymer foil. Alternative option is to use air pressurized NIL system. Figure 1.17 shows the mechanical properties of the polymer depending on the pressure.
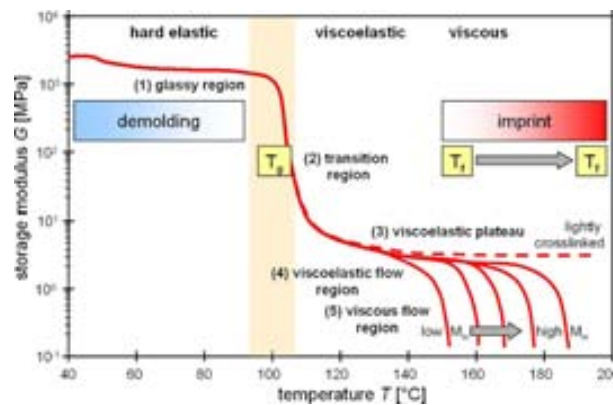
Figure 1.7. Mechanical properties of polymers dependent on temperature and pressure. It is also represented that these properties varies in function of molecular weight and cross-linking [38].

Several works and simulation have been performed to observe the cavity-fill process during the imprints. Hirai et al. were the first to investigate the polymer deformation process by numerical simulation [39] and they were compared with experimental results in [40]. In [41] is widely explained the mechanism of the cavity filling, Figure 1.8 shows the results of the simulation when different size cavities are filled [42].

It was found that the required pressure increased not only for high-aspect-ratio patterns, but for low-aspect-ratio patterns as well. This is because for wide trenches the pressure is not evenly distributed as a result of the polymer flow resistance, and the polymers fill in from the edges with a slower filling rate than at the center of the cavity. The pressure also increases when the initial thickness of the polymer film decreases to less than twice the mold depth. This again can be attributed to the increased resistance of polymer flow in the confined nanofluidic channels formed between the mold protrusions and the substrate surface. These results agree very well with experimental observations.

14

Figure 1.8. Deformation profiles for (a) increasing cavity width holding indenter width and film thickness constant [43].

When thermal NIL is performed, it is normal to see spot-like and mound-like filings on the resist, not in the patterned areas, but in area around, see Figure 1.9. Heyderman et al. [44] explain that this phenomena could be addressed as a result of polymer compression between two boundaries, the polymer film buckles due to local inhomogeneities of the polymer viscosity or elasticity and form the observed features, possibly enhanced by capillary forces. When applied pressure is low and the contact between the stamp and the substrate is uncompleted, the mound-like features could be observed also in the patterns. This and other phenomena of the polymer flow behavior are explained in [45].
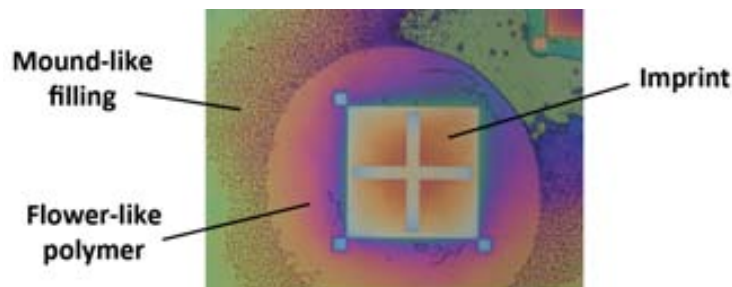
Figure 1.9. Optical microscope image of an imprint. The cross and the squares are perfectly imprinted. The surrounding area has the flower-like polymer aspect and around of it the typical mound-like filling observed in most of the imprints.

Besides, necessary temperature for a successful imprint is basically based on the glass transition temperature of the polymer. The T_g is the critical temperature at which the polymer changes its behavior from being 'glassy' to being 'rubbery', as it is depicted in Figure 1.10. The imprint is usually performed 70°C- 90°C above the T_g, so the polymer reaches a viscous flow state. The demolding is performed 20°C below the T_g to preserve the imprinted pattern after the mold is removed [46], not being critical the chosen temperatures in this range, Figure 1.7.

15
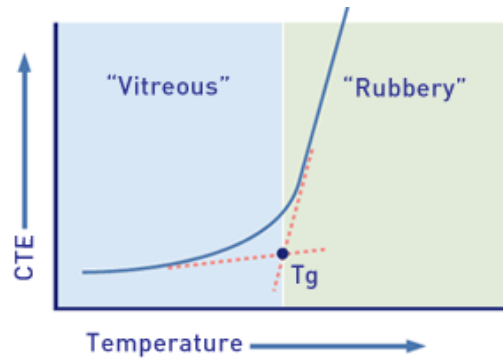
Figure 1.10. In this graph it is represented the change of the polymer from "vitreous" to Rubbery" as function of temperature.

When planning an imprint experiment, it is also important to consider the geometry and distribution of the patterns in the stamp. In contrast with what happens in photolithography, in NIL processes gratings with small regular structures in the submicrometer range can be molded within a fraction of a second, while the large unstructured areas can take minutes to fill. This phenomena is simplified comparing with a macroscopic situation. It is easier to insert a thin needle in a rubbery substrate than a pen.

When micro and nanoareas must coexist in the same stamp, the design of the stamp can be optimized within the limitation given by the application, i.e. avoid large protrusions sizes and density variations over large areas, e.g. by backfilling empty stamps with dots and arrays with small width. Example of backfilling technique was proposed in this thesis for the fabrication of interdigitated nanoelectrodes stamps. The devices are compounded of nanoareas (digits) and microarea (pads). As it can be seen in Figure 1.11, the nanodigits are around 100 nm width and pads have a larger of 100 μm. In order to avoid the troubles obtained by imprinting patterns of different sizes, the pads where designed as large grating. Moreover, around the devices arrays of dots were also placed to fill the extensive area between patterns. However, it was demonstrated that the optimum way to fabricate these devices is by combination of photolithography and nanoimprint lithography, for pads and nanodigits fabrication, respectively.
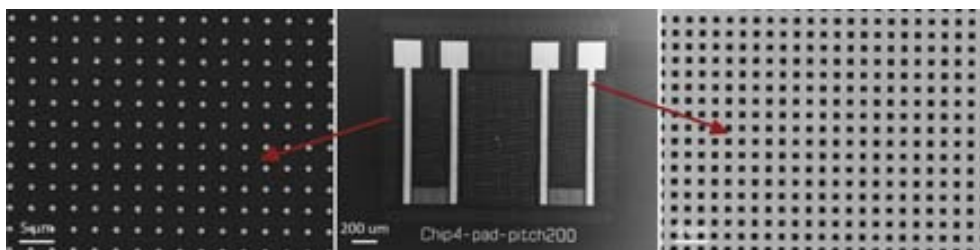
Figure 1.11. SEM images of a stamp fabricated at the CNM during this thesis. In the center it can be seen overall image of the stamp compounded by two interdigitated devices with nanodigits and micropads, all around the devices a large array of dots was fabricated to compensate the flow of the polymer, left. Right, inset of the pads based on a net shape.

1.1.1.i *Thermal NIL equipment*

The thermal nanoimprint equipment used during this thesis is *Obducat 4 inch*, from Obducat [47], placed at the CNM's clean room. This tool is flexible to use substrates from chip size to 4 inch wafers. It can apply temperatures up to 350 °C and pressure up to 80 bars applied by air. The imprint process is parallel, i.e. single imprint is performed for each substrate. Aluminum foils are used to improve the homogeneity of the imprints. Due to the simplicity of the tool (no arms, no multi stage…) it is highly useful for basic research.
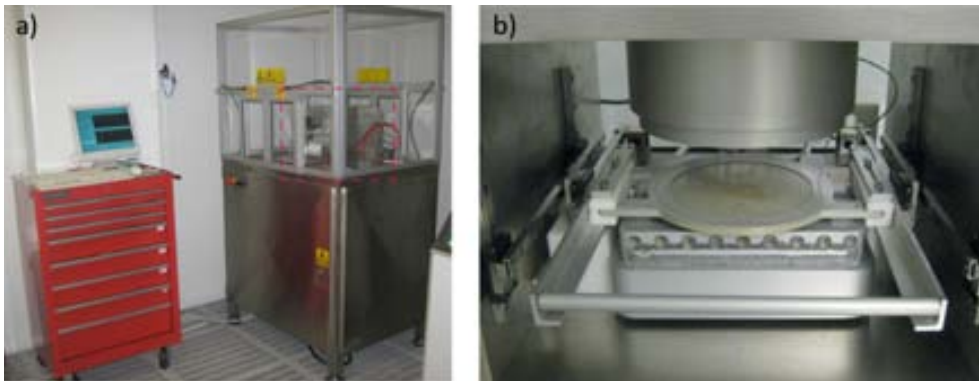
Figure 1.12. Thermal nanoimprint located at the CNM's clean room, from Obducat.

1.1.2 UV nanoimprint process

UV-NIL follows the basic principle of thermal nanoimprint, which is to replicate the patterns in a stamp into a substrate. The main difference is that, while in thermal NIL the resist is molded by heat and pressure, in the case of UV-NIL the liquid-resist fills the patterns by capillarity and is cured by UV light. The rheology of the polymer is similar to thermal NIL, but as the resist is liquid and low temperatures and pressures are applied the process is simplified. Figure 1.13 shows the steps followed during a standard UV-NIL process.
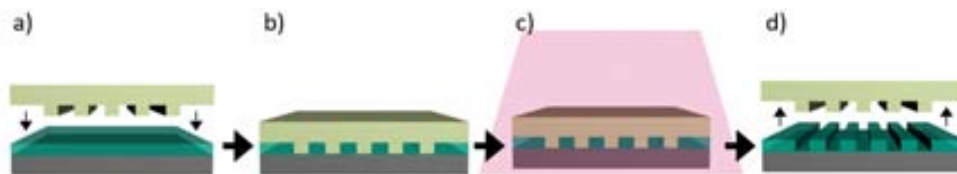
Figure 1.13 Description of the UV-NIL process: a) the template is aligned and press the substrate. b) Liquid UV-resist fills the nanopatterns in the template by capillarity. c) Then the resist is cured by UV light. d) Finally when the template is raised patterns are transferred to the resist.

1.1.2.i Step & Flash

The most common UV-NIL variant is the Step & Flash imprint lithography. It gives chance to replicate many times a small template along the substrate, reducing the high cost of the fabrication of a substrate-size stamp. In the recent years, industry has select S&F UV-NIL as candidate to bring nanoimprint lithography to the market.

Steps to performed step and flash UV-NIL are depicted in Figure 1.14. First, the resist must be locally deposited on the substrate. It is necessary to accurately dispense the resist droplets only on the area that will be immediately imprinted, in order to avoid the exposition of the surrounding resist. Then, the template is aligned with the substrate and taken down to be in contact with the resist. UV-light is applied to cure the resist. When the resist is cured the template is raised and moved to the next field to perform the subsequent imprint.
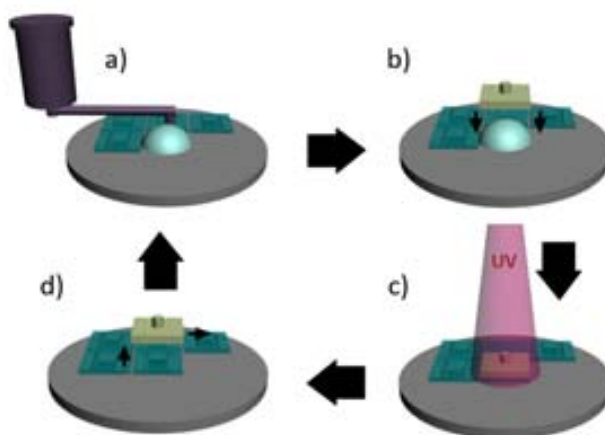
Figure 1.14. S&F UV-NIL process: a) UV resist is locally dispensed on the substrate. b) The template goes down to press the resist c) Resist is cured by UV light. d) The template is raised and moved to the next field.

Step and repeat process can be also used for thermal nanoimprint, for instance the NPS 300 (SUSS) equipment placed at the CNM has UV-NIL but also thermal NIL S&R capabilities. However, thermal NIL is slower because the resist must cool down to release the stamp, therefore the essence of the S&R is somehow lost. In addition, when thermal NIL is performed the resist is expanded, consequently the alignment used in S&R become more complicated.

1.1.2.ii UV-NIL equipment

Step & repeat UV-NIL processes presented in this thesis where developed at The Molecular Foundry (Berkeley) using the Imprio 55 from Molecular Imprint Inc. [48]. It is designed to imprint 4 and 6 inch wafers by step and flash process.

Figure 1.15. Imprio 55, Molecular Imprints, S&F UV-NIL equipment.

1.2   STAMP FABRICATION

Since the quality of the imprint will be directly related with the stamp, its fabrication is the most significant step. First of all, choice of stamp material must be done. In principle any material with high strength and durability can be used. In practice other consideration are taken into account, for instance in thermal NIL hardness (the stamp material must have higher Young's modulus than the printable polymer), compatibility with micro/nanofabrication, thermal expansion and aimed application must be consider. Due to the well-known processing of silicon, silicon oxide and silicon carbide and their appropriate hardness and durability, they have been extensively used to fabricate stamps [16,46,49]. Figure 1.16a shows a Si stamp fabricated during this thesis at the CNM. The nanopatterns are placed in a mesa in the center of the stamp.

In case of UV-NIL, aspects like hardness or thermal expansion are less relevant since the process is performed at lower pressure and usually at room temperature, due to the lower viscosity of the resist. Nevertheless, the stamp used in UV-NIL must be transparent for the UV-light, therefore materials such as quartz or silica are used. Figure 1.16b shows a quartz stamp fabricated during this thesis at The Molecular Foundry (Berkeley) to be used in the Imprio 55. The nanopatterns on the stamp are directly patterned on HSQ.
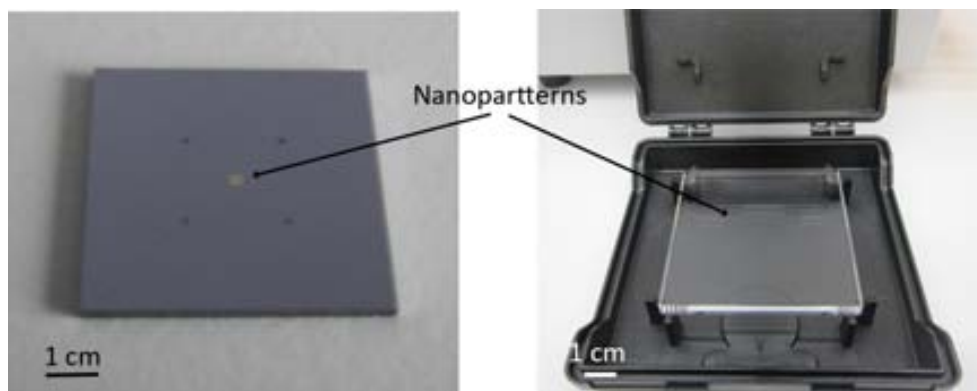
Figure 1.16. a) Image of Si mesa-stamp for thermal NIL fabricated during this thesis at the CNM. b) Image of a quartz mesa-stamp used in Imprio55 (Molecular Imprints). Nanopatterns on the stamp are directly fabricated of HSQ.

Two principal approaches are used to fabricate patterns on the stamp by means of traditional fabrication processes, such as e-beam lithography or photolithography. First one is used to obtain *female* stamps, which means that the patterns are cavities. Second method is suited to produce male stamp, when the patterns come up from the substrate, protrusions. These variants depend on the final patterns desired on the surface. First step is common for both methods, the substrate is covered with a resist that subsequently is exposed by e-beam or photolithography. In case of *female* stamps, Figure 1.17a, remaining resist from lithography is used as mask during the etching of the substrate. For male stamps, Figure 1.17b, after the lithography the patterns are defined in metal by means of lift-off. The remaining metal will behave as mask during the etching of the substrate. At first, fabrication of female stamps seems to be simpler method because it has fewer steps, however the use of resist as mask for dry etching is not a trivial issue. Frequently the resist does not support the entire etching and it is etched before to obtain the desired height of patterns. Moreover, usually it is more complicated to imprint cavities than protrusions, since the resist must flow inside the holes. From female stamp male stamp can be obtained, and vice versa, by performing intermediate imprint and use it as stamp [50].

Furthermore, when the substrate is dielectric material (i.e. quartz), the e-beam exposition could be importantly worsened owing to the charging effects. Several methods have been developed to avoid the distortion of the exposition, such the deposition of a thin metal layer or spincoat a conductive polymer [51].
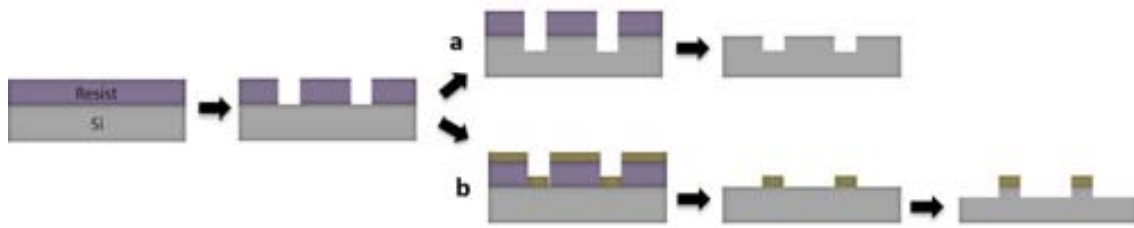
Figure 1.17. Main methods to fabricate nanoimprint stamp by e-beam lithography. After the e-beam lithography and development of the resist: a) the resist is used as a mask during the etching of the substrate. b) Evaporation of metal is performed, the metallic structures remained after the lift-off will behave as mask during the etching of the substrate.

It has been widely demonstrated that when the patterns of the stamp are placed on top of a terrace, it helps to focus the pressure applied during the imprint, consequently more homogeneous imprints are obtained. These type of template are known as mesa-stamps [52,53]. Figure 1.18 represents a mesa-stamp.
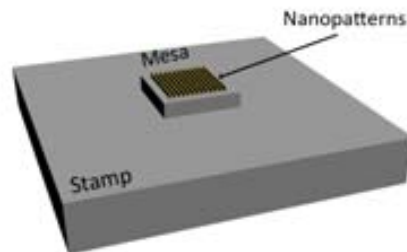
Figure 1.18. Sketch of the mesa-stamp.

Figure 1.19 shows microscope images of two imprints, on the left an imprint performed with a stamp without mesa, a flat stamp. In this stamp there was a large are without patterns and just in a small area nanopatterns. Due to inhomogenities on the stamp surface, resist or on the applied pressure, unsuccessful patterning was achieved. On contrary, picture on the right shows an imprint performed using a mesa-stamp, the imprinted area seems to be homogeneous and the flower-like shape can be appreciated around the mesa.
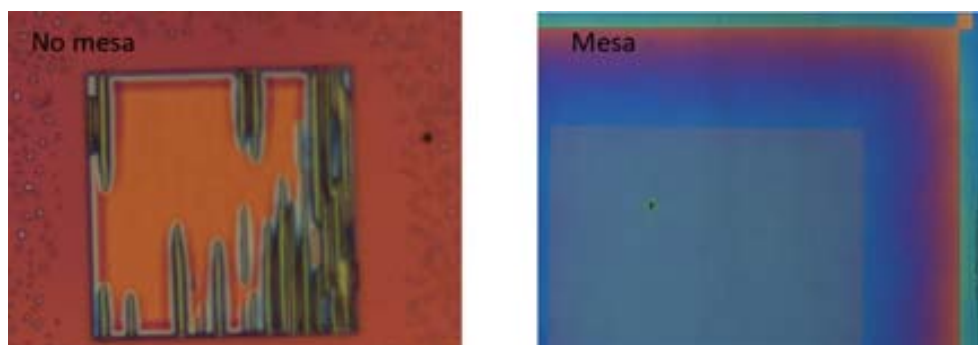
Figure 1.19. Microscope images of a) an unsuccessful imprint performed with a flat stamp. b) Imprint performed using a mesa-stamp. The applied pressure is fussed ion the nanopatterns and homogeneous imprint is obtained.

1.2.1 Anti-sticking layer

Various approaches have been developed to avoid the resist got stuck in the template during the imprint: coat the stamp with an anti-sticking material [54], non-sticking resists [55], non-sticking stamp materials, modification of stamp and resist surfaces, dissolvable polymer stamps [38]. The coating of the stamp with an antisticking material is the most popular method. Silanes are the material usually used to coat the templates. There are different types of silanes, during this thesis 1H, 1H, 2H, 2H-perfluo-octyltriethoxysilane (FTS13) have been used. As Figure 1.20 represents, silanes react with the OH groups in the surface of the stamp, while HCl is released.
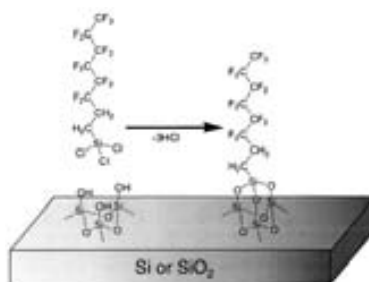
Figure 1.20. Sketch of the silanes reaction on the Si or SiO$_2$ surface [54].

For the coating of the stamp with silanes, first of all the template is subjected to 3 minutes of oxygen (or ozone) plasma to enhance the formation of OH groups on the surface. Then the template is exposed to FTS13 atmosphere in vacuum during one hour. The vacuum is used on the one hand to obtain a clean deposition of the product, but also to avoid the reaction of the FTS13 with the atmospheric water particles.

Figure 1.21. Globe box used to deposit silanes under vacuum atmosphere.

The time that the stamp must be under silanes atmosphere is relevant issue for the proper coating. The contact angle between the sample and a droplet of water was measured for that. As Figure 1.22 demonstrates, when the sample is

not silanized the silicon surface is totally hydrophilic, however, when anti-sticking layer is deposited it becomes hydrophobic, so the resist does not get stuck. It was seen that 30 min on silanization was the optimum time to deposit the anti-sticking layer.

No silanized	15 min silanization	30 min silanization
65°	98°	107°
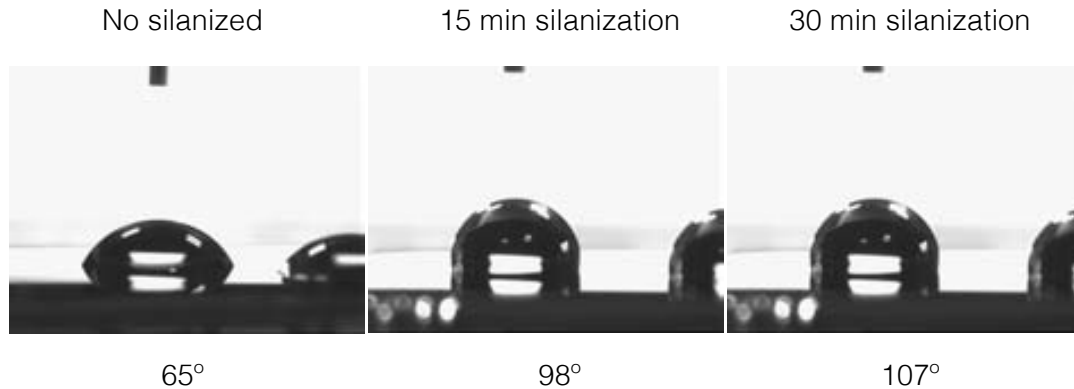
Figure 1.22 Calibration of the silanization time. When the sample does not have anti sticking layer it is totally hydrophilic. When the sample is silanized it become hydrophobic.

1.3 NIL MATERIALS

Many polymers can be imprinted with high resolution, and even polymers without known thermoplastic behavior can sometimes be patterned using pressure or/and heat [56,57]. Certainly, the suitable polymers to be used in NIL must be easily deformable under applied pressure and should have a sufficient mechanical strength as well as good mold-releasing properties to maintain their structural integrity during the de-molding process. For some application it is also highly recommended to have good etching properties for the subsequent dry etching [46,58].

Nanoimprint resist are usually divided in two main groups, the resist used for thermal NIL and resist for UV NIL.

The ideal polymers used in thermal NIL are the ones who have a defined T_g, such as PMMA, what provides better control of the viscosity. These kind of polymers usually have low molecular weight (Mw), typically between 25 and 100 kg/mol. Besides, when UV-NIL is performed, the resist must be sensible to the UV light, it changes from liquid state to solid when UV light is applied.

In the last decades big effort have been done to improve and find method to perform nanoimprint lithography. Nowadays, even the optimization of the NIL is still going on, the attention has been focus in the possibility to imprint new materials. Polymers have been usually patterned by Nil to create an intermediate mask for the subsequent processes. However, NIL has also

23

interesting applicabilitys on the structuration of functional materials, for instance directly patterned titania-based polymer [59].

1.4   POST PROCESSING

Frequently, the fabrication of a device does not end with the nanoimprint lithography, normally the patterns are desired to be transfer into the substrate or defined on other materials, like metals. The process occurred after the NIL are so-called *post-processes*, In Figure 1.23 some of the most common combinations are showed.
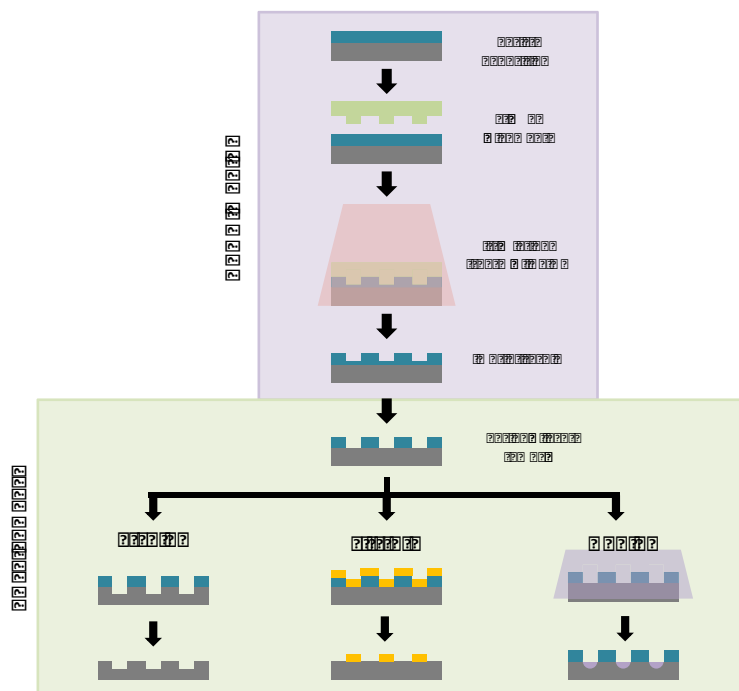
Figure 1.23. Lithography process and post-processes. In general, the first stage is to create a resist mask by NIL process and then several post-processes are possible, such as etching, lift-off or doping.

1.4.1   Residual layer

After all imprint processes there is an unavoidable thin layer of polymer remaining under the stamp, so-called residual layer.   Stefan's equation evidence that the displacement of fluid over large distance via thin channels requires a large force, or small displacement rate [38]. In particular, as the residual layer becomes very thin, the resistance grows rapidly, and it is no longer possible to displace all the material within a finite time:

$$F = -\frac{3\pi R^4}{4h_0^3}\frac{dh}{dt}\eta_0$$

In this equation F is the applied force, R is the disc radius, $2h_0$ is the separation between the discs and η_0 is the viscosity of the fluid. More detailes about the explanation Stefan's equation can be found in [38]

In the cases that it is desired to transfer the pattern to the substrate, the removal of the residual layer is necessary, represented in Figure 1.24.
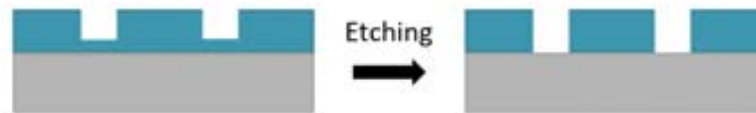
Figure 1.24. Removal of the residual layer after nanoimprint lithography.

Since reaction ion etching (RIE) has high control on the directionality, it is typically used to etch the residual layer. But also wet etching or other etching techniques can be used. It is usually stated that the maximum resolution achievable by nanoimprint is directly related with the dimensions of the patterns in the stamp. Nevertheless, when a post-process is needed, it must be also considered that the rougher techniques used to remove the residual layer could reduce the control of the critical dimension (CD).

1.4.2 Pattern transfer

As it is graphically explained in Figure 1.23, after the removal of residual layer, different fabrication approaches can be followed. The remaining resist can be straight used as a mask, so the obtained patterns will be cavities in the substrate. The resist can be also used as mask to exclusively dope exposed areas. If metallic patterns are targeted, metallization of the sample and lift-off must be performed. The lift-off process has been repeatedly used along this thesis, it is explained on detail in Annex 1.

1.5 NIL: USE AND APLICATIONS IN INDUSTRY

Nanoimprint lithography is being widely used and demonstrated as useful for research technology. Reflection of that effect is then enhancement of published papers related to NIL. Every year the number of paper importantly increases, specially in Asia, where they move to publish few tens of paper between 1995 and 2000, to be the first producer with almost 1700 papers between 2006 and

2011. Comparing to the past, Europe was ahead but has not been able to keep up with the fast growing nanoindustries in Asia.

The development in patents is similar to the articles. Asia has grown quickly and has now more patents than Europe. Although North America has slightly more patents than Asia, which indicates that, they too are developing and using this area of nanoscience more and more. These dates can be observed in Figure 1.25.
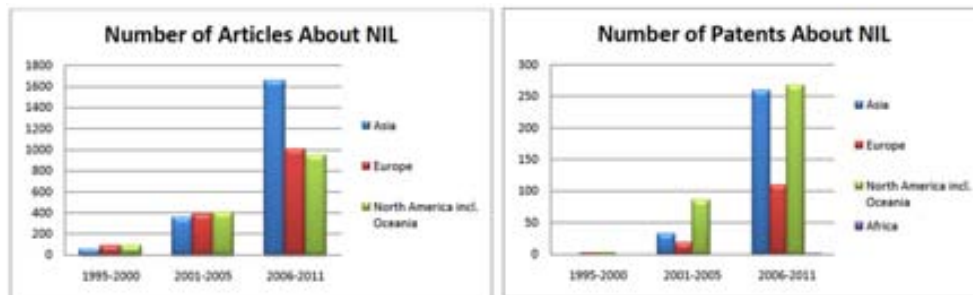
Figure 1.25. Enhancement of (left) published papers and (right) patents during the last years in Asia, America and Europe.

However, it is being harder to make it a room in the industry. The resolution obtained by nanoimprint is more than enough to achieve the exigencies established by the semiconductor roadmap. The simplicity and price of NIL is also an advantage to introduce in the industry. However, the defectivity and low yield are till now the most critical technical issues [60]. Even in the last decades hard work have been done to reduce the density of defects in the imprints, it is still too high for some industry application. Defects can be originated from many sources, from template or wafers to the process and materials. Due to the fact that NIL is contact technique, that is the stamp and the substrate are in physical contact, any imperfection in the process is crucial. When a particle is placed between the template and substrate, the defect is not restricted to this area, but also the surrounding area (even the hole imprint) can be affected. Moreover, in step & flash process, the fact that the stamp becomes dirty in one imprint, it will have negative influence in the subsequent imprints [61].

In Figure 1.26 some of the most common nanoimprint defects are collected [62]. Line break, mouse bite and bridge are general defects in all lithography process. Non-fill or Z axis defect are specifics defect from nanoimprint. The rest of defects are owing to particles before, during or after the NIL process.
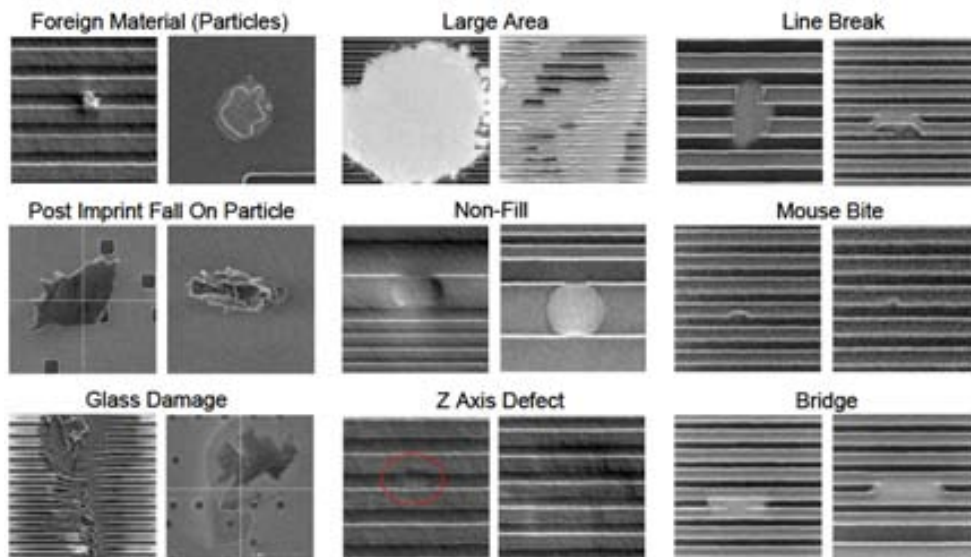
Figure 1.26. SEM imagen of the most common defects in nanoimprint lithography. [62]

Though nanoimprinting has been developed for 17 years, many people have been focusing on the electronic and magnetic recording applications that have extremely stringent requirement on defectivity level. But there are plenty of other applications that are defect tolerant, such as LED fabrication developed by Kim et al. [63,64] or the recently conducted research on dissolving microneedles to create a better and less painful way to insert vaccines and drugs [65].

One of the recently developed successful application of nanoimprint lithography in the industry is the Kindle Paperwhite ebook from Amazon [66]. The main component to illuminate the screen has been structured by nanoimprint. Essentially, there is an optical fiber that is laid across the display and a nanoimprinted light guide helps provide the even distribution of light, this mechanism can be seen in Figure 1.27. More information can be found in this video [67].
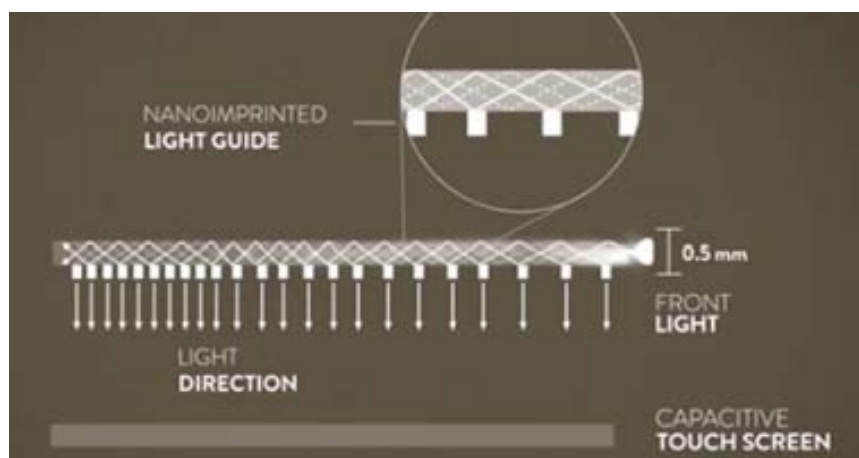
Figure 1.27 Kindle Paperwhite light distribution mechanism [66].

1.6   STRUCTURATION OF A NOVEL THERMAL NIL POLYMERS

Normally, nanostructuration of thermoplastic polymers by nanoimprint lithography is performed as a low-cost alternative to other lithographys, such as e-beam lithography. However, it can be also used to structure polymers that are not sensible to electrons, for instance PTT, PET, PVC… As part of this thesis nanostructuration of semicrystaline polymers have been performed for three main applications: i) PTT and PET as alternative polymer to fabricate soft lithography stamps. ii) P(VDF-TrFE) ferromagnetic copolymers to be used in non-volatile memories. And iii) PBCA as model amorphous polymer to study the capability of Grazing Incidence Small Angle X-ray Scattering (GISAXS) technique to characterize NIL stamps and nanoimprinted polymers, Figure 1.28.
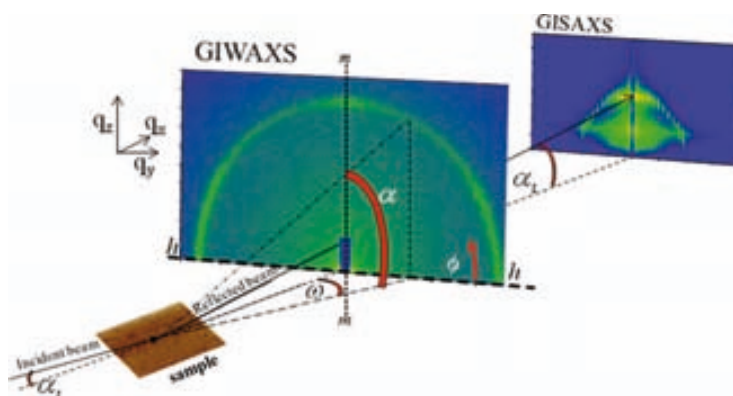
Figure 1.28. Scheme of a GIWAXS and GISAXS experiment. The scattering plane, containing both the direct and the specular beams, intersects the 2D detector along the meridian, m-m line. The horizon, h-h line, is the intersection between the sample and the 2D detector planes that are perpendicular to each other. Each point on the pattern can be characterized by the exit angle, a, and the out of scattering plane angle x. In the detector plane, an azimuth angle / can be defined useful to account for oriented patterns. A much longer sample-to-detector distance is required for a GISAXS experiment tan for a GIWAXS one. The incidence angle was enlarged for the sake of clarity.

These works were performed in collaboration with the group of Professor Tiberio Ezquerra in the Instituto de Estructura de la Materia, from CSIC in Madrid. This group is expert in fundamental physical characterization of materials, they performed the characterization and analyses of the samples at the BW4 beamline (HASYLAB, DESY, Hamburg, Germany). The fabrication of the stamps for thermal nanoimprint and the sample preparation (i.e. optimization of the polymer layer deposition and nanoimprint lithography process) were performed at the CNM.

1.6.1 Nanostructuration of semi-crystalline polymers by thermal NIL

Semicrystalline polymers, as for example PET (poly(ethyleneterephthalate)) and PTT (poly-(trimethylene terephthalate)), represent approximately two thirds of the annual production of synthetic polymers. As a consequence of their large polymer chain length, their intrinsic structure alternates regions of crystalline and amorphous phases, with dimensions in the range of nanometers. They present great versatility in terms of mechanical performance because the crystalline phase can provide the system with a high resistance to fracture (strength) while the amorphous one can provide a high capacity for mechanical energy absorption before fracture (toughness). One possibility is to use these polymers to fabricate stamps for soft lithography, as an alternative to PDMS, provided that they can be structured at the nanometer scale. In this context, we have studied the possibility to structure the surface of semi-crystalline polymers at the nanometer scale by using thermal nanoimprint lithography. Recent works have shown a similar approach [68,69].

PET and PTT were dissolved in trifluor acetic acid at a concentration of 20 mg/mL and deposited on silicon substrates by spin coating, obtaining uniform layers of 120-170 nm thickness as measured by ellipsometry. The films prepared in this way were amorphous as determined by Grazing Incidence X-ray Scattering and Atomic Force Microscopy (AFM). Mesa-type silicon stamps were used, the area of the mesa was 2 x 2 mm^2, (250 nm height) and it was fabricated by means of optical lithography and wet isotropic silicon etching (see appendix 4). On top of each mesa, arrays of lines with pitches from 150 nm to 250 nm were defined by electron beam lithography on a 100 nm layer of PMMA 950 k, 20 nm of aluminum evaporation and resist lift-off. The resulting metal patterns were used as a mask for reactive ion etching, height of the lines was 140 nm. Before the imprinting process, stamps were silanized in order to avoid the sticking of the polymer. Figure 1.29 represents the mesa-stamp and in appendix 3 more details od the mesa fabrication can be found.
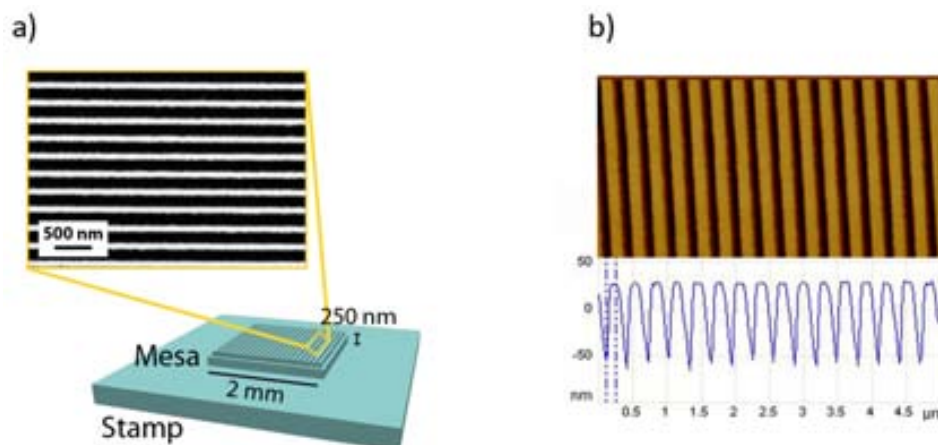
Figure 1.29 Mesa-stamp used for this work. a) Sketch of the patterns on top of the mesa-stamp and SEM image of the patterns. b) AFM image of the stamp.

Optimal conditions for the imprinting process were investigated. It was necessary to perform the process at temperatures considerably higher than the polymer glass transition temperature PTT (T_g = 44ºC) and PET (T_g = 75ºC). Figure 2 and 3 show examples of imprints performed on PTT under the following conditions: Temperature: 150 ºC, pressure: 40 bar and time: 300 s.
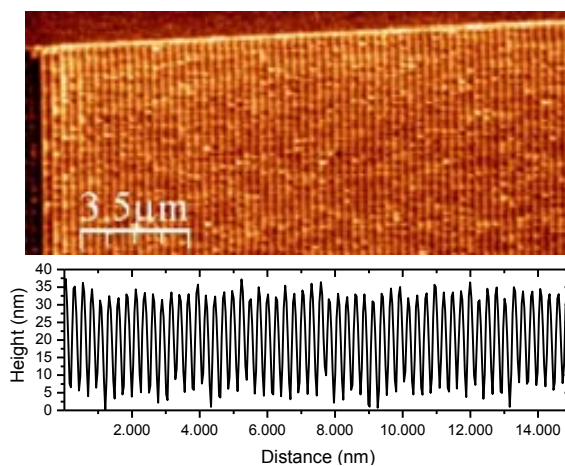
Figure 1.30 AFM image of the nanoimprinted PTT layer.

1.6.2 GISAX experiments for the stamp and imprints characterization

Structural characterization of nanoimprint lithography stamps and structured polymers are commonly accomplished by scanning electron microscopy and atomic force microscopy. The visualization of nanostructures in real space has obvious advantages since it allows direct morphological and topographical information about the patterning to be obtained. However, quite frequently visualization is restricted to small and superficial areas of the sample. Unlike microscopy, X-ray scattering techniques provide structural information in the reciprocal space. In principle, any array of motifs arranged periodically along a specific direction will be easily recognized by its X-ray diffraction pattern recorded with the X-ray beam perpendicular to the direction of periodicity. In this case, the X-ray pattern should exhibit intensity spots on a line, the separation between spots being proportional to the reciprocal of the period. To perform X-ray diffraction on surface nanostructures it is very convenient to work under total X-ray reflection conditions [70]. The diffraction pattern provides statistical information integrated over a large sample area covered by the footprint of the incident beam on the material surface. Therefore, the scattering pattern can deliver structural information averaged over an area of several tens of micrometres. Consequently, diffraction can provide supplementary information to microscopy. The technique of grazing-incidence small-angle X-ray scattering

(GISAXS) has been successfully applied to structurally characterize a great variety of surfaces of both hard [70,71] and soft materials [72,73].

The potential of grazing-incidence X-ray scattering techniques have been evaluated for the structural investigation of both hard (stamp) and soft (polymer) model gratings [74].

Hard silicon gratings (Si thermal NIL stamp) consisting of arrays of lines and trenches were fabricated on mesa-type silicon stamps. The area of the mesa was typically 2 x 2 mm (250 nm height) and it was defined by means of optical lithography and wet silicon etching. On top of each mesa, arrays of lines with width from 100 to 150 nm were defined by EBL and lift-off. Lines of 60 nm width, 300 nm pitch and 150 nm height lines were obtained, Figure 1.31a.

Poly(bisphenol A carbonate) (PBAC) (Lexan ML3021A,SABIC I-P(Innovative Plastics), $Mw=44.4 \cdot 10_3$ g/mol, $M_n=23.5 \cdot 10_3$ g/mol has been used as a model amorphous polymer. PBAC exhibits a glass transition temperature $T_g = 145^oC$. PBAC was dissolved in chloroform, with a concentration of 20 g/L. Polymer films with a thickness of about 150 nm was obtained by spin coating. Gratings on PBAC polymer were obtained by imprinting 150 nm polymer layer, previously spin coated. Above depicted stamp was used to perform the imprints, at temperature of 180 ^oC, 40 bar and 5 minutes, Figure 1.31b.
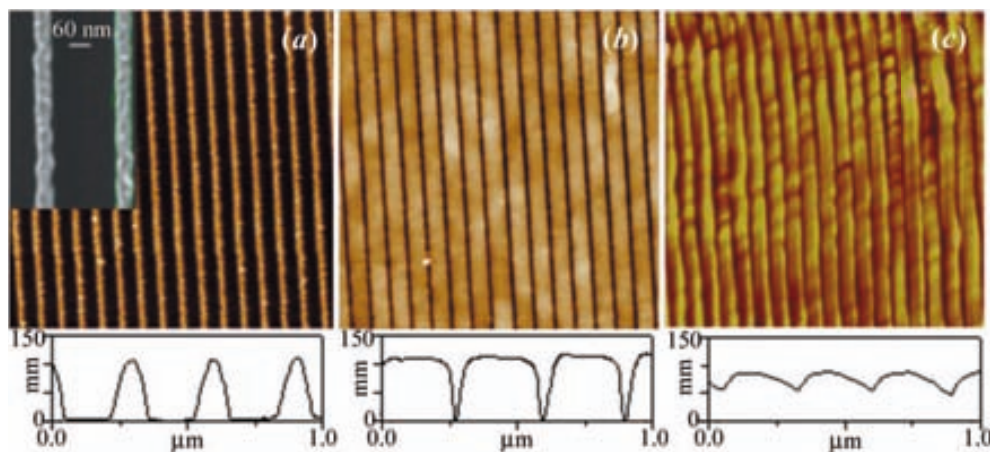
Figure 1.31 AFM height images (5 _ 5 **m**m) of (**a**) the hard grating nanofabricated on silicon by e-beam lithography, (**b**) the soft grating nanofabricated on poly(bisphenol A carbonate) by nanoimprint lithography by using the hard grating shown in (**a**) as a stamp, and (**c**) the soft grating nanofabricated on poly(bisphenol A carbonate) by LIPSS. The height profile along a line perpendicular to the ripples/lines is shown below. The inset in (**a**) is a SEM image of the sample.

Figure 1.32 shows characteristic GISAXS patterns for the different gratings investigated here. The hard silicon grating (Figure 1.32a) exhibits, as the dominant feature, the presence of spots on a semicircle whose radius is related to the incidence angle used ($\alpha i \approx 0.4^o$). These spots are accompanied by weaker

scattering in the vertical direction. The spots are consecutive orders of the first one (nearest to ω=0°) and their spacing is related to the grating pitch. Essentially similar features are observed for the soft grating nanofabricated on PBAC by NIL by using the silicon hard grating as a stamp Figure 1.32b. These results were compared with PBAC structured by laser induced periodic surface structuring (LIPSS), Figure 1.31c. However, a very different pattern is observed. Here scattering is distributed on elongated vertical rods along the ω axis; these rods are also consecutive orders of the first one and their spacing is the reciprocal value of the grating pitch. For this pattern the use of a circular beam stop, instead of the vertical stripe one, allows us to see the scattering along the meridian ($ω = 0°$).

It has been previously reported that the reciprocal space of a grating observed at grazing angles consists of many truncation rods reflecting the periodicity of the grating [75,76]. The scattering pattern at grazing angles of such systems has been interpreted as being due to the intersection of the truncation rods with the Ewald sphere, giving rise to the appearance of diffraction spots located on a semicircle [71]. Besides the characteristic scattering on the semicircle, the patterns shown in Figs. Figure 1.32a and Figure 1.32b exhibit significant scattering around α= 0.2°. It is known that at exit angles equal to the critical one there is an amplification of the scattering signal, referred to as a Yoneda peak, which indicates the presence of diffuse scattering [77]. This effect is even clearer for the LIPSS grating (Figure 1.32c). More results and simulation of the GISAXS pattern have been reported in [74]. As conclusion it can be stated that GISAXS can be used to structurally characterize hard and soft gratings of nanotechnological interest. GISAXS patterns of different hard and soft gratings, recorded with the lines parallel to the beam, present characteristic features that can be associated with the level of order along the direction of periodicity and the length of the lines.
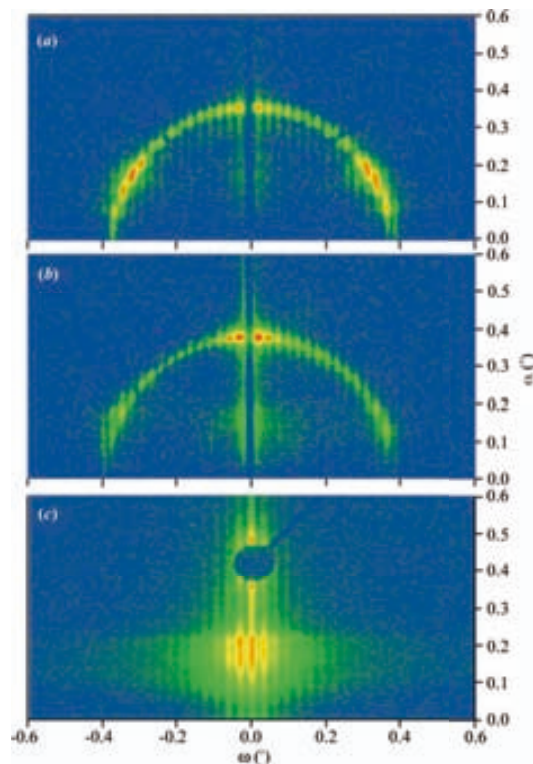
Figure 1.32 Experimental DISAXS pattern of (**a**) the hard Si grating, (**b**) the soft polymer (PBAC) grating nanofabricated by NIL and (**c**) the soft polymer (PBAC) grating nanofabricated by LIPSS.

1.6.3 Structuration of ferroelectric polymers by thermal NIL

The development of polymer non-volatile memories, defined as devices where the information is stored permanently without the requirement of continuous electrical feed, depends on the effective fabrication of devices with high density of information. Several prototypes have already been proposed [78]. In principle, the simplest approach would be to use single spin-coated thin films of ferroelectric materials, with thickness smaller than 100 nm, and with the possibility of a readily integration with flexible complementary metal oxide semiconductor devices or other organic electronic devices [79]. Poly(vinylidene fluoride-co-trifluoroethylene) copolymer P(VDF-TrFE), are mostly proposed candidates for the development of organic memories since they exhibit excellent ferro, piezo and pyroelectric properties.

However, P(VDF-TrFE) thin films typically exhibit roughness levels that make them not suitable for the development of nanocontrolled devices [80]. As revealed by recent Piezoresponse Force Microscopy (PFM) studies [81], the control of the polarization in P(VDF-TrFE) thin films can be problematic mainly due to the strong heterogeneity of the crystalline morphology leading to non-uniform local fields which leads to remote domain nucleation and non-uniform spreading of the ferroelectric domains, see Figure 1.33a.

In this work, it was developed nanogratings on thin films of P(VDF-TrFE), prepared by thermal nanoimprint, to improve the management of writing and reading high density of information [49].

P(VDF-TrFE) 76/24 was solved in N,N-dimethylacetamide (Sigma-Aldrich) with a concentration of 40 g/l. it was spincoated to obtain 100 nm thick layer of polymer. Silicon stamp used to perform the imprints was a silicon stamp prepared by electron beam lithography, metal deposition lift-off, and reactive ion etching. The nanostructured array on the stamp covers an area of (1.5 x 1.5 mm^2). The resulting height of the lines was 135 nm, as determined by Atomic Force Microscopy (AFM). The arrays of lines and trenches were fabricated on mesa-type silicon stamps to facilitate the imprinting process (see annex 4). The area of the mesa was 2 x 2 mm^2 and 400 nm height, it was defined by means of optical lithography and wet silicon etching. To facilitate stamp separation after embossing, stamps were coated with a monolayer of perfluorodecyltrichlorosilane deposited from the gas phase. The imprints were performed with the thermal NIL form Obducat laced at the clean room of the CNM. The imprints were performed at 180 ºC and 40 bar during 5 minutes.
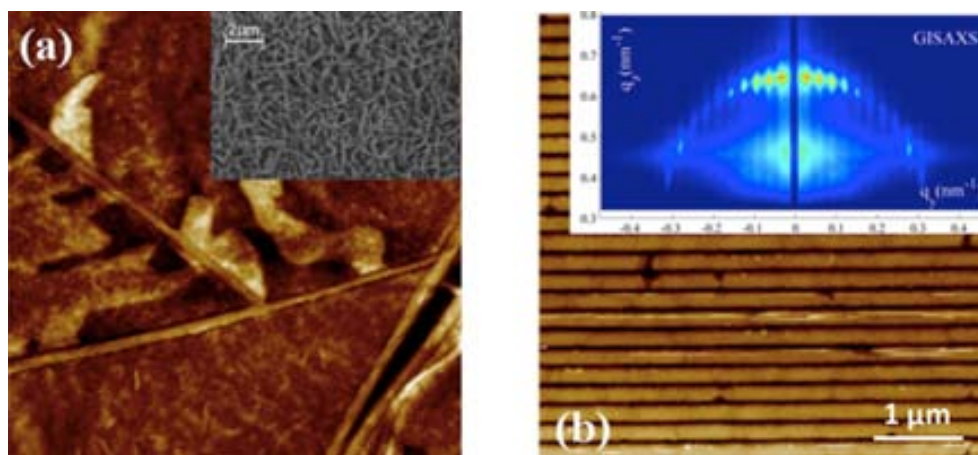
Figure 1.33AFM topography images of a) P(VDF-TrFE) thin film (inset shows a SEM micrograph) and of b) P(VDF-TrFE) grating prepared by NIL. Inset shows a GISAXS pattern.

The obtained structuration of the ferroelectric polymer was characterized by AFM Figure 1.33b and SEM. This morphology was also supported by GISAXS experiments, Figure 1.33b, which were performed at the BW4 beamline (HASYLAB, DESY, Hamburg, Germany). Details about the experiments and farther results are depicted in [49].

This results evidence that nanostructuring by NIL can be a straight forward approach to improve the control of the polarization in ferroelectric polymer films that can readily become an alternative to produce organic ferroelectric memories.

REFERENCES CHAPTER 1

1. Josep Saldaña, V. P. *Nanoparticles before nanotechnology*. Vol. ebook series 3 (2013).

2. Saison-Francioso, O. *et al.* Plasmonic Nanoparticles Array for High-Sensitivity Sensing: A Theoretical Investigation. *The Journal of Physical Chemistry C* 116, 17819-17827, (2012).

3. Sanvicens, N. & Marco, M. P. Multifunctional nanoparticles – properties and prospects for their use in human medicine. *Trends in Biotechnology* 26, 425-433, (2008).

4. Eustis, S. & El-Sayed, M. A. Why gold nanoparticles are more precious than pretty gold: Noble metal surface plasmon resonance and its enhancement of the radiative and nonradiative properties of nanocrystals of different shapes. *Chemical Society Reviews* 35, 209-217, (2006).

5. Jain, P., Huang, X., El-Sayed, I. & El-Sayed, M. Review of Some Interesting Surface Plasmon Resonance-enhanced Properties of Noble Metal Nanoparticles and Their Applications to Biosystems. *Plasmonics* 2, 107-118, doi:10.1007/s11468-007-9031-1 (2007).

6. Kittelson, D. B. Engines and nanoparticles: a review. *Journal of Aerosol Science* 29, 575-588, (1998).

7. ITRS. http://www.itrs.net/news.html.

8. F, H., Y, S., A, G., MA, M. & L, B. Polymer imprint lithography with molecular-scale resolution. *Nano Lett.* 4, 2467 (2004).

9. Cavin, R. K., Lugli, P. & Zhirnov, V. V. Prolog to the Section on Science and Engineering Beyond Moore's Law. *Proceedings of the IEEE* 100, 1718-1719, (2012).

10. ITRS. http://www.itrs.net/Links/2011ITRS/2011Chapters/2011Lithography.pdf.

11. Han, K.-S. *et al.* Fabrication of 3D nano-structures using reverse imprint lithography. *Nanotechnology* 24, 045304 (2013).

12. Stewart, M. D., Johnson, S. C., Sreenivasan, S. V., Resnick, D. J. & Willson, C. G. Nanofabrication with step and flash imprint lithography. *Journal of Micro/Nanolithography, MEMS, and MOEMS* 4, 011002-011002, (2005).

13. Irmscher, M. *et al.* High resolution nanoimprint templates for dual damascene: fabrication and imprint results. 69210D-69210D, (2008).

14. Chou, S. Y., Krauss, P. R. & Renstrom, P. J. 4129-4133 (AVS).

15. Fernanadez-Cuesta, I. *NanoImprint Lithography: Developments and nanodevice fabrication*, UAB, (2009).

16. Senn, T. *Process development for nanostructuring and 3D micro/nanointegration*, (2012).

17. Costner, E. A., Lin, M. W., Jen, W.-L. & Willson, C. G. Nanoimprint Lithography Materials Development for Semiconductor Device Fabrication. *Annual Review of Materials Research* 39, 155-180, (2009).

18. Plachetka, U. *et al.* Wafer scale patterning by soft UV-nanoimprint lithography. *Microelectronic Engineering* 73, 167-171 (2004).

19. Y, X. & GM, W. Soft lithography. *Annu. Rev. Mater. Sci.* 28, 153 (1998).

20. SA, R. & CS, C. Microcontact printing: a tool to pattern. *Soft Matter* 3, 168 (2007).

21. 3D Microstructured Surfaces Obtained by Soft-Lithography Using Fast-Crosslinking Elastomeric Precursors and 2D Masters. *Advanced Functional Materials* (2007).

22. Devaraju, N. S. G. K. & Unger, M. A. Pressure driven digital logic in PDMS based microfluidic devices fabricated by multilayer soft lithography. *Lab on a Chip* 12, 4809-4815 (2012).

23. Gates, B. D. *et al.* New approaches to nanofabrication: molding, printing, and other techniques. *Chemical reviews* 105, 1171-1196 (2005).

24. Xia, Y. & Whitesides, G. M. Soft lithography. *Annual review of materials science* 28, 153-184 (1998).

25. Eleftheriou, E. *et al.* Millipede - a MEMS-based scanning-probe data-storage system. *Magnetics, IEEE Transactions on* 39, 938-945, (2003).

26. Khang, D. Y., Yoon, H. & Lee, H. H. Room-Temperature Imprint Lithography. *Advanced Materials* 13, 749-752, (2001).

27. Sun, H., Liu, J. & Chen, D. Nanoimprint lithography for complex 3D micro-nano structures replication under low temperature. 74020U-74020U, (2009).

28. Khang, D.-Y. & Lee, H. H. Room-temperature imprint lithography by solvent vapor treatment. *Applied Physics Letters* 76, 870-872 (2000).

29. Mele, E., Di Benedetto, F., Persano, L., Cingolani, R. & Pisignano, D. Multilevel, Room-Temperature Nanoimprint Lithography for Conjugated Polymer-Based Photonics. *Nano Letters* 5, 1915-1919, (2005).

30. Kim, J. Y., Choi, D.-G., Jeong, J.-H. & Lee, E.-S. UV-curable nanoimprint resin with enhanced anti-sticking property. *Applied Surface Science* 254, 4793-4796, (2008).

31. M., C. *et al.* Step and flash imprint lithography: a new approach to high-resolution patterning. *SPIE* (199).

32. Stuart, C. & Chen, Y. Roll in and Roll out: A Path to High-Throughput Nanoimprint Lithography. *ACS Nano* 3, 2062-2064, (2009).

33. Ahn, S. H. & Guo, L. J. Large-Area Roll-to-Roll and Roll-to-Plate Nanoimprint Lithography: A Step toward High-Throughput Application of Continuous Nanoimprinting. *ACS Nano* 3, 2304-2310, (2009).

34. Dumond, J. J. *et al.* High resolution UV roll-to-roll nanoimprinting of resin moulds and subsequent replication via thermal nanoimprint lithography. *Nanotechnology* 23, 485310 (2012).

35. Nanotypos. <http://www.nanotypos.com>

36. Nanotechweb. <http://www.nanotechweb.org>

37. SY, C., PR, K. & PJ, R. Imprint of sub-25 nm vias and trenches in polymers. *Appl. Phys. Lett.* 67, 3114 (1995).

38. Schift, H. Nanoimprint lithography: An old story in modern times? A review. *Journal of Vacuum Science & Technology B: Microelectronics and Nanometer Structures* 26, 458-480 (2008).

39. Hirai, Y. *et al.* 2811-2815 (AVS).

40. Hirai, Y., Konishi, T., Yoshikawa, T. & Yoshida, S. 3288-3293 (AVS).

41. Rowland, H. D., Sun, A. C., Schunk, P. R. & King, W. P. Impact of polymer film thickness and cavity size on polymer flow during embossing: toward process design rules for nanoimprint lithography. *Journal of Micromechanics and Microengineering* 15, 2414 (2005).

42. Scheer, H.-C., Bogdanski, N., Wissen, M., Konishi, T. & Hirai, Y. Profile evolution during thermal nanoimprint. *Microelectronic Engineering* 83, 843-846 (2006).

43. H. D. Rowland, W. P. K., A. C. Sun, and P. R. Schunk. Impact of Polymer Film Thickness and Cavity Size on Polymer Flow during Embossing: Towards Process Design Rules for Nanoimprint Lithography. *Sandia National Laboratories* SAND2006-4864 (2006).

44. Heyderman, L., Schift, H., David, C., Gobrecht, J. & Schweizer, T. Flow behaviour of thin polymer films used for hot embossing lithography. *Microelectronic Engineering* 54, 229-245 (2000).

45. HC, S., M, W., N, B. & S, M. Issues and requirements of polymers for thermal NIL. *J. Photopolym. Sci. Technol.* 20, 539 (2007).

46. Guo, L. J. Recent progress in nanoimprint technology and its applications. *Journal of Physics D: Applied Physics* 37, R123 (2004).

47. Obducat. <http://www.obducat.com>

48. Imprints, M. <http://www.molecularimprints.com>

49. Martinez-Tong, D. E. *et al.* Improving information density in ferroelectric polymer films by using nanoimprinted gratings. *Applied Physics Letters* 102, 191601-191601-191605, (2013).

50. Schulz, H. *et al.* Master replication into thermosetting polymers for nanoimprinting. *Journal of Vacuum Science & Technology B: Microelectronics and Nanometer Structures* 18, 3582-3585 (2000).

51. Peroz, C. *et al.* Digital spectrometer-on-chip fabricated by step and repeat nanoimprint lithography on pre-spin coated films. *Microelectronic Engineering* 88, 2092-2095, (2011).

52. Taylor, H., Smistrup, K. & Boning, D. Modeling and simulation of stamp deflections in nanoimprint lithography: Exploiting backside grooves to enhance residual layer thickness uniformity. *Microelectronic Engineering* 88, 2154-2157 (2011).

53. Schleunitz, A., Spreu, C., Haatainen, T., Klukowska, A. & Schift, H. Fabrication of mesas with micro-and nanopatterned surface relief used as working stamps for step and stamp imprint lithography. *Journal of Vacuum Science & Technology B: Microelectronics and Nanometer Structures* 28, C6M37-C36M40 (2010).

54. Beck, M. *et al.* Improving stamps for 10 nm level wafer scale nanoimprint lithography. *Microelectronic Engineering* 61–62, 441-448, (2002).

55. Finn, A. *et al.* High aspect ratio pattern collapse of polymeric UV-nano-imprint molds due to cleaning. *Microelectronic Engineering* (2013).

56. Mele, E. *et al.* Polymeric distributed feedback lasers by room-temperature nanoimprint lithography. *Applied Physics Letters* 89, 131109-131109-131103 (2006).

57. Mäkelä, T. H., Majander, P. & Ahopelto, J. (Helsinki, 2005).

58. Schift, H. *et al.* Fast heating and cooling in nanoimprint using a spring-loaded adapter in a preheated press. *Microelectronic Engineering* 84, 932-936, (2007).

59. Pina-Hernandez, C. *et al.* A route for fabricating printable photonic devices with sub-10 nm resolution. *Nanotechnology* 24, 065301 (2013).

60. Malloy, M. & Litt, L. C. Technology review and assessment of nanoimprint lithography for semiconductor and patterned media manufacturing. *Journal of Micro/Nanolithography, MEMS, and MOEMS* 10, 032001-032001, (2011).

61. Hirai, Y., Yoshida, S. & Takagi, N. Defect analysis in thermal nanoimprint lithography. *Journal of Vacuum Science & Technology B: Microelectronics and Nanometer Structures* 21, 2765-2770 (2003).

62. Malloy, M., Litt, L. C., Johnson, S., Resnick, D. J. & Lovell, D. Jet and flash imprint defectivity: assessment and reduction for semiconductor applications. 797006-797006, (2011).

63. Byeon, K.-J., Cho, J.-Y., Kim, J., Park, H. & Lee, H. Fabrication of SiN< sub> x</sub>-based photonic crystals on GaN-based LED devices with patterned sapphire substrate by nanoimprint lithography. *Optics Express* 20, 11423-11432 (2012).

64. Kojima, R., Takahashi, T. & Mizawa, T. UV-Nanoimprint Lithography with Film Mold for LED-PSS Fabrication Process. *Journal of Photopolymer Science and Technology* 26, 105-108 (2013).

65. Kam, K. R. & Desai, T. Nano-and microfabrication for overcoming drug delivery challenges. *Journal of Materials Chemistry B* (2013).

66. Amazon. <http://www.amazon.com>

67. Amazon, K. <http://youtu.be/XrHhLP2TXA4>

68. Hu, Z., Tian, M., Nysten, B. & Jonas, A. M. Regular arrays of highly ordered ferroelectric polymer nanostructures for non-volatile low-voltage memories. *Nat Mater* 8, 62-67 (2009).

69. Rebollar, E. *et al.* Assessment and Formation Mechanism of Laser-Induced Periodic Surface Structures on Polymer Spin-Coated Films in Real and Reciprocal Space. *Langmuir* 27, 5596-5606, (2011).

70. Renaud, G., Lazzari, R. & Leroy, F. Probing surface and interface morphology with Grazing Incidence Small Angle X-Ray Scattering. *Surface Science Reports* 64, 255-380, (2009).

71. Yan, M. & Gibaud, A. On the intersection of grating truncation rods with the Ewald sphere studied by grazing-incidence small-angle X-ray scattering. *Journal of Applied Crystallography* 40, 1050-1055 (2007).

72. García-Gutiérrez, M. C. *et al.* X-ray microdiffraction and micro-Raman study on an injection moulding SWCNT-polymer nanocomposite. *Composites science and technology* 67, 798-805 (2007).

73. Müller-Buschbaum, P. in *Applications of Synchrotron Light to Scattering and Diffraction in Materials and Life Sciences* 61-89 (Springer, 2009).

74. Rueda, D. R. *et al.* Grazing-incidence small-angle X-ray scattering of soft and hard nanofabricated gratings. *Journal of Applied Crystallography* 45, 1038-1045, (2012).

75. Metzger, T., Kegel, I., Paniago, R. & Peisl, J. Grazing incidence x-ray scattering: an ideal tool to study the structure of quantum dots. *Journal of Physics D: Applied Physics* 32, A202 (1999).

76. Baumbach, T. & Lübbert, D. Grazing incidence diffraction by laterally patterned semiconductor nanostructures. *Journal of Physics D: Applied Physics* 32, 726 (1999).

77. Yoneda, Y. Anomalous surface reflection of X rays. *Physical review* 131, 2010 (1963).

78. Kusuma, D. Y. & Lee, P. S. Ferroelectric Tunnel Junction Memory Devices made from Monolayers of Vinylidene Fluoride Oligomers. *Advanced Materials* 24, 4163-4169, (2012).

79. Naber, R. C. G., Asadi, K., Blom, P. W. M., de Leeuw, D. M. & de Boer, B. Organic Nonvolatile Memory Devices Based on Ferroelectricity. *Advanced Materials* 22, 933-945, (2010).

80. Kang, S. J. *et al.* Localized Pressure-Induced Ferroelectric Pattern Arrays of Semicrystalline Poly(vinylidene fluoride) by Microimprinting. *Advanced Materials* 19, 581-586, (2007).

81. Sharma, P., Reece, T. J., Ducharme, S. & Gruverman, A. High-Resolution Studies of Domain Switching Behavior in Nanostructured Ferroelectric Polymers. *Nano Letters* 11, 1970-1975, (2011).

SECTION II

Functional nanoparticles

Functional nanoparticles

A nanoparticle is defined as a single element with individual properties and at least one of its dimensions smaller that 200 nm. Having a size between the molecular and bulk solid-state structures, nanoparticles exhibit hybrid properties. As of today, many of these properties are not completely understood, representing a current challenge for theoreticians. The main characteristic of nanoparticles is their different behavior from the corresponding bulk material, which make them attractive for many new electronic, optical or magnetic applications.

However, "nanoparticles are too often, in scientific and non-scientific circles, perceived as *invented*, while we think they should be understood as *discovered*", as V. Puntes states in [1]. Nanoparticles have been always present in nature, e.g. the aerosol nanoparticles that come off the volcanos [2,3], the diversity of nanominerals [4] or the production of nanotubes during a forest-fire [5]. Furthermore, humans have also used nanoparticles along the history unintentionally, from the Lycurgus cup in 4th century AD [6] to the pigments of the tattoos nowadays [7].

In recent years, many research works have been focused in the study of nanoparticles, analyzing their properties, finding new synthesis routes or applying them in innovative applications. Most of the nanoparticles used in these investigations have been produced at lab-level. Traditionally, nanoparticles have been synthesized by chemical methods, most frequently by the next three: dispersion of performed polymers, polymerization of monomers and ionic gelation or coacervation of hydrophilic polymers. But, with the progress of nanofabrication techniques, more and more physical processes have been developed to fabricate them. These techniques are normally divided in two groups; bottom-up procedures, such as CDV for carbon nanotube growing [8,9], and top-down techniques, usually lithography techniques as stencil, spheres or nanoimprint [10].

This section presents two different approaches on the fabrication and characterization of functional nanoparticles.

Lithography techniques are an especially interesting alternative when nanoparticles arrays of specific shape, size or material are needed and also when a particular distribution of the particles on a substrate is required. However, these techniques have some drawbacks as the lack of definition or high cost. Chapter 3 of this thesis presents a new fabrication approach that

overcomes the mentioned handicaps. The fabrication process is based on the combination of stencil and nanoimprint concepts. These nanoparticles have specific optical characteristics that made them suitable for localized surface plasmon resonance (LSPR) sensors.
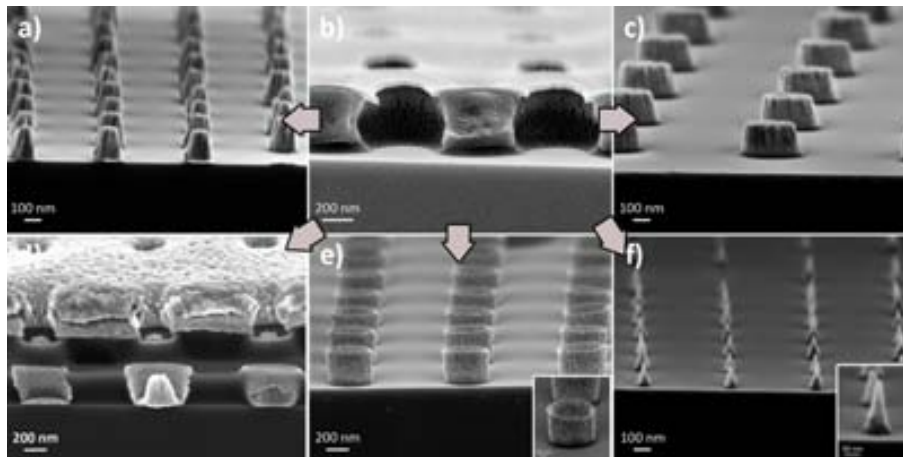

Figure 0.1 (a, c-f) SEM images of the variety of nanoparticles fabricated following the hard-mask nanoimprint process. (b) SEM image of the hard mask before the metallization.

Sensors based on arrays of nanoparticles are of high interest in fields like medicine or environment. On the other hand, the study of single-molecules has motivated the development of sophisticated electronic devices from individual molecules. The primary problems that face the so-called molecular electronics field, are measuring and predicting electron transport. A key requirement in all these studies is the ability to measure the conductivity of a single nanoparticle. Even though several works have reported successful single nanoparticle contacting approaches, up to date there is a lack of reliable and robust methods to contact individual nanoparticles at large scale. Chapter 4 of this thesis presents an innovative technology that allows contacting individual NPs with high degree of reliability. Such a strategy presents several advantages, such as simplified fabrication, high throughput for contacting a large number of single NPs and potentiality for large-scale fabrication.

The proposed technology is based on exploiting the highly insulating properties of a thin nanocomposite layer formed by an epoxy based polymer with embedded, properly functionalized NCs or NPs. The epoxy based polymer serves to support and electrically insulate the NPs. By properly tuning the concentration of the NPs in the host polymer and controlling the nanocomposite film thickness (in order to keep it smaller than the NP diameter), the nano-objects can be individually contacted by using top and bottom electrodes. The control of NP dispersion in the host matrix represents a crucial point in the nanocomposite preparation, since issues as phase separation, aggregation and

inhomogeneous distribution of the nanoscale components in the host phase may occur [11].

In this perspective, the use of colloidal chemistry routes is extremely advantageous as it provides NCs and NPs surrounded by a layer of organic molecules, which coordinates their surface and enables their compatibility with different physical and chemical environment. Thus, the synthesized organic capped NCs and the commercial metal NPs can be embedded in the polymer by simply exploiting the use of a common or compatible solvent for both the polymer and the NPs [12].

AFM characterization of the nanocomposite has shown that a two-dimensional confinement of the nanocrystals inside the polymer layer has been achieved. Preliminary results of the electrical characterization show the feasibility of the technological approach [13].
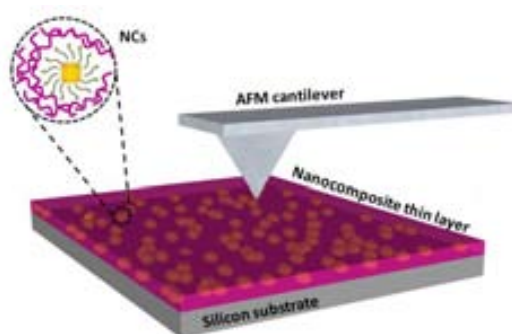

Figure 0.2 Representation of the nanoplatform developed to contact single nanoparticles by AFM tip. The nanoparticles are embedded in an ultrainsulating resist. A very thin layer of the nanocomposite is spincoated on the substrate,

REFERENCES INTRODUCTION SECTION II

1.   Josep Saldaña, V. P. *Nanoparticles before nanotechnology*. Vol. ebook series 3 (2013).

2.   Martin, R. S. *et al.* Composition-resolved size distributions of volcanic aerosols in the Mt. Etna plumes. *Journal of Geophysical Research: Atmospheres* 113, D17211, (2008).

3.   Buseck, P. R. & Adachi, K. Nanoparticles in the Atmosphere. *Elements* 4, 389-394, (2008).

4.   Hochella, M. F. *et al.* Nanominerals, Mineral Nanoparticles, and Earth Systems. *Science* 319, 1631-1635, (2008).

5.   Sassen, K. & Khvorostyanov, V. I. Cloud effects from boreal forest fire smoke: evidence for ice nucleation from polarization lidar data and cloud model simulations. *Environmental Research Letters* 3, 025006 (2008).

6.   Leonhardt, U. Optical metamaterials: Invisibility cup. *Nat Photon* 1, 207-208 (2007).

7.   Høgsberg, T., Loeschner, K., Löf, D. & Serup, J. Tattoo inks in general usage contain nanoparticles. *British Journal of Dermatology* 165, 1210-1218, (2011).

8.   Varanasi, C. V. *et al.* (AIR FORCE RESEARCH LAB WRIGHT-PATTERSON AFB OH, 2013).

9.   Rius, G. *et al.* Response of carbon nanotube transistors to electron beam exposure. *Microelectronic Engineering* 84, 1596-1600, (2007).

10.   Canelas, D. A., Herlihy, K. P. & DeSimone, J. M. Top-down particle fabrication: control of size and shape for diagnostic imaging and drug delivery. *Wiley Interdisciplinary Reviews: Nanomedicine and Nanobiotechnology* 1, 391-404, (2009).

11.   Ingrosso, C., Panniello, A., Comparelli, R., Curri, M. L. & Striccoli, M. Colloidal Inorganic Nanocrystal Based Nanocomposites: Functional Materials for Micro and Nanofabrication. *Materials* 3, 1316-1352 (2010).

12.   Ingrosso, C. *et al.* An Epoxy Photoresist Modified by Luminescent Nanocrystals for the Fabrication of 3D High-Aspect-Ratio Microstructures. *Advanced Functional Materials* 17, 2009-2017 (2007).

13.   Alayo, N., Paniello, A., Striccoli, M., Lucia Curri, M. & Pérez-Murano, F. Towards individual electrical contact of nanoparticles in nanocomposites. *Microelectronic Engineering* 88(8), 2439-2443.

2. Nanoplatform

Nanoparticle science is dedicated to understand the changes in fundamental properties of material as function of the size [1]. In particular, when the nanoparticles has a single-domain crystalline lattice they are so-called nanocrystals (NC) [2]. The high interest in nanocrystals principally comes from the electron confinement provided by NCs, which is a robust instrument to manipulate the electronic, optical and magnetic properties of a solid material [3].

One of the most used applications of nanocrystals has been the fabrication of nonvolatile memory devices. Prime et al. [4], Tseng et al. [5] and others [6-8] fabricated memory devices by a structure consisting of a composite film, i.e. a mixture of nanoparticles and resist, sandwiched between two metal electrodes. The conductive properties of the polymer are improved due to the nanocrystals embedded in it. These works take advantage of the influence of nanocrystals in the bulk composite. However, the work presented by Steinberg et al. [9] shows an approach to study the local charging dynamics on the surface of colloidal nanorods (NR) based on tracing the time domain electrical transport through individual nanorods. Other works around contacting single nanoparticles can be found in the literature [10-12], such as biological sensors [13] or LSPR study of DNA [14].

Due to this explosion of new properties it has originated an intensive research towards the contacting individual nanoparticles that satisfy the unknowns about their single properties and behavior [15-17]. Even though there are some previous works where single nanoparticles characterization has been successfully reported, up to date there is a lack of reliable and robust methods to contact individual nanocrystals with consistency. In this work, an innovative technology that allows to contact individual nanocrystals with high degree of reliability is presented. This technology presents several advantages in comparison with reported methods, such as simplified fabrication, high throughput for contacting a large number of single NCs and the possibility of large-scale fabrication.

This technology consists of a silicon substrate on which a nanocomposite thin layer is deposited. The layer is made of semiconductor nanocrystals embedded in an insulating epoxy based negative photoresist, which serves to insulate and support the nanoparticles (Figure 2.1).
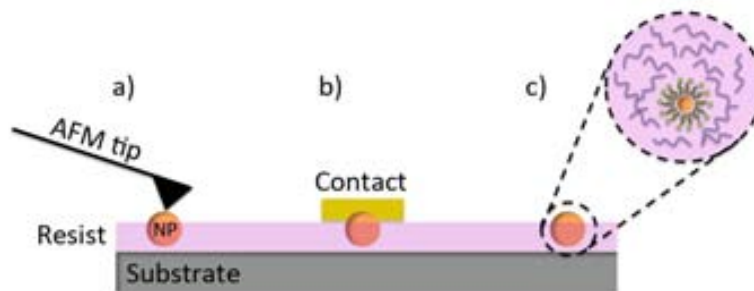
Figure 2.1. Sketch of the technology presented in this work. Different ways to contact nanoobjects: a) by AFM probe or b) conventional contacts. c) Detail of the incorporation on the NP to the polymer by means of ligands.

The incorporation of inorganic NC into polymer material opens a door to the development of composites with new functionalities. Polymer nanocomposites are object of great attention due to the possibility of combing the attractive physical and chemical properties of nanocrystals with the versatile and reliable processing capabilities of polymers.

Nanocomposites are considered to be a high-impact class of material because the particularly attractive characteristic to take advantage of the unique size-dependent properties of nanoparticles into a large-scale production method [18-20]. Because of the high multifunctionality of the nanocomposite materials, they have been studied in many fields such as sensors, light-emitting diodes, optical switches, optical devices, waveguides, etc [21].

This work is developed within the frame of Nanoplatform Project, in which the Nanofabrication group of the *Instituto de Microelectrónica de Barcelona*, IMB-CNM (CSIC) collaborates with a group from the *Consiglio Nazionale delle Ricerche – Instituto per i Processi Chimico Fisici sezione di Bari* (CNR-IPCF), Italy. This project is based on the knowledge generated by the finished FP6 Novopoly (Strep) project [22], in which an epoxy based resist and its insulating characteristics were developed and characterized. Moreover, the feasibility of incorporating NCs in the resist was already confirmed.

The realization of the presented devices has required the adaptation and optimization of existing technologies, synthesis procedures, characterization techniques and protocols. The aim of this fabrication has been the generation of a new and complete understanding of original interactions, interface behavior and/or even unexpected phenomena occurring at NPs and NCs level.

This general objective has deserved the accomplishment of the following partial objectives:

1. Optimization of the synthesis and functionalization of the NPs and NCs to obtain interesting properties, by means of their convenient incorporation into the polymer matrix.

2. Finding the proper conditions to disperse and incorporate the NPs and NCs into the polymer to obtain a uniform density of NPs and NCs.

3. Optimization of the process to create ultrathin layer of nanocomposite on top of the substrate.

4. Development of methods based on nanolithography to fabricate contacting electrodes with precise control, at the nanometer scale.

5. Investigation of the electrical properties of single NPs and NCs, and performing statistics analysis using a large number of single NPs and NCs in order to investigate new and unexpected performances.

At the CNM, the nanocomposite optimization, contact fabrication and characterization of the device (point 3, 4 and 5) have been performed. Whereas synthesis and functionalization of the NCs and the conditions to incorporate them in the polymer were previously developed by CNR-IPCF (point 1 and 2).

2.1. MATERIALS

One of the most important issues in the development of a device is the adequate choice of the used materials. Particularly in this case, that the fabricated system takes advantage of the insulating characteristic of the resist and the semiconducting properties of the NCs. In the present section, the characteristics and synthesis method of the epoxy based resist and the nanocrystals are presented.

2.1.1. Epoxy based resist (mr-EBL 6000.1)

The role of the resist is fundamental for the success of the technology. The resist serves to insulate and support the nanoparticles. The mr-EBL 6000.1 3% Negative Tone Photoresist [23,24] was developed in the frame of FP6 Novopoly (Strep) project [22]. This material is an epoxy based resist similar to SU-8 negative photoresist. Negative photoresist are materials that become insoluble in developing solutions when exposed to optical radiation [25], they were the first materials used to pattern semiconductor devices [26].

mr-EBL 6000.1 resist was chosen for the present development due to its adequate properties, such as its high electrical resistivity (especially after curing) and the capability of achieving ultrathin layers. Other specific properties of the mr-6000.1 resist are: electron beam sensitive, suitable as an etch mask, exhibiting high resistance during dry and wet etching, excellent thermal stability of the resist patterns, high resolution capability and development in organic

solvent. More details of physical properties of the resist solution can be found in [27].

In order to obtain thinner spincoated layer, the viscosity of the resist was reduced. For this purpose Thinner Photoresist ma-T 1045 (Micro-resist technology GmbH) was used, which is basically composed of anisole in the 80-100 % concentration.

2.1.2. Synthesis and properties of nanoparticles

The fascinating properties of nanocrystals are determined by their size, which is intermediate between atomic and molecular size regimes. The synthesis process of nanoparticles must be carefully optimized and carried out, since this is the point that controls the growth of the particles.

The synthesis of the nanoparticles have been carried out by Dr. Lucia Curri, Dr. Marinella Striccoli and Dr. Anna Paniello from Consiglio Nazionale delle Ricerche – Instituto per i Processi Chimico Fisici sezione di Bari (CNR-IPCF), partners in Nanoplatform project.

After the synthesis of the nanocrystals they are incorporated in the resist in order to create nanocomposite. The addition of the NC must be done with a precise control of the dispersion. One of the most decisive points for this process relies on controlling the dispersion of the nanoparticles in the polymer. Actually, NPs keep a strong tendency to aggregate, which is harmful to maintain their size-dependent properties. Three main ways to overcome this difficulty can be found in the literature: a) adding inorganic precursor to the polymer, b) mixing the nanoparticles with monomers or c) coating the nanoparticles with polymeric ligands and mix them with the polymer (Figure 2.2) [28].
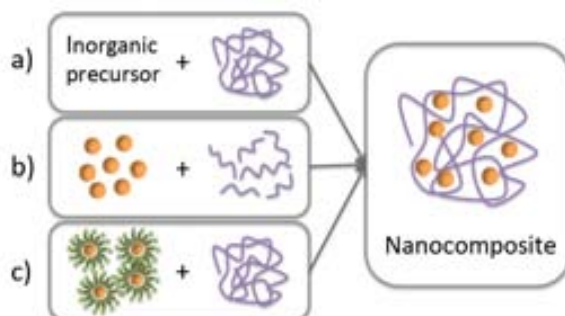

Figure 2.2. The three main method used in the bibliography to create nanocomposites. a) adding inorganic precursor to the polymer. b) Mixing the nanoparticles with monomers. c) Coating the nanoparticles with polymeric ligands.

The method followed in the current work is to attach a polymeric ligand to the nanocrystals and then mix them with the resist, Figure 2.2c, which help their processing and the dispersion in the polymer. A suitable ligand should have in one side high affinity for nanoparticles surface (e. g. amine, thiol or phosphoric group) and in the other side a functional group that allows the solubility of the nanoparticles in different solvents like a polymer (such as alkyl chain) [29]. Figure 2.3 shows a sketch of a nanoparticle covered by a bifunctional ligand.
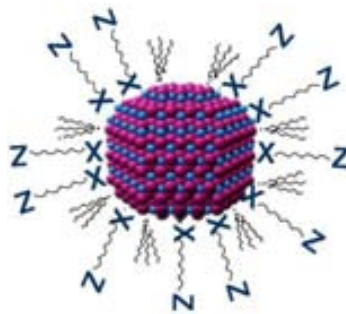

Figure 2.3. Surface functionalization of nanoparticles to enhance their affinity to the polymer. X represents a chemical functional group with a high affinity for nanoparticles. Z represents a functional group that allows the solubility of the NPs in the polymer.

The synthesis and functionalization of the nanoparticles' surface was done simultaneously by a chemical synthesis technique, specifically, by Colloidal Solution method. The colloidal system consists of dividing one of the substrates in tiny particles and disperses them over a second substrate. Normally, the size of the colloidal particle ranges between 1 nm and 1μm.

High temperature was applied to dissociate the organometallic precursors in the presence of surfactants which dynamically coordinate the NCs surface. The surfactants control particle growth and prevent aggregation. The process was monitored at real time by UV spectroscopy. Furthermore, characterization of the NCs was performed after the synthesis by Infrared (IR), transmission electron microscopy (TEM) and X-ray Diffraction (XRD).

For this project different type of nanocrystals and nanoparticles have been used in order to characterize their electrical and optical properties: TiO_2, Fe_2O_3, CdSe/ZnS and Au commercial nanoparticles. Their synthesis and characterization are described in the next sections.

2.1.2.i. TiO_2 nanoparticles

The prepared TiO_2 nanorods have elongate shape and size around 3-5 nm x 10-30 nm. The particles present semiconducting, photocatalytic and optical characteristics [30]. Figure 2.4a shows TEM image of synthesized TiO_2 nanaorods and in the right graph it can be seen that its maximum absorbance happens at 325 nm wavelength [31].
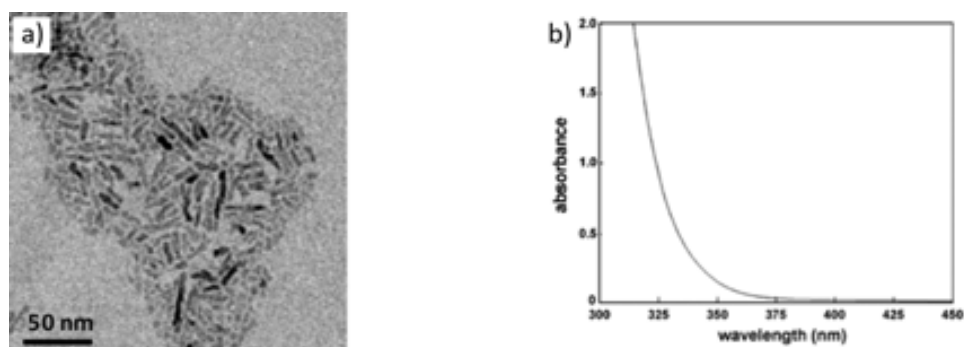
Figure 2.4 TEM image of TiO$_2$ nanorods (a). Absorbance graph of TiO$_2$ NRs (b)

The synthesis of TiO$_2$ nanorods was performed following the fast hydrolysis method described in [32,33]. The used materials were: titanium tetraisopropoxide (TTIP, 99.999%) as precursor, oleic acid (90%) as capping agent and trimethylamino-N-oxide dihydrate or anhydrous (TMAO, 98%) as catalyst for TTIP hydrolysis.

In a typical preparation, 70 g of OLEA were dried at 120 °C during 1 hour under stirring in a three-neck flask. Then, it was cooled down to 80-100 °C. 15 mmol of TTIP was added to the OLEA and stirred for 5 minutes. On the other hand, 5 ml of aqueous 2 M TMAO was added with a syringe by a rapid injection. The mixture was left in a close system at 100 °C for 48 hours. Figure 2.5 shows sketch of TiO$_2$ nanorods synthesis set up.
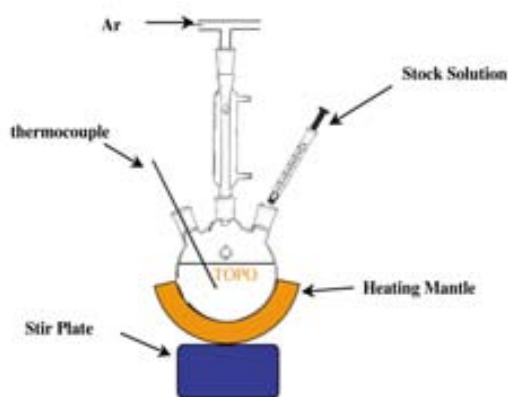

Figure 2.5. Sketch of nanocrystals' synthesis set up.

Once the reaction was finished, the TiO$_2$ particles were separated from their growing solution adding ethanol and then subjected to several cycles of redissolution in chloroform (CHCl$_3$) and precipitation with ethanol to wash out residual surfactants.

2.1.2.ii. *Fe₂O₃ nanoparticles*

The elaboration of iron oxide nanodots (NDs) was done using oleic acid and oleyl amine (OLEAM) as capping layer. The diameter of the nanodots was between 8-10 nm (Figure 2.6) and their main applications are its biocompatibility, magnetism, catalytic and sensor [34]. In Figure 2.6 Hysteresis cycle demonstrates the magnetic character of Fe_2O_3 nanodots.
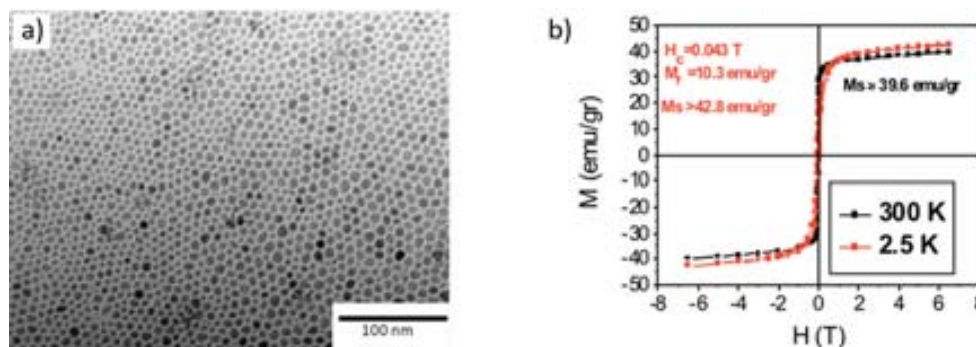

Figure 2.6: TEM image of Fe_2O_3 nanodots. Hysteresis cycle of the Fe_2O_3 NDs demonstrates their magnetic character.

The chemicals used during the synthesis were: iron pentacarbonyl (Fe(CO)5, 98 %) as precursor, 1-octadecene (ODE, 90 %) as solvent, oleic acid (90 %) and oleyl amine (70 %) was the capping agents and dodecan-1.2-diol (1,2-DDIOL, 90 %) to reduce Fe^{+3} and as oxygen donor [33].

In a typical synthesis, 3 mmol of OLEAM, 6 mmol of OLEA, 2.5 mmol of DDIOL and 20 ml of ODE are mixed in a three-neck flask. The mixture was heated during 20 min at 120 °C, then it was heated up to 300 °C under nitrogen flux. In the meantime, 1 ml of $Fe(CO)_5$ solution (normally 2 M in previously degassed ODE) was prepared in the glove box. The $Fe(CO)_5$ solution was added in the three-necked flask with a syringe by a rapid injection. The set up of the particle synthesis can be seen in Figure 2.5.

After the injection of the $Fe(CO)_5$, along incubation time is needed before the nucleation takes place and when a supersaturation threshold is reached. When the synthesis is finished, extraction and purification process were performed. Acetone : isopropanol (1:1) mixture is added to the reaction solution and then centrifuged. The precipitate was washed with a mixture of acetone and isopropanol in order to remove the precursor and the surfactant. This process is repeated three times.

2.1.2.iii.   CdSe/ZnS nanoparticles

The synthesis of CsSe/ZnS was performed in two steps by the recipe proposed by Talapin et al. [35]: first CdSe nanocrystal solution is prepared and starting from there the CdSe/ZnS core-shell nanocrystals are synthesize.

In a typical synthesis of CdSe, 1 mmol of trioctylphospine selenium (TOPSe) and 1.35 mmol of dimethylcadmium (DMCd) were dissolved in 5 ml of TOP and rapidly injected into a vigously stirred mixture of 10 g of trioctylphosphine oxide (TOPO) (99%) and 5 g of hexadecylamine (HAD), which is used as capping layer, heated to 300 °C. Injection resulted in an immediate nucleation of nanoparticles displaying a broad adsorption maximum around 450 nm.

Afterwards, CdSe/ZnS core-shell nanocrystals were prepared mixing 2.5 ml of previously prepared CsSe solution with 5 g of TOPO and 2.5 g of HAD and heated to 220 °C.

2.1.2.iv.   Au commercial nanoparticles

These commercial gold nanoparticles were purchased from PlasmaChem Company [36] with size of 6.5 ± 1.5 nm. They are soluble in hexane, benzene, toluene and chloroform. The gold nanoparticles were chosen to carry out the experiments because of the metallic, photocatalytical, optical, charge transport, sensor and biocompatibility properties. Figure 2.7 (left) is a TEM image of Au commercial NPs, (right) it can be seen that the maximum absorbance of the Au NPs is 530 nm wavelength.
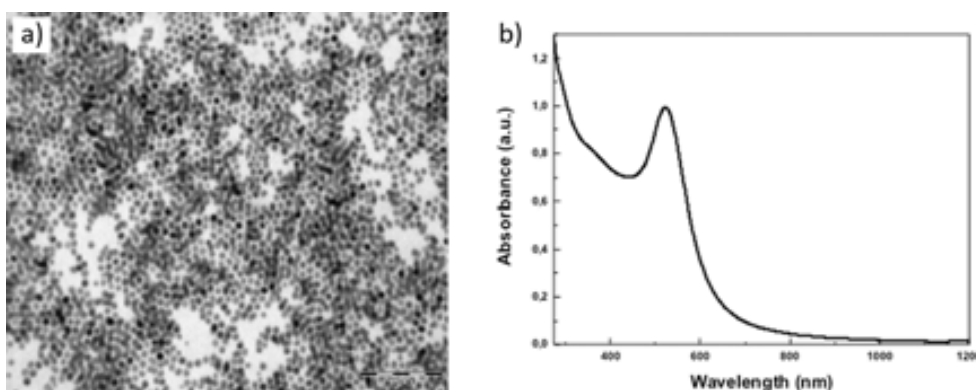

Figure 2.7. TEM image of Au commercial NPs (a). Absorbance graph of commercial Au NP (b).

2.2. PLATFORM DESIGN AND FABRICATION

The design and fabrication of platform to test the technology is the main part of the work. It is over this platform where nanocrystals embedded in the resist are deposited. Because of the novelty of the materials utilized for the development of the technology, it was necessary to optimize the deposition of the nanocomposites in the substrate, as well as the fabrication of the nanoelectrodes. The fabrication of the samples was performed in the clean room facilities of the IMB-CNM under controlled ambient conditions.

2.2.1. Design of the platform

The main objective of the presented technology is to achieve the contact of individual nanoparticles. The set up proposed during this work consist of a platform that allows nanocrystals to be individually contacted.

The elements of the platform are a silicon substrate, a composite formed of nanocrystals embedded in an insulating resist and in some cases gold electrodes to make easier the contact between NCs and AFM probe (Figure 2.8).
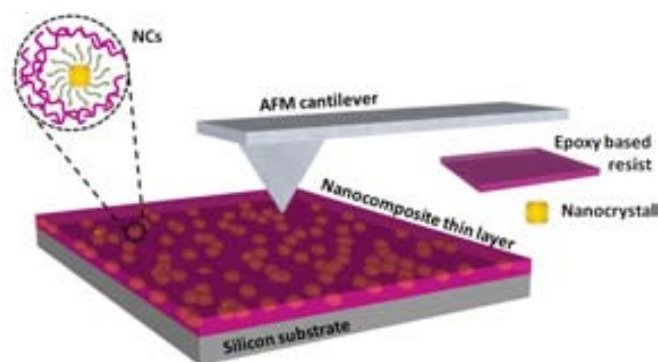

Figure 2.8. Main elements of the platform which allows the individual contact of the NC. In the left, the silicon chip with the nanocomposite deposited on top. In the right, gold electrodes are fabricated on the platform to facilitate the contact between AFM probe and NCs.

2.2.2. Fabrication process

One of the main advantages of the present technology is the simplified fabrication. After cleaning of the substrate and preparing the composite by mixing the resist dilution with the nanoparticles, it is spincoated, followed by a soft baking process. Each of these steps is explained in more detail:

- Preparation of the substrate

The substrate of the sample is 1 cm x 1 cm silicon chips cut from 4 inch wafers. In order to obtain reliable and interferenceless results it is basic to make a deep cleaning of the samples. The method used to clean the silicon chips must be selected in agreement with the potential dirt and type of the surface. In this case it was enough to dip the chip in acetone and the rinse them in isopropanol (IPA).

- Resist dilution

The thickness of the deposited resist is proportional to the resist viscosity (which is determined by the dilution) and to the spincoating parameters. The dilution of the resist was made mixing the resist mr-EBL 6000.1 3% and the thinner ma-T thinner and shake the mixture with a magnetic stirring. In this case 1:10 and 1:12 (mr-EBL 6000.1 3% : ma-T thinner) were needed.

- Nanocrystal dilution

After the synthesis of nanocrystals at IPCF, they were dissolved in chloroform and sent to CNM. When less concentrated dissolution than the initial one is needed, it is rediluted adding the corresponding volume of chloroform for the desired concentration.

- Incorporation the nanocrystals into the resist.

Nanocomposite materials consist of the mixture between inorganic nanoparticles and polymer matrix. Since inorganic nanoparticles do not have adequate mechanical and processing properties, they need a host material, i.e. polymer [37].

Once the NCs are synthesized and the resist dilution done, the mixture of both elements is carried out in adequate proportions. For the suitable dispersion of the NC it is important to maintain the resist-nanocrystal proportions: 100 μl of nanocrystal dissolution was added to 2.5 g of diluted resist and then stirred.

- Nanocomposite deposition

The success of this work depends on the reproducible generation of desired polymer film thickness and profile uniformity, since on this depends most of the characteristics of the sample, as the homogeneity, thickness, arrangement of the nanoparticles in the resist…

Spincoating was chosen as deposition method due to easy use and ability to achieve uniform thin layers. The spincoater utilized along this work is the Wafer Spinner POLOS 200 (CpK Industries, LLC).

In order to achieve a high-quality spincoating process the substrate must be very clean as well as dried. Any speck of dust or humidity in the chip could be the cause of a not homogeneous resist layer or of a bad adherence between the substrate and the polymer. This is the reason because after cleaning the substrate, and just before the spincoating, the samples are baked in the hot plate at 150°C during one minute to remove the possible humidity.

Once the chips are ready the spincoating process is carried out at the speed of 8000 rpm during 45 seconds with an acceleration of 400 rpm/sec.

- Soft bake

After spincoating, the samples are baked in the hot plate in order to partially evaporate the solvent of the resist and increase the density of the film. It is important to make a ramp of temperature starting from 65°C to 95°C during 15 minutes, since a fast evaporation of the solvent would produce bubbles in the surface of the resist layer.

2.2.3. Optimization of the nanocomposite layer

The ability to characterize the nanocrystals in the platform totally depends on the way that particles are exposed to the exterior. Due to the relevance of having the nanocrystals properly placed, the optimization of the nanocomposite layer is extremely important. In the present section, the studies performed to achieve an optimum disposal of the nanocrystals are explained.

During this work, the thickness of the film deposited onto the silicon chips is measured by ellipsometry [38]. Since it is unavoidable to find inhomogeneities along the sample, it is advisable to make more than one measurement in each sample. The values of the resist layer thickness presented in this document are the average of three-four measurements per sample.

2.2.3.i.   *Study of the optimum conditions for resist deposition*

There are two main phenomenons that affect the thickness of the deposited resist layer: the parameters of the spincoating and the properties and dilution of the polymer.

It is well known that the deposited initial volume of resist does not affect the final resist layer thickness during the spincoating process. Moreover, for the set speed the resist layer thickness decreases rapidly at the beginning, but immediately slows down. However, as Figure 2.9 shows, the resist layer thickness is strongly linked to the viscosity of the polymer. Increasing the polymer dilution, its fluid viscosity is reduced and thus the final film thickness is considerably diminished.
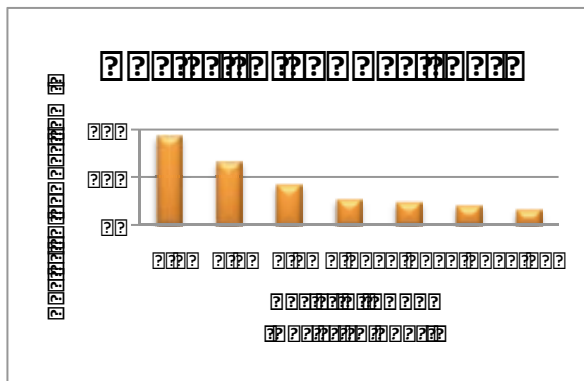

Figure 2.9. Obtained film thickness for different resist dilutions. Spincoating parameters: 8000 rpm, during 45 s with an acceleration of 400 rpm/s.

From the characterization of the deposited resist layer, it was observed that the optimal dilutions were 1:10 and 1:12 to obtain 9 nm and 12 nm of resist respectively. Higher dilution ended in non-homogeneous films. The spincoating parameters were always 8000 rpm, during 45 s with an acceleration of 400 rpm/s.

2.2.3.ii.   *Study of the optimum conditions for oxygen plasma etching*

It has been observed that when the polymer layer is deposited on the substrate, nanocrystals are hidden by polymer thin layer covering their surface. That happens because of the high affinity between the nanocrystal ligands and the polymer. Since it is necessary to contact nanocrystals, it is needed to remove the resist layer covering them.

With the aim of removing few nanometers of resist, keeping the properties of the nanocrystals, soft oxygen plasma etching process was carried out.
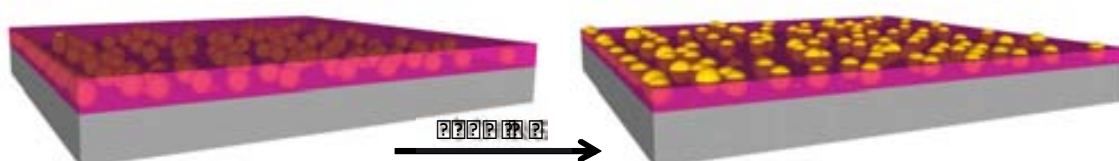

Figure 2.10. Soft oxygen plasma was applied to expose the NPs to the exterior.

The equipment used at the CNM to perform the oxygen plasma was Tepla 300 (Plasma System). The system generates plasma subjecting a gas (i.e. oxygen gas) to magnetic fields in low pressure. Due to the acceleration and collision of free electrons de gas molecules are separated and dissociated. When the chain reaction has finished almost a neutral mixture of molecules, electrons, positive ions and free radical is obtained.

In order to find out the optimal conditions to remove few nanometer of resist, calibration of the equipment was done, see Table 1. Selected conditions for our experiments were power of 300 W and times of 12 and 18 s.

Table 1.Calibration of mr-EBL 6000.1 3% layer etching, with initial thickness around 25 nm. The values represented are the nanometers of resist removed after etching.

	200 Wats	300 Wats	500 Wats
30 s	0	4.37	X
18 s	0	2.45	4.9
12 s	1.04	1.9	1.77

X: not performed experiments

2.2.4. Fabrication of micro/nanoelectrodes for electrical characterization

At first, it was planned to perform electrical measurements contacting directly AFM probe with nanocrystals in the surface of the samples. As soon as the first experiments were done it was observed that direct contact between the probe and NCs was unsuccessful (section 4.2). Thus, as a way for facilitating the measurement of electrical properties of nanocrystals an array of micro/nanoelectrodes was fabricated in some of the samples, see Figure 2.11.

The electrodes performed through this work were patterned by Electron Beam Lithography (EBL or e-Beam). However, Nanoimprint lithography (NIL) techniques are also feasible for higher throughput of fabrication.
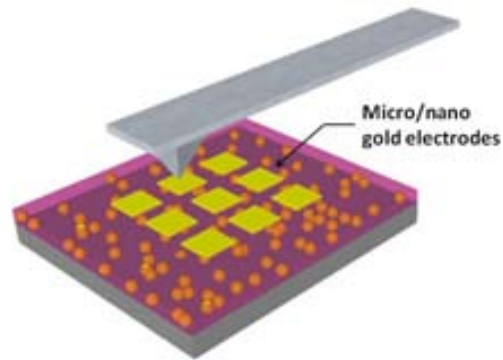
Figure 2.11. Sketch of the nanoplatform with gold electrodes fabricated on top of the nanocomposite in order to facilitate the electrical contact with the AFM tip.

2.2.4.i.   *Au electrodes by e-beam lithography*

Electron Beam Lithography has been selected to fabricate the electrodes because it permits to make patterns with nanometric resolution. Electrodes in a range between 250 nm and 1 mm have been fabricated. The pattern design consists of 1 x 1 mm arrays of squares, of 100 μm x 100 μm, with a pitch of 300 μm. The squares in diagonal are composed, at the same time, of smaller square electrodes with sizes of 1 μm x 1 μm, 0.5 μm x 0.5 μmm, 0.25 μm x 0.25 μm and pitch of 2 μm, it is shown in Figure 2.12.
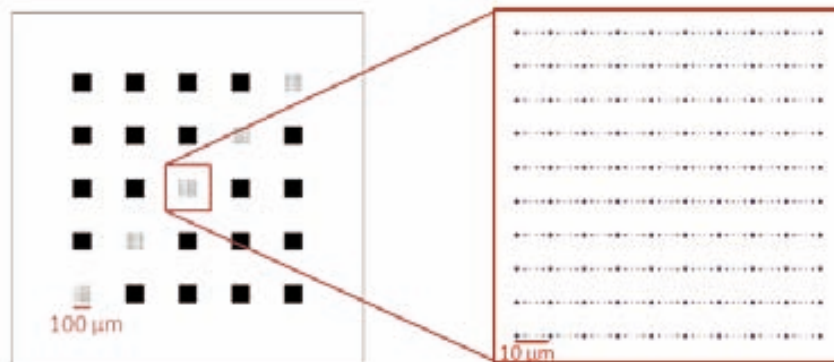
Figure 2.12. Electrode design consisting of squares of 100 μm x 100 μm, 1 μm x 1 μm, 0.5 μm x 0.5 μmm and 0.25 μm x 0.25 μm.

As it is shown in Figure 2.13, the first stage of the fabrication is the deposition of e-beam sensible resist, in this case PMMA 950 k A2 was used (Microchem) [39] and thin layer of 100 nm was deposited by spin coating.
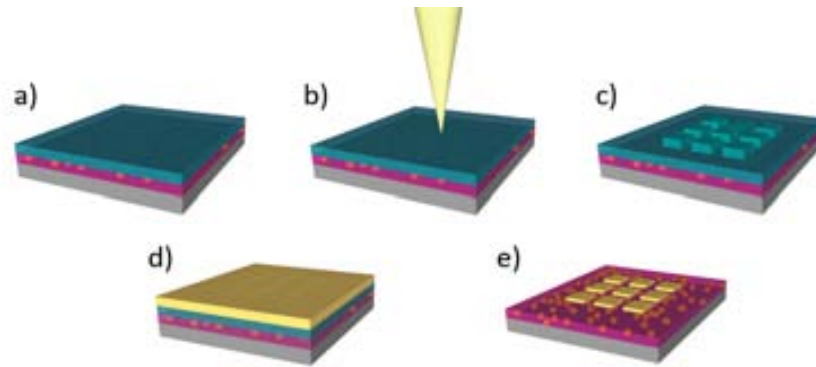
Figure 2.13. Micro/nanoelectrodes fabrication process.

Fabrication of the electrodes was developed with the e-beam writer available at the CNM, the Raith 150 Two (Raith) [40]. For yielding the desired electrodes gun aperture of 20 μm, beam current 80-100 pA, EHT 10 kV, work distance 10 mm and dose factor of 100 μAs/cm^2 were applied. Then the resist was developed on MIBK : IPA (1:3) during 30 s and rinsed in IPA in order to stop the reaction.

Once the design was patterned in the resist, metallization was performed. 3 nm of Chromium and 20 nm of gold were deposited. The Cr aimed to improve the adhesion between nanocomposite and gold. Figure 2.14 shows the success fabrication of the electrodes after the lift-off.
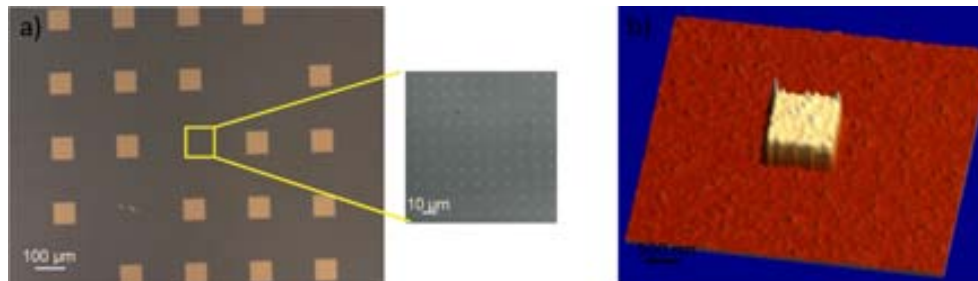

Figure 2.14. Optical microscopy image of the metalized electrodes (left). AFM 3D image of 1 μ m x 1 μm gold electrode (right).

As it can be seen in Figure 2.15, when only gold is deposited, due to its bad adhesion, the electrodes are peeled off, in this image the smallest electrodes are pulled out and the big ones are neither well defined.
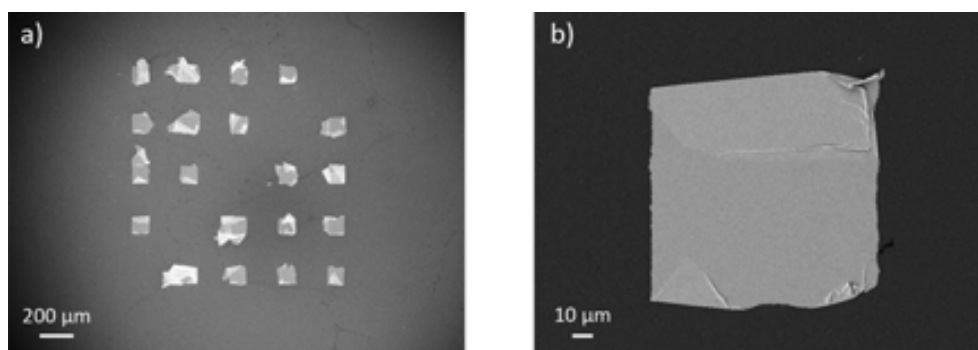
Figure 2.15. SEM image of the metalized electrodes after lift-off process. Left, can be observed that the smallest electrodes are pulled out (up/out) and the big ones are neither well defined. Right, detail of one of the big electrodes.

2.3. CHARACTERIZATION AND RESULTS

2.3.1. Characterization of the polymer layer

All of the samples presented in this section were fabricated following the protocol described in 2.3.2 part. A first set of samples was fabricated using resist : thinner (1:2) dilution and $4 \cdot 10^{-3}$ M concentration for TiO_2 and Fe_2O_3 NPs and 4mg/ml for Au commercial NPs[1], Figure 2.16.

Different observations can be made regarding AFM images of these samples: i) Concentration of nanoparticles in the surface was much lower than expected, especially in the case of gold NPs. Probably due to the fact that the resist thickness (~25 nm) was larger than the size of the NPs (~10 nm), so most of the NPs could not be seen in the images because they were embedded in the resist. ii) Nanoparticles in the surface seem to be aggregated. Probably interdigitation among the alkyl chain of the surfactants occurred. iii) Dense resist layer covering the nanoobjects[2]. That can also happen because the attractive force made by the ligands to link NPs and resist.

---

[1]As gold NPs are commercial, the concentration is given in units used by PlasmaChem Company.
[2] As we cannot assume that what is seen in the AFM images are isolated nanoparticles, we will refer to them as "nanoobjects" (NO).
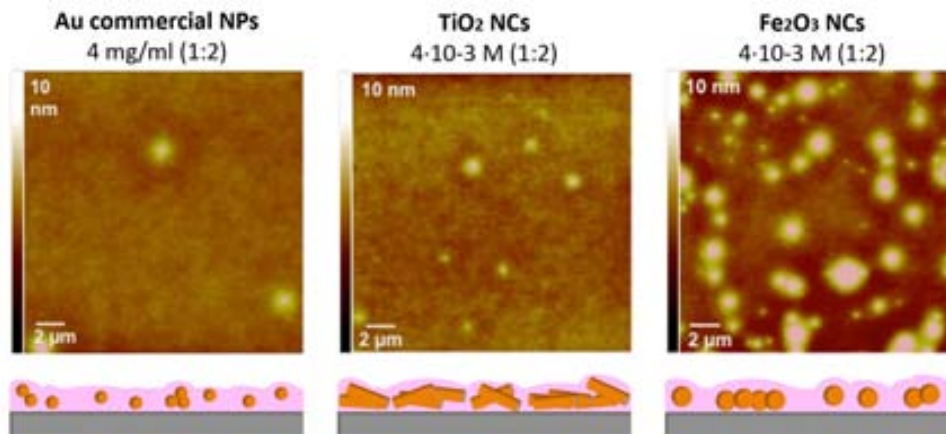
Figure 2.16. AFM images of the first set of samples, low concentration and aggregation of particles is seen in the surface. Below, graphic sketch of the cross section of the samples based on the proposed explanation.

With the aim of improving the achieved results next actions were performed:

- Further dilution of the resist to reduce the film thickness. The most outstanding point to get thin resist layer is to dilute the resist. After the optimization process saw in point 2.3.3, the optimize conditions to achieve a resist thin film were 1:12 and 1:10 resist dilution to obtain resist layer of 9-10 nm and 10-12 nm, respectively.

- Improvement of the washing and purification for TiO_2 and Fe_2O_3 nanoparticles. After the synthesis process the nanoparticles were deeply washed with methanol (see section 2.2). In order to get purer NPs this cleaning process was repeated several times.

- Compare commercial gold nanoparticles with smaller particles synthesized at the lab.

New batch of samples was prepared taking in account the last points. For TiO_2 and Fe_2O_3 NPs samples can be observed in AFM images shows in Figure 2.17 and Figure 2.18 that the used of new conditions enhanced the number of nanoobjects in the surface of the resist layer. But there was still a large amount of polymer around the nanocrystals.
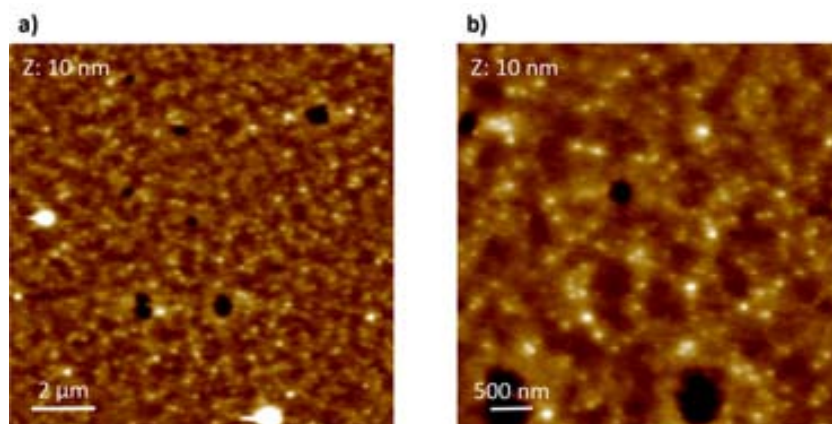
Figure 2.17. AFM images of the TiO$_2$ NPs samples fabricated based on new conditions: concentration of $4 \cdot 10^{-3}$ M and resist dilution 1:12.
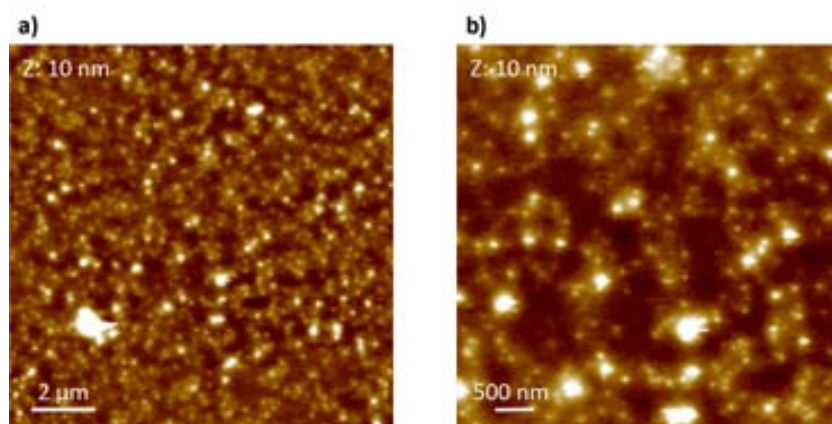

Figure 2.18. AFM images of the Fe$_2$O$_3$ NPs samples fabricated based on new conditions: concentration of $4 \cdot 10^{-3}$ M and resist dilution 1:10.

As it can be seen in Figure 2.19, no significant improvement could be noticed in the samples using bigger gold particles. Only that as the resist layer has become thinner, it looks less homogeneous.
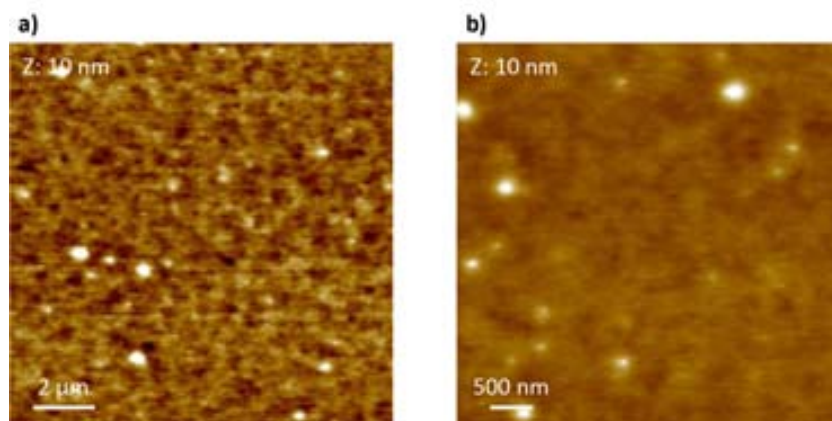

Figure 2.19. AFM images of the commercial Au NPs samples fabricated based on new conditions: concentration of 4mg/ml and resist dilution 1:10.

64

In accordance with the previous results it was observed that using new conditions the concentration of TiO_2 and Fe_2O_3 nanocrystals in the surface was significantly increased. However, it seems that nanocrystals were not totally exposed to the exterior, owing the attraction of the surfactants of the NC towards the resist, thin resist layer remains on top of the nanocrystals. A soft oxygen plasma etching was performed on the samples with the intention of remove few nanometers of resist and liberate the NPs to the outside.

2.3.1.i. *4.1.1 Oxygen plasma etching*

Oxygen plasma etching was applied to samples of TiO_2, Fe_2O_3 and Au commercial NPs fabricated with the new conditions. The parameters used for the etching were optimized in section 2.3.3.

After plasma etching it was observed an obvious increase of nanoobjects on the surface of TiO_2 (Figure 2.20) and Fe_2O_3 samples (Figure 2.21). The emphasis to remove the polymer layer around the nanoparticles fall on the suspicion that it can interfere in the characterization of the nanoparticles. For Au NPs there was not any notable difference after plasma etching (Figure 2.22), they had totally different behavior than TiO_2 and Fe_2O_3 nanocrystals.
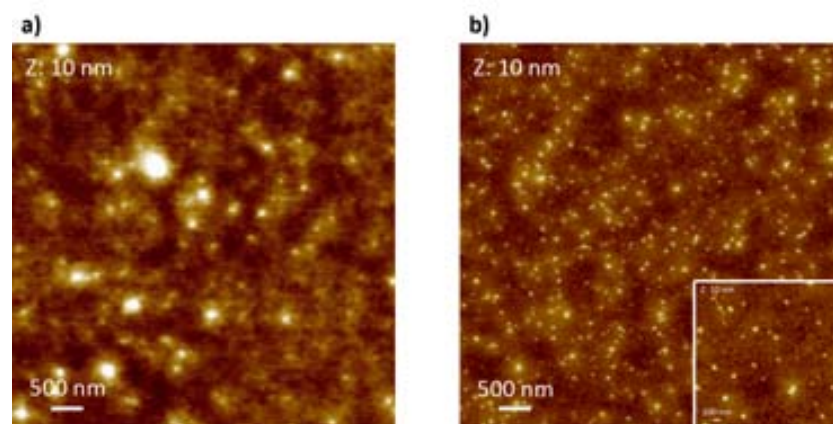

Figure 2.20. TiO_2 NPs sample with concentration of $4 \cdot 10^{-3}$ M, 1:12 dilution before plasma (a) and after 300 W 30 s of plasma (b).
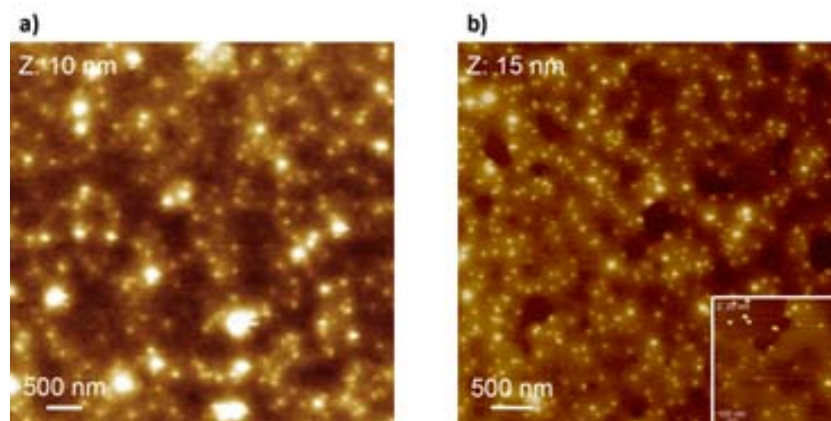
Figure 2.21. Fe_2O_3 NPs sample with concentration of $4\cdot10^{-3}$ M, 1:12 dilution. a) Before plasma, b) after 300 W 30 s of plasma.
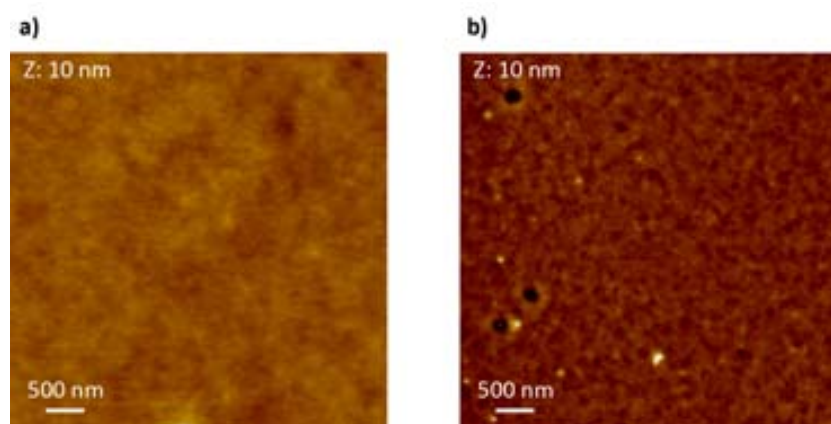

Figure 2.22. Au NPs sample with concentration of 4 mg/ml, 1:10 dilution before plasma (a) and after 300 W 30 s of plasma (b).

Insisting in the importance of find out if the nanoobjects were covered by resist, particular area of the sample was studied with AFM. Some areas where the resist layer was not homogeneous were seen in these samples. There were some *islands* where practically there was not resist. After plasma etching this phenomenon was intensified. In most of the cases the thicker resist layer was accumulated around the nanoobjects, so most of the *islands* were free of nanoobjects. However, nanoobjects were found in some of the *islands*, they were characterized by AFM (Figure 2.23). The phase of these images shows differences between the objects inside and outside of the *island*. Thus, most likely, the nanoobjects out of the *island* are covered of resist.
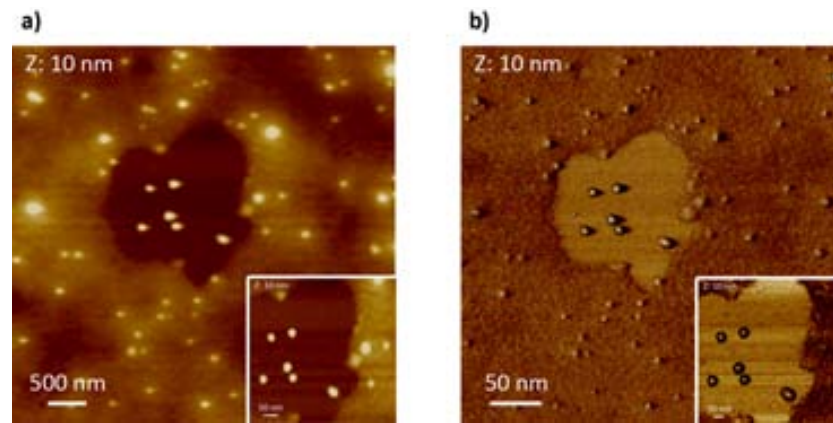
Figure 2.23. AFM image of one of the *islands* found in a sample of Fe_2O_3 NPs with concentration of $4 \cdot 10^{-3}$ M, 1:12 dilution, after 300 W 30 s of plasma.

SEM characterization was carried out in order to clarified the uncertainly situation show by the AFM. The images seen in Figure 2.24 were performed with Auriga (Zeiss), due to the particular characteristic of this equipment it was possible to make images to isolator samples. On the one hand, those images show that the size of the objects is similar to expected, what means that the so-called nanoobject were in fact isolated nanocrystals. Due to the convolution of tip it difficult to demonstrate by AFM.
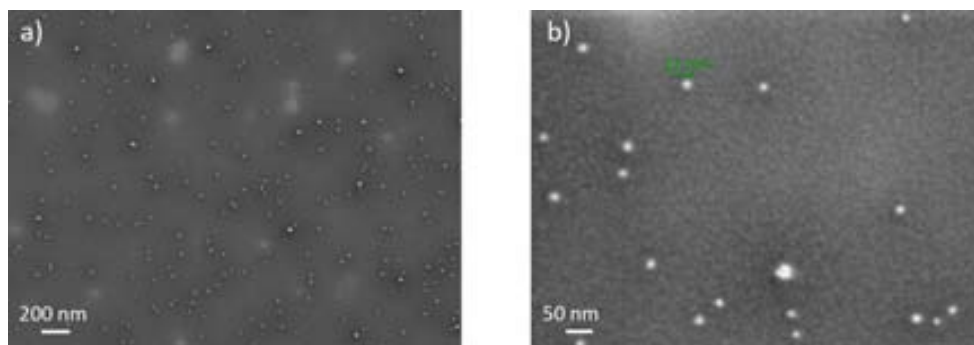

Figure 2.24. SEM images made by Auriga (Zeiss), these are Fe_2O_3 nanodots $4 \cdot 10^{-3}$ M (1:12) Samples.

On the other hand, if we compare SEM images of nanoparticles before plasma (Figure 2.25) and after it Figure 2.24, it is clear that in the first case NP are covered by a resist layer which is removed after the etching.
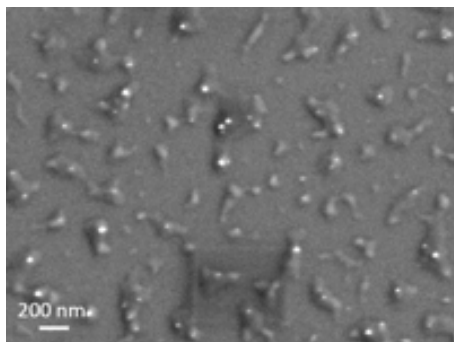
Figure 2.25. SEM image of a Fe_2O_3 nanodots $4\cdot10^{-3}$ M (1:12) Sample before the oxygen plasma etching. It can be clearly see that the particles are covered by resist.

2.3.1.ii.   *4.1.2 Comparison of commercial gold and CdSe/ZnS nanoparticles*

Two hypotheses were suggested to explain why gold nanoparticles cannot be seen in the characterization: the first one was aimed to the smaller size of the Au NPs comparing with TiO_2 and Fe_2O_3. The other side, was related to the surfactants of the Au NPs. The commercial NPs were covered with different surfactants than the NC synthesized during this work. Therefore, the connection between NP and resist is weak and the particles *fly away* during the spincoating. In order to find out the reason, CdSe/ZnS nanoparticles were synthesized ate the IPCF, which are smaller NPs than commercial gold NPs, but synthesized with the same surfactants as TiO_2 and Fe_2O_3 were prepared and characterized.
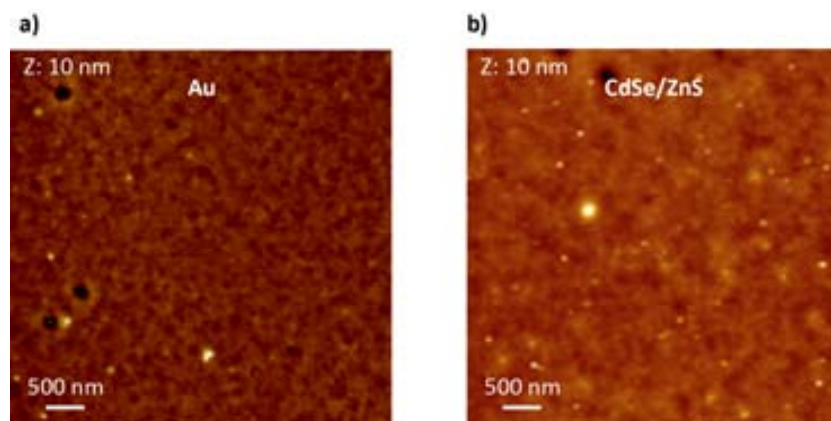
Figure 2.26. AFM images of (right) Au NPs sample with concentration of 4 mg/ml, 1:10 dilution and (left) CdSe/ZnS NPs sample, $5\cdot10^{-7}$ M, 1:10 dilution.

As it is observed in Figure 2.26 CdSe/ZnS NPs can be distinguished in the polymer, while Au NPs are not appreciated. Thus, most likely, the difficulty to place the Au commercial NPs in the nanocomposite is that surfactant covering them is not adequate to link the NPs with the resist.

2.3.2. Electrical characterization

First experiments to perform electrical measurements were done with direct contact of the AFM tip in the surface of the samples, without electrodes. Since the resist is rather soft, it is damaged when scanning with AFM tip. Furthermore, applying a voltage on top of the surface it is observed that the resist is removed and the silicon started to oxidize, as it can be seen in Figure 2.27. This made difficult the measurements for contact modes. Due to the short time that the AFM tip is in contact with the surface in tapping mode, it is not good method either.
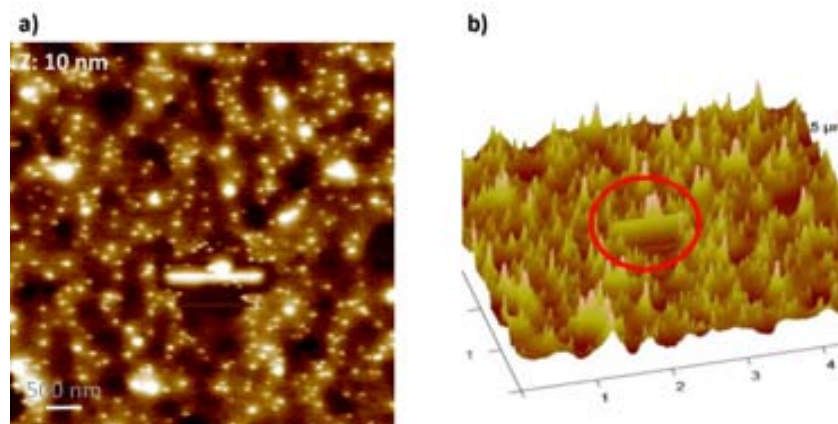
Figure 2.27. AFM image of Fe_2O_3 NPs sample ($4 \cdot 10^{-3}$ M, 1:12 dilution), after applying a voltage the resist get melt and the silicon oxide starts to grow. Right, 3D image of the oxidation.

More measurements were done by means of electric field in order to do not damage the sample (Figure 2.28). Some sign can be observed in the Phase of the AFM image, but not obvious.

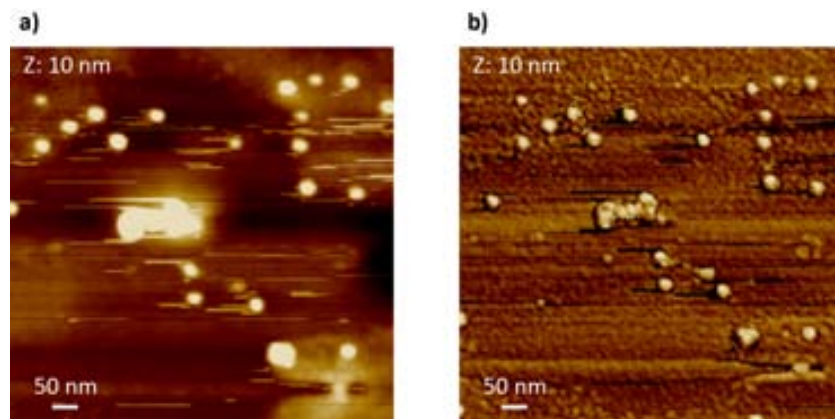Figure 2.28. AFM image of Fe_2O_3 NPs sample ($4 \cdot 10^{-3}$ M, 1:12 dilution) sample after 300 W, 18 s of plasma performed when applying low voltage, (left) the phase of this image.

As it has been seen, the method of contacting AFM probe directly with the nanocrystals in the surface has some troubles to be carried out. On one hand, the small dimension of the probe and the nanocrystals made the link difficult. Furthermore, because the soft characteristic of the polymer when a voltage was applied, it is removed immediately. In order to overcome the contacting difficulties gold electrodes were fabricated for the purpose of contact nanocrystals (section 2.3.4.i).

The electrical measurements using electrodes were performed adding Tuneling AFM (TUNA) module, from Veeco, to the AFM. It is a variable gain amplifier, which converts the low current from the AFM tip into a voltage. The gains are 1 pA/V, 10 pA/V, 1 nA/V and 100 nA/V. TUNA works analogous to Conductive AFM (c-AFM), but with higher sensitivities. A selectable bias voltage is applied between the conductive tip and sample. By maintaining a constant force between tip and sample, simultaneous topographic and current images are generated, enabling the direct correlation of local topography with electrical properties.
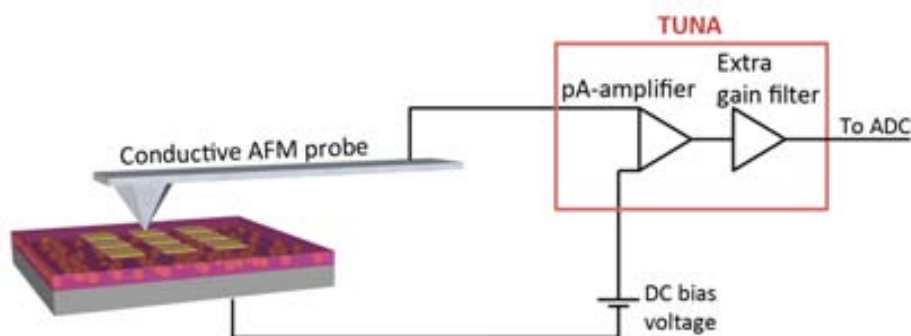
Figure 2.29. Sketch of the system used to perform electrical measurement of the samples.

The first electrical characterization was done using 100 μm x 100 μm electrodes. After the validation of these measurements, smaller electrodes of 1 μm x 1 μm were used for higher accuracy. Preliminary results presented in this document are inconclusive, but enough to prove that there is an enhancement of the current flowing through the samples in presence of nanocrystals. Curves presented in this work have been performed with 1 μm x 1 μm electrodes.

Before make the first electrical measurement of the nanocrystal samples, the electrical behavior of the resist must be studied. When applying a voltage to samples whose resist is free of nanocrystals it is reproducibly observed that no current is thronging the sample, represented in Figure 2.30.

Figure 2.30. Current curve measured in samples without nanoparticles.

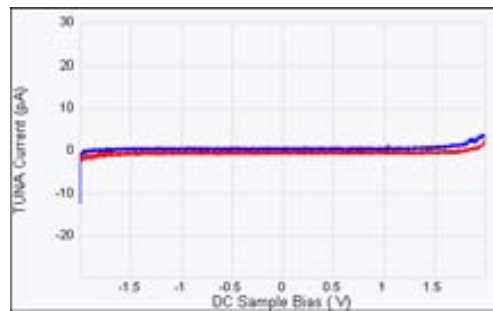When the same experiment is performed for samples with nanocrystals the conductivity changes in the way that can be observed: from 2 V for TiO_2 Figure 2.31a samples and from 1.5 V for Fe_2O_3 samples Figure 2.31b.
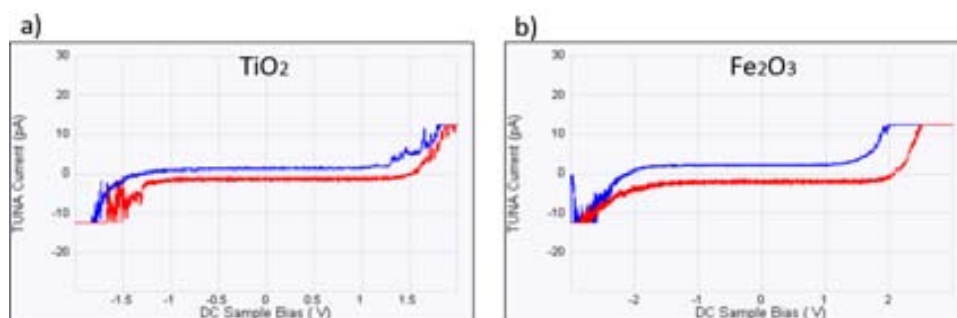
Figure 2.31. a) Current curve of TiO_2 sample and b) Fe_2O_3 samples. In both cases, the current alters when applying a voltage higher than 1.5 V.

In the case of gold nanoparticles the current also changes when applying a voltage, but there is a high variability between measurements due to the inhomogeneity of the nanocomposite. In Figure 2.32 can be observe the differences between three measurements made to the same sample.
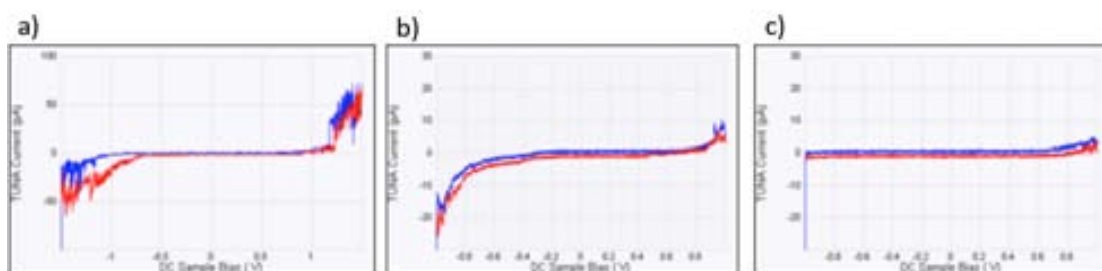
Figure 2.32.Three electrical measurement of the same gold nanocomposites sample (4 mg/ml, 1:12).

More experiments should be performed in order to have statistical conclusions about the conductivity of the samples. But this first approach to the electrical measurements shows a sort of enhancement of the current in presence of nanocrystals. As conclusion it can be stated that the presented nanoplatform is a suitable method to study electrical behavior of nanocrystals, even further development is needed for the single nanoparticle detection.

2.4. CONCLUSIONS OF CHAPTER 2

In this work an innovative technology has been developed to contact single nanocrystals in order to characterize their individual properties. This method consists of depositing on top of a silicon substrate a nanocomposite ultrathin layer based on semiconductor nanocrystals and a highly insulating resist. On the nanocomposite film gold electrodes have been fabricated in order to allow contacting nanoobjects.

It was proved that the characteristics of the nanocomposite are essential issue for the successful fabrication of the platform. On the synthesis of NCs as on the characteristics of the resist as well as on the mixing of both is based the nanocomposite's advantages. The insulating properties of the resist make possible the single analysis of nanoobjects. Moreover, the optimization of the nanocrystals synthesis is fundamental to control them growth and properties.

The method used for creating the nanocomposite is to mix the NCs covered with specific ligands and resist. Due to the low interaction between the nanocrystals and the polymer it is necessary to cover the NCs with a surfactant's capping layer in order to overcome this difficulty. Since an excess of capping layer cause aggregation between particles and reduces the conductivity, strong washing and purification of the nanoparticles was carried out.

After the optimization process of the resist deposition carried out along this work the relevance of next fabrication issues was determined:

- The thickness of the film is mainly dependent on the dilution of the resist.

- Performance of oxygen plasma etching is convenient for removing some nanometers of the resist covering NCs.

- The reason because commercial gold nanoparticles cannot be detected in not related with the size, but with the covering ligands.

It was established that the fabrication of gold micro and nanoelectrodes in the surface of the platform is necessary for an adequate electrical contacting of nanocrystals. The electrodes were successfully fabricated by e-beam lithography. During this fabrication process it was checked that for the metallization it is completely necessary a thin layer of chrome before gold deposition.

Even the performed preliminary electrical measurements are not conclusive, they show a difference between samples with nanocrystals and without. That is a positive indication to advance in the development of the presented technology.

The realization of this work opens a promising door in the progress of devices based on the individual contacting of nanocrystals. For the improvement of the platform optimization of some processes should be carried out:

- Synthesis of nanocrystals with shorter surfactants' molecules. Since the long polymeric chain of the capping agents could affect in the aggregation of the particles and also in the loss of electrical current, smaller ligands as cysteines could be proved.

- Development of gold nanoparticles in order to avoid the weak adhesion of the commercial Au NPs to the resist.

- Improvement of oxygen plasma etching. In order to achieve more homogeneous film of resist the possibility to deposit thicker layer of resist could be studied.

- The setting up of Nanoimprint technology for fabricate the nanocontacts in large-scale is a promising alternative.

- Fabrication of larger number of samples for more precise statistical study.

Finally, it should be pointed out that during this work an innovative technology for contacting nanocrystals has been presented. At this time last optimization of the platform and new electrical measurements are being carried out. So far, the characterization performed shows promising results, validating the technology proposed for contacting single nanocrystals.

REFERENCES CHAPTER 2

1.   Rao, C. N. R., Kulkarni, G. U., Thomas, P. J. & Edwards, P. P. Size-Dependent Chemistry: Properties of Nanocrystals. *Chemistry - A European Journal* 8, 28-35 (2002).

2.   Schmid, G. *et al.* Generation and electrical contacting of gold quantum dots. *Colloid Polym Sci* 286, 1029-1037, (2008).

3.   Xia, Y., Xiong, Y., Lim, B. & Skrabalak, S. E. Shape-Controlled Synthesis of Metal Nanocrystals: Simple Chemistry Meets Complex Physics? *Angewandte Chemie International Edition* 48, 60-103, (2009).

4.   Prime, D. & Paul, S. First contact-charging of gold nanoparticles by electrostatic force microscopy. *Applied Physics Letters* 96, (2010).

5.   Tseng, R. J., Huang, J., Ouyang, J., Kaner, R. B. & Yang. Polyaniline Nanofiber/Gold Nanoparticle Nonvolatile Memory. *Nano Letters* 5, 1077-1080, (2005).

6.   Ouyang, J., Chu, C.-W., Szmanda, C. R., Ma, L. & Yang, Y. Programmable polymer thin film and non-volatile memory device. *Nat Mater* 3, 918-922 (2004).

7.   Kanwal, A., Paul, S. & Chhowalla, M. Organic memory devices using C-60 and insulating polymer. *Materials and Processes for Nonvolatile Memories* 830, 349-353 (2005).

8.   Prakash, A., Ouyang, J., Lin, J. L. & Yang, Y. Polymer memory device based on conjugated polymer and gold nanoparticles. *Journal of Applied Physics* 100, (2006).

9.   Steinberg, H. *et al.* Electrical Current Switching in Single CdSe Nanorods. *Nano Letters*, (2010).

10.   Thelander, C. *et al.* Gold nanoparticle single-electron transistor with carbon nanotube leads. *Applied Physics Letters* 79, 2106-2108 (2001).

11.   Hipps, K. W. MOLECULAR ELECTRONICS: It's All About Contacts. *Science* 294, 536-537, (2001).

12.   Nahum, E. *et al.* Transport and Charging in Single Semiconductor Nanocrystals Studied by Conductance Atomic Force Microscopy. *Nano Letters* 4, 103-108, (2003).

13.   Wu, C., Bull, B., Christensen, K. & McNeill, J. Ratiometric Single-Nanoparticle Oxygen Sensors for Biological Imaging. *Angewandte Chemie International Edition* 48, 2741-2745, (2009).

14.   Schneider, T. *et al.* Localized surface plasmon resonance (LSPR) study of DNA hybridization at single nanoparticle transducers. *J Nanopart Res* 15, 1-10, (2013).

15.   Ding, W. Micro/Nano-particle Manipulation and Adhesion Studies. *Journal of Adhesion Science and Technology* 22, 457-480 (2008).

16.   Zhu, J. *et al.* On-chip single nanoparticle detection and sizing by mode splitting in an ultrahigh-Q microresonator. *Nat Photon* 4, 46-49, (2010).

17.   Tang, N. *et al.* Coil-in-Coil Carbon Nanocoils: 11 Gram-Scale Synthesis, Single Nanocoil Electrical Properties, and Electrical Contact Improvement. *ACS Nano* 4, 781-788, (2010).

18.   Farmer, S. C. & Patten, T. E. Photoluminescent Polymer/Quantum Dot Composite Nanoparticles. *Chemistry of Materials* 13, 3920-3926, (2001).

19.   Balazs, A. C., Emrick, T. & Russell, T. P. Nanoparticle Polymer Composites: Where Two Small Worlds Meet. *Science* 314, 1107-1110, (2006).

20.   Jordan, J., Jacob, K. I., Tannenbaum, R., Sharaf, M. A. & Jasiuk, I. Experimental trends in polymer nanocomposites--a review. *Materials Science and Engineering A* 393, 1-11 (2005).

21.   Kruis, F. E., Fissan, H. & Peled, A. Synthesis of nanoparticles in the gas phase for electronic, optical and magnetic applications--a review. *Journal of Aerosol Science* 29, 511-535 (1998).

22.   DJ, S., S, J., H, L., M, H. & DG, C. Three-dimensional nanofabrication with elastomeric phase masks. *J. Phys. Chem. B* 111, 12945 (2007).

23.   Microresist. *Micro resist technology (GmbH)*, <http://www.microresist.de>

24.   Martin, C. *et al.* Electron beam lithography at 10 keV using an epoxy based high resolution negative resist. *Microelectronic Engineering* 84, 1096-1099.

25.   Lee, K. Y. *et al.* 3012-3016 (AVS).

26.   Lorenz, H. *et al.* SU-8: a low-cost negative resist for MEMS. *Journal of Micromechanics and Microengineering* 7, 121-124 (1997).

27.   MD, S. & CG, W. Imprint materials for nanoscale devices. *MRS Bull.* 30, 947 (2005).

28.   Voigt, A. *et al.* Improved properties of epoxy nanocomposites for specific applications in the field of MEMS/NEMS. *Microelectronic Engineering* 84, 1075-1079.

29.   Tamborra, M. *et al.* Nanocrystal-Based Luminescent Composites for Nanoimprinting Lithography13. *Small* 3, 822-828 (2007).

30.   Peng, H., Li, J., Li, S.-S. & Xia, J.-B. First-Principles Study on Rutile TiO2 Quantum Dots. *The Journal of Physical Chemistry C* 112, 13964-13969, (2008).

31.   Cozzoli, P. D., Kornowski, A. & Weller, H. Low-Temperature Synthesis of Soluble and Processable Organic-Capped Anatase TiO2 Nanorods. *Journal of the American Chemical Society* 125, 14539-14548, (2003).

32.   Sciancalepore, C. *et al.* TiO2 nanorods/PMMA copolymer-based nanocomposites: highly homogeneous linear and nonlinear optical material. *Nanotechnology* 19, (2008).

33.   Buonsanti, R. *et al.* Seeded Growth of Asymmetric Binary Nanocrystals Made of a Semiconductor TiO2 Rodlike Section and a Magnetic γ-Fe2O3 Spherical Domain. *Journal of the American Chemical Society* 128, 16953-16970, doi:10.1021/ja066557h (2006).

34.   Islam, M. A. & Xia, S. G. Electrostatic properties of maghemite (gamma-Fe2O3) nanocrystalline quantum dots determined by electrophoretic deposition. *Journal of Physics-Condensed Matter* 21, (2009).

35.   Talapin, D. V., Rogach, A. L., Kornowski, A., Haase, M. & Weller, H. Highly Luminescent Monodisperse CdSe and CdSe/ZnS Nanocrystals Synthesized in a Hexadecylamine–Trioctylphosphine Oxide–Trioctylphospine Mixture. *Nano Letters* 1, 207-211, (2001).

36.   S, R. & RT, B. Simulation of fluid flow in the step and flash imprint lithography process. *Proc. SPIE* 5751, 200 (2005).

37.   Ingrosso, C. *et al.* An Epoxy Photoresist Modified by Luminescent Nanocrystals for the Fabrication of 3D High-Aspect-Ratio Microstructures. *Advanced Functional Materials* 17, 2009-2017 (2007).

38.   Feijter, J. A. D., Benjamins, J. & Veer, F. A. Ellipsometry as a tool to study the adsorption behavior of synthetic and biopolymers at the air-water interface. *Biopolymers* 17, 1759-1772 (1978).

39.   MicroChem. http://microchem.com.

40.   MC, M., H, A., D, W. & JR, H. Highly ordered nanowire arrays on plastic substrates for ultrasensitive flexible chemical sensors. *Nat. Mater.* 6, 379 (2007).

3. TOP DOWN FABRICATION OF NANOPARTICLES BY NANOIMPRINT LITHOGRAPHY USING HARD MASK CONCEPT

3.1 NANOPARTICLES ARRAYS FOR BIOSENSING

The advantage of having arrays of nanoparticles (NP) has been evidenced in a large number of fields [1] such as solar cells [2,3], growth of nanowires [4], plasmon resonance [5,6], enhancement of Raman spectroscopy [7], photochemical detection [8,9], etc. Metallic nanoparticles with defined geometry are key elements for the fabrication of highly sensitive, fast response, low cost sensors.

Localized surface plasmon resonance (LSPR) have been studied intensively as one of the promising phenomena for the development of nanobiosensors for medical diagnosis, monitoring of diseases, and the detection of environmental pollutants because of their high sensitivity, label-free detection, low sample volumes, low-cost instruments, and real-time detection [10-12]. In general, the biosensing based in the vis-NIR range. The extinction of the conduction electrons in the metal nanoparticle (NP), induced by the incident photons or electrons with the specific resonant energy. The peak wavelength, extinction magnitude of LSPR spectra, and decay length of the LSP field are highly dependent upon the size, shape, interparticle spacing, and composition of noble metal nanostructure. Understanding how NP structures affect these LSPR properties, optimizing nanostructure design, and improving their sensitivity/detection limit are important issues of current LSPR biosensor research [13].

These applications require the massive production of nanoparticles and its accurate positioning at specific locations on larger-size structures or devices. There are several well-established chemical methods to synthesize NPs [14]. However, reliable processes to control the position and orientation of the NPs on substrates are still not fully developed [15,16]. In this respect, the production of NPs following a top down lithography-based approach, gives better results regarding the order or the particles on the substrate. Several processes have demonstrated the feasibility to fabricate NP arrays, such as polymer nanosphere lithography [17,18], nanostencil lithography [19],

electron beam induced deposition 🔲🔲🔲🔲🔲🔲 electron beam lithography 🔲🔲🔲🔲 or nanoimprint lithography 🔲🔲🔲🔲 usually in combination with a lift-off process. However, all of them still present drawbacks, such as limitation on the aspect ratio, weak definition of the patterns and low throughput. In the case of NIL, the thickness of the resist limits the maximum height of the nanoparticles. Stencil lithography presents some limitations to control the shape and dimensions of the particles due to the blurring and dispersion of the metal during the evaporation [24]. Electron beam induced deposition presents as a main drawback the low throughput, and polymer nanosphere lithography can only produce a limited shape of the nanoparticles. Comparison between these techniques is presented in Table 3-1.

Table (3-1). Comparison of lithography techniques for top-down fabrication of metallic nanoparticles.

	Spheres lithography	e-beam lithography	Stencil lithography	Nanoimprint lithography
	Willets et al. Annu. Rev. Phys. Chem. 2007	Near et al. Nanoletters 2012	Vazquez-Mena et al. ACS Nano 2011	Jüchter et al., SPIE 2013
Well ordered structures	✓	✓	✓	✓
Positioning control	✗	✓	✓	✓
Easy variation size/shape	✗	✓	✓	✓
Well defined patterns	✗	✓	✗	✓
High aspect-ratio structures	✗	✗	✓	✗
High yield	✓	✗	✓	✓

In this thesis a new approach that combines thermal NIL together with the definition of a hard mask is presented, inspired by previous works (Peroz et al. [25], Dhuey et al. [26] and Bergmair et al. [27]). It overcomes most of the limitations of other techniques and enables the large-scale production of nanoparticles with heterogeneous composition. We show that this process is highly adequate for the massive fabrication of nanoparticles with different geometries, such as cones, cups or dots, and that it is applicable to a large variety of materials and substrates. The simultaneous advantages of high throughput, capability for variable composition and three-dimensional control reveals the high applicability of the process to diverse areas like plasmonics, biosensing and nanomagnetism.

The capability of the fabricated nanoparticles to be used as LSPR sensors was demonstrate by their optical characterization. The absorbance peak of these nanoparticles appears displaced respect the peak of the bulk material. Moreover, the plasmonic behavior was detected when they were covered with dielectric layers, which caused a change in the reflection index and displaced the transmission signal 🔲🔲🔲🔲🔲🔲

3.2 FABRICATION OF NANOPARTICLES BY NANOIMPRINT LITHOGRAPHY

Since 1996 when S. Chou [30] developed the nanoimprint lithography, many works have used this technique to fabricate nanometer scale structures and devices with high throughput over large areas.

Figure 3.2 depicts the NIL process to fabricate metallic nanoparticles. First, the NIL resist is spincoated onto the substrate. Then, the stamp is imprinted on the resist while apply heat and pressure or UV radiation. After the stamp is taken apart, the residual resist layer is removed. Then the sample is metallized. Finally, the lift-off is performed, defining the metallic pattern on the substrate.
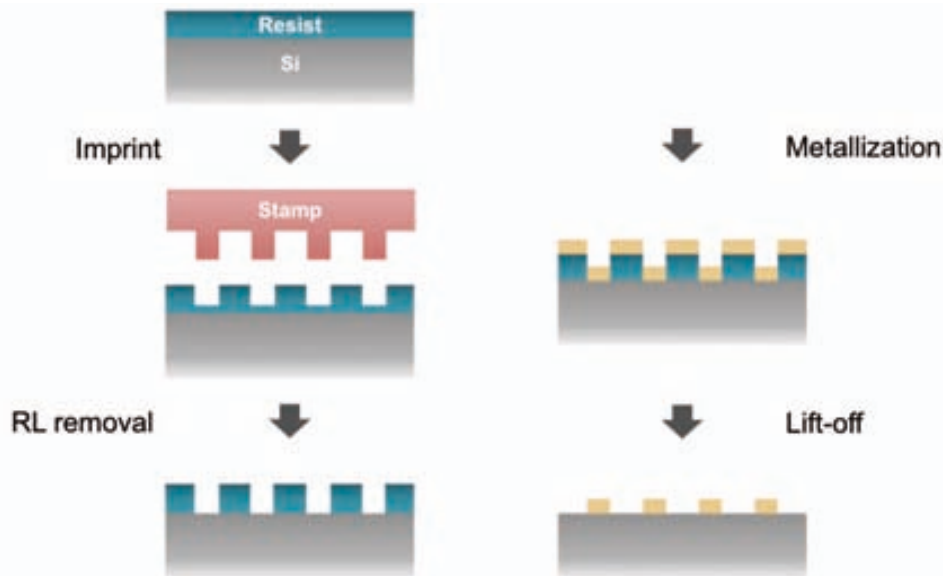

Figure 3.1 Standard fabrication of nanoparticles by nanoimprint lithography and lift-off.

NIL is a simple, fast and low cost technology, but the removal of the residual layer and the post-processing complicates the practical realization of specific nanostructures. Especially, when high aspect ratio metallic nanopatterns are desired, the lift-off is usually difficult due to the resist profile. In this thesis, these problems have been overcome by the presenting method, suitable undercut of the resist under the hard mask is obtained, so it facilitated the lift-off after the deposition of metal or other materials by sputtering and evaporation.

3.2.1 Hard mask based thermal NIL process

We present novel fabrication method that enables the production of nanoparticles with different shapes, sizes, densities and materials. First a trilayer configuration is prepared on the substrate. Here a SiO_2 hard mask is defined on the substrate by means of thermal nanoimprint and RIE, see Figure 3.2. Once the hard mask is ready, the bottom resist that supports the mask is etched. The advantageous undercut produced due to the isotropic etching of the bottom resist will facilitate the subsequent lit-off of the

patterns. The advantage is the decoupling of the resist layer where NIL is performed (top) from the resist layer where the metal is defined (bottom). Note that this method can be also performed with UV-NIL nanoimprint lithography, only by changing the top thermoplastic resist for a UV-curable resist.

This multilayer configuration was originally developed at The Molecular Foundry for two applications that shared equally challenging objectives, such as the definition of high aspect ratio nanometric structures and a high yield production. The first of these applications was the fabrication of the interdigitated nanoelectrodes described on Section III of this thesis. The second one consisted on the fabrication of sub-10 patterns to be used in optical applications. Further information regarding this last topic can be found in Giuseppe Calafiore's master thesis [31].
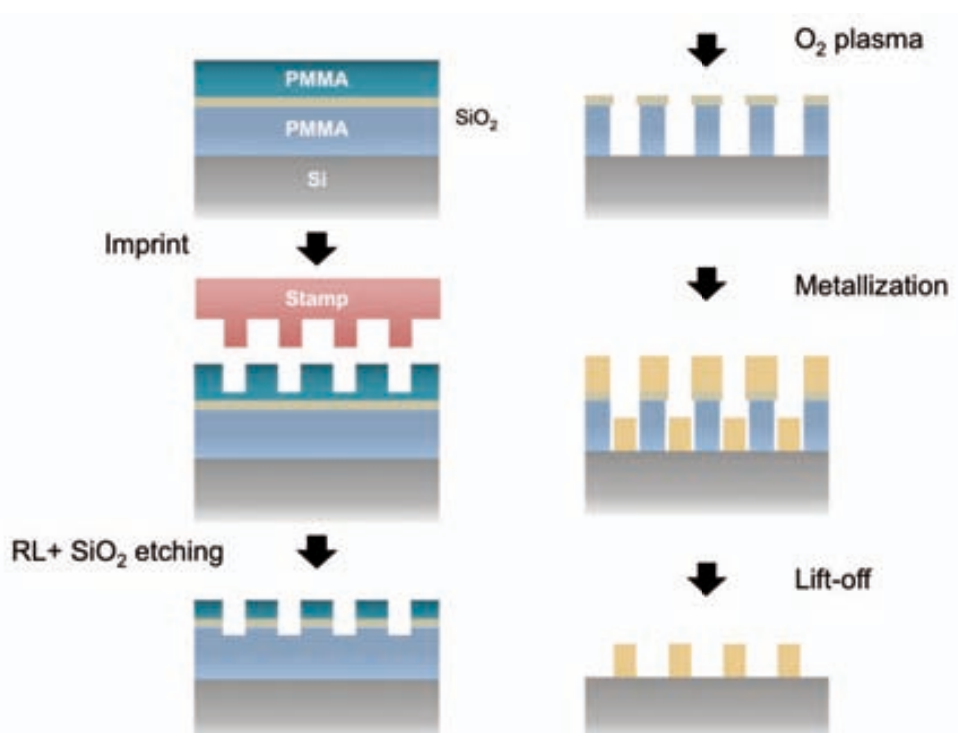

Figure 3.2 Nanoparticle fabrication by nanoimprint lithography using the multilayer configuration

First, a silicon or glass substrate is covered with a tri-layer structure consisting of a PMMA 950 k Mw A7 bottom layer (400 nm thickness), a thin layer of SiO_2 deposited by PECVD (Plasma-enhanced chemical vapor deposition) (23 nm) (25 sccm of SiH_4, 955 sccm of N_2 and 1000 sccm of N_2OHI) and a 100 nm thick top layer of PMMA 75 k Mw, see Figure 3.3a. The top PMMA layer is patterned by thermal NIL. We have used silicon stamps with arrays of nanometer scale dots fabricated by e-beam lithography, Al deposition, lift-off and reactive ion etching. Typical dimensions of the dots are 75 nm, 150 nm and 400 nm width and half-pitch. The surface of the stamps has been functionalized with an anti-sticking layer of FTS13 deposited in a nitrogen atmosphere. The NIL process is performed at a temperature of 180 °C and 40 bar of pressure for 5 minutes. The system is let to cool down to 80 °C while keeping the 40 bar of pressure,

see Figure 3.3b. This process can also be performed with UV-NIL, simply by changing the thermoplastic resist for a UV-curable resist [25]. In this case, the NIL stamp contained arrays of dots of 400 nm diameter.
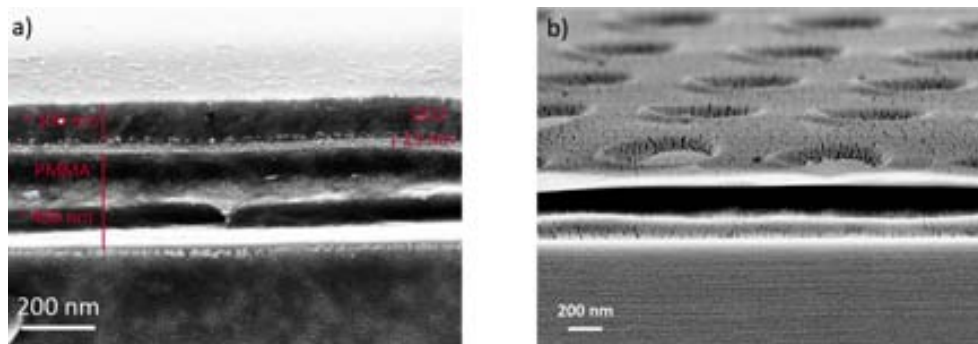

Figure 3.3 SEM image of the substrate, SiO₂ thin layer between PMMA layers.

After the NIL process, the PMMA residual layer is removed and the SiO$_2$ layer is patterned by reactive ion etching (50 sccm of C$_4$F$_8$, source power of 450 W and chuck power of 50 W). The SiO$_2$ patterned layer acts then as a mask for the etching of the bottom PMMA layer in oxygen plasma, Figure 3.4a. As the oxygen plasma etches isotropically the PMMA, it forms an undercut in the PMMA layer. This is the key aspect of the process: the hard mask defined by NIL allows to obtain a large undercut and a large separation from the substrate Figure 3.4b.
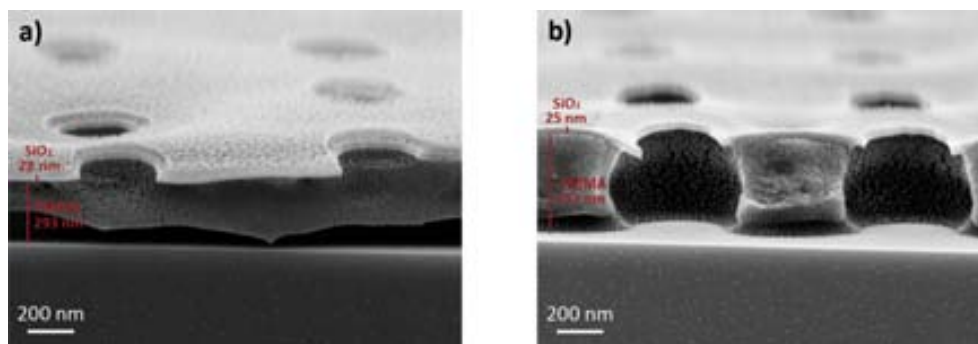

Figure 3.4 SEM images after a) etching of the residual layer of the NIL and SiO2, b) oxygen plasma to remove the sacrificial PMMA layer.

The nanoparticles are defined by depositing metal either by e-beam evaporation or by RF-sputtering, followed by a lift-off process. The lift-off was performed on dichloromethane during 15 min. In order to obtain better results of the lift-off, the sample is sonicated in acetone during 1 minute. It is remarkable that by using this process, the lateral dimensions of the particles are defined by the dimensions of the holes in the SiO$_2$ layer (i.e. dimensions of the stamp), while the height is controlled by the deposition time. In this sense, high aspect ratio nanoparticles can be obtained since the thickness of the bottom PMMA layer does not influence lateral resolution and at the same time its undercut profile facilitates the lift-off process, see Figure 3.5.
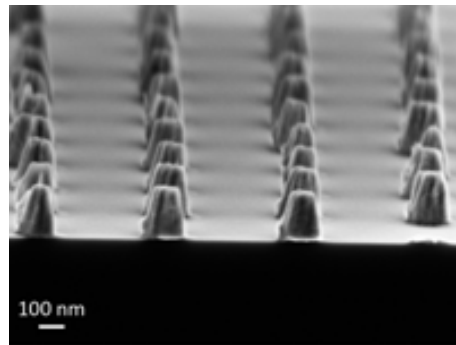
Figure 3.5 SEM images of nanoparticles after the lift-off, diameter of the particles is 150 nm and 200 nm height.

3.2.2 Stencil vs. nanoimprinted hard mask

The principle of hard mask has been used in micro and nanofabrication since a long time ago. It is used to locally deposit material and etch or modify the substrate [32,33]. The well-known stencil lithography or shadow mask is a good example of hard mask use. Stencil technique uses an external hard mask to locally deposit material by evaporation. This mask is usually a silicon or silicon nitride membrane with apertures [34], see Figure 3.6. Stencil mask does not touch the substrate, so the process is free of resist. This is an important advantage, when fragile substrates are used, since no resist processing is required. Moreover, it is very versatile regarding the materials that can be deposited.
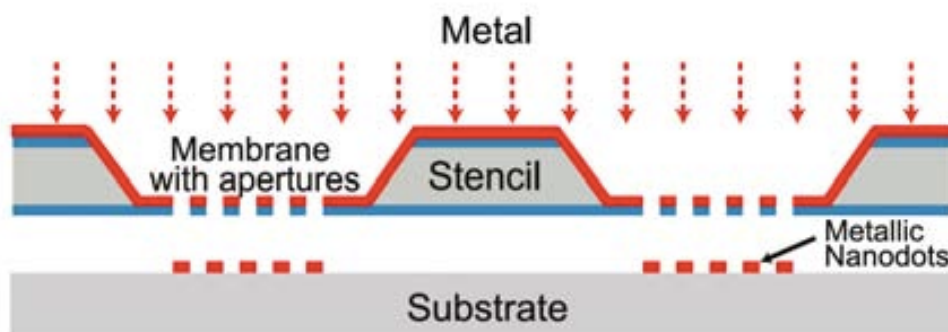

Figure 3.6. Simplified drawing of stencil lithography. A stencil containing membranes with apertures is fixed on top of a substrate. Then, during the evaporation of the metal, the material passing through the stencil is deposited on the substrate, reproducing the stencil apertures [19].

However, the surface topography and the slight curvature of conventional silicon wafers lead to a non-uniform contact between the substrate and the mask, with separations of at least few microns. As it can be observed in Figure 3.7a, the stencil-substrate gap, in addition to the surface diffusion of the material during the deposition, produces the blurring phenomenon known in stencil lithography. Blurring becomes a drawback when precision patterns are required. This situation is extendedly explained

in [24,35]. In some works, spacers of well-known height have been placed between substrate and mask in order to obtain a uniform gap [34]. In this way the diffusion is controlled but not avoided.

In the presenting process, a thick resist layer supports the mask, see Figure 3.7b. Since the resist is homogeneously deposited on the substrate, the non-uniformities of the sample are compensated and nanometric mask-substrate distance is uniform in the entire sample. Moreover, the inherent surface diffusion of the metal is blocked by the resist
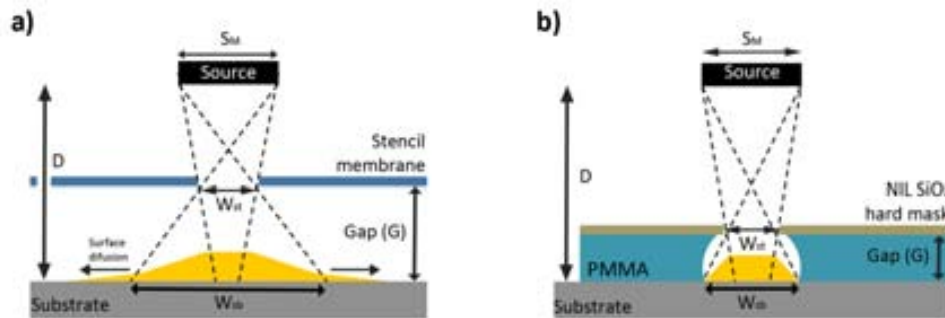

Figure 3.7. Representation of the metal deposition in the case of typical stencil (a) and the process using the SiO_2 hard mask fabricated by NIL, adapted from [19] (b). It can be observed that in both cases the metal takes slope shape due to the source-mask-substrate geometry. In the stencil case, a spread shape of the deposited structures is obtained due to the blurring effect. In the NIL process the blurring is blocked by the PMMA walls.

3.3   RESULTS OF EVAPORATION AND SPUTTERING METALLIZATION

Using the process described above, arrays of nanoparticles of diverse shapes and materials have been fabricated. First, we discussed separately the results obtained with metal deposition by e-beam evaporation and the ones obtained by RF-sputtering. Finally, the results of the optical characterization of the arrays of particles are presented.

3.3.1   Nanoparticles defined by e-beam evaporation

Cylindrical and pyramidal nanoparticles are obtained by e-beam evaporation because the metal deposition is performed with a high degree of directionality. In this work, stamps with dots of 50, 150 and 400 nm with separation of 400, 350 and 400 nm respectively have been used. The deposition rate was 1.2 Å/s, at 8000 V and the ATC Orion deposition system (AJA International, Inc) was used. Figure 3.8 shows an example of an array of nanoparticles fabricated by evaporating 200 nm of Au, previously 10 nm of Ti were deposited to improve the adhesion on the substrate.
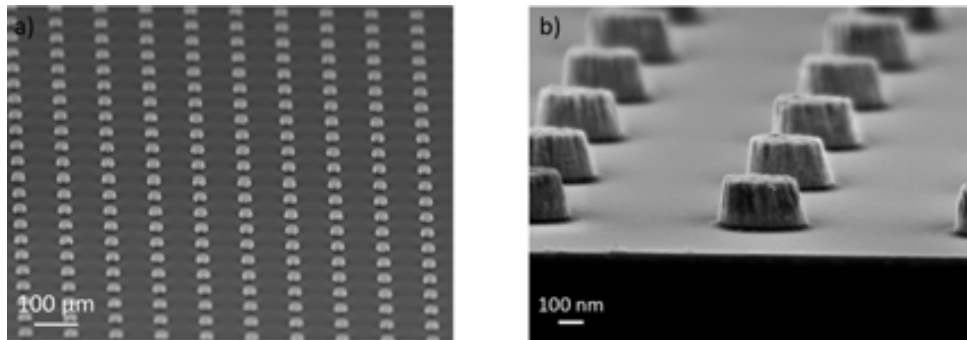
Figure 3.8 SEM images of nanoparticles fabricated by the multilayer configuration and e-beam evaporation. Diameter of the nanoparticles is 400 nm and height is 200 nm.

There are two effects that influence the three-dimensional shape of structures, blurring and clogging. These same effects have also being studied for the case of nanostencil lithography [35,36].

Blurring causes the widening of the lateral dimensions of the metal nanoparticle. Blurring occurrence is due to two factors: geometrical shadowing at the edges of the structure and surface diffusion of metal atoms after deposition. Geometrical blurring depends on the relation between metal source-mask-substrate distances, the diameter of the metal source (S) and the mask aperture diameter (X). As schematically represented in Figure 3.9, it can be observed that during material deposition there is a central area (A) where the entire source contribute to the metal deposition, and a side area (B) where the material is provided only by a partial zone of the source. The smaller is the mask-substrate gap (G) in relation with the metal source- mask distance (D), the lower the blurring of the material will be, Figure 3.9. The maximum extension of the blurring is determined by Wcrit=(G)(S)/(D) and in practice, it can be lower for highly directional deposition. In the present case, the mask-substrate gap (G) is considerably smaller (bottom PMMA thickness, 400 nm) than in a standard stencil configuration, where the smallest gap has the dimension of few microns. In our case, the geometrical blurring of the structures is practically non-existent.
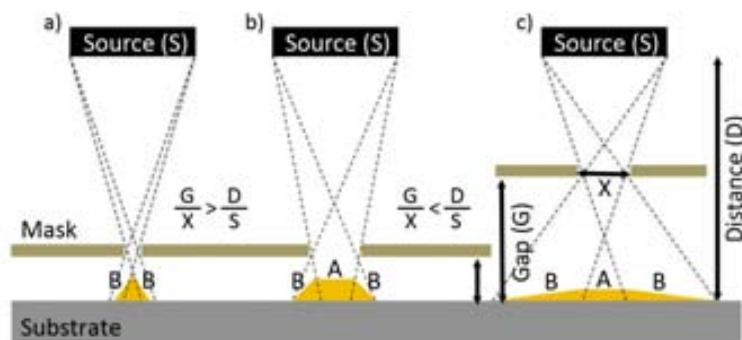

Figure 3.9 Scheme illustrating the material flux profile. a) Mask aperture size is lower than the critical dimension, so the material is partially received from the source. b) When mask aperture is larger than the critical size two areas are distinguished on the particles, (A) where material is received from the entire source and (B) where material partially arrives. c) When substrate-mask gap is larger, the blurring is bigger, so the material is more diffused on the substrate. Adapted from [35].

Clogging has a strong influence in the final tree-dimensional shape of the nanoparticles. During the evaporation of the sample, the diameter of the apertures in the SiO$_2$ hard mask gradually reduces due to the material deposition on the sidewalls of the openings, until it eventually clogs. The reduction of aperture width due to direct material deposition depends on the angle distribution of the incident material flux, magnitude of the surface diffusion and the characteristic of the material to be stuck in the sidewalls. This phenomenon has been widely studied in previous works [36]. The clogging effect can be reduced by appropriate treatments, such as surface modification and cleaning of the stencil.
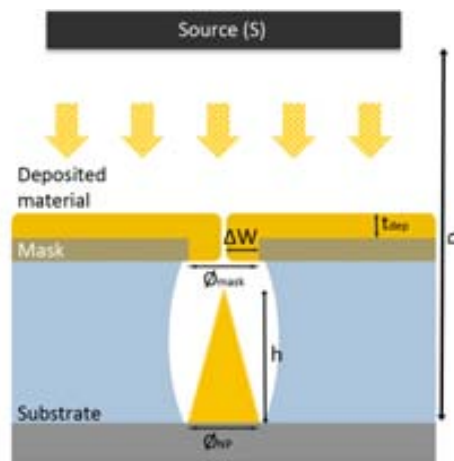

Figure 3.10 Representation of clogging effect adapted to our configuration. Right, SEM image of the cones obtained using this technique.

Several works have made important improvements to reduce the clogging effect, such as surface modification of the stencil [37]. We have taken advantage of the clogging effect to fabricate large arrays of cone shape metallic nanoparticles arrays, which is quite challenging using standard lithography methods. Conic nanoparticles are extremely interesting due the specific optical absorbance signal obtained due to their sharp tip.
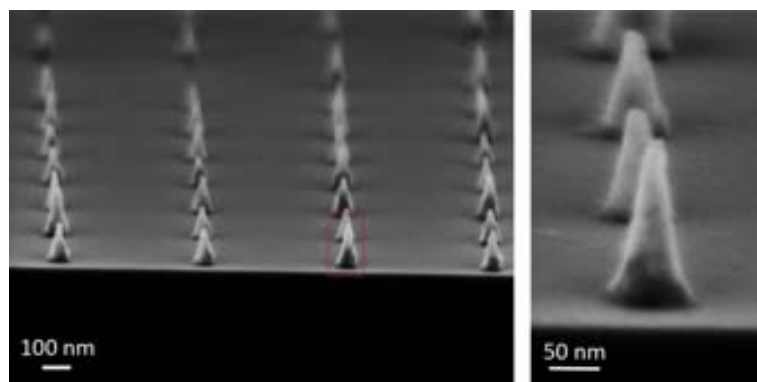

Figure 3.11 SEM image of the cones fabricated using the nanoimprinted hard mask method. Cone shape obtained owing to the clogging effect.

The geometry of the cones is defined by the diameter of the apertures and its reduction, as a function of the metal deposition. Assuming a vertical metal deposition with perfect directionality, the cone angle α is determined by the relation between the height of the nanostructure h and the lateral deposition of metal in the apertures, ΔW:

$$\Delta W = h / \tan \alpha \qquad\qquad\qquad (3\text{-}1)$$

The maximum pattern height is achieved when the apertures of the mask are completely closed, what happens when the deposition of material in the apertures (ΔW) is larger than half the initial diameter of the hole ($\emptyset_{0\ mask}$):

$$\Delta W > \emptyset_{0\ mask} / 2 \qquad\qquad\qquad (3\text{-}2)$$

For the specific example of Figure 3.11, α is determined from the SEM images to be 77º and the deposited material thickness is 200 nm, ΔW is 40 nm. That means that the mask aperture was reduced on 80 nm (ΔW is the reduction per side). Since the initial aperture was 75 nm, the hole of the mask was completely clogged and cone shape NPs were achieved.

3.3.2 Nanoparticles defined by sputtering metallization

When metal deposition is performed by RF-sputtering, ions are pulled out from the source material in vapor form and deposited on the substrate. The target material atoms are spread in every direction, providing a non-directional coverage in the entire surface. The lack of directionality causes the sides of the cavity below the SiO_2 hard mask apertures will be metalized. The undercut obtained during the second etching and the SiO_2 mask (see Figure 3.2) enables the lift-off although the bottom PMMA is totally covered by metal. As a combination of the specific resist-mask configuration and the characteristic of sputtering metallization, *empty* nanoparticles replicating the shape of the cavity were obtained, producing *nanocup-like* nanoparticles, Figure 3.12.
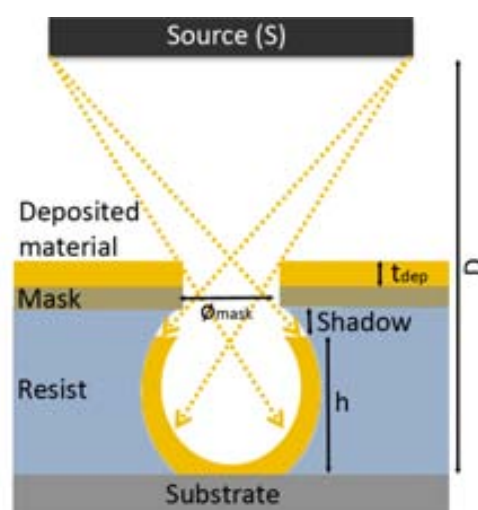

Figure 3.12 Sketch of the fabrication of nanocups by RF-sputtering.

Figure 3.13 shows nanocups fabricated using 400 nm diameter stamp and 100 nm gold sputtering, before (a) and after (b) the lift-off. Previously 10 nm of Ti were deposited to improve the adhesion. The equipment used to perform the sputtering was 903MRC (Materials Research Corporation), at 500 W, $8 \cdot 10^{-3}$ mbar, source-sample distance of 7-8 cm and source area 15 x 30 cm^2.
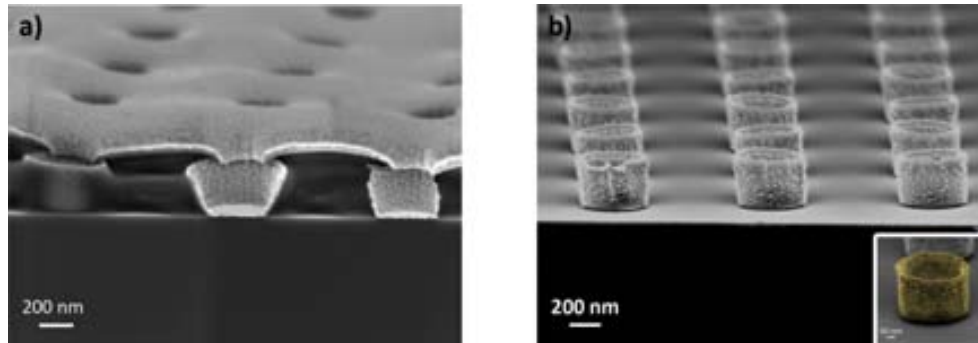

Figure 3.13. SEM images of the metal nanocups, a) before the lift-off and b) after. Diameter of the stamp was 400 nm and 100 nm Au are deposited.

Gold sputtering of 100 nm and 300 nm layers were performed in separated samples. Since the metal volume is distributed in all the area of the nanocups, the added metal in each point does not vary that much, and the shape of the nanocup does not change when more metal is deposited. Figure 3.14 shows nanocups after 300 nm of gold were deposited. Note that the height of the nanocups is given by the shape of the bottom PMMA layer, but not by the deposited metal layer.
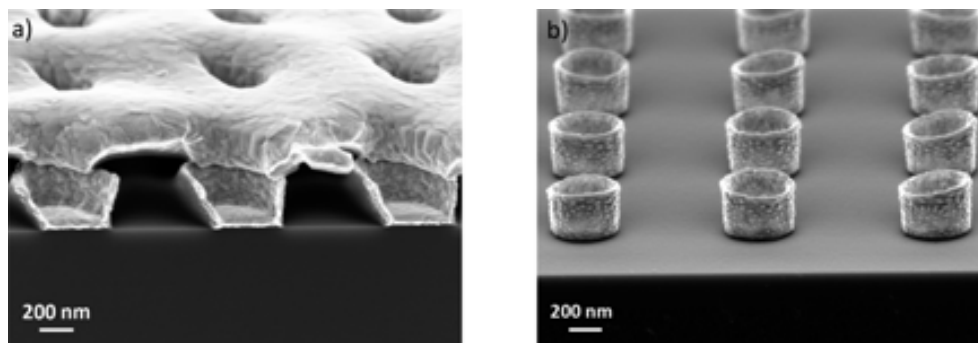

Figure 3.14. SEM images of the metal nanocups, a) before the lift-off and b) after. Diameter of the stamp was 400 nm and 300 nm Au were deposited.

On the other hand, the walls of the nanocups need a minimum thickness to stay up. For instance, Figure 3.15 shows the case when 20 nm of gold are deposited, the walls of the cup are too thin and they flew away in the subsequent steps.
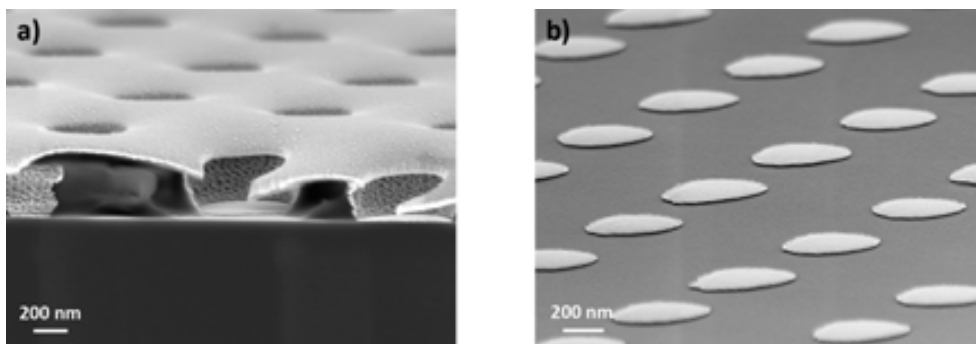
Figure 3.15 SEM images of the metal nanocups, a) before the lift-off and b) after. Diameter of the stamp was 400 nm and 20 nm Au were deposited. The walls of the nanocups were not rigid enough to stay up.

The sputtered metal is distributed all around the surface of the cavity. It has been quantitatively demonstrated that the metal volume in the nanocups is the same as the metal volume on a nanodot after using the same stamp and deposit the same thickness of metal, represented in Figure 3.16. For the case that a stamp with dots of 400 nm of diameter is used and 100 nm of metal are deposited, metal volume for the hypothetical dots is $4 \cdot 10^{-6} \pi$ nm^3 and $4.3 \cdot 10^{-6} \pi$ nm^3 for the experimental nanocups. These values can be considered equivalent, the small variation between them could be attributed to an error when measuring the dimensions of the nanocups by SEM.
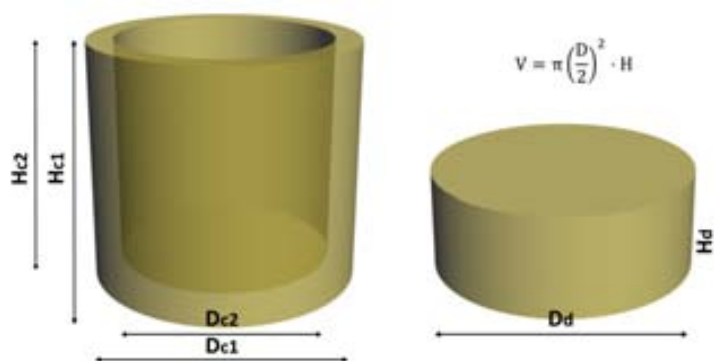

Figure 3.16 Representation of the volumes of a cup (left) and a dot (right).

The parameters used during the sputtering are highly relevant for the successful fabrication of nanocups. The same process was repeated using a different equipment. The new equipment was a RF-sputtering from Ferrotec, located at the University of Barcelona. Table 3-2 shows the parameters used to optimize the process in the new equipment.

Table (3-2). Parameters used for the fabricated nanocups using Ferrotec equipment.

Sample	Temperature (°C)	Pressure (mbar)	Power (W)	Time (min)	Metal (nm)
a	458	$4 \cdot 10^{-3}$	290	58	150
b	100	$4 \cdot 10^{-3}$	20	30	150
c	52	$4 \cdot 10^{-3}$	10	190	150
b	100	$9 \cdot 10^{-3}$	20	205	150

The results obtained from the fabrication of nanocups using the parameter presented in Table (3-2), are shown in Figure 3.17. It seems that extremely high temperature and power melt the bottom PMMA and deform the shape of the nanocups, as it happens in case a. In case b and d, 100 °C and 20 W give the impression to be still aggressive conditions to grow nanocups. Moreover, in the inset of Figure 3.17 it can be observed that when more assertive parameters are used, the directionality of the deposition is enhanced, and thus more metal is accumulated in the center of the particle. Optimum parameters for this equipment are given in case c, low temperature (52 °C) and low power (10 W), but long time (190 minutes) to replicate the nanocups obtained with the first equipment.
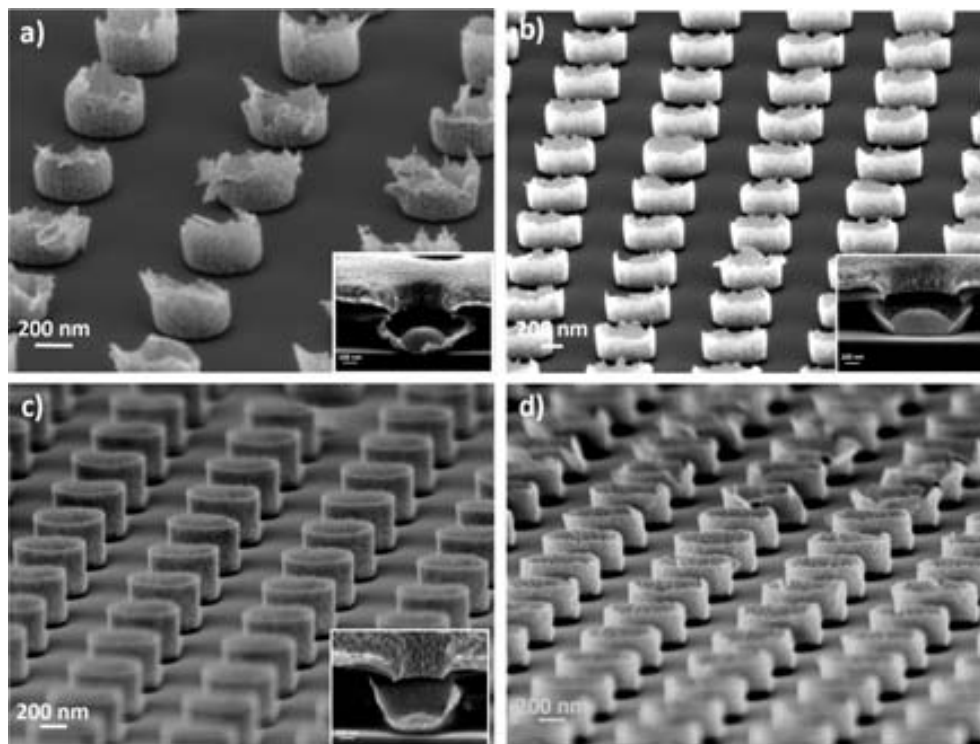

Figure 3.17. Nanocups fabricated with the Ferrotec sputtering. Different conditions were used for each sample.

Experimentally seen situations were confirmed by simulations performed using de *Sentaurus Process* form Synopsys software. Figure 3.18a shows the model used for the simulations, as the hard mask configuration is symmetric, only half of it was simulated. When a vertical single beam is used to carry out the metallization, i.e. e-beam evaporation, the metal is deposited just on the center of the cavity, there is not contact between the nanoparticle and the bottom resist. In addition it is noticed that the hard mask starts to clog due to the deposition of metal on top of it.
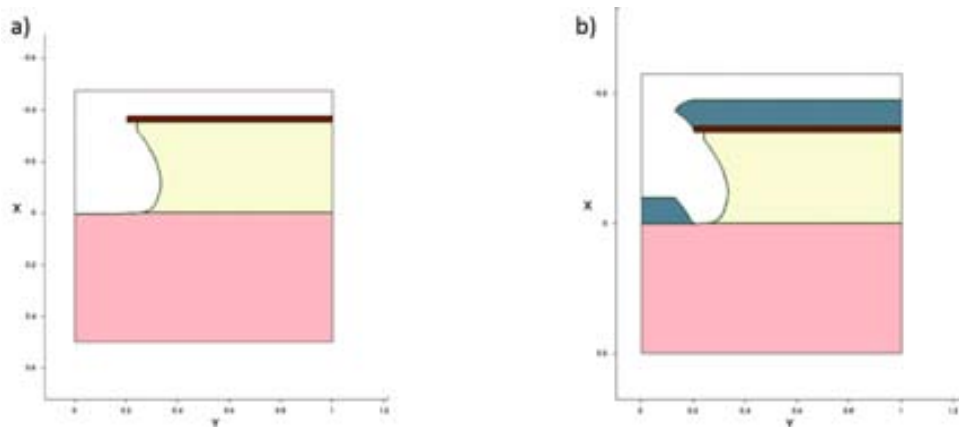

Figure 3.18 Results of the simulation performed to study the metal deposition related with the hard mask and the cavity on the bottom resist. a) Half cavity was simulated because the system is symmetric. b) Deposition of metal by a single vertical beam, the metal is placed just on the center of the cavity.

It was also simulated the case when the metal incident is uniform in all the directions (truly simulation was performed as if they would be four beams with different incident angles 0º, 20º, 40º, 60º). In this case the metal is deposited on the wall of the bottom resist, as it has been experimentally seen when sputtering metallization is carried out. When the deposition of the metal is totally uniform in all the directions, Figure 3.19a, it seems that slightly more metal is deposited on the center of the particle, comparing with the case when higher weight is given to the tilted beam and less to the vertical, Figure 3.19b. That agrees with the experimental results presented in Figure 3.17, when more assertive parameters are used, and thus more directional, higher amount of metal is deposited on the center.
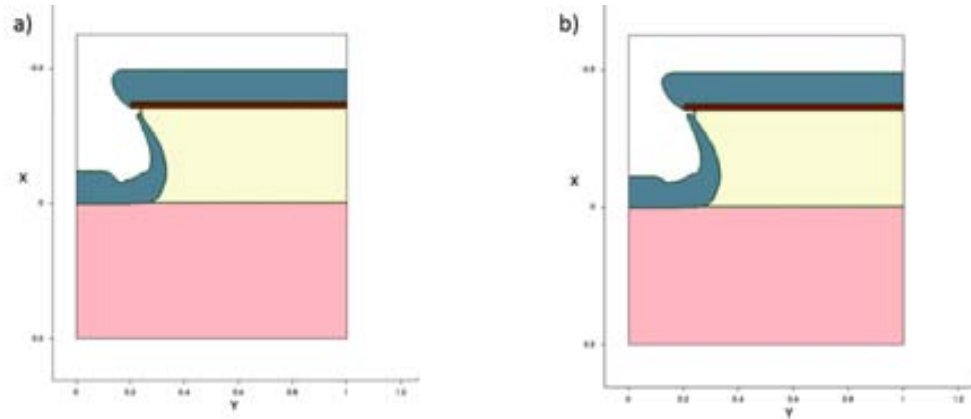
Figure 3.19 Results of the simulations when a) deposition of metal uniformly in all the direction. b) Deposition of metal in all the directions, with higher weight in the tilted beam and less in the vertical.

The complementary shape that present the nanoparticles depending on the metal deposition methods and the good performance of the NIL-hard mask approach for lift-off process enable the possibility to build-up nanoparticles with heterogeneous composition. By performing a deposition sequence constituted by a RF-sputtering deposition to fabricate cup shaped nanoparticles followed by a directional deposition made by e-beam evaporation allows to obtain the nanoparticles shown in Figure 3.20, nanocups made of 100 nm Au and filled with 300 nm high aluminum dots.
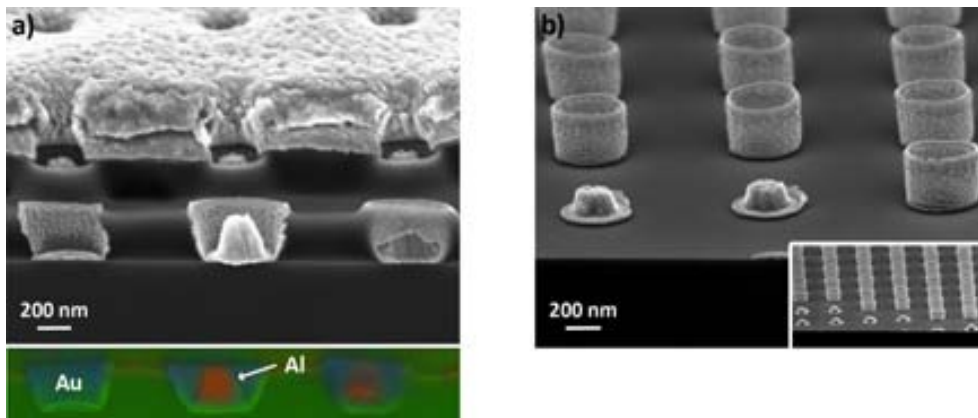

Figure 3.20 SEM images of nanocups, 400 nm diameter and 100 nm of deposited gold, filled with 300 nm of Al. a) Image previous to perform the lift-off process, at the bottom a EDX image represent the different materials in the sample, being red aluminum, blue gold and green the carbon of the PMMA. a) Image after the lift-off. When the cross-section of the sample was performed, some of the cups flew away, thus the aluminum of the interior of the cups can be observed.

3.4   OPTICAL CHARACTERIZATION OF THE NANOCUPS

Metallic nanoparticles with defined geometry are key elements for the fabrication of highly sensitive, fast response, low cost sensors, based on the optical properties of the

nanoparticle. Localized surface plasmon resonance (LSPR) sensors have been studied intensively as one of the promising nanobiosensors for medical diagnosis, monitoring of diseases, and the detection of environmental pollutants. In this section, the LSPR behavior of our nanocups is presented. Displacements of the absorbance peak has been observed, first due to the structuration of the particles and then when they are covered by thin layer of dielectric material.

3.4.1   LSPR principle

When matter is exposed to light, a number of processes can occur, such as absorption of the light, scattering at the same frequency as the incoming light (Mie or Rayleigh scattering), re-emission of the absorbed light, or enhancement of the local electromagnetic field of the incoming light thus enhancing any spectroscopic signals from the molecules at the material surface, that is, surface-enhanced spectroscopy, such as surface-enhanced Raman scattering.

In the case of gold nanoparticles, all these properties are strongly enhanced owing to the unique interaction of the light with the free electrons in the metal particles [38]. When gold nanoparticles are exposed to optical radiation, the electric field of the light causes the collective oscillation of the conduction-band electrons at the surface of the particle, with respect to the ionic core of the nanoparticle. The coherent oscillation of the metal free electrons in resonance with the electromagnetic field is called the surface plasmon resonance (SPR) [38]. For gold nanospheres, this resonance occurs in the visible spectral region at approximately 520 nm, which is the origin of the brilliant red color of the nanoparticles in solution. The excitation of the SPR results in the enhancement of the photophysical properties of gold nanoparticles.
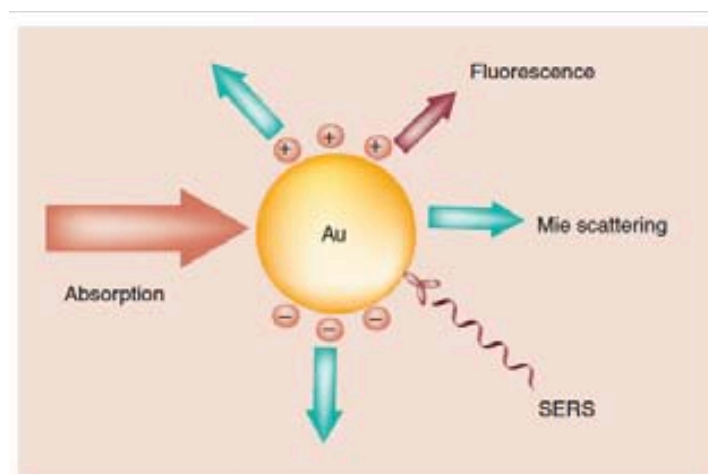

Figure 3.21 important optical processes resulting from the interaction of light with a gold nanoparticle [38].

For the case of localized surface plasmons, light interacts with particles much smaller than the incident wavelength. This leads to a plasmon that oscillates locally around the

nanoparticle with frequency known as the LSPR [18]. Similar to SPR, the LSPR is sensitive to change in the local dielectric environment.
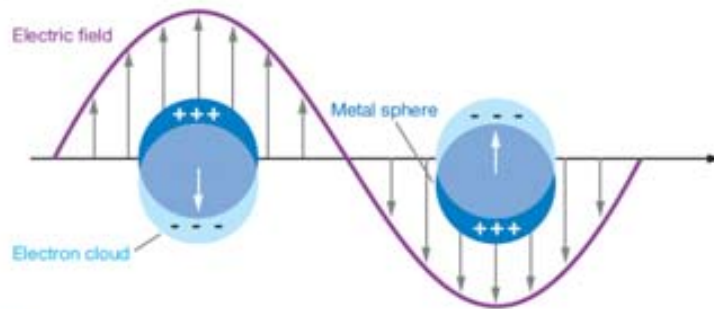

Figure 3.22 representation of the electric field in resonance with the NPs electron cloud [18].

3.4.2   Results and discussion

The nanocups have been optically to prove their capability as LSPR sensors, using the UV and visible spectrophotometer (specord 205, Analytic Jena) placed at the University of Barcelona. As it can be seen in Figure 3.23, when light is applied to the nanocups, the absorbance signal displaces to higher wavelength, compared with a continue gold layer. These nanocups were fabricated on a 170 μm thick glass substrate (Carl Roth GmbH), they have diameter of 400 nm and 100 nm gold were deposited.
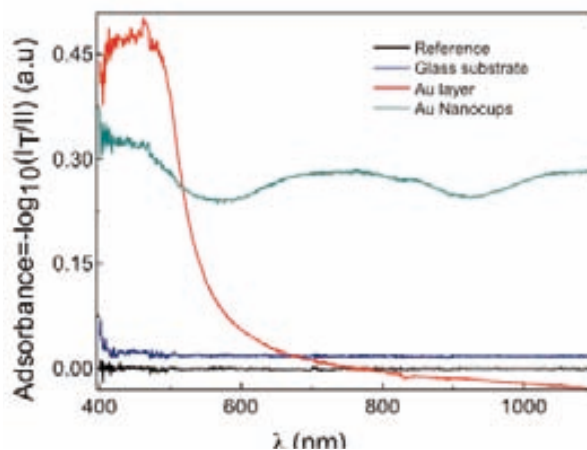
Figure 3.23 Absorbance spectra where the signal of the continue gold layer and nanocups are compared. The signal obtained from the nanocups was displaced to higher wavelengths.

This measures were repeated in several points of the same sample and in separate samples with the same type of nanocups in order to prove the repetitivity of the technique. Figure 3.24 A and B represent two different samples and I-V measured points in each of them.
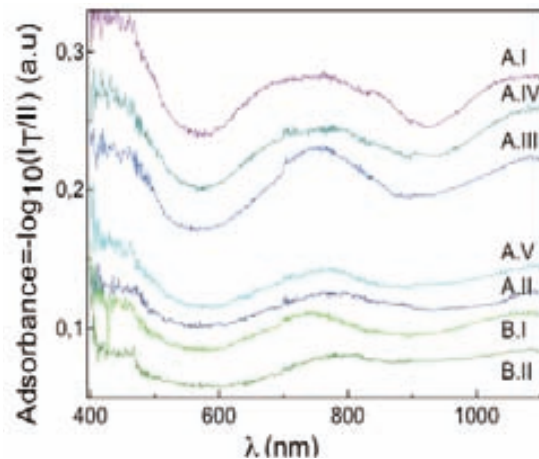
Figure 3.24 absorbance of the nanocups in separated samples (A and B) and in different points of each of their (I-V).

Similar to the SPR, the LSPR is sensitive to changes in the local dielectric environment. The relation between the LSPR and the local dielectric environment was demonstrated by covering the gold nanocups with a 10 nm Al_2O_3 layer, deposited by ALD, in order to create a dielectric-metal state. The transmission and reflection caused by the nanocups before and after the covering was studied in Figure 3.25.
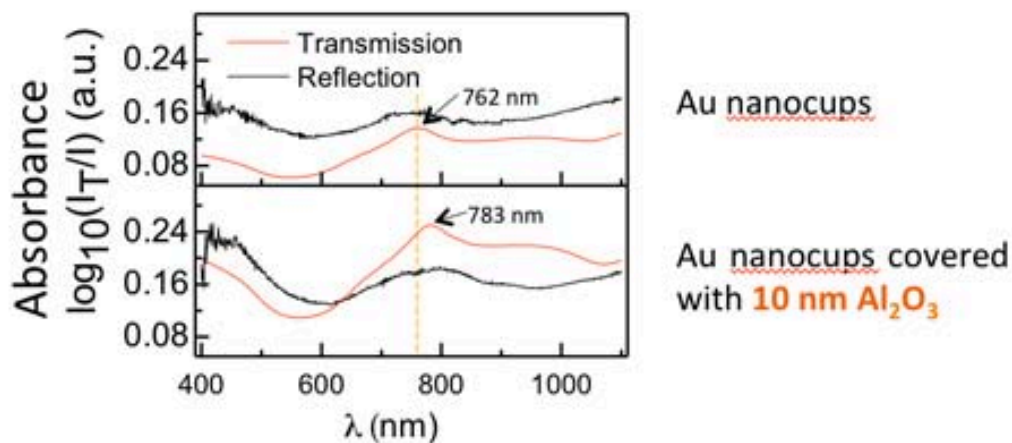

Figure 3.25 Transmission and reflection measured in gold nanocups before and after Al_2O_3 covering. Displacement of the signal occurs due to the dielectric covering.

Displacement of the transmission signal occurs due to the reflection index modification caused when covering the nanocups with a dielectric layer. The transmission signal was moved from 762 nm wavelength to 783 nm.

3.5   PROPOSED CHARACTERIZATION AND APPLICATION

3.5.1   Optical characterization of individual nanoparticles

These measurements demonstrate that the nanoimprinted hard mask based technology is capable to fabricate promising nanoparticles that could be used as LSPR sensors. Nevertheless, there is still a hard work to do in order to better understand the relevance of the shape, size, separation and material of the nanoparticles.

An important issue that we are studying during the time that this thesis is being written is the relevance of the separation between nanoparticles. There are several works that mention the disadvantage of having arrays of particles, or at least rather close particles [18,19]. It seems that the coupling of the signals of nearby nanoparticles interfere in the final results. It could happen that better results are obtained using isolated (or very separated) nanoparticles. This point will be analyzed by the performance of SNOM (scanning near-field optical microscopy) test to the nanoparticles. By this technique we want to characterize the contribution of a single nanoparticle.

3.5.2   Feasible applications

This chapter has been focused in the use of nanocups as LSPR sensors. However, the nanoparticles arrays fabricated using the hard mask concept can also be used in other interesting applications. Some of them will be explained below.

The first one is the use of nanocones as antennas. Biodevice science is rapidly growing, some of these devices need nanometric antennas to be inserted in cells. This process is relevant because there are few micro/nano technologies that allow the fabrication of cone shape particles. Even less methods are able to make arrays of cones in a high throughput method.

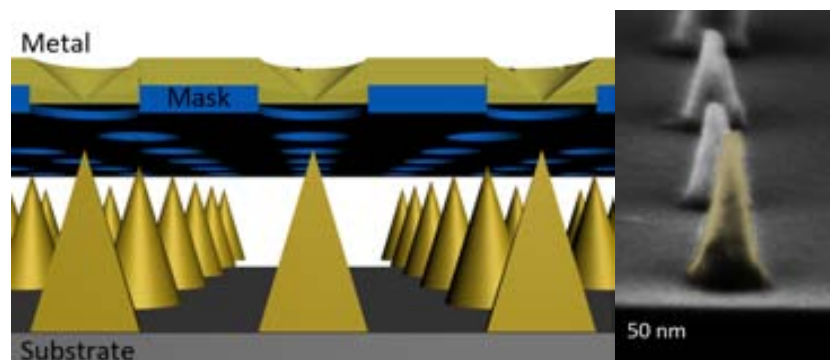Figure 3.26. Left, sketch of the nanocones fabrication by means of clogging effect. Right, SEM image of the nanocones obtained by the hard mask method.

In order to demonstrate the feasibility of the next application, gold nanocups were fabricated on top of interdigitated microelectrodes, see Figure 3.27. First, interdigitated electrodes were fabricated by means of optical lithography and lift-off. The digits were 5

95

μm width and pitch 10 μm. Then, the multilayer thermal nanoimprint process was followed on top of the interdigitated electrodes. Stamp with dots of 400 nm of diameter and the same separation was used, 100 nm of gold was deposited by RF-sputtering. This application can be used on the one hand to enhance the active area of the electrodes. On the other hand, it can also be employed to fabricate nanocups of a different material than the digits, in this way, the device could be functionalized with distinct groups.
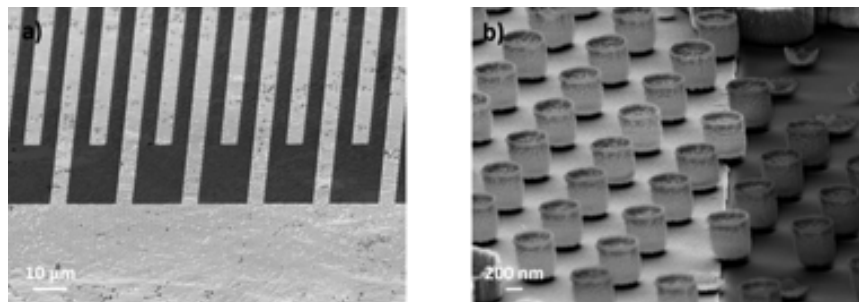

Figure 3.27. SEM images of gold nanocups fabricated on top of μIDEs.

Another proposed application, which is currently been developed, consists on the release of the nanoparticles fabricated by nanoimprint process from the. As it is depicted in Figure 3.28, the process is similar to the hard mask multilayer process developed in this work, but under the bottom PMMA an extra sacrificial layer is placed. This sacrificial layer must support the whole process until the end. When arrays of nanoparticles are fabricated on top of the sacrificial layer, the sacrificial layer will be dissolved and the particles will be released. This process is specially interesting when nanoparticles with combined materials are desired or nanoparticles with characteristic size or shape, which would be difficult to obtain by traditional chemical methods.
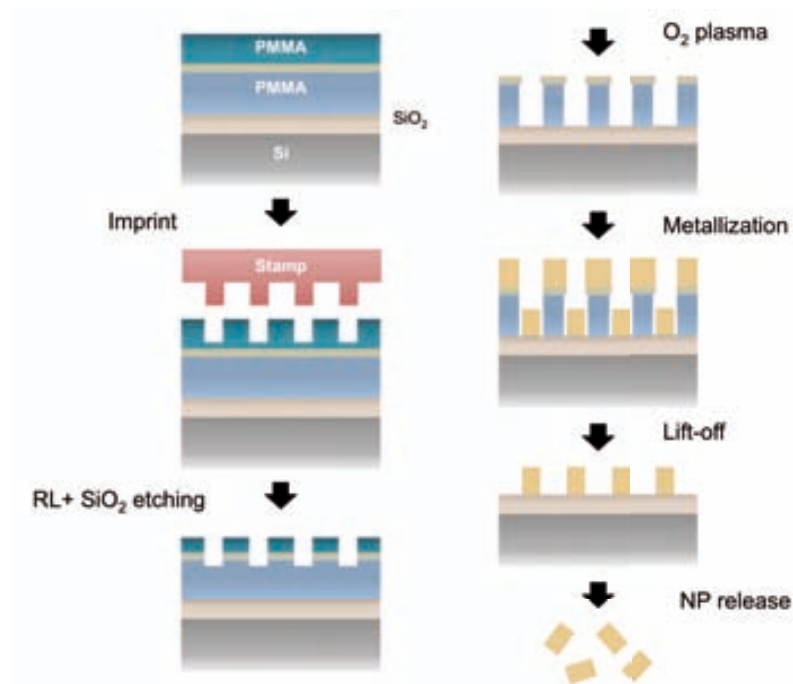

Figure 3.28. Nanoimprinted hard mask process to release nanoparticles.

3.6   CONCLUSIONS OF CHAPTER 3

Metallic nanoparticles with defined geometry are key elements for the fabrication of highly sensitive, fast response, low cost sensors. For example, localized surface plasmon resonance (LSPR) in metallic nanostructures stands out as a significant option for biomolecular sensing. It requires the massive production of nanoparticles and its accurate positioning at specific places of larger-size structures or devices. While established chemical methods to synthesize NPs exists, reliable processes to control the position and orientation of the NPs on substrates are still not fully developed. On the other hand, when the production of the NPs follows a top down lithography-based approach, a higher degree of order can be easily achieved. Several processes have demonstrated the feasibility to fabricate NP arrays. However, all of them still present drawbacks, such as limitation on the aspect ratio, weak definition of the patterns or low throughput.

In this chapter a new approach that combines thermal NIL together with the definition of a hard mask has been presented. It overcomes most of the limitations that other techniques have, and it enables the large-scale production of nanoparticles with heterogeneous composition.

This technique consists on the fabrication of a SiO_2 hard mask on top the substrate by means of thermal nanoimprint lithography. Between the hard mask and the substrate there is a thick layer of PMMA, which is etched by oxygen plasma. The cavity formed in the bottom PMMA facilitated the subsequent lift-off and enabling the definition of NPs with diverse three-dimensional geometry. In particular, it has been demonstrated that cone-like or cup-like NPs can be obtained depending on the metal deposition process (e-beam evaporation or RF-sputtering). Array of cone-like NPs formed by exploiting the clogging effect in small apertures during the e-beam metal evaporation. Cup-like nanoparticles are obtained due to the non-directionality of the sputtering, they take the shape of the bottom PMMA layer cavities. In addition, the combination of both metal deposition processes allows obtaining NPs with heterogeneous composition.

The capability of the particles to be used as LSPR sensors was demonstrated by absorbance and transmittance techniques. Specific displacement of the absorbance peak is detected, related with the bulk material. It was observed a sift on the transmittance when the particles are covered with a dielectric layer. This results refroze the theory about the LSPR behavior.

The simultaneous advantages of high throughput (NIL), variable composition and three-dimensional control reveal the high applicability of the process to diverse areas like plasmonics, biosensing and nanomagnetism.

REFERENCES CHAPTER 3

1.   Genov, D. A., Sarychev, A. K., Shalaev, V. M. & Wei, A. Resonant Field Enhancements from Metal Nanoparticle Arrays. *Nano Letters* 4, 153-158, (2003).

2.   Yang, M., Li, J., Lin, F. & Zhu, X. Absorption Enhancements in Plasmonic Solar Cells Coated with Metallic Nanoparticles. *Plasmonics*, 1-7, (2013).

3.   Spinelli, P. *et al.* Plasmonic light trapping in thin-film Si solar cells. *Journal of Optics* 14, 024002 (2012).

4.   Huang, J., Chiam, S. Y., Tan, H. H., Wang, S. & Chim, W. K. Fabrication of Silicon Nanowires with Precise Diameter Control Using Metal Nanodot Arrays as a Hard Mask Blocking Material in Chemical Etching. *Chemistry of Materials* 22, 4111-4116, (2010).

5.   Saison-Francioso, O. *et al.* Plasmonic Nanoparticles Array for High-Sensitivity Sensing: A Theoretical Investigation. *The Journal of Physical Chemistry C* 116, 17819-17827, (2012).

6.   Yeshchenko, O. A., Kondratenko, S. V. & Kozachenko, V. V. Surface plasmon enhanced photoluminescence from fullerene C_{60} film on Au nanoparticles array: Resonant dependence on excitation frequency. *Journal of Applied Physics* 111, 124327-124327-124325, (2012).

7.   Shan, G., Zheng, S., Chen, S., Chen, Y. & Liu, Y. Multifunctional ZnO/Ag nanorod array as highly sensitive substrate for surface enhanced Raman detection. *Colloids and Surfaces B: Biointerfaces* 94, 157-162, (2012).

8.   Willner, I., Patolsky, F. & Wasserman, J. Photoelectrochemistry with Controlled DNA-Cross-Linked CdS Nanoparticle Arrays. *Angewandte Chemie International Edition* 40, 1861-1864, (2001).

9.   Sugimura, H., Mo, S., Yamashiro, K., Ichii, T. & Murase, K. Photochemical Assembly of Gold Nanoparticle Arrays Covalently Attached to Silicon Surface Assisted by Localized Plasmon in the Nanoparticles. *The Journal of Physical Chemistry C* 117, 2480-2485, (2012).

10.   Alvarez-Puebla, R. A. *et al.* Gold nanorods 3D-supercrystals as surface enhanced Raman scattering spectroscopy substrates for the rapid detection of scrambled prions. *Proceedings of the National Academy of Sciences* 108, 8157-8161, (2011).

11.   Haes, A. J., Hall, W. P., Chang, L., Klein, W. L. & Van Duyne, R. P. A Localized Surface Plasmon Resonance Biosensor: First Steps toward an Assay for Alzheimer's Disease. *Nano Letters* 4, 1029-1034, (2004).

12.   Gómez-Hens, A., Fernández-Romero, J. M. & Aguilar-Caballos, M. P. Nanostructures as analytical tools in bioassays. *TrAC Trends in Analytical Chemistry* 27, 394-406, (2008).

13. Anker, J. N. *et al.* Biosensing with plasmonic nanosensors. *Nat Mater* 7, 442-453 (2008).

14. González, E., Arbiol, J. & Puntes, V. F. Carving at the Nanoscale: Sequential Galvanic Exchange and Kirkendall Growth at Room Temperature. *Science* 334, 1377-1380, (2011).

15. Gong, J., Zu, X., Mu, W. & Deng, Y. In situ self-assembly synthesis of gold nanoparticle arrays on polystyrene microspheres and their surface plasmon resonance. *Colloid Polym Sci* 291, 239-244, (2013).

16. Scheeler, S., Ullrich, S., Kudera, S. & Pacholski, C. Fabrication of porous silicon by metal-assisted etching using highly ordered gold nanoparticle arrays. *Nanoscale Research Letters* 7, 1-7, (2012).

17. Brodoceanu, D. *et al.* Fabrication of metal nanoparticle arrays by controlled decomposition of polymer particles. *Nanotechnology* 24, 085304 (2013).

18. Willets, K. A. & Van Duyne, R. P. Localized Surface Plasmon Resonance Spectroscopy and Sensing. *Annual Review of Physical Chemistry* 58, 267-297, (2007).

19. Vazquez-Mena, O., Sannomiya, T., Villanueva, L. G., Voros, J. & Brugger, J. Metallic Nanodot Arrays by Stencil Lithography for Plasmonic Biosensing Applications. *ACS Nano* 5, 844-853, (2010).

20. Mangold, M. A., Weiss, C., Dirks, B. & Holleitner, A. W. Optical field-enhancement in metal nanoparticle arrays contacted by electron beam induced deposition. *Applied Physics Letters* 98, 243108-243108-243103, (2011).

21. Dreaden, E. C., Near, R. D., Abdallah, T., Talaat, M. H. & El-Sayed, M. A. Multimodal plasmon coupling in low symmetry gold nanoparticle pairs detected in surface-enhanced Raman scattering. *Applied Physics Letters* 98, 183115 (2011).

22. Near, R., Tabor, C., Duan, J., Pachter, R. & El-Sayed, M. Pronounced Effects of Anisotropy on Plasmonic Properties of Nanorings Fabricated by Electron Beam Lithography. *Nano Letters* 12, 2158-2164, (2012).

23. Lee, S.-W. *et al.* Highly Sensitive Biosensing Using Arrays of Plasmonic Au Nanodisks Realized by Nanoimprint Lithography. *ACS Nano* 5, 897-904, (2011).

24. Vazquez-Mena, O. *et al.* Reliable and Improved Nanoscale Stencil Lithography by Membrane Stabilization, Blurring, and Clogging Corrections. *Nanotechnology, IEEE Transactions on* 10, 352-357, (2011).

25. Christophe Peroz, G. C., Scott D. Dhuey, Nerea Alayo, David Gosselin, Marko Volger, Deidre Olynick, Stefano Cabrini. Single-digit nanofabrication by UV step-and-repeat nanoimprint lithography. *SPIE* (2013).

26. Scott Dhuey, C. P., Giuseppe Calafiore, Nerea Alayo, David Gosselin, Deirdre Olynick, Stefano Cabirini, . in *EIPBN* (Nashville, TN (USA), 2013).

27. Bergmair, I. *et al.* Single and multilayer metamaterials fabricated by nanoimprint lithography. *Nanotechnology* 22, 325301-325306, (2011).

28. Petryayeva, E. & Krull, U. J. Localized surface plasmon resonance: Nanostructures, bioassays and biosensing—A review. *Analytica Chimica Acta* 706, 8-24, (2011).

29. Tokareva, I., Minko, S., Fendler, J. H. & Hutter, E. Nanosensors Based on Responsive Polymer Brushes and Gold Nanoparticle Enhanced Transmission Surface Plasmon Resonance Spectroscopy. *Journal of the American Chemical Society* 126, 15950-15951, (2004).

30. Chou, S. Y., Krauss, P. R. & Renstrom, P. J. 4129-4133 (AVS).

31. Calafiore, G. *Step and repeat UV nanoimprint lithography: development of new applications and ultimate pattern resolution.*, Politecnico di Torino, (2012).

32. Carrara, S. *et al.* Memristive-biosensors: A new detection method by using nanofabricated memristors. *Sensors and Actuators B: Chemical* 171–172, 449-457, (2012).

33. Ziaie, B., Baldi, A., Lei, M., Gu, Y. & Siegel, R. A. Hard and soft micromachining for BioMEMS: review of techniques and examples of applications in microfluidics and drug delivery. *Advanced Drug Delivery Reviews* 56, 145-172, (2004).

34. Deshmukh, M. M., Ralph, D. C., Thomas, M. & Silcox, J. Nanofabrication using a stencil mask. *Applied Physics Letters* 75, 1631-1633 (1999).

35. o. Vazquez-Mena, L. G. V., V. Savu, K. Sidler, P. Langlet, J. Brugger. Analysis of the blurring in stencil lithography. *Nanotechnology* 20 (2009).

36. Lishchynska, M. *et al.* Predicting mask distortion, clogging and pattern transfer for stencil lithography. *Microelectronic Engineering* 84, 42-53, (2007).

37. Kölbel, M. *et al.* Shadow-Mask Evaporation through Monolayer-Modified Nanostencils. *Nano Letters* 2, 1339-1343, doi:10.1021/nl025784o (2002).

38. Huang, X., Jain, P. K., El-Sayed, I. H. & El-Sayed, M. A. Gold nanoparticles: interesting optical properties and recent applications in cancer diagnostics and therapy. *Nanomedicine* 2, 681-693 (2007).

SECTION III

Interdigitated nanoelectrodes

Interdigitated nanoelectrodes

During the last decades, research on biochemical detection has been exploiting the improved sensing properties that appear when the sensing element has a size that is comparable with the target elements, which is typically (far) below 100 nm. The benefit of reducing the electrodes size has been widely proved. However, the yield of nanosensor fabrication is still a challenge that must be overcome.

During this thesis we have gone through the fabrication of an electrochemical nanosensor that improves the detection limits and selectivity of actual sensors. Moreover, we have made a vast effort to optimize the fabrication of the sensor with a considerable success. Our sensor, depicted in Figure 1, is based on two arrays of comb-shaped metallic electrodes with nanometric dimensions, collected each of them in micropads and fabricated on insulator substrate. This kind of sensor arrays is called *interdigitated nano-electrodes* (nIDEs).

The most sensitive and critical part of these structures corresponds to the area right in-between two facing nanoelectrodes. For this reason, when not only the electrode width, but also the electrode spacing is reduced below 100 nm, the sensitivity increases drastically [1-4]. At the end, this will imply the use of less quantity of analyte, a faster performance, smaller device size, the possibility of integration to carry out parallel complementary assays, and ultimately, to use the devices for label-free real time single molecule detection [5]. This represents an enormous impact in biomedicine, allowing the introduction of new medical detection procedures, for example by developing high sensitivity portable systems, or for diminishing the costs of therapeutic drug development.
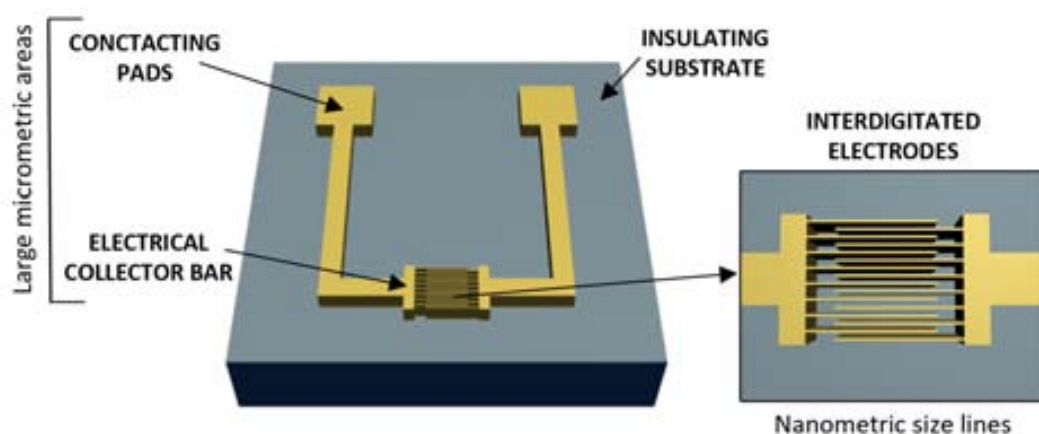

Figure 1. Sketch of an interdigitated electrode. The device is composed by an array of digits. Half of the digits are assembled in a collector bar and the other half to another collector bar, followed by micropads that allow external electrical connection. The device is fabricated on top of insulator substrate.

Interdigitated electrodes as sensors for biochemical detection have been widely used during the last years. They can be used in many different operation modes: (i) as electrochemical sensors, by detecting changes of electrochemical reactions due to the changes in the analyte composition, and (ii), as impedimetric sensors, by monitoring the change of impedance in the vicinity of the electrodes.

Initial results of the exceptional sensitivity of nIDEs have been previously obtained [2-7]. However, these results can just be considered as a proof-of-concept, since they have been obtained with a reduced number of experiments due to the lack of a fabrication method able to supply a larger number of devices. This limitation precludes a full quantitative analysis of the actual performance of the devices, since the complete determination of the device sensitivity and resolution requires a complete set of experiments and so, a large number of identical devices. During this thesis we have given a step forward in the state of the art, not only by diminishing the device characteristic dimensions, but also by using wafer-scale fabrication techniques, such as electron beam and nanoimprint lithography (NIL) for their production, see Figure 2. In next chapters, different fabrication approaches will be intensively explained, comparison between techniques and benefits of each of them will be discussed.
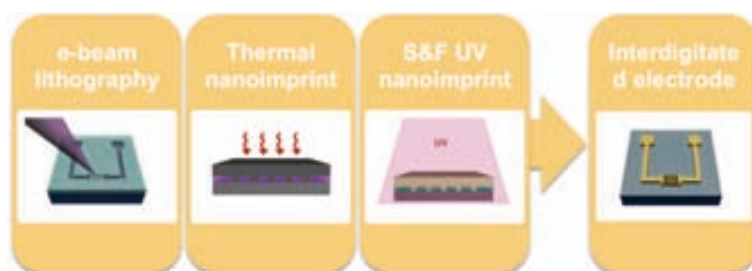

Figure 2. Three different approaches have been carried out to fabricate interdigitated electrodes: direct e-beam lithography, thermal NIL and Step & Flash UV-NIL.

Specifically three methods have been used to fabricate IDEs: direct e-beam lithography, presented in **Chapter 5** and thermal nanoimprint and step & flash UV-NIL, presented in **Chapter 4**. The first one takes advantage of the reproducibility and high-resolution characteristics of EBL, nowadays it is one of the most reliable nanofabrication techniques [8-10]. However, it is expensive and has low throughput. For these reason, in the course of this thesis we moved to a higher throughput and lower cost technique such as nanoimprint lithography [11,12]. NIL is based on the replication of a nanopatterned stamp by the mechanical deformation of a polymeric resist [13], the most expensive step of this technique is the fabrication of the stamp. Once the stamp is manufactured, high volume of devices can be produced with high throughput and low cost. The main difference between thermal NIL and UV-NIL is the energy source used to cure the resist. In the case of thermal NIL the resist is

patterned by high temperature, while in UV-NIL the resist is cured by UV-light. UV-NIL was developed after thermal-NIL with the aim to reduce the time required to heat up and cool down the resist [14]. Moreover, as the resist used for UV-NIL has lower viscosity, polymer rheology has less complication. In addition, in this thesis the UV-NIL has been performed using a step & repeat equipment, which gives the chance to replicate a small stamp many times along the wafer. By these improvements of the technique we get closer to the requirements demanded by the industry [11].

In both cases, thermal NIL and S&F UV-NIL, novel fabrication method developed during this thesis has been applied. These methods are based on the hard mask concept explained in Chapter 3. All the techniques presented in this work have in common the e-beam lithography, either for direct IDEs fabrication by EBL or NIL. In the case of NIL, EBL is used to achieve high-resolution patterns in the stamps, see Figure 3.

Once the electrodes are fabricated they must be packaged in order to allow electrical connection with external equipment. The design of a packaging according to the specific characteristic of the sensors is fundamental for the good handing of the device. Two packaging designs have been developed: on the one hand the standard PCB strips. On the other hand a methacrylate holder was designed for the particular necessities of our device. Both of them have been developed at the CNM and their specific characteristics will be explained in Chapter 5.

The interdigitated electrodes have exceptional characteristics to perform voltammetry experiments. Each of the digits arrays can be separately polarized and the molecules between them measured. When the gap between digits comes to nanodimensions the device become more suitable to detect biomolecules, such as DNA, proteins, enzyme, due to the fact that they have similar dimensions. Moreover, the smaller is the gap, the faster will be the answer obtained from one digit to the next one. If the size of the digits is smaller than the diffusion layer, overlap of the flux will happen, and so enhancement of the measured current.

In order to demonstrate the operability of the sensors, the well-known ferricyanide solution was electrochemically characterized at different concentrations. Then, Dopamine was selectively detected by means of redox cycling reactions. Details of the electrochemical experiments will be explained in Chapter 6.
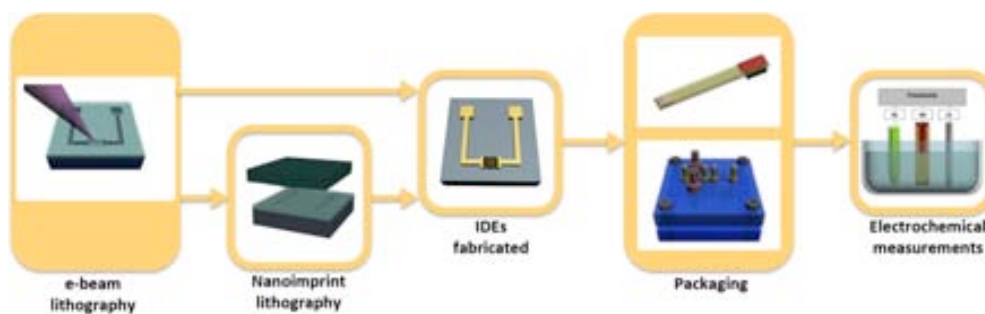
Figure 3. Schematic summary of this section. EBL is used to directly fabricate IDE and to make the stamp used to prepare IDEs by NIL. The devices are packaged in two different approaches. Finally, electrochemical characterization of the IDEs is performed.

Figure 3 shows a graphical summary of the contents of this section. We have fabricated interdigitated electrodes for performing label-free biosensing experiments, which can fulfil the needs of sensitivity required by many biomedical applications, while at the same time keeping affordable production costs, what will guarantee a real industrial applicability in the mid-term.

REFERENCES INTRODUCTION SECTION III

1.   Singh, K V *et al.* Nanoparticle-Enhanced Sensitivity of a Nanogap-Interdigi Electrode Array Impedi. Bios. *Langmuir* 27,13931-13939, (2011)

2.   Singh, K. *et al.* 3D nanogap interdigitated electrode array biosensors. *Anal Bioanal Chem* 397, 1493-1502, (2010).

3.   Hayashi, K, Takahashi, J-i, Horiuchi, T, Iwasaki, Y & Haga, T Development of Nanoscale Interdigitated Array Electrode as Electrochemical Sensor Platform for Highly Sensitive Detection of Biomolecules. *Journal of The Electroch. Society* 155, J240-J243,(2008).

4.   Ueno, K., Hayashida, M., Ye, J.-Y. & Misawa, H. Fabrication and electrochemical characterization of interdigitated nanoelectrode arrays. *Electrochemistry Communications* 7, 161-165, (2005).

5.   Bonanni, A. *et al.* DNA hybridization detection by electrochemical impedance spectroscopy using interdigitated gold nanoelectrodes. *Microchim Acta* 170, 275-281, (2010).

6.   Finot, E. *et al.* Performance of interdigitated nanoelectrodes for electrochemical DNA biosensor. *Ultramicroscopy* 97, 441-449, (2003).

7.   Tang, X. *et al.* Direct protein detection with a nano-interdigitated array gate MOSFET. *Biosensors and Bioelectronics* 24, 3531-3537, (2009).

8.   Mohammad, M., Muhammad, M., Dew, S. & Stepanova, M. in *Nanofabrication* (eds Maria Stepanova & Steven Dew) Ch. 2, 11-41 (Springer Vienna, 2012).

9.   Tseng, A. A., Kuan, C., Chen, C. D. & Ma, K. J. Electron beam lithography in nanoscale fabrication: recent development. *Electronics Packaging Manufacturing, IEEE Transactions on* 26, 141-149, (2003).

10.   Pfeiffer, H. C. Direct write electron beam lithography: a historical overview. 782316-782316, (2010).

11.   Malloy, M. & Litt, L. C. Technology review and assessment of nanoimprint lithography for semiconductor and patterned media manufacturing. *Journal of Micro/Nanolithography, MEMS, and MOEMS* 10, 032001-032001, (2011).

12.   Costner, E. A., Lin, M. W., Jen, W.-L. & Willson, C. G. Nanoimprint Lithography Materials Development for Semiconductor Device Fabrication. *Annual Review of Materials Research* 39, 155-180, (2009).

13.   SY, C., PR, K. & PJ, R. Imprint of sub-25 nm vias and trenches in polymers. *Appl. Phys. Lett.* 67, 3114 (1995).

14.   M, C, S, J, M, S, S, D & TC, B Step and flash imprint lithography: a new approach to high-resolution patterning. *Proc. SPIE* 3676, 379 (1999).

4. NIL process for the fabrication of n-IDEs

In recent years, the possibility of fabricating structures with nanometric dimensions in a controllable and reliable way with high throughput and low cost has turned the nanoimprint lithography (NIL) into an interesting technology for the industry to fabricate nanodevices at mass production. This objective has moved us to demonstrate the possibility to fabricate interdigitated electrodes (IDEs) by this big potential technology. Moreover, unlike in e-beam lithography, the isolator character of the substrate does not affect to the quality of the imprint, thus materials such as quartz or glass can easily be used. We have developed new approach to improve the fabrication of IDEs by thermal NIL (at the CNM) and Step & Flash UV-NIL (at The Molecular Foundry). This approach is based on the multilayer configuration explained in Chapter 3, where a SiO_2 hard mask is fabricated by NIL to enable the fabrication of high aspect ratio nanostructures. In both cases a single e-beam exposition is performed to fabricate the stamp, then lots of replications are performed in a mouldable resist.

The fabrication of the devices has been performed in two steps: In the first one, the nanodigits are prepared by nanoimprint lithography and lift-off. The micropads are subsequently fabricated by optical lithography, as Figure 4.1 shows. This division of step is due to the long e-beam exposition time needed to expose the large pads areas on the stamp. Therefore, the price of the stamp considerably increases when the pads are included. Furthermore, the most important reason to fabricate digits and the pads separately is the fact that the imprint results get worse when micro and nanopatterns are imprinted at the same time, as it has been previously demonstrated [1,2].
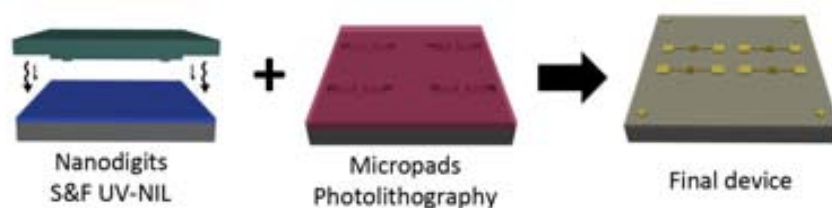

Figure 4.1 Fabrication of interdigitated electrodes has been performed in two steps, first replication of nanodigits by NIL and then micropads by photolithography.

First stage of nanodigits fabrication by NIL is the preparation of the stamp. This is the most critical point since the quality of the final pattern will be absolutely related with the characteristics of the stamp. After the fabrication of the template the imprinting process is performed, in this stage it is fundamental to find out optimal imprinting-temperature, pressure and time to get desirables patterns. Finally post-processes such as etching, metallization and lift-off are carried out to transfer the digits into the substrate. Next, pads are fabricated by photolithography and lift-off. Alignments marks placed on the stamp allow the successful combination of the technologies.

The imprints were performed using the thermal imprint equipment placed at the CNM's cleanroom, from Obducat [3].

4.1 THERMAL NIL FOR n-IDEs FABRICATION

4.1.1 Template fabrication

The silicon stamp used to fabricate interdigitated electrodes by thermal NIL was a mesa-type stamp. It has been previously demonstrated that when the nanopatterns of the stamp are placed in a stage, the applied pressure focuses in the imprinted area, consequently the imprint results considerably improve [4]. For more information read in Chapter 1.

The mesa has been fabricated on silicon substrate by photolithography and wet etching (annex 4). Four mesas, each of them of 3 x 3 mm^2, have been fabricated on a 15 mm x 15 mm stamp. On top of each mesa an array of digits has been defined by electron beam lithography on a 130 nm bilayer of PMMA 495k and 950 k (MicroChem), energy of 10 KV have been applied, at 90 pA and dose 100 μC/cm2. 20 nm of aluminum were deposited by e-beam evaporator and the lift-off was performed in acetone. Note that aluminum patterns cannot be immersed on Stripper to facilitate the lift-off, since this solvent removes thin layers of aluminum. The resulting metal patterns were used as a mask for reactive ion etching: 20 sccm SF_6 and 30 sccm C_4F_8, source power 220 W, chuck power 20 W were applied during 200 s. In Figure 4.2 fabrication steps of the nanopartterns are explained. The resulting width of the lines is 150 nm, 300 nm pitch and 130 nm height. Before the imprinting process, stamps were silanized in order to avoid the sticking of the polymer (annex 3).
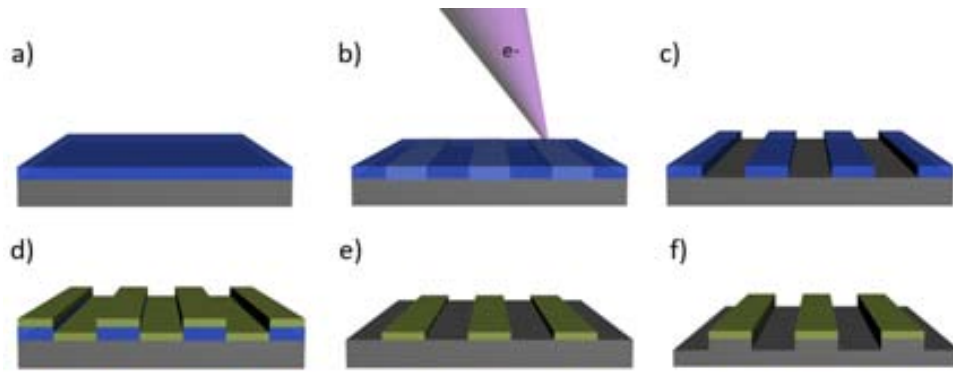
Figure 4.2. Fabrication of protrusions on silicon stamp: a) 100 nm of PMMA are spin coated on Si substrate. b) e-beam exposition is carried out. c) Development of the PMMA is performed. d) 20 nm of Al are evaporated e) lift-off is performed. Finally f) the Si is etched using the Al patterns as a mask.

4.1.2 Thermal NIL process

Thermal nanoimprint lithography is the process where a thermoplastic resist is structured due to applied pressure and temperature above the glass transition temperature of the polymer.

The imprint process developed for the interdigitated electrodes fabrication is based on the multilayer configuration explained in Chapter 3. By thermal NIL and RIE a SiO_2 hard mask is defined. The mask is used to selectively etch the bottom PMMA with O_2 plasma. The height of the deposited metal is related with the bottom PMMA, thus high aspect ratio digits can be achieved. There are two main reasons to improve on the aspect ratio of the digits: The first one is that the half-life of the sensors is partially related with the thickness of the metal. Thin digits are brittle and do not support continue electrical measurements, after a certain measurements they peel off. In addition, when the height of the digits is higher than a critical dimension, the reaction happening in the sidewall provides a relevant contribution.

In the fabrication of interdigitated electrodes by means of thermal NIL we have taken advantage of the multilayer configuration explained in Chapter 3. In this way a hard mask has been fabricated by NIL on the substrate and then it has been used to etch the bottom PMMA, as it can be observed in Figure 4.3. This technology enables an easy lift-off and the deposition of thicker metal layers.
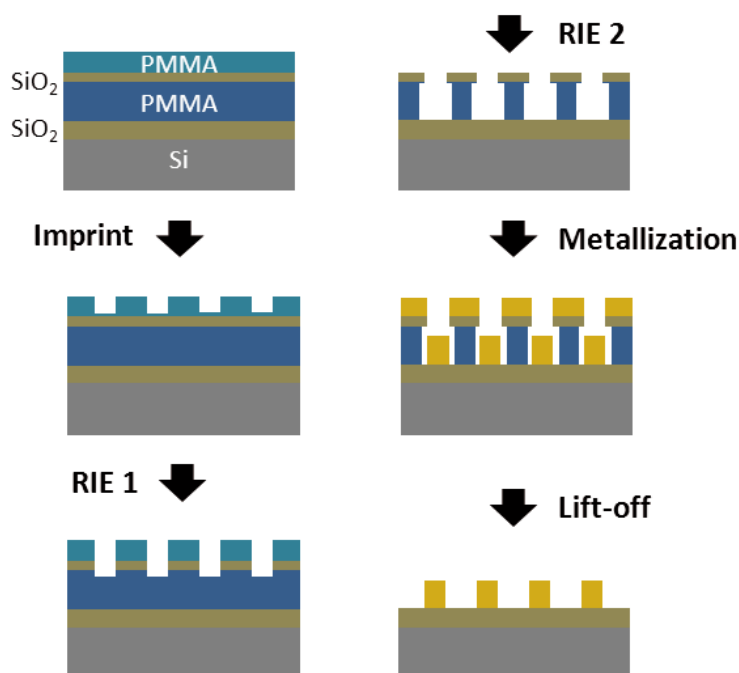
Figure 4.3. Fabrication process of IDEs by thermal NIL.

4.1.3 Results

The devices have been fabricated on silicon wafers coated with 2 μm of SiO_2, to obtain isolator substrate. The first stage of the process consists on the preparation of a sandwich type substrate composed by a silicon wafer, PMMA thick layer (370 nm), a thin layer of SiO_2 deposited by PECVD (23 nm) (SiH_4 25 sccm, N_2 955 sccm, N_2OHl 1000 sccm) and 100 nm layer of PMMA 75 K (MicroChem).

Secondly, thermal imprint is carried out in the top PMMA layer. First the substrate and the stamp are heated up till 180 °C and maintained at this temperature during two minutes. Then, at the same temperature, 40 bar of pressure are applied during 5 minutes. At that point, the system is cooled down until 80 °C while the pressure is kept at 40 bar, see Figure 4.4.
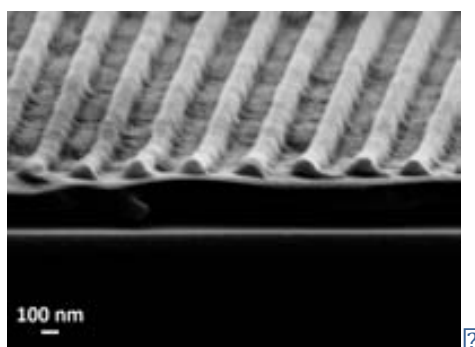

Figure 4.4. In the SEM image imprint of the digits can be observed.

Then, in a first step of RIE, the residual layer and the SiO_2 are etched, thus the hard mask is structured, see Figure 4.5a. In a second RIE step the thick layer of PMMA is etched using the SiO_2 as a mask, observe in Figure 4.5b that suitable undercut is formed.
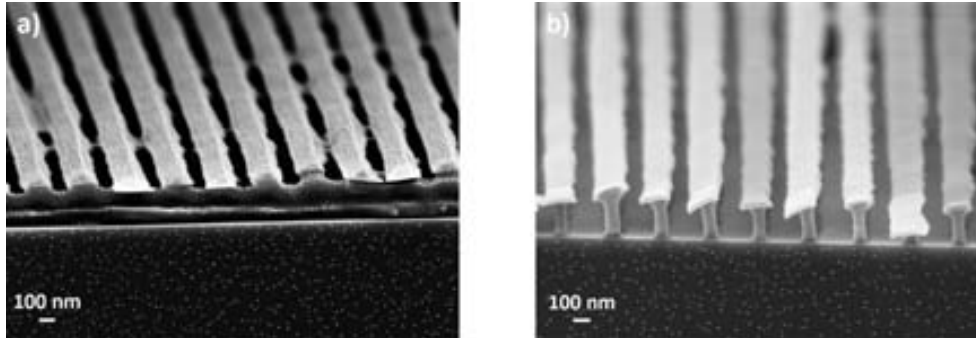

Figure 4.5. SEM images of a) first RIE where the residual layer of the imprint and the SiO2 are etched, hard mask is produced, b) second RIE where the bottom PMMA is etched.

The obtained undercut facilitates the subsequent lift-off, where 6 nm of Cr and 200 nm of gold were deposited and the remaining excess resist and metal are removed by the performance of lift-off in acetone. As a result of this process arrays of digits are achieved. It is remarkable that by using this process, the resolution is not dependent on the thickness of the bottom PMMA layer, so that high aspect ratio nanostructure can be reliably performed by metal lift-off. It is difficult to obtain IDEs with 200 nm of metal by e-beam, the thickness needed for that is too high to obtain suitable resolution.
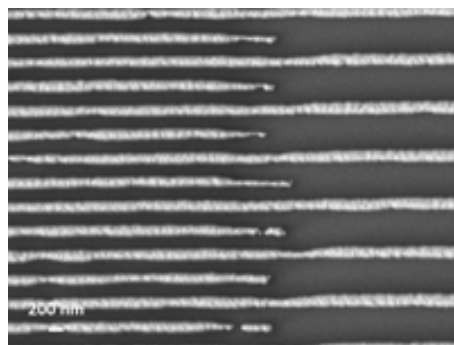

Figure 4.6. SEM image on the metallic digits after the lift off.

4.2 STEP & FLASH UV-NIL PROCESS FOR n-IDEs FABRICATION

4.2.1 Template fabrication

Interdigitated electrodes fabricated by S&F UV-NIL were addressed to be used in the holder type packaging, therefore they follow the design presented in Chapter 5.

As Figure 4.7 shows, the template gathers four arrays of digits with areas of 500 μm x 500 μm, the width of the digits is 50 nm and pitch 100 nm. The separation between arrays is 9.5 mm in x-axis and 5.5 mm in y-axis. Moreover, several alignment marks are distributed around the template, in order to facilitate the subsequent alignment with the optical lithography mask.
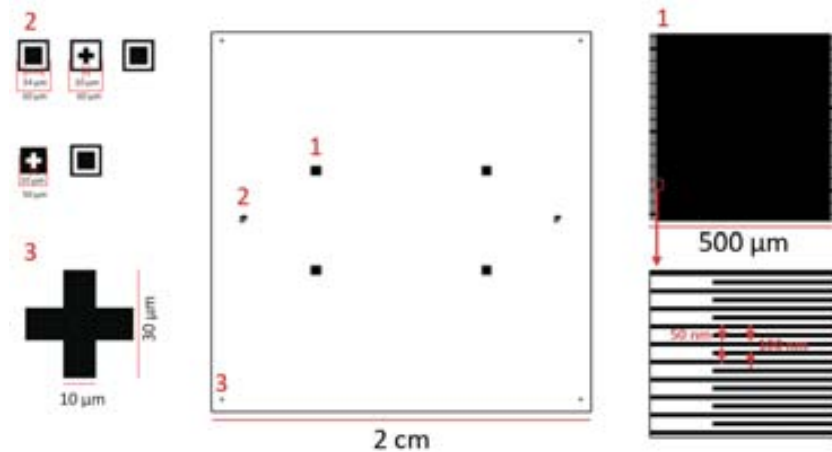

Figure 4.7. a) Sketch of the digits arrays and the alignment marks that will be fabricated by nanoimprint lithography. b) Sketch of how the final device would look like.

A square quartz template base with a centered imprint mesa was fabricated to used in Imprio 55. The commercial base has an area of 65 x 65 mm^2, which is the specific dimension required by the manufacturer of the equipment, the imprinting mesa is 25 x 25 mm^2. Nanoarrays on top of the mesa have been directly patterned by e-beam lithography into Hydrogen Silsesquioxane (HSQ) resist without etching step. Figure 4.8 shows the steps followed to obtain HSQ patterns on the quartz template.
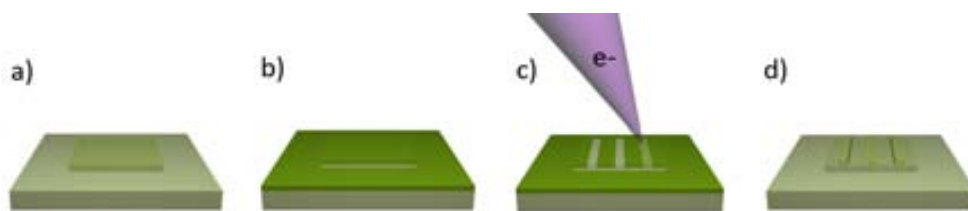
Figure 4.8. Fabrication of nanopatterns on quartz stamp to be used in Imprio 55: a) Base of the template is a quartz square of 65 mm^2 with an imprint mesa of 25 x 25 mm^2. b) It is spincoated with 90 nm of HSQ. c) The desired patterns are exposed by e-beam. d) Finally the HSQ is developed.

HSQ is a high-resolution negative tone e-beam resist. The HSQ monomer formula is $H_8Si_8O_{12}$, Figure 4.9. When the resist is cross-linked by e-beam or wavelengths below $\lambda = 157$ nm it gets parameters similar to SiO_2, i.e. hard material that can only be removed by dry etching or HF.
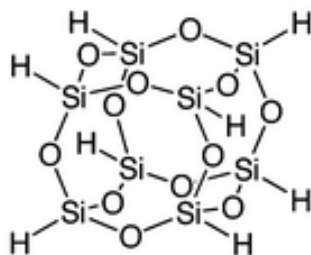

Figure 4.9. Chemical formula of HSQ.

The specific fabrication parameters for the stamp used in this work have been the next ones: Commercial negative HSQ resist diluted at 6% volume in methyl isobutyl ketone is spin coated 2000 rpm to obtain a film thickness around 90 nm. To minimize charging effects and thermal heating during EBL exposure, a 60 nm thick layer of conductive polymer (Aquasaved from Mitsubishi Rayon) is spin coated on the top of the HSQ film. Salty development in aqueous mixture of 1 wt.% NaOH for 4 min allows reaching high contrast and resolution down to 10 nm.

Previous to perform the imprint process, the stamp must be coated with 1H, 1H, 2H, 2H-perfluo-octyltriethoxysilane (FTS13) in order to avoid the resist get stuck (annex 3).

4.2.2 Step & Flash UV-NIL

UV-NIL is the type of nanoimprint lithography where the patterns are transferred by curing the resist with UV-light. Owing to the fact that high quality stamp is fabricated by e-beam lithography, the most expensive and delicate step of NIL technology is the fabrication of the template. Step & Flash nanoimprint

technology enables the replication of a small template along the wafer, reducing the high cost of a substrate-size stamp. This is the reason because during the last years the industry has paid especial attention to S&F UV-NIL [5].

In many cases the main difficulty of this process is the dispensing of the resist [6]. Since several imprints are performed in the same wafer, the resist must be locally dispensed in each imprinting field, in order to avoid the exposition of the surrounding resist. The volume of dispensed resist must be accurate and related with the pattern to obtain as less residual layer as possible. With the aim to avoid the possible complication of the dispenser, the pre-spincoating approach proposed by Peroz et al. [7,8] has been followed. Owing to the sophisticated properties of the mr-UVCur21 (Microresist)[ref microresist], the resist can be pre-spincoated at the beginning of the process on the whole wafer without risk to be damaged after each exposition. mr-UVCur21 is a purely organic (silicon-free) material composed of multifunctional acrylate monomers and a mixture of photo-initiators. The specific chemistry of the resist prevents it from cross-linking in presence of oxygen, limiting its UV curing to the imprinted area. Consequently, the process follows the steps mentioned in Figure 4.10, the resist is spin-coated at the begging in the whole surface of the substrate, then the template is aligned on the substrate, lowered and the UV exposition is performed. Next, the stamp is moved to the following imprint-field and the process is repeated.
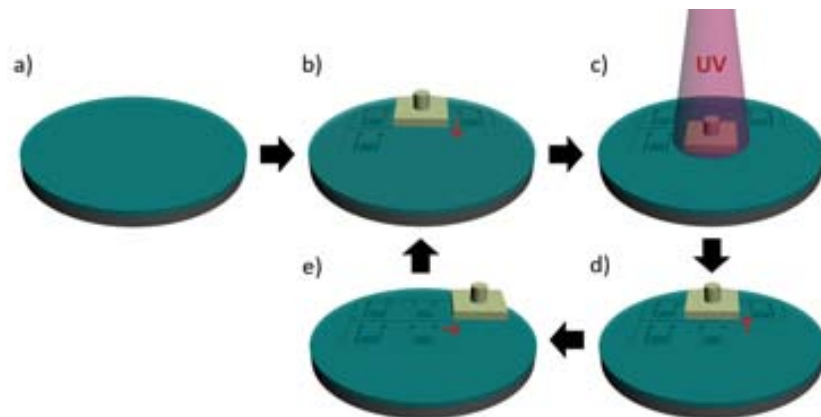

Figure 4.10. S&F UV-NIL process by pre-spincoating protocol: a) wafer is completely spin-coated with mr-UVCur21, b) stamp is aligned in the imprinting-field and lowered to be in contact with the substrate, c) the resist under the template is cured by UV-light. d) When the first imprint is finished, the stamp is raised and e) moved to the next imprinting-field and following imprint begins.

In Figure 4.11 images of the successful imprint that Peroz et al. [7] obtained by using the pre-spincoat S&F UV-NIL method can be seen.
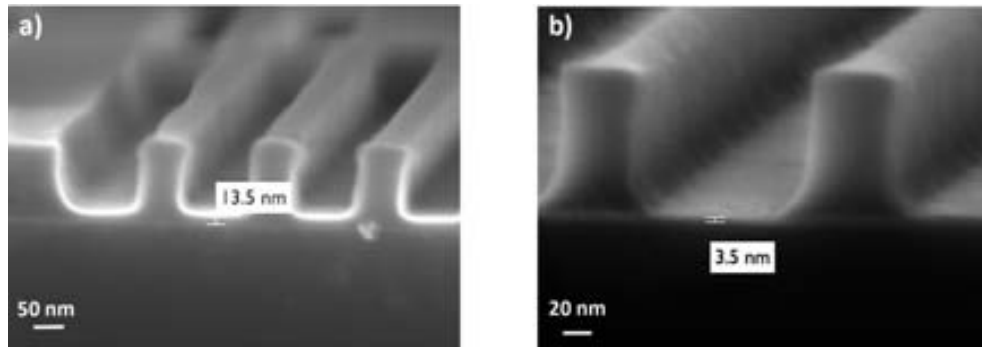
Figure 4.11 SEM images of examples of mr-UVCur 21 resist imprinted. Courtesy of Peroz et al. [7].

mr-UVCur21 has excellent properties for the selective imprint and also high plasma etch resistance, and no residuals remain after O_2 plasma etching [9]. Although these are exceptional characteristic for an S&F UV-NIL resist, it has the inconvenient of been insoluble in common solvents. Therefore in order to perform the necessary lift-off to fabricate the electrodes, a sacrificial layer was deposited between the substrate and mr-UVCur21 layer [10], in a so-called bilayer configuration.

4.2.3 Multilayer configuration for Step & Flash UV-NIL

In this case, the bilayer configuration is composed of silicon substrate coated with 200 nm thermal SiO_2, 100 nm sacrificial layer and 90 nm of mr-UVCur21. First the mr-UVCur21 is imprinted and after the residual layer removal, the patterns will be transferred to the sacrificial layer by reactive ion etching. Subsequently, the sample is evaporated and the lift-off is performed, dissolving the sacrificial resist in an adequate solvent the metal and the UV-resist onto of the sacrificial resist are removed while the desired metallic patterns remain. In Figure 4.12 the whole process followed using the bilayer configuration is explained.
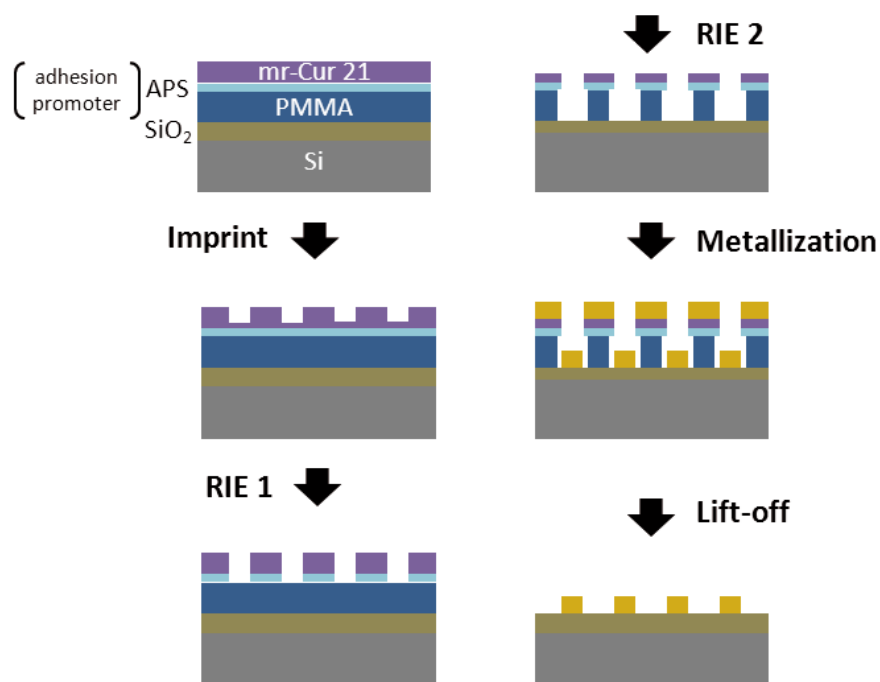
Figure 4.12. Sketch of the interdigitated electrodes fabrication by means of UV-NIL using bilayer configuration.

Different lift-off resist were test to conform the bilayer configuration, such as LOR and PMMA, but the adhesion of the mr-UVCur21 to them was very weak. As it can be seen in Figure 4.13 it seems that during the imprint the two resist are mixed obtaining a bad quality monolayer imprint. Even using the APS (adhesion promoter) and applying ozone treatments no improvements of the imprints was detected. Consequently, it was necessary to deposit an intermediate layer that has good adhesion to the sacrificial layer and also to the APS. As an intermediate material, ultrathin layer of SiO_2 was deposited by PECVD. This new configuration is the so-called *multilayer configuration*.
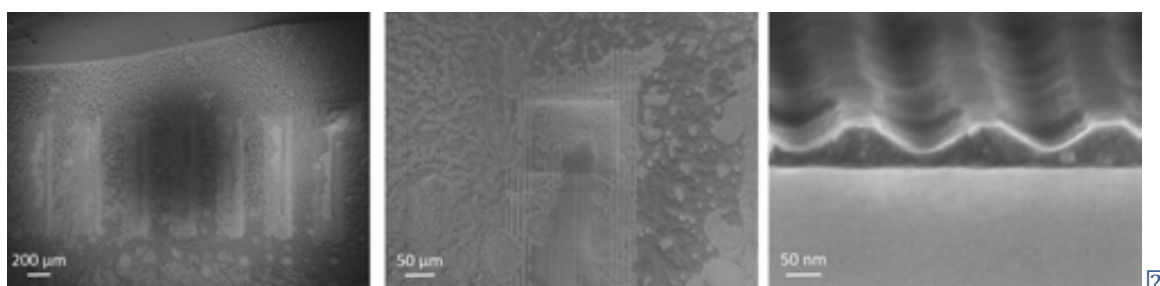

Figure 4.13. SEM images show the imprint made on bilayer configuration. It can be appreciated that the adhesion of the mr-UVCur21 to the sacrificial layer is weak and they mixture.

The etching recipe used to etch the residual layer of mr-UVCur21, also etches SiO_2. Thus, the process is the same as the one show in Figure 4.12, but using the multilayer configuration that can be seen in Figure 4.14.

Figure 4.14. Ultrathin layer of SiO_2 (10 nm) was deposited between the APS and the PMMA to improve the adhesion between both materials.

4.2.4 Results

The characteristics and thickness of each component of the multilayer substrate are important for the successful process, especially when the lateral dimensions of digits and gaps reduce their size. A trade-off on the thickness of the sacrificial layer must be found; on the one hand it must be thick enough to perform a successful lift-off. At the same time, it will be limited by the undercut obtained in the PMMA during the second etching (see Figure 4.12). The thicker the bottom resist, the larger the undercut. In this case that the dimensions of the digits and the gaps are considerably narrow, 50 nm each, accurate controlled of the dimensions must be achieve to avoid the collapse of the lines, as it can be seen in Figure 4.15.
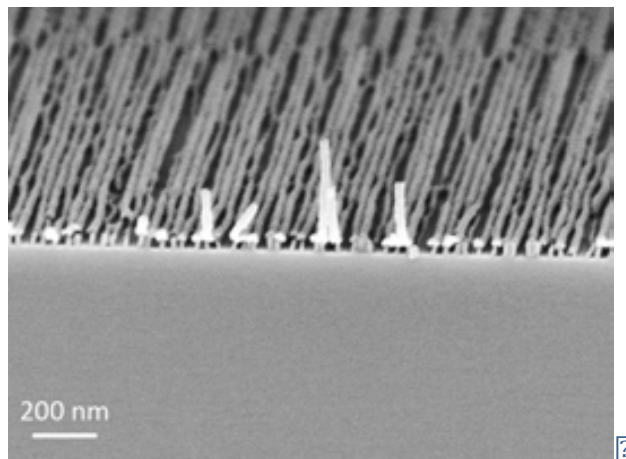

Figure 4.15. SEM image of collapsed lines due to an excess of undercut.

The substrate used for the process was silicon wafer coated with 200 nm of thermal SiO_2. The multilayer configuration was compound of: 100 nm of PMMA 950 k C2 (MicroChem) deposited by spincoating at 1000 rpm during 45 s and then baked in the hot plate at 180 °C during 1 minute. Second, the wafer was coated with 10 nm of SiO_2 by plasma-enhanced chemical vapor deposition (PECVD) (Plasmalab) using 850 sccm silane (SiH_4), 710 sccm nitrous oxide (N_2O) under a 20 W reflective power and at 150 °C, low temperature was applied to protect the sacrificial resist. Next stage was the spincoating of 5 nm

of the adhesion promoter APS (Microresist Technology) and 100 nm of mr-UVCur21 60nm (Microresist Technology). The APS was deposited at 4000 rpm during 45 seconds and baked in the oven at 150 °C 5 min. The mr-UVCur21 60nm was spincoated at 1000 rpm during 45 s and baked in the hot plate at 60 °C during 1 min. Figure 4.16 shows the *multi-layer* configuration of PMMA / SiO$_2$ / APS / mr-UVCur21 (due to the small thickness of APS it cannot be distinguish in the image).
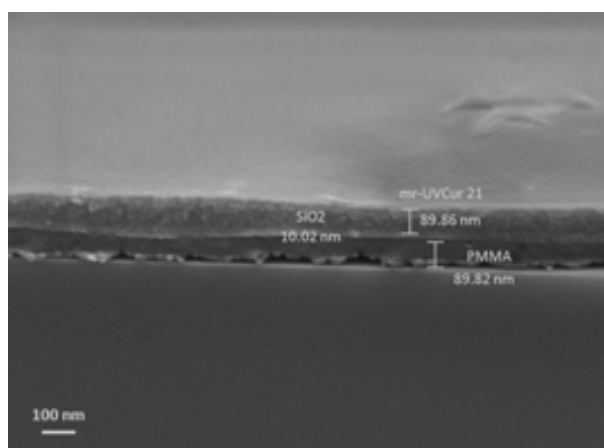

Figure 4.16. Multilayer configuration for the pre-spincoating step & flash UV-NIL process: PMMA / SiO$_2$ / mr-UVCur21

Once the substrate was ready, the imprints were performed using Imprio 55 (Molecular Imprints) step & flash nanoimprint equipment, placed at The Molecular Foundry clean room, which allows imprinting up to 8 inch wafers. Lines of 50 nm and pitch 100 nm were obtained on mr-UVCur21 applying an imprint force of 30 N during 120 s. SEM images of the imprinted digits can be seen in Figure 4.17. (Note that slight modification on the vertical dimensions can be seen in the SEM images because the resist melts or swells during the performance of the images due to the electron irradiation.)
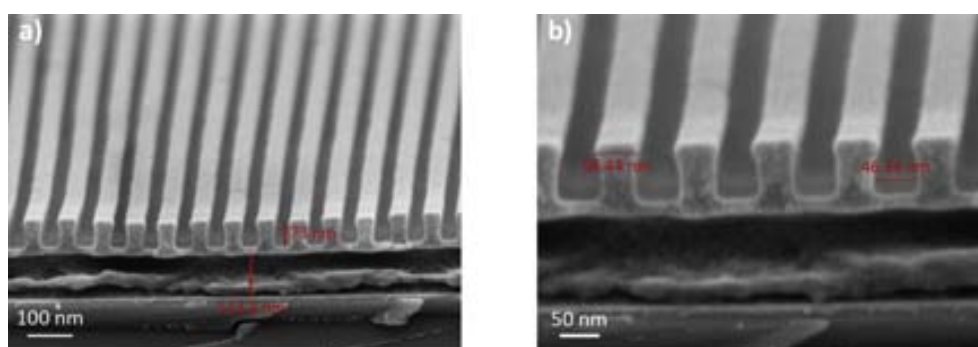

Figure 4.17. SEM images that shows the imprint of the digits performed on the mr-UVCur21.

After the imprints, the residual layer and sacrificial layer must be etched. Due to the small dimension of our patterns, reactive ion etching was the most accurate and controllable method to perform the process. Pattern transfer was carried out

in two steps, in the first one the residual layer, the silicon oxide layer and part of the PMMA layer were removed, in the second one the remaining PMMA was removed (see Figure 4.12).

First etching step was performed using 25 sccm of CHF_3, 5 sccm of O_2 with a power of 100 W during 155 s. This recipe etches all the layers used in the multilayer configuration with similar etching rates, 3.8 Å/s for mr-UVCur, 5 Å/s for PMMA and for SiO_2 was negligible. It was used to etch the residual layer of mr-UVCur21, SiO_2 layer and part of the sacrificial PMMA, higher selectivity etching was needed to etch the rest of the PMMA. Figure 4.18 shows the results of the first etching step.
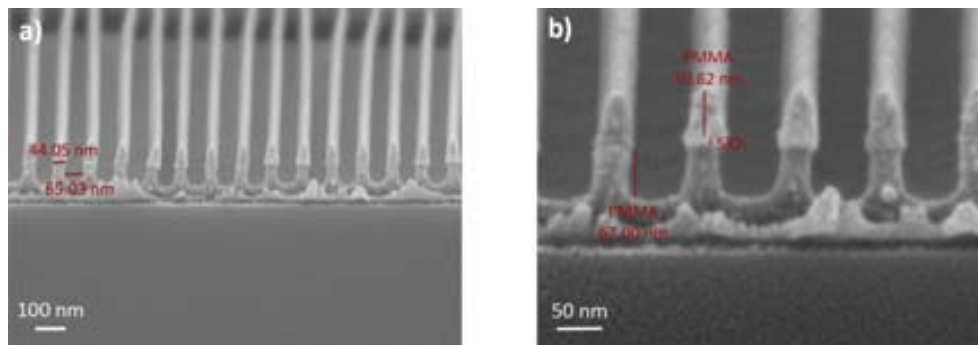

Figure 4.18 SEM images of the nanostructures after the etching of the residual layer, SiO_2 and part of the bottom PMMA.

Oxygen plasma was used to etch the remaining PMMA, 100 sccm of O_2 were used at 30 W power during 130 s. The selectivity of this recipe between the mr-UVCur and PMMA is 1:2 and extremely higher for SiO_2. Owing the isotropic character of the oxygen plasma, a considerable undercut is achieved on the PMMA, which will be very adequate for the lift-off, as Figure 4.19 shows. Since an excessive undercut would cause the collapse of the patterns, a trade-off between both recipes must be established.
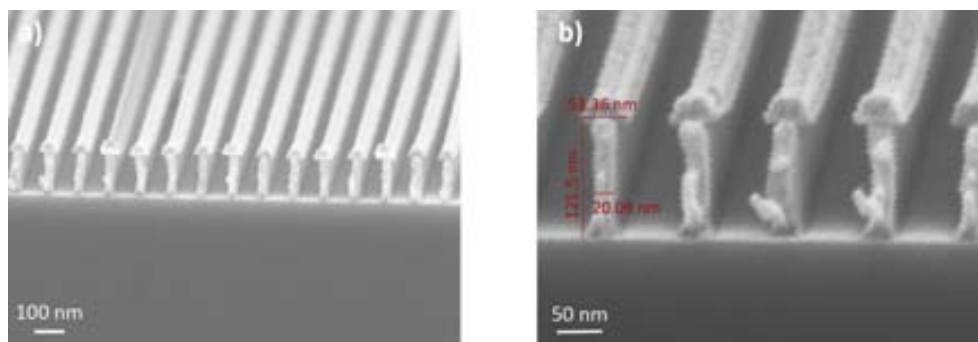

Figure 4.19. SEM images of the nanodigits after the second etching process, note the undercut formed on the bottom PMMA.

121

Once the patterns were totally transferred to the substrate, deposition of the metal and the lift-off were carried out. First, 5 nm of Cr and 30 nm Au were deposited by e-beam evaporator (Semicore), the Cr was deposited in order to improve the adhesion between substrate and gold. Figure 4.20 shows SEM images of the sample after the metal evaporation and before the lift-off. It can be observed that thanks to the undercut of the PMMA the metal do not contact the resist, which is very helpful to perform the lift-off. Note that due to the high aspect ratio of the patterns, during the manipulation of the sample the top of the pillars (mr-UVCur and SiO_2 *hat*) *flew off*.
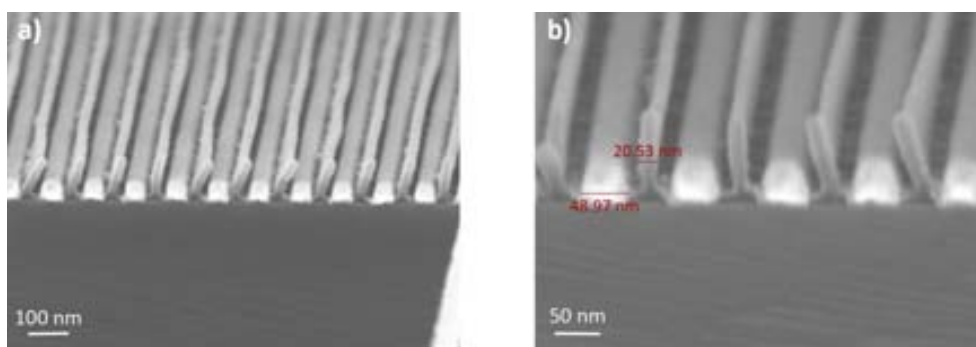

Figure 4.20. SEM images of the metallized sample, before the lift-off. Note that the SiO2 "hat" has disappeared during the manipulation of the samples.

The lift-off was carried out dipping the samples in dichloromethane during 15 min and then 1 minute of ultrasonic in acetone bath. Then samples are rinsed in isopropanol (IPA). Figure 4.21 shows SEM images of the sample after lift-off. It can be observed that the dimensions of the metallic patterns approximately correspond to the original dimensions on the stamp.
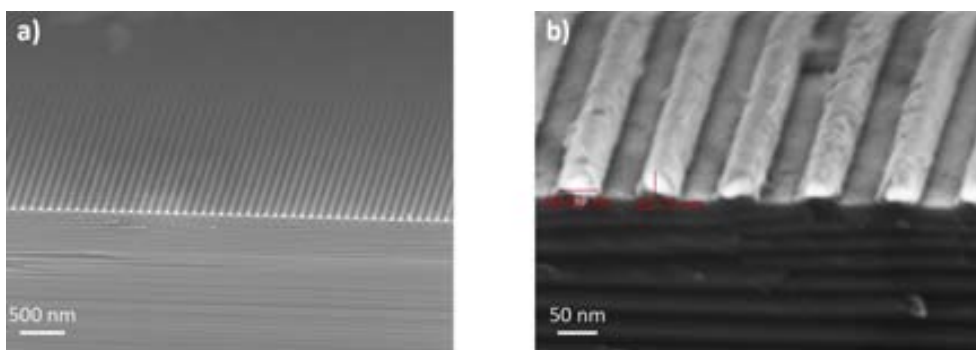
Figure 4.21. SEM images of the gold nanodigits after the lift-off.

4.2.4.i   Miniaturization of the lines

The multilayer configuration was developed at The Molecular Foundry for two different applications at the same time. The first one is the preparation of interdigitated nanoelectrodes. The second one, the fabrication of sub-10 patterns to be used in optical applications. This work was framed on the Giuseppe Calafiore master thesis [11].

Following the multilayer configuration, progresses in the miniaturization of the patterns were obtained. Metallic lines down to 14 nm width were achieved, the smallest lines in the state of the art fabricated by this method.

Due to the isotropic characteristics of the PMMA etching, the sacrificial layer thickness must be related to the minimum dimension of the patterns. When the lines become narrower the sacrificial layer thickness must be also reduced. As consequence, the evaporated metal layer must be thinner for a successful lift-off. For 14 nm lines 34 nm of PMMA, 5 nm of SiO_2 and 21 nm of mr-UVCur21 were deposited. In the same way as in previous samples, the PMMA, APS and mr-UVCur were deposited by spincoating and the SiO_2 by PECVD at 150 °C, see Figure 4.22.
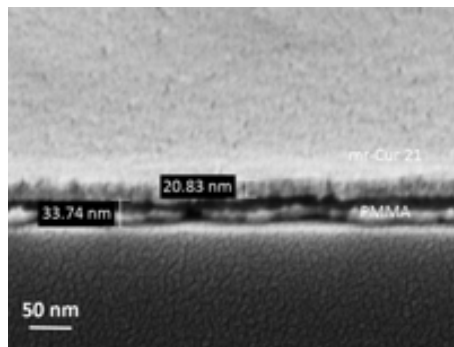

Figure 4.22. SEM image of the multi-layer configuration used to miniaturize the lines.

The template used to perform the imprint was fabricated by ALD spacer double patterning technique [12] a robust strategy for fabricating and replicating nanoimprint templates with sub-10 nm patterns that overcome the limits of resolution imposed by electron beam lithography (EBL), photoresists and etching processes. The imprints were performed using Imprio 55, applying the same conditions as in the previous imprints. Figure 4.23 demonstrates that almost no residual remained after the imprint, since 10 nm of material under the patterns correspond to the SiO_2 (5 nm) and the APS (5 nm).
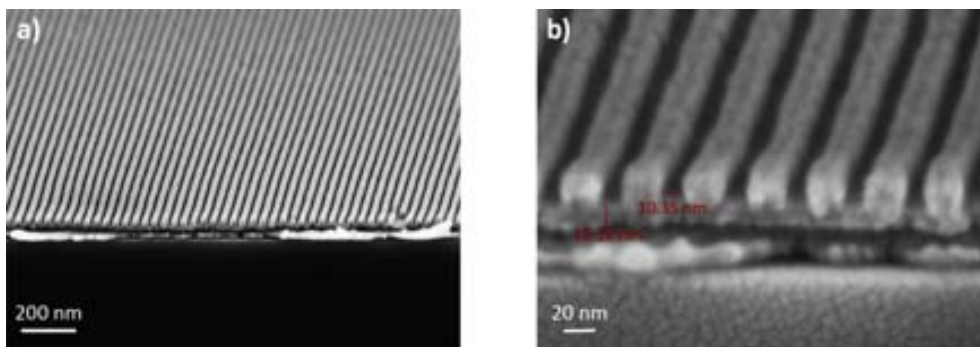

Figure 4.23. SEM images of the imprints.

123

In a first etching step the residual layer of the imprint and part of the PMMA were removed, see Figure 4.24a. Then the rest of the PMMA layer was removed by oxygen plasma. The same etching conditions as the ones presented in the previous section were applied. Figure 4.24b shows the undercut obtained after the etching.
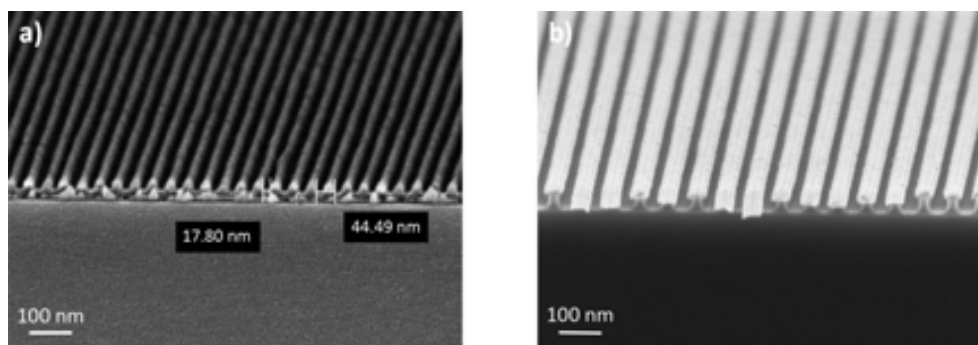

Figure 4.24. SEM images of a) the result of the first RIE step where the residual layer, SiO_2 and part of the PMMA are etched. b) After the O_2 plasma the remaining PMMA was etched.

After the pattern transfer, 5 nm of Cr and 10 nm of Au were deposited by e-beam evaporation at high vacuum to allow vertical deposition. As it can be seen in Figure 4.25a the metal is deposited on top of the mr-UVCur and in the free spaces on the substrate, but the walls of the resist are free of metal, which is very adequate for the lift-off. In Figure 4.25b the result of the lift-off is presented, lines of 14 nm were obtained with pitch 40 nm.
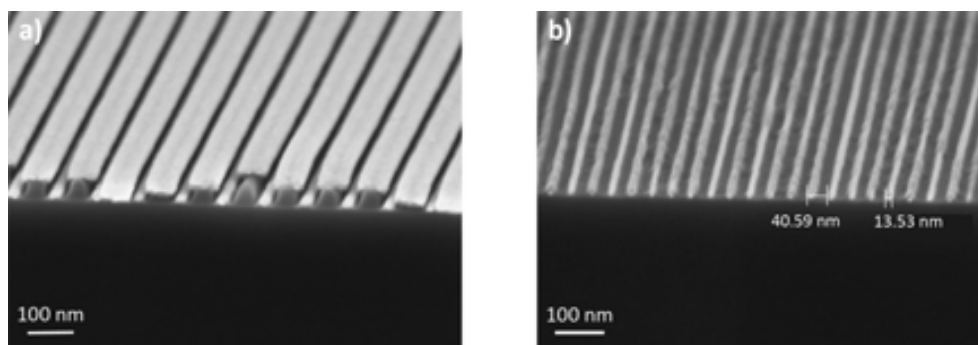
Figure 4.25. SEM images of a) the sample after metallization. Metal is deposited in the trenches of the lines and also on top of the PMMA, but it does not touch the sidewalls of the resist, which enables the lift-off. b) sample after the lift-off, digits of 14 nm were achieved.

The achievement of 14 nm width lines with pitch 40 is a step forward in the reliable fabrication of patterns by S&F UV-NIL, with extremely interesting applications in fields such as optical detection. However, these delicate lines are inappropriate for the fabrication of interdigitated electrodes. On the one hand, the thin metal layer of the digits would present low stability during the measurements. Moreover, the narrow separation between digits notably increases the chance to get a shortcut due to any tiny particle or defect of the lift-off.

REFERENCES CHAPTER 4

1.   Schift, H. Nanoimprint lithography: An old story in modern times? A review. *Journal of Vacuum Science & Technology B: Microelectronics and Nanometer Structures* 26, 458-480 (2008).

2.   Fernanadez-Cuesta, I. *NanoImprint Lithography: Developments and nanodevice fabrication*, UAB, (2009).

3.   Obducat. <http://www.obducat.com>

4.   H Schift, L. J. H., M Auf der Maur and J Gobrecht. Pattern formation in hot embossing of thin polymer films. *Nanotechnology* 12, 173 (2001).

5.   Malloy, M. & Litt, L. C. Technology review and assessment of nanoimprint lithography for semiconductor and patterned media manufacturing. *Journal of Micro/Nanolithography, MEMS, and MOEMS* 10, 032001-032001, (2011).

6.   Kim, K.-d., Jeong, J.-h., Sim, Y.-s. & Lee, E.-s. Minimization of residual layer thickness by using the optimized dispensing method in S-FILTM process. *Microelectronic Engineering* 83, 847-850, (2006).

7.   Peroz, C. *et al.* Single digit nanofabrication by step-and-repeat nanoimprint lithography. *Nanotechnology* 23, 015305 (2012).

8.   Peroz, C. *et al.* Digital spectrometer-on-chip fabricated by step and repeat nanoimprint lithography on pre-spin coated films. *Microelectronic Engineering* 88, 2092-2095, (2011).

9.   Micro-resist_technology_GmbH. http://www.microresist.de

10.   Bergmair, I. *et al.* Single and multilayer metamaterials fabricated by nanoimprint lithography. *Nanotechnology* 22, 325301-325306,

11.   Calafiore, G. *Step and repeat UV nanoimprint lithography: development of new applications and ultimate pattern resolution.*, Politecnico di Torino, (2012).

12.   Scott Dhuey, C. P., Giuseppe Calafiore, Nerea Alayo, David Gosselin, Deirdre Olynick, Stefano Cabirini, . in *EIPBN*   (Nashville, TN (USA), 2013).

5. Fabrication and packaging of n-IDEs by electron beam lithography

Electron beam lithography (e-beam or EBL) is based on the exposition of electron-sensitive resist using a focused beam of electrons. This is rather time consuming and expensive technique, but at the same time it is extremely reproducible, reliable and able of obtaining high resolution [1,2]. That is why EBL is frequently used to fabricate prototypes of nanodevices. In this thesis interdigitated electrodes were fabricated by EBL as proof of concept.

The initial batch of devices was completely fabricated by e-beam lithography and lift-off. This method needs long e-beam exposition time, which makes the devices expensive and time consuming, thus the efficiency of the technology is low. In order to reduce the exposition time and consequently enhance the throughput of the fabrication, a second generation of devices was produced preparing nanoareas and microareas separately. On the one side the nanodigits were exposed by e-beam lithography and on the other side the micropads by optical lithography, which provides adequate resolution in the micrometric range.

Once the interdigitated electrodes are fabricated they should be packaged in order to facilitate the electrical contact of the sensor with electronic equipment and allow working in liquid environment. Two different packaging have been developed during this thesis: *Strip type PCB* and *Holder* type packaging. The first one is a standard printed circuit boar with a cavity to place the electrodes and the metal wires to make the electrical bonding. The second one is a methacrylate holder that contains a place for the chip, metallic pins to allow physical electrical contact and optional microfluidic system. Moreover this holder has the advantage of been reusable for different chips.

5.1   n-IDES FABRICATION PROCESS

5.1.1   All e-beam fabrication

First approach of sensor was fabricated by the exposition of the complete devices by e-beam lithography, i.e. the nanodigits and the micropads. The interdigitated electrodes are extremely delicate devices, they are composed by thousands of nanometric strips, the smallest particle between the digits could cause a shortcut of nanolines, consequently no defects are allowed. For this reason two identical devices were prepared in each chip, in case that one of them is damaged the other one will be as backup. Figure 5.1a shows a section of wafer with several devices fabricated at the same time and Figure 5.1b is a detail of two identical IDEs.
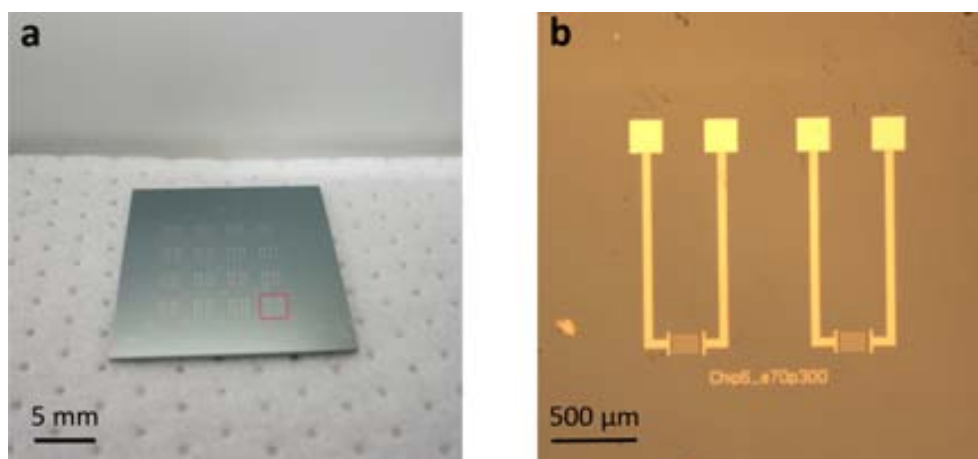

Figure 5.1. a) Optical microscope image of a chip containing two identical gold IDEs with area of 200 μm x 100 μm. b) Picture of a chip with 32 electrodes divided in 16 sub-chips.

The IDEs were fabricated on top of a silicon substrate coated with 200 nm of thermal SiO_2, in order to form an isolator surface. The electron-sensitive resist used for the e-beam exposition was PMMA 950 k A2 (Microresist) [3], a 100 nm thick layer was deposited by spincoating. Then the substrate was heated at 180 °C in the hot plate during one minute to evaporate the solvent of the resist, which is anisol. After the preparation of the substrate the electron beam exposition was carried out. The equipment used was Raith 150Two (Raith) [4] placed at the CNM. The exposition was performed under next parameters, EHT 10 kV, Aperture 20 μm, 100 μAs/cm^2 dose. After the e-beam exposition the resist was developed in MIBK : IPA (Methyl Isobutyl Ketone : Isopropanol) 1:3 solution during 30 s to remove the exposed resist and then rinsed in IPA to stop the reaction. Subsequently, the patterns were defined on gold by e-beam evaporation of 8 nm of Cr and 15 nm of Au, the Cr is used to improve the adhesion between gold and substrate. Finally, lift-off was performed in acetone

128

(for more details see Annex 1). Figure 5.2 represents the steps followed to fabricate IDEs by EBL.
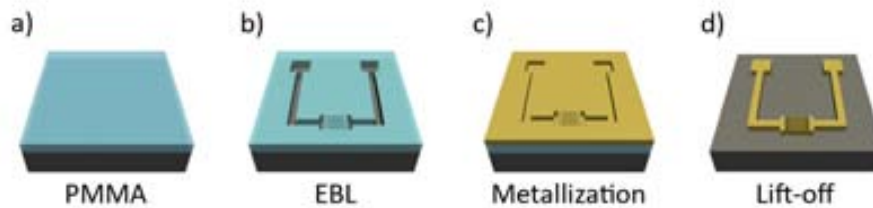

Figure 5.2. Complete interdigitated electrode fabrication process by e-beam lithography: a) Thin layer of PMMA is spincoated on a silicon substrate coated with 200 nm of SiO_2. b) e-beam lithography and development of the resist are carried out. c) The sample is metallized with Cr/Au by e-beam evaporation. d) Lift-off is performed in acetone.

As it is seen in Figure 5.3 interdigitated electrodes arrays with area 200 x 100 μm^2 and digits of 130 nm width and pitch 300 nm were achieved.
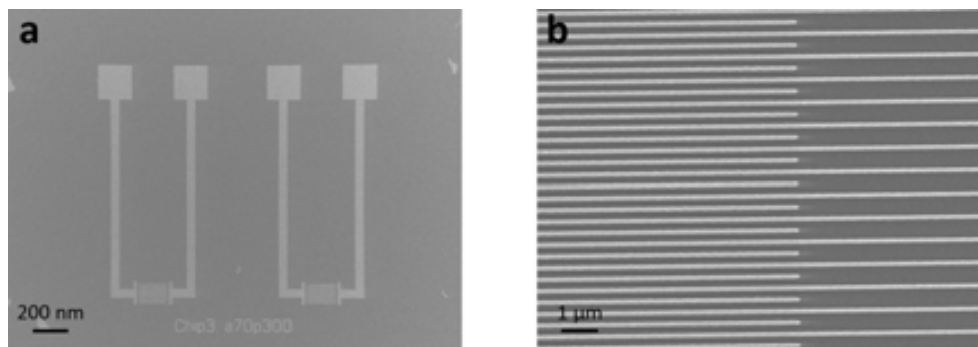

Figure 5.3. SEM images of gold interdigitated electrodes fabricated by e-beam on a silicon chip covered with 200 nm of SiO_2. a) Two identical devices with digits arrays of 200 x 100 μm^2. b) Detail of the digits where the interdigitated area and non-interdigitated area overlap.

The process to fabricate complete devices by e-beam has two main inconvenient: i) In the first place the long exposition time needed to make them. Most of this time is spent to exposing the micropads. Therefore it makes sense to fabricate only the nanodigits by e-beam lithography and then the pads by optical lithography, considering that the pads are microareas and they do not need such precise resolution. ii) In addition, when the fabrication of a device is performed resist lithography, usually, the final thickness of metal is determined by the polymer layer thickness. In this case the thinner the PMMA layer, the better the resolution of the e-beam lithography, and thinner the metal that can be deposited. Thus, for 100 nm of PMMA around 30 nm of metal can be deposited. However, such a thin layer of metal in the pads ended in an unsuccessful electrical bonding during packaging. When photolithography is performed, the thickness of the resist is higher, hence the allowed thickness of

the metal layer is larger. The combination of both techniques gives chance to the deposition of different metal layer thickness in the same device.

5.1.2   Combination of e-beam and optical lithography

Next generations of electrodes were fabricated taking advantage of photolithography and e-beam lithography techniques. Photolithography is a faster and less expensive method, capable of defining patterns with a resolution up to 0.5 μm. Therefore, rather suitable to pattern micropads of the devices. On the other hand, e-beam lithography was used to expose the nanodigits, which need a higher resolution technique due to them nanodimensions. Using this procedure two different layouts of electrodes were designed, addressed to the two different packaging models developed during this thesis, see Figure 5.4.
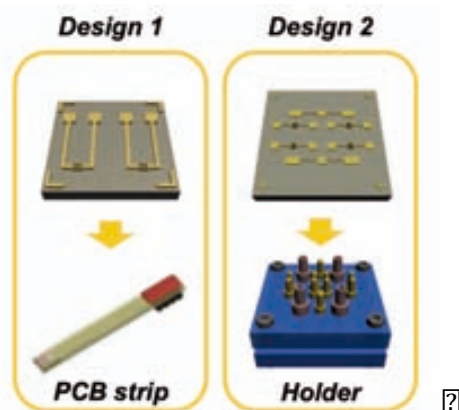
Figure 5.4. Two devices designs developed in this thesis: Design 1 to be used with PCB type packaging and Design 2 with Holder type packaging.

5.1.2.i   *Design 1, IDEs for PCB packaging*

Printed circuit board (PCB) strips were used to facilitate the electrical connection between the electrodes and the electrical equipment as well as to allow working in liquid environment. The PCB model developed at the CNM has place for chips up to 3 x 3 mm^2 and electrical connection for five pads, all of them oriented to the same direction. Therefore, the design of our chips was leaded by these requirements, Figure 5.5 shows a example of PCB packaging and final design of the devices.

Figure 5.5. Images of the PCB strip packaging. a) Complete PCB. b) Inset of the PCB strip of the area where the chip is paced. Details of the wire bonding can be appreciates. c) Image of 3 x 3 mm^2 single chip with two IDEs, similar to the one placed on the PCB.

First stage of IDEs production was the fabrication of the pads by optical lithography at wafer scale. Figure 5.6a presents the layout of the photolithography mask (CNM603) used to expose the pads. The wafer is divided in chips of 3 x 3 mm^2. Each chip holds pads for the sensors and additional gold strip to behave as counter electrode, as can be seen in Figure 5.6b.
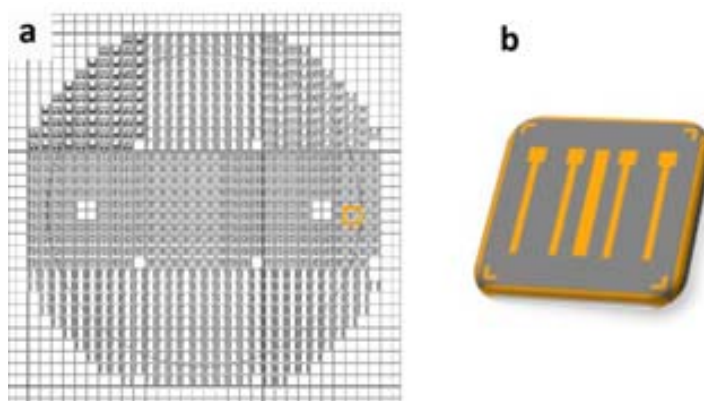
Figure 5.6. a) Layout of CNM603 mask composed of 3 x 3 mm^2 chips. b) Design of an individual chip with two pair of pads for the later fabrication of two sensors. Between the sensors there is a gold strip that will work as a counter electrode.

Photolithography was performed following the steps summarized in Annex 2. Then wafer was metallized with 15 / 100 nm of Cr / Au and the lift-off was performed in acetone. After the fabrication of the pads, the wafer is cut in nine sections to facilitate the manipulation of the sample during EBL. Each of this section includes 100 chips, as it is seen in Figure 5.7.

Figure 5.7. Right, Single chip with two pair of pads and counter electrode. Left, section of wafer holding 100 chips with pads.

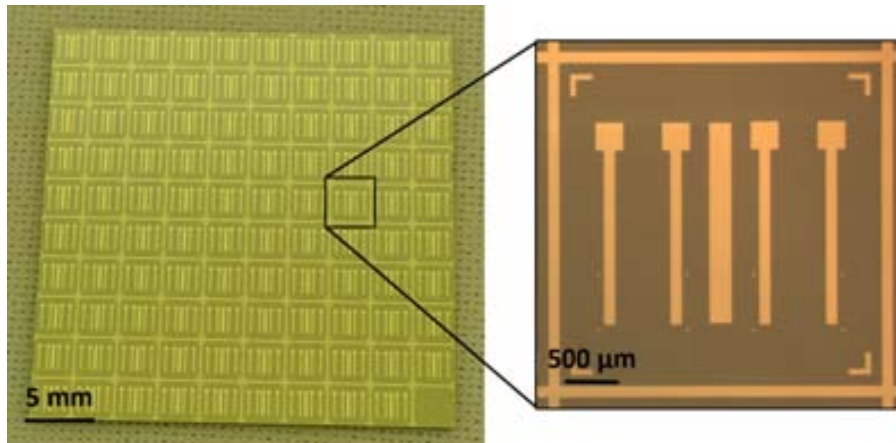Then, fabrication of the nanodigits was performed following the steps represented in Figure 5.8.

a) First, the substrate is baked up to 100 °C during 1 minute in the hot plate to dehydrate. Then 100 nm of PMMA 950 k 2A (Microchem) [5] are spun and baked during 1 minute at 180 °C to evaporate the solvent (anisol).

b) After that, the e-beam exposition is carried out using Raith150 Two (Raith) equipment, EHT 10 kV, Aperture 20 μm and 100 $\mu As/cm^2$ were applied. The nanodigits were exposed between the pads using the aligning marks previously patterned by photolithography. After the exposition the resist is developed on MIBK (Methyl Isobutyl Ketone) during 30 seconds and the reaction is stopped by rinsing the sample 30 seconds in IPA.

c) Next the sample is metallized with 5 nm of Cr and 20 nm of Au using an e-beam evaporator, the Cr is used to improve the adhesion between the and substrate.

d) Finally the lift-off is performed in acetone (see annex 1 for further details).

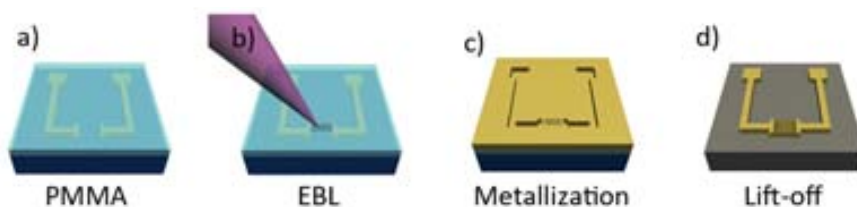Figure 5.8. Fabrication of nanodigits by e-beam lithography: a) 100 nm of PMMA are spun on the substrate. b) e-beam exposition and development are carried out. c) The sample is metallized with 5/20 nm Cr/Au. d) The digits are defined by the lift-off performed in acetone.

Figure 5.9 shows image of the chip with 200 IDEs completely fabricated. One the sensors are fabricated they are cut in single chips using a die cutter.

Previously the chip is covered with resist to avoid the IDEs get dirty and damaged.
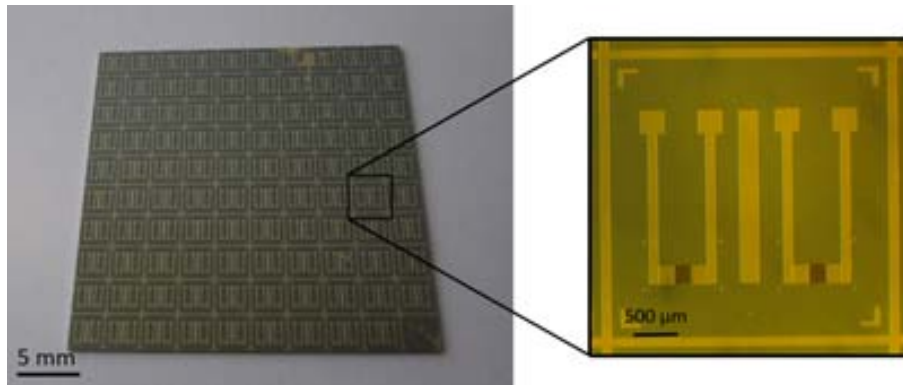

Figure 5.9. Image of a wafer section holding 100 chips of 3 x 3 mm^2. Each chip has two complete devices, pads and nanodigits of 150 nm width, pitch 300 nm and active area of 200 x 200 μm^2. It can also observe a detail of a single chip.

5.1.2.ii *Design 2, IDEs for holder type packaging*

The PCB strips are very compact and useful packaging for sensors. However the wire bonding is laborious and time-consuming step. In addition it requires considerable manipulation of the chip, with the consistent risk of damage the fragile sensors. Seeing that, a more reliable and simple packaging was developed in the progress of this thesis. The new design is a methacrylate holder where the chips are placed and electrically contacted by exterior metallic pins, thus the complex wire bonding is no required, see Figure 5.10. This holder can be used for different devices by simply changing the chip, which is very useful during the process of developing and characterizing the sensor. Consequently, the design of the electrodes was also modified in order to fit in the new holder.

Figure 5.10. Holder type packaging is composed of a methacrylate frame with cavity for a 2 x 2 cm2 chip and orifices for 4 screws, 10 metallic pins and 4 connector tubes.

The new generation of electrodes was completely produced at wafer scale, from the fabrication of the nanodigits and the pads, until the passivation layer. In this case bigger chips were used to facilitate the manipulation and in this manner reduce the chance of detriment during the handling. The chips are 2 x 2 cm^2 and each of them holds four IDEs arrays, with two lateral pads of 500 x 500 μm^2 each. Four counter electrodes were included in the design, each couple share the pads. There is place for nine chips in every wafer. Unlike the PCB strip, in the methacrylate holder the pads are vertically connected. Thus, in order to do not hinder the placement of the connection pins, the pads were placed as far separated as possible from each other. However, presumed eddy current must be avoided by the reduction of the pads area. Thus, a trade-off must be achieved for the length of the pads. Horizontal separation between digits arrays is 9.5 mm and the vertical separation is 5.5 mm. The design of an individual chip and the whole wafer can be observed in Figure 5.11.
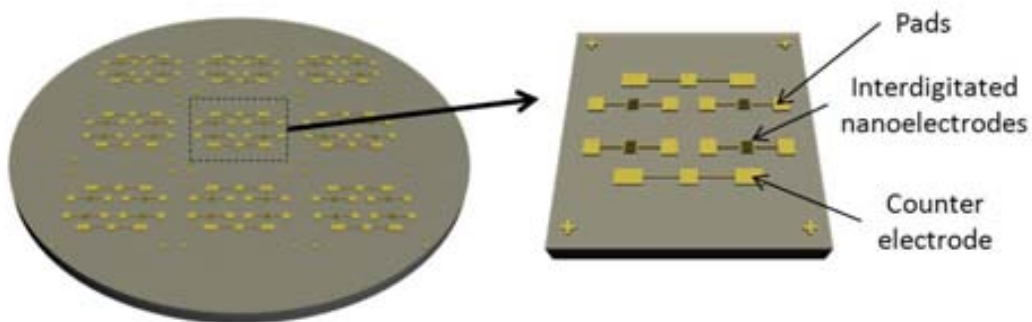
Figure 5.11. Sketch of a wafer holding nine 2 x 2 cm^2 chips (left). Each chip is composed of four electrodes and four counter electrodes (right).

- Nanodigits fabrication

First stage of the fabrication is the e-beam exposure of the nanodigits, then the microareas were patterned by photolithography.

First generation of IDEs produced for the methacrylate holder were exposed with the e-beam lithography system, Vistec VB300UHR EWF [6], placed at the Molecular Foundry's cleanroom. The devices were produced on 4 inch silicon wafers coated with 200 nm SiO$_2$ in order to obtain an isolator substrate. Then the wafer was metallized with 5 nm of Cr and 25 nm of Au by e-beam evaporation. Since the ZEP is not soluble in acetone, the lift-off was performed in dichloromethane. In Figure 5.12 can be observed a 500 x 500 μm^2 interdigitated electrode array, the digits are 50 nm width and 100 pitch. At the

present these are the smallest interdigitated electrodes in the largest area found in the literature.
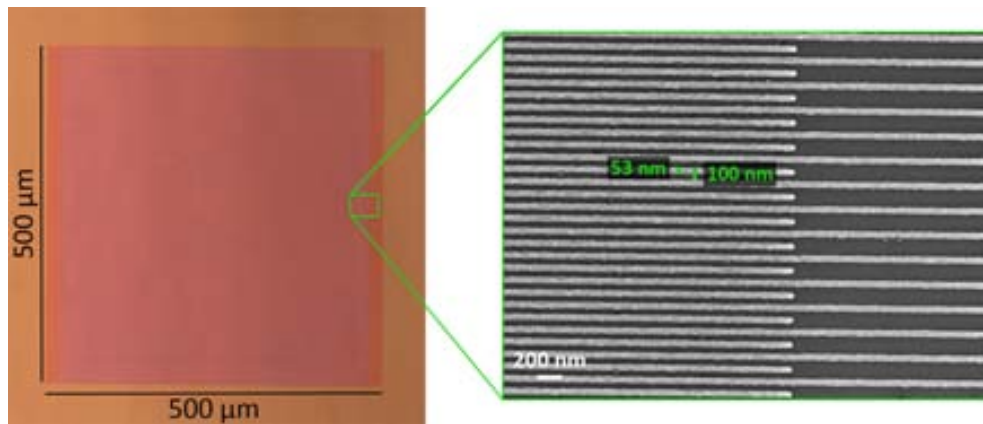
Figure 5.12. Interdigitated electrodes fabricated by e-beam and lift-off. On the left, optical microscope image of a 500 x 500 μm^2 array of digits. On the right, a SEM image inset of the digits in the position where interdigitated area and non-interdigitated area converge. The digits are about 50 nm width and pitch 100 nm.

- <u>Pads fabrication</u>

After the fabrication of the nanodigits, the pads were defined by photolithography. The protocol used to perform the exposure is explained in Annex 2. 5/100 nm of Cr/Au were deposited by e-beam evaporation, after the subsequent lift-off the fabrication of the IDEs was finished. Figure 5.13 show image of a whole wafer after the fabrication of the devices, nanodigits by e-beam lithography and pads by photolithography. In each wafer 36 IDEs are achieved, shared out in nine 2 x 2 cm^2 chips.

Figure 5.13. Image of the whole wafer with the completely fabricated devices.

In Figure 5.14a detail of one of the chips can be observed. In each chip there is place for 4 sensors. The interdigitated electrode array takes 500 x 500 μm^2, the length of the bars b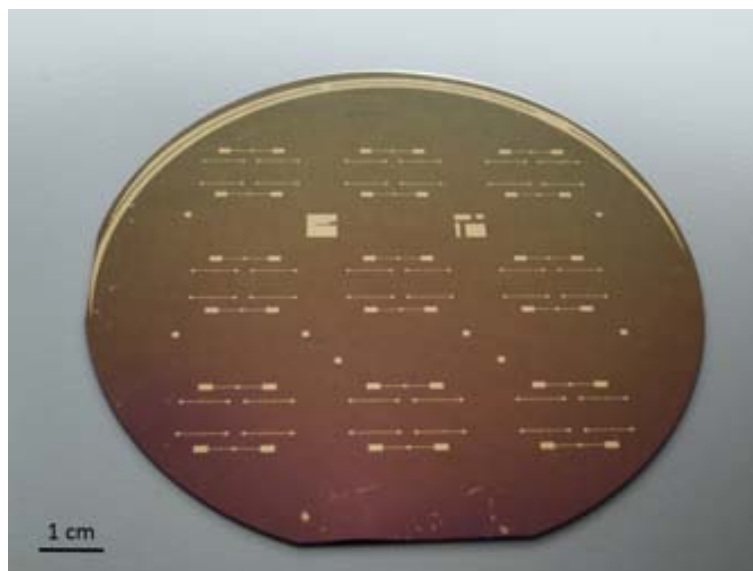etween the collector bars and the pads is 3 mm and the pads 500 x 500 μm^2. The total length of each sensor is 7.5 mm and the maximum height 500 μm.

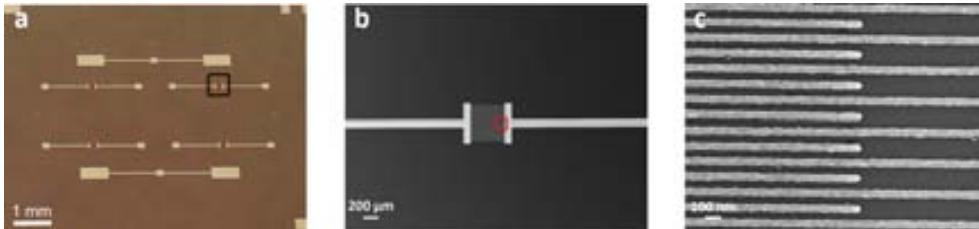Figure 5.14. a) image of a 2 x 2 cm^2 single chip holding four IDEs. b) SEM image of the array of lines collected by the collector bars. c) SEM image of a detail of the 50 nm width and 50 nm separation digits where the interdigitated and non-interdigitated areas are merged.

2.2.2 Multi-area devices

Even though e-beam lithography is a well-known technique, the fabrication of interdigitated nanoelectrodes is complex. High number of lines very close from each other must be exposed and no imperfections are allowed for the correct operation of the device. The most common defects are the overexposure due to the proximity of the lines, underexposure in the non-interdigitated areas trying to solve the first problem, collapse of the lines, fragments of metals remaining from the lift-off…[1]. Smaller the width and pitch of the digits are, the higher the chance to nullify the device due to one or more of these defects.

This problem not only affect to e-beam fabrication, but also to the rest of the technologies when working close from the limit of the technology. Electronic device manufacturers are aware of this situation, especially when designs move to 28 nm and smaller nodes the production yield drastically decreases. In order to overcome this situation, engineers can take precautions during the design of the device. Logic designers usually include redundant logic or memory cells. These can be used to repair faults, which will increase yield even though the die is partially defective [7].

The idea of redundant *blocks,* is to design several of the problematic blocks or parts in the layout of the device. After the fabrication of the original device each block is characterized and the *Bad Blocks* are removed. Devices with Bad Blocks have the same quality level and the same AC and DC characteristics as devices where all the blocks are valid. A Bad Block does not affect the

performance of valid block because it is isolated from the bit line and common source line. This methodology is usually employed for the flash memories fabrication, as usb memories [8].

Based in the Bad Block concept, we modified the design of the interdigitated electrodes in order to increase the fabrication yield. The large 500 x 500 μm^2 area was replaced by several smaller areas. Each area connected with metallic bars to the big pads of the general device. This way, if one of the areas is damaged it can be easily disconnected from the rest of the device by FIB or other techniques. A pad was placed in each collector bar to facilitate the electrical characterization of each block with the connection proves.

Figure 5.15 shows one of the multiarea IDEs fabricated at the CNM using the Raith 150 Two equipment. It is compound of three area of 200 x 200 μm^2, digits of 170 nm and pitch 300 nm and 25 nm of metal thickness. Figure 5.15a represents the case when one of the block is damaged and isolated by cutting the collector bar with FIB.
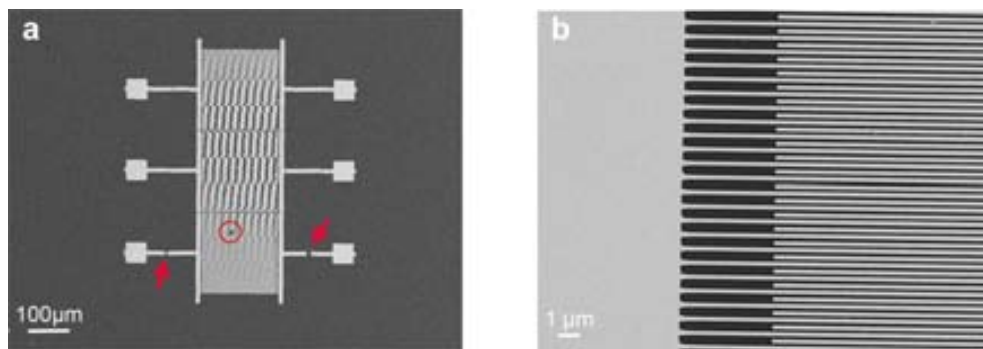
Figure 5.15. SEM images of the multilayer n-IDEs. a) Shows the three blocks of arrays. It can be observe that due to a defect in the bottom block it was disconnected from the rest. B) Detail of the nanodigits.

5.2   IDES PACKAGING PROCESS

As it has been explained along this chapter, IDEs of two different designs have been fabricated to be placed in respective holders. PCB type packaging is focused in a compact format of packaging. Meanwhile, the methacrylate holder is highly appropriate to used during the characterization and proof of concept of the sensor due to the easy and fast electrical contact of the chip. Moreover, it allows the integration of a microfluidic system.

5.2.1 Packaging with PCB

The PCBs used for packaging the devices are composed of a plastic strip with five metal wires that make possible the connection between the IDEs' pads and the electrical system. At the bottom of the PCB strip there is a 3 x 3 mm^2 cavity to place the chip, Figure 5.16.

Figure 5.16. Schematic figure of the PCBs used to package the IDEs. Courtesy of Fernandez-Cuesta [9].

Prior to the packaging, a selective passivation of the chip has to be performed in order to isolate the whole surface except for the areas corresponding to the pads and the digits.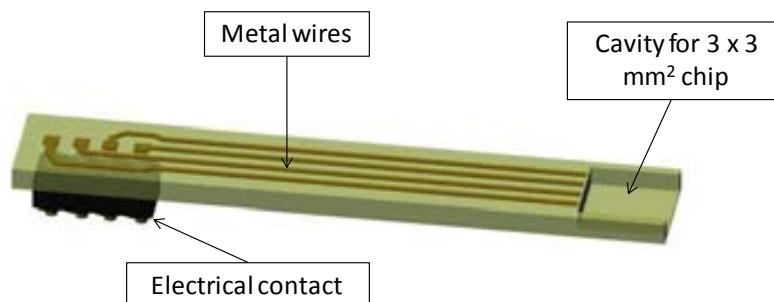 For this purpose, the chip is covered with a resist that defines the exposed areas and also protects the device from scratching during manipulation. The pads must be exposed to allow the connection with the PCB's wires. The exposed area over the digits limits the reaction area, avoiding possible reactions between the analyte and the gold strip that connects the digits and the pads, which could cause signal distortions.

The encapsulation process can be aggressive for the fragile digits of the n-IDEs, therefore the active area remain protected during the whole packaging process. The resist above the digits is removed just before the measurements. The material used to passivate the device was PMMA. PMMA was chosen because it is not a photoresist, thus exposed area can be under light during the encapsulation without suffering any variation. The steps carried out for the passivation are explained bellow, Figure 5.17:

a) The whole chip is covered with 400 nm thick PMMA thick layer.

b) The area of the pads is exposed by e-beam lithography.

c) Development of the resist is performed by dipping the chip 30 s in MIBK developer and 30 s in IPA in order to stop the reaction. Thus the pads are opened to the outside.

d) A second e-beam exposition is performed on the active areas of the IDEs.

e) The development of the second lithography is performed after the encapsulation of the chips to the PCB strip. Thus the digits remain protected during the process.

f) Finally the exposed area is developed, leaving the digits open and ready for the measurements.
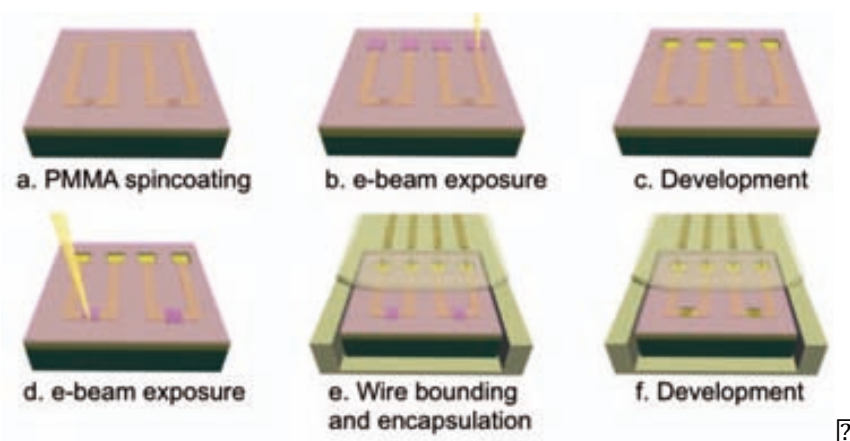
Figure 5.17.Steps followed for the passivation of the devices extracted from [9].

Once the chip is placed and connected to the PCB, the whole strip and the top of the chip are protected with an epoxy resist, Epotec®. Figure 5.18 represents the PCB strip after the passivation and packaging of the device. Figure 5.5 shows a picture of the real system.
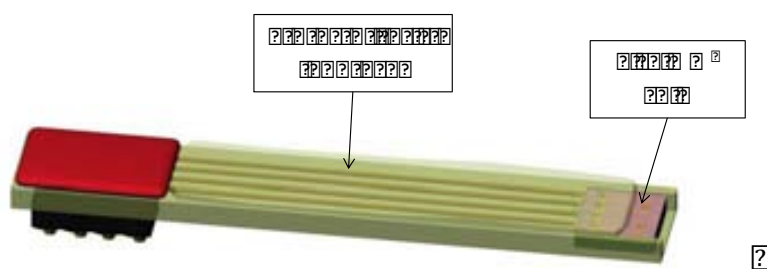
Figure 5.18. Schematic image of the PCB after the passivation of the chip and packaging. Courtesy of Fernandez-Cuesta [9].

Just before used the sensor the PMMA on top of the digits (that it was previously exposed by e-beam) must be developed. The development is carried out as usual by the immersion of the chip in MIBK:IPA (1:3) during 30 s and then rinse in IPA. Once the digits are open to the exterior the device is ready to start working.

Figure 5.19 shows the measurement set up used to measure nIDEs packaged on PCBs. Electrochemical measurements were performed using a CE-WE-RE

configuration. Pt commercial counter electrode and Ag/AgCl commercial reference electrode were used, IDEs played the roll of working electrodes in the system. The three electrodes were connected to a potentiostat (Autolab, GPES) and controlled by GPES software. The analyte was placed in a recipient were the electrodes were immersed.

Figure 5.19. Shows complete set-up to perform electrochemical measurements in liquid.

First measurements were performed using ferricyanide was measured to check the correct operation of the sensors. The interdigitated used to perform the measurements have a 130 nm digits and 300 nm pitch in a 200 x 200 μm^2 area. However, Figure 5.20a voltammogram shows that there is not a clear ferricyanide oxidation and reduction peaks. Most likely that happens because the electrode is still passivated with remains of PMMA.

As the chips used in the PCBs have a size of 3 x 3 mm^2, when the resist is spincoated in so small chips, the border effect is magnified and the resist layer become non-homogeneous, with a variability of at least of 500 nm. Thus the accurate dose necessary to expose the resist is uncertain. When low dose is applied thin resist layer could remain on the electrodes, which would passivate and nullified the digits. At the same time, overexposition of the PMMA makes larger the exposition area with the risk to open the collector bars.
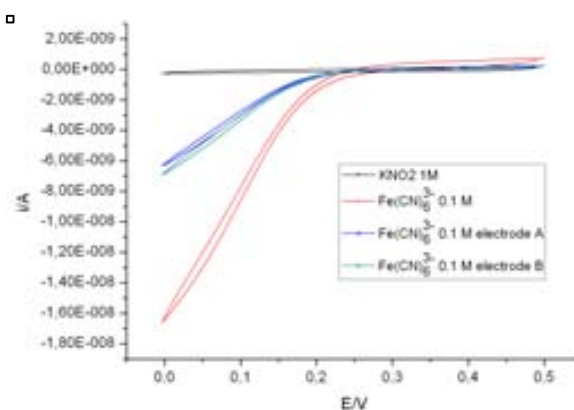

Figure 5.20. a) Voltammogram of Fe(CN)$_6^{3-}$ 10^{-3} M performed to each electrode separately and both together and compared with KNO$_3$ 1 mM signal.

140

Due to the inconvenient of the small chip dimension required for the PCB packaging, as well as the reduction of operational devices owing to the significant manipulation required to make the wire bonding, specific packaging, addressed for the nIDEs was designed. This new encapsulation is much more reliable and user-friendly, it overcomes all the drawback presented with the PCB.

5.2.2 Holder type packaging and microfluidic

The new packaging is based on a methacrylate holder with room to place the silicon chip and electrical and liquid connectors [10,11]. Moreover, the new packaging also includes a microfluidic system. It is a 2.5 x 2.5 cm^2 and 1 cm height methacrylate frame with a cavity of 2 x 2 cm^2 to place the sensing chip, and holes for the screw, metallic pins and connector tubes. There are four screws, one in each corner to link the base and the cover of the holder. There are 10 metallic pins, 8 for the connection of the IDEs pads and two for the connection of the counter electrode pads. 4 connector tubes are placed for the entrance and exit of two microfluidic channels. Figure 5.21 shows schematic view of the holder and its parts.
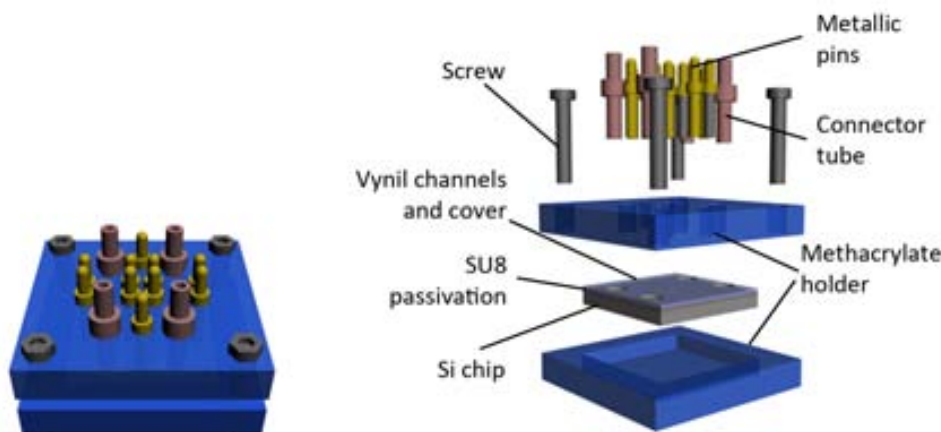
Figure 5.21. Holder type packaging. In the right different parts of the holder are depicted.

The passivation and microfluidic were fabricated on the silicon chips, at wafer scale. The passivation was carried out by a photolithography on 500 μm layer of SU8 (Microchem), annex 5. The whole chips is covered with SU8 unless the digits and the counter electrodes to perform the measurements and the pads to allow the electrical connections. After the SU8 deposition the wafer is cut to use the individual chips, see Figure 5.22.
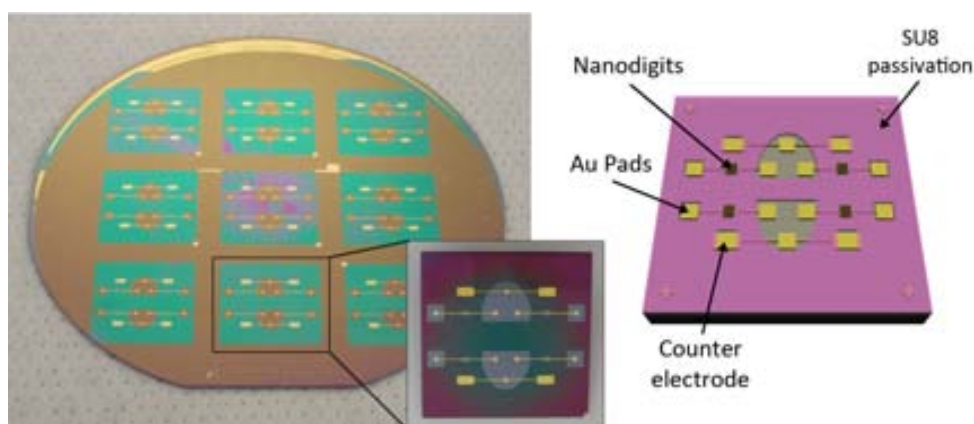
Figure 5.22. Picture of the silicon wafer with nine chips of electrodes, covered with the SU8 passivation, inset of one of the chips can be seen. On the right, there is a schematic representation of one of the chips.

It has been observed in measurements performed with n-IDEs that when the analyte is enclosed around the digits higher efficiency, better control, increased reproducibility and limitation in the diffusion of the redox compound are obtained. As it was demonstrated by I-Jane Chen, 2011 et al. [12,13], including microchannels to the device is a reliable strategy to keep the analyte confined. Usually, electrolytically generated bubbles hinder the function of the microchannels. For this reason gas permeable polymers are highly recommended, such as vinyl. In this work the 1 mm width channel were defined by means of a vinyl adhesive and covered with a COP (Cyclic Olefin Polymer) film. Both of the layers have the apertures for the pins contact and the analyte entrance and exit tubes. Thickness of the vinyl layer is 130 μm, consequently this is the height of the channel, Figure 5.23.
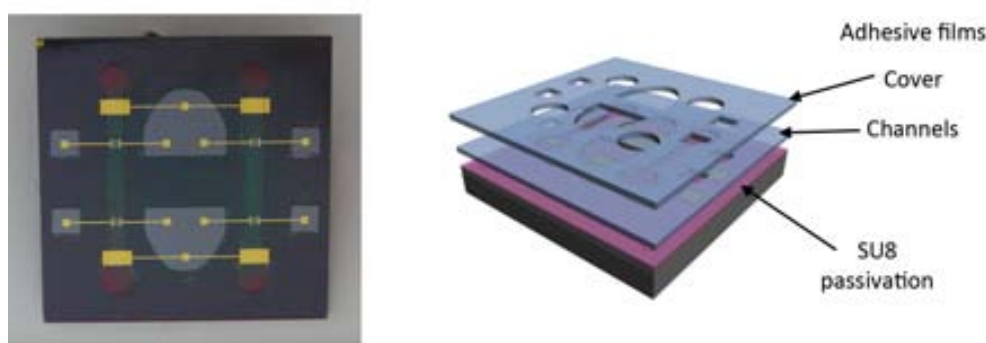
Figure 5.23. Picture of one of the chips with four IDEs and the two adhesive layers. On the right the different part of the system are represented.

The channels also have the task to protect the nanodigits. Since the sensors are covered with the COP film they are shielded from the scratches caused by the manipulation and from the dust. After the passivation of the digits and preparation of the channels, the device is placed in the methacrylate holder.

142
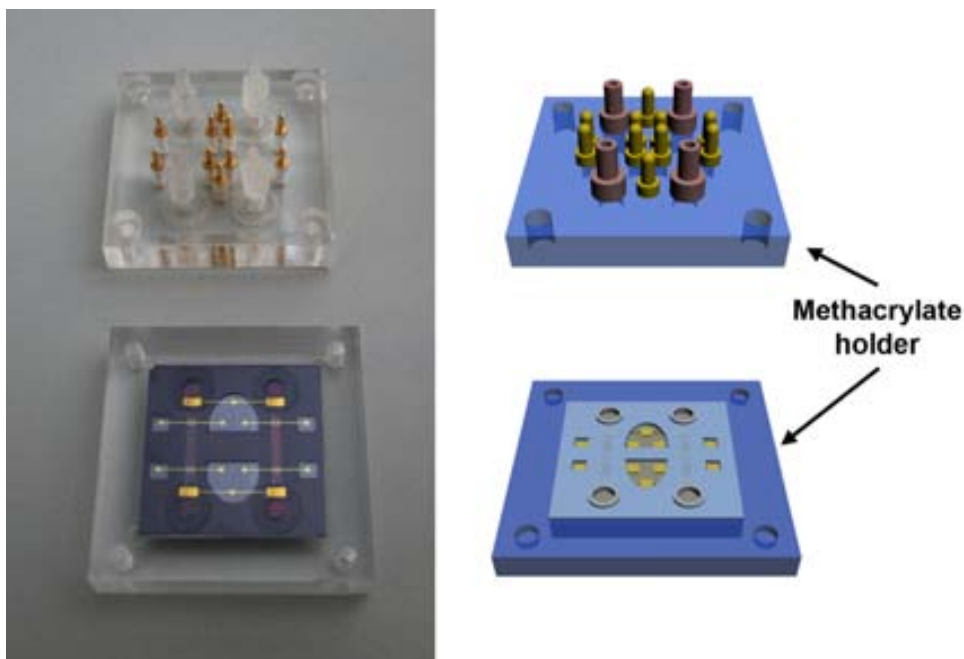
Figure 5.24. Picture and sketch of the chip placed on the methacrylate holder.

In Figure 5.25 can be observed the whole set-up to perform electrochemical measurement with the IDEs placed in the methacrylate holder. This packaging has been a highly relevant advance in the development of this thesis and it will be able to apply in futures applications. Besides all the technological advantages that this holder means, importantly reduces the cost of the device. When sensors are placed in PCBs, the most expensive part is the performance of the wire bonding and packaging, which must be done individually for its device. Contrary, the methacrylate holder has a very simple contact connection, moreover the chips can be easily exchanged by simple unscrew and screw up.

The high sensitivity of the n-IDEs, the possibility to perform label-free and fast measurements as well as the advantages of having the analyte confined in microchannels, make them optimum candidates to be included in a polymeric lab-on-a-chip. This would lead to very promising devices for diverse applications, especially in the field of biosensing. In this particular field the amount of sample is usually limited and has a complicated matrix, in which many molecules interfere with the measurements. Furthermore, if we take into account the option of large scale fabrication of IDEs by nanoimprint lithography, the cost of the device extremely decreases, opening the possibility to use them to the general public.

Figure 5.25. Complete set-up of the holder for the IDEs characterization.

5.2.3 Comparison between PCB and holder packaging

Two type of packaging have been developed during this thesis. The first one is a standard PCB strip widely used in microelectronic, which is compact and easy to use. However, it is not the most suitable option for the presenting application, it has the disadvantage that during the preparation of the strip considerable manipulation of the chip must be done. As the devices are very fragile, an important number of devices are lost during the packaging. Moreover, the wire bonding is frequently difficult due to the fact that in our nIDEs the metal layer in the pads is too thin. This issue can be solved by the performance of a new lithography, metallization and lift-off process on the pads. However, in most of the fabrication processes the addition of extra processes involves enhancement of the cost, time and risk to damage the devices.

Due to the inconvenient of the standard PCB packaging, a new packaging method more accurate for the characteristics of the n-IDEs was developed. The methacrylate holder permits the easy exchange of samples, since the electrical connections are made just by the physical contact of the pads with external metallic pins. Therefore, with a single holder many devices can be measured, with %100 of good electrical connection and minimum chance to damage the sensor by the manipulation. Moreover, the microchannels are a big advantage respect the protection of the IDEs, the devices are enclosed in the channels and the chance to be scratched is minimize. They are also important to confine the analyte and enhance the measured signal. In addition, the volume of analyte needed to fill the channels is several orders of magnitude smaller than the

needed to immerse the PCB strip and the external sensors. Besides, the methacrylate holder is slightly bigger than the strip, but especially for the study of the sensors is much more effective. Table 5-1 shows the main physical parameters of both packagings.

Table 5-1. Physical parameters of PCB strip and methacrylate holder.

	PCB	Methacrylate holder
Packaging size	15 x 1 cm^2	2.5 x 2.5 cm^2
Chip size	3 x 3 mm^2	2 x 2 cm^2
Devices per chip	2	4
Manipulation of the chip	High	Low
Analyte volume needed	30 ml	50 μl

It is remarkable that the dimensions and design of the packagings presented in this thesis were chosen due to them suitability for this work. As future work, there is the feasibility to optimize the dimensions and design of the packaging aiming different applications.

In conclusion

REFERENCES CHAPTER 5

1. Mohammad, M., Muhammad, M., Dew, S. & Stepanova, M. in *Nanofabrication* (eds Maria Stepanova & Steven Dew) Ch. 2, 11-41 (Springer Vienna, 2012).

2. Pfeiffer, H. C. Direct write electron beam lithography: a historical overview. 782316-782316, (2010).

3. Micro-resist_technology_GmbH. http://www.microresist.de

4. Raith. http://www.raith.com.

5. MicroChem. http://microchem.com.

6. GmbH, V. E. B. http://www.vistec-semi.com.

7. Bailey, B. Design for manufacturing and yield. *EDN* (2013).

8. hynix, S. 16Gb NAND Flash H27UAG8T2B manual. (2010).

9. Fernanadez-Cuesta, I. *NanoImprint Lithography: Developments and nanodevice fabrication*, UAB, (2009).

10. González-Guerrero, M. J. *et al.* Rapid Prototyping of a Membraneless Glucose/O2 Microfluidic Enzymatic Biofuel Cells using Pyrolyzed Photoresist Film Electrodes. *Lab Chip* (2013).

11. Abad, L. *et al.* Design and fabrication of a COP-based microfluidic chip: Chronoamperometric detection of Troponin T. *ELECTROPHORESIS* 33, 3187-3194, (2012).

12. Chen, I. J. & White, I. M. High-sensitivity electrochemical enzyme-linked assay on a microfluidic interdigitated microelectrode. *Biosensors and Bioelectronics* 26, 4375-4381, (2011).

13. McKnight, T. E., Culbertson, C. T., Jacobson, S. C. & Ramsey, J. M. Electroosmotically Induced Hydraulic Pumping with Integrated Electrodes on Microfluidic Devices. *Analytical Chemistry* 73, 4045-4049, (2001).

?. Interdigitated electrodes for selective detection of dopamine

Dopamine (DA) neurotransmitter is implicated in the modulation of many cognitive processes. Dysfunction of dopamine production plays a vital role in various illnesses [1], such as Parkinsons's disease [2,3], Huntinton's disease [4] or attention deficit-hyperactivity disorders [5,6]. Due to the clinical relevance of this neurotransmitterr's concentration, many works have been dedicated to find out a reliable technique to detect its concentration [7-9].

Moreover, dopamine is a standard redox molecule, consequently it is usually employed for electroanalytical studies, Figure 6.1. However, detection of dopamine becomes complicate in serum due to the presence of ascorbic acid (AA) and other catecholamines. Ascorbic acid (vitamin C) acts as antioxidant in living organism and it is also a cofactor in many enzymatic reactions, Figure 6.2.
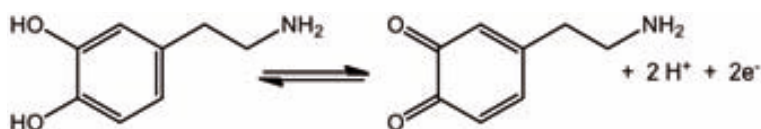
Figure 6.1. Reversible redox process of Dopamine.
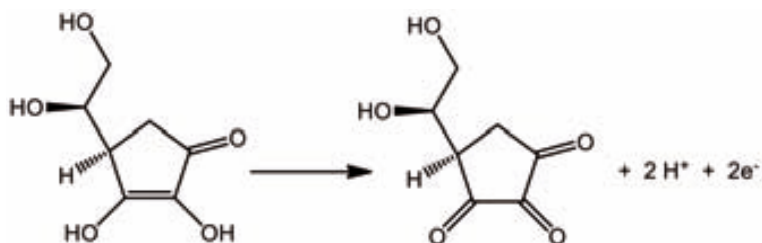
Figure 6.2. Irreversible redox process of Ascorbic acid.

These organic molecules are oxidized at nearly the same potential, which results in an overlapped voltammetric response [10,11]. During this thesis this drawback has been overcome by a selective detection of dopamine taking advantage of its reversible redox behavior and redox cycling method. Redox cycling technique does not need physical modification of the sensor, it works by setting one of the working electrodes to a fixed potential, while the other electrode is swept from positive to negative potentials. Continues oxidation and

reduction of the molecules take place from one working electrode to the other. Due to the enhancement of the redox-couple concentration gradient in the proximities of the electrode, the measured current increases. Dopamine shows a reversible redox reaction, while ascorbic acid oxidation takes place irreversibly. Therefore, when redox cycling is carried out, oxidation response of both species will be overlapped, but only dopamine's reduction will be detected.

Interdigitated nanoelectrodes are especially suitable sensors to perform redox cycling experiments. Each of the digits in the array behaves as a working electrode and the redox cycling happens between them. When the gap between electrodes is reduced, the diffusion of the molecules is lower and as a consequence, the concentration gradient in the proximity of the sensors increases. The measured current will be proportional to this concentration gradient, and so the current will be intensified.
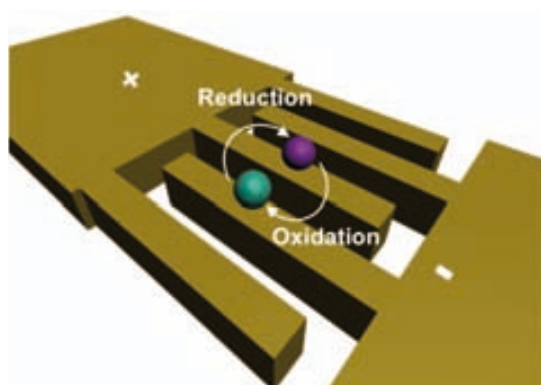
Figure 6.3. Representation of redox cycling using interdigitated electrodes.

A brief introduction to basic electrochemistry principles is presented can be found in Annex 6. For the sake of simplicity, this introduction has been limited to only the essential concepts. Nevertheless, extensive electrochemistry literature exist in the bibliography [12-14].

6.1 ELECTROCHEMICAL SENSORS

An electrochemical sensor is a device that after chemical interaction between the analyte and the sensing area, transforms chemical or biochemical information of quantitative or qualitative type into an electrical useful signal Figure 6.4 [15]. Clark and Lyons reported the first electrochemical biosensor in 1962 [16], known as "enzyme electrode". It used the enzyme glucose oxidase (GOx) for an amperometric measurement of dissolved oxygen. Since then, the use of electrochemical sensors to determine concentrations and other parameters of biological interest represents a rapidly expanding field [17]. Due

148

to their high sensitivity and selectivity, portable field-based size, rapid response time and low-cost, electrochemical sensors have found a great interest in fields such as clinical chemistry.

Figure 6.4. Operating principle of a electrochemical sensor

There is a wide variety of electrochemical sensors [12,17,18] and modes to classify them attending to their function, size, material or shape. During this thesis, the research have been focused in interdigitated electrodes sensors, specifically on the relevance of reducing their dimensions to the nanoscale and the different ways to achieve this goal. We have demonstrated the operability of the sensors by the detection of standard molecules using different electrochemical methods. As it will be shown, a signal enhancement is achieved due to the miniaturization of the digits and gaps.

6.1.1.i *Electrochemical sensor components*

Electrochemistry implies the transfer of charge from an electrode to another phase, which can be a solid or a liquid sample. During this process chemical changes take place at the electrodes and the charge is conducted through the bulk of the sample. Both the electrode reactions and/or the charge transport can be modulated chemically and serve as the basis of the sensing process.

A typical electrochemical cell consists of a three-electrode configuration: counter, working and reference electrode, all of them in contact with the analyte solution, Figure 6.5.

- **Working electrode (WE)**: is the electrode were the studying reaction occurs. Generally is made of novel metals. In this thesis the interdigitated electrodes have been used as working electrodes.

- **Reference electrode (RE)** is use to measure the working electrode potential. The reference electrode should have a constant electrochemical potential. Normally it is made of a material with well-known redox potentials. During this thesis an Ag/AgCl electrode has been used.

 Counter or **auxiliary electrode (CE)** is a conductor that completes the cell circuit. Counter electrode is used to carry the current of the cell. No reaction should happen in this electrode, thus it is usually made of inert material. Moreover, the counter electrode must have larger area than the working electrode to avoid limitations on the measured current.

Other essential components of the cell are the solution and the instrumentation. The solution is composed by the analyte, i.e. the molecule under study, but also of an electrolyte. The electrolyte is an ionic molecule that allows the flow of the current along the solution. The three electrodes must be immersed in the solution.

The potentiostat is the standard instrument to apply voltage to and detect current from the electrodes to apply/receive the signal to/from the solution, it transforms the chemical signal into a useful electrical signal. Bipotentiostat is a variant from the potentiostat able to control two different working electrodes. In this work Autolab (Metrohm) [19] have been used as bipotentiostat.
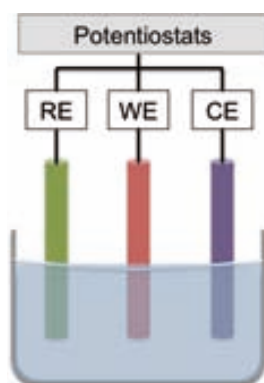
Figure 6.5 Electrode configuration: Reference, working and counter electrodes are immersed in the solution that contains the analyte and the electrolyte. The three electrodes are connected by an external potentiostat.

6.1.1.ii *Interdigitated nanoelectrodes*

Different strategies have been developed to improve the characteristics of the electrochemical sensors; the use of new materials (e.g. silicon, polymer, paper) and also variations of designs (e.g. spheres, bands, disks, cylinder) [20]. During the last decades, the attention has been centered in redesign the sensors to the analyte scale or the diffusion layer dimensions, which fundamentally contributes to the improvement of the sensitivity, mostly in micro and nano scale.

Some of the most relevant benefits of reducing the electrodes dimensions for electroanalysis are mentioned next [20]:

- They can be used in high resistivity media because, due to their low Faradic currents, they suffer from very small ohmic (iR) drops.

- Miniaturized electrodes also display lower background currents, which are proportional to electrode area.

- They are in general more sensitive because they experience much higher current densities than macroelectrodes.

- These devices can be used in the study of fast electron transfer and homogeneous kinetic processes because, in addition to the previous advantages, they respond very fast to concentration changes.

- Much smaller sample volumes are needed.

This work has been focused on the miniaturization of interdigitated electrode arrays to nanometric dimensions, which is a technological challenge. When micro and nanometric electrodes are applied, arrays of electrodes are commonly used because the current measured by a single electrode is usually negligible for the macroscopic external equipment. These sensors are composed of two arrays of nanoelectrodes in a interdigitated configuration, the nanoelectrodes of each array are collected by a microbar and ended in micropads to allow the electrical connection, see Figure 6.6.
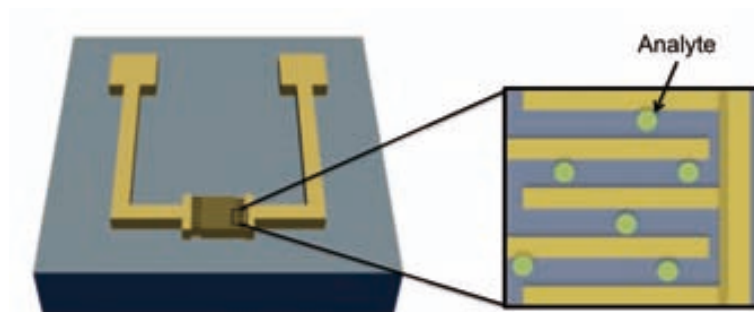
Figure 6.6 Sketch of interdigitated electrodes. The sensing of the analyte happens in the gap between electrodes.

Sensing of the molecules happens in the gap between electrodes. Therefore, best results are obtained when this gap is similar to the size of the molecule that is desired to detect (Figure 6.7). In general terms, it can be stated that the smaller the gap the higher the sensitivity.

Figure 6.7. When the dimensions of the gap and the analyte are similar, the sensor has a higher selectivity and sensitivity.

Moreover, small gap between the electrodes means shorter response time. As a consequence, there is an enhancement of the signal, Figure 6.8a. In addition, the amount of analyte needed for the measurement is lower, owed to the smaller area of the electrode, Figure 6.8b.
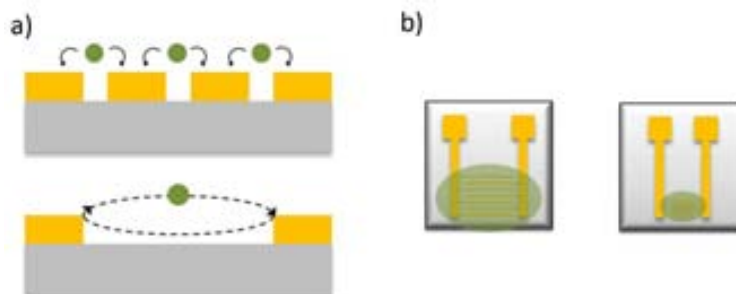
Figure 6.8. a) Shorter response time is obtained for smaller electrode gap. b) Less analyte is needed when the area of the electrode is smaller.

Figure 6.9 represents the electrodes configuration used for the electrochemical characterization of n-IDEs. Reference electrode, counter electrode, and both working electrodes of the n-IDEs have been connected to a bipotentiostat, thus different potentials could be applied to each WE.
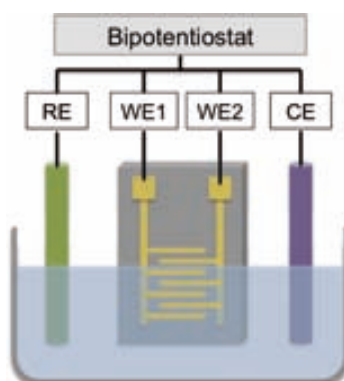
Figure 6.9. Electrodes configuration using separately the two working electrodes of the interdigitated electrodes. All the electrodes are connected to a bipotentiostat, thus two different potentials can be applied to the WEs.

The importance of electrochemical sensors added to the fascinating characteristic of devices miniaturization, make the nIDEs sensors attractive for a large number of fields and applications, e.g. measuring of biological nanomolecules such as DNA, proteins, or enzymes.

6.2 ELECTROCHEMICAL METHODS

Many different measurement methods have been developed to study chemical reactions [14]. The following section is mainly focused on voltammetric methods, which are benefited by the small dimension of the interdigitated nanoelectrodes.

Voltammetry techniques study the current resulting from the application of a potential wave function to the working electrode, usually with respect to a reference electrode. Cyclic voltammetry and redox cycling have been used for the detection of Dopamine.

6.2.1 Cyclic voltammetry

Linear voltammetry consist on applying a linear potential sweep from initial potential E_1 to E_2 and register the current produced during the process due to the oxidation or reduction of the specie. If we step forward and after reaching E_2 we sweep back to E_1, the oxidation and reduction peak of the specie will be represented, this technique is named cyclic voltammetry. Moreover, by using cyclic voltammetry, quantitative information about the redox states and electron transfer kinetic can be studied.

Figure 6.10 shows a typical example of cyclic voltammetry graph, where the oxidation and reduction peaks are observed. This kind of measurements are especially interesting to find out the oxidation and reduction peaks of a specie to perform other subsequent electrochemical techniques.
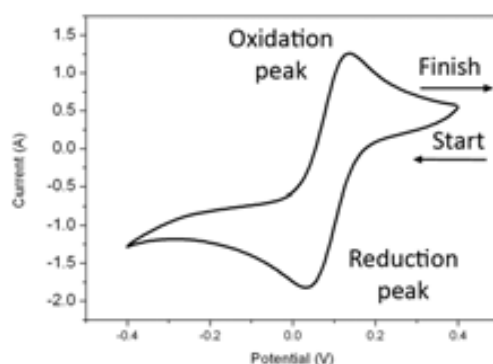
Figure 6.10 Typical cyclic voltammetry curve. Oxidation and reduction peak are presented.

During the characterization of the interdigitated electrodes, cyclic voltammetry has been very useful technique to check the correct operation of the sensors, but also to detect undesired shortcut between digits. In a correct situation, the current detected for each of the working electrodes of the IDE must be half of the current detected for both electrodes connected to each other. In the case

that this current has the same value as the single electrodes' curve, it means that there is a shortcut between the working electrodes. When a shortcut is manifested, the bipotentiostat detects a single electrode for the whole sensor.

When redox reaction does not happen on the electrodes surface (for example because the specie in the solution is not electrochemically active or the electrodes are covered by a impenetrable material), only the capacitive current due to the charge and discharge of the electrodes is measured, Figure 6.11.
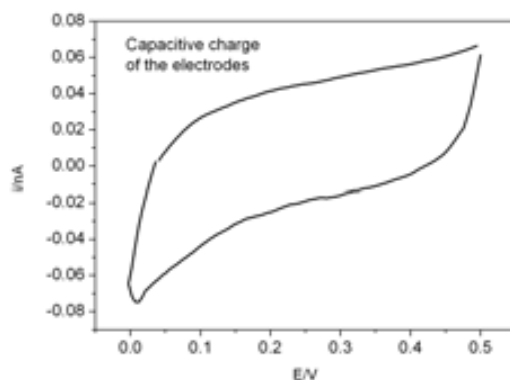
Figure 6.11. Example of a voltammogram where only the capacitive current is detected.

6.2.2 Redox cycling

Redox cycling is an adaptation of the standard voltammetry to improve the selectivity of the sensor. An extra working electrode is added to the CE-WE-RE configuration. While the first working electrode is fixed to a determined potential the other one cyclically sweeps from E_1 to E_2, thus the molecules enter in an oxidation and reduction cycle between both electrodes, Figure 6.12. Consequently, the concentration gradient in the immediacy of the electrodes increases and so the detected current remarkably increases. The number of times that the signal increases respect to the signal measured after voltammetry is the amplification factor and it will determine the time that a molecule needs to diffuse. When the separation between electrodes decreases, the time that a molecule needs to reach the other electrode and change its state also decreases, which results in an increase of the amplification factor.

Figure 6.12. Sketch of cyclical redox reaction happening during the redox cycling process. While one of the working electrodes oxidizes the molecules in the solution the other electrode reduce them.

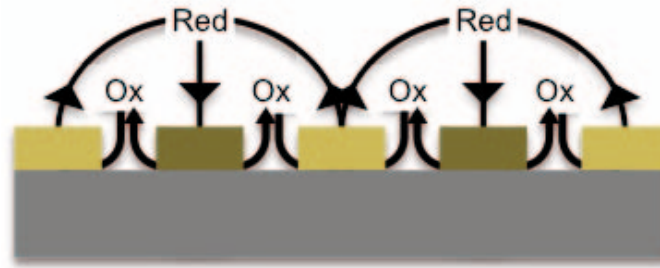In a typical redox cycling curve, the applied potential is represented vs. the registered current. As it can be seen in Figure 6.13, two curves are observed (dark blue): oxidation of the molecule (represented with positive values) and the reduction of the molecule (in negative values). Figure 6.13 shows the important current increment obtained by means of redox cycling technique, compared to the light blue curve obtained by cyclic voltammogram of the same molecule.
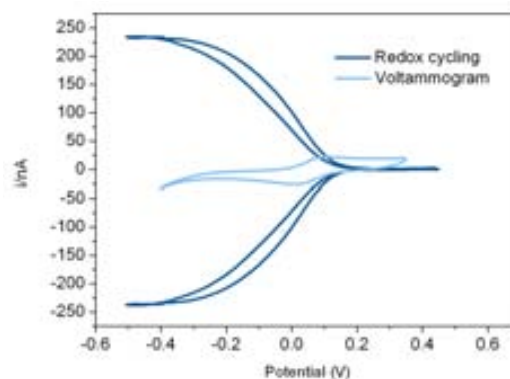
Figure 6.13. Typical redox cycling curve obtained form a redox couple (green line). In positive values oxidation is represented and in negative reduction. The red line corresponds to the cyclic voltammetry of the same redox couple. It is notable the signal enhancement due to the redox cycling.

6.3   MODELING AND SIMULATION

The enhancement of the signal due to the miniaturization of the IDEs and the redox cycling procedure has been demonstrated by finite element simulations. There is a direct relation between the dopamine concentration gradient in the stagnant layer and the current. The higher is the concentration near the electrode, the higher the flow of electroactive molecules towards the electrode, thus higher will be the detected current. Dopamine concentration gradient have been simulated using Comsol Multiphysics software [21]. Taking advantage of

the periodicity of the structure, only a basic cell has been considered, Figure 6.14.

Figure 6.14. Representation of the half-cell used to make simulations. As it is depicted in the picture, when redox cycling is performed the concentration gradient is symmetric, thus it is adequate to simulate half-cell.

The diffusion coefficient of dopamine is $0.54 \cdot 10^{-9}$ cm$^2 \cdot$s^{-1} [22] and the same diffusion coefficient has been assumed for the oxidized specie. It is hard to know the real stagnant layer formed between the electrode and the solution, thus it has been assumed to be 15 μm for all the s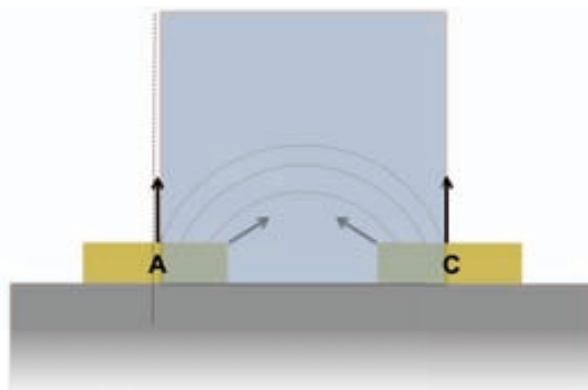imulations, which is an arbitrary value adjusted according to the experimental voltammogram results. Concentration of dopamine was determined to be 10^{-4} M.

In order to demonstrate the enhancement of the signal due to redox cycling in comparison with non-redox cycling process, both situations have been simulated. Moreover, the relevance of having nanometric dimensions of the digits has been confirmed by comparing the results of 150 nm width digits and 1.5 μm width digits electrodes.

First simulations were performed for nanometric IDEs. The physical characteristics of the electrodes were based on the device used to perform the experiments: digits width of 150 nm, pitch 300 nm, active area of 600 x 150 μm^2 and 25 nm thick metal layer.

Figure 6.15 represents results of the dopamine concentration simulation on non-redox cycling experiments using n-IDEs. Dopamine concentration gradient is orthogonal to the electrode surface. When moving away from the electrode and closer to the solution, the dopamine concentration increases. Figure 6.16 shows the vertical profile of the concentration gradient just on top of the digits. This vertical profile shows the linear relation between the concentration gradient and the distance from the digit.

Figure 6.15 Results of the simulation of the dopamine concentration gradient obtained from non-redox cycling experiments when using dopamine 10^{-4} M and nIDEs of 150 nm, width, 300 nm pitch and 600 x 150 μm^2.
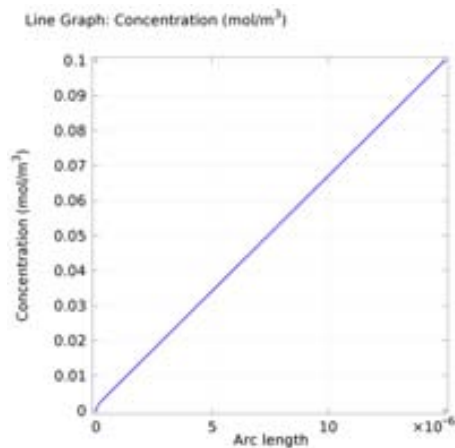
Figure 6.16. Dopamine 10^{-4} M vertical diffusion profile for non-redox cycling using nanometric IDEs.

However, when redox cycling is performed, Figure 6.17, dopamine concentration gradients close to the electrodes increase due to the movement of molecules from one electrode to another. In this case the diffusion of the molecules is more important between the electrodes than from the electrodes to the solution.
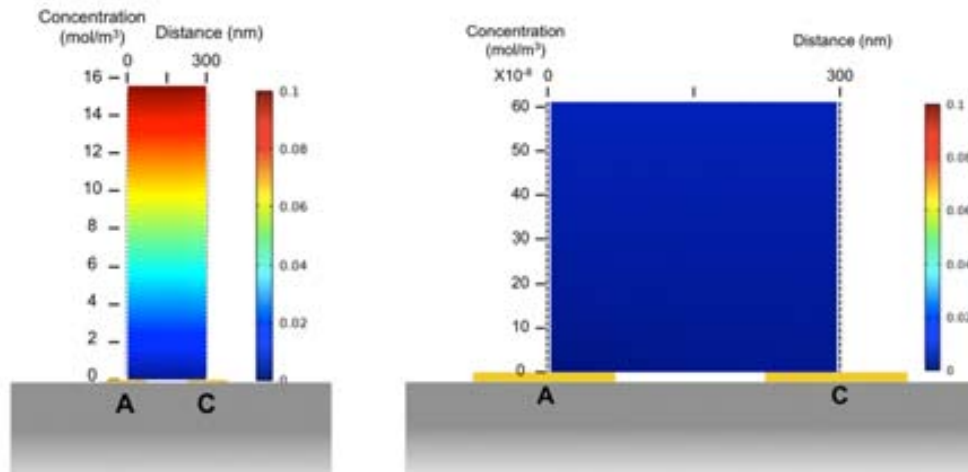
157
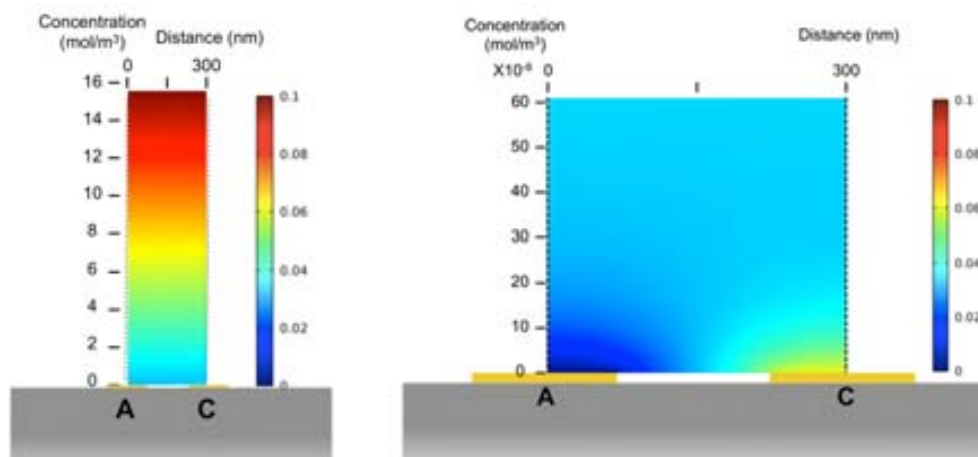
Figure 6.17. Results of the simulation of the dopamine concentration gradient obtained from redox cycling experiments when using dopamine 10^{-4} M and nIDEs of 150 nm width, 300 nm pitch and 600 x 150 μm^2.

Figure 6.18 shows the diffusion profile of dopamine for redox cycling experiments corresponding to the configuration of the nIDEs nIDEs. The concentration gradient rapidly increases close to the digit due to the contribution of nearest electrodes, then the concentration changes linearly with respect to the distance.
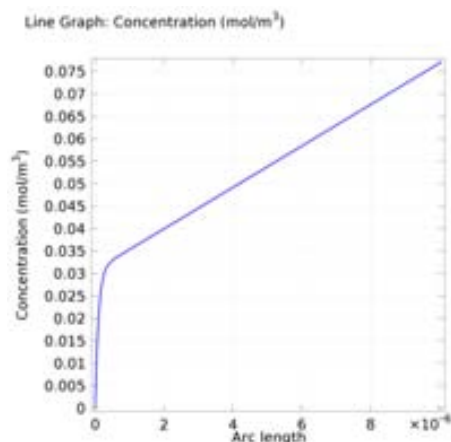
Figure 6.18. Dopamine 10^{-4} M vertical diffusion profile for redox cycling using nanometric IDEs.

The current calculated from the simulation of redox cycling gives a value of 942 nA for the anode and 962 nA for the cathode. While the current calculated for non-redox cycling simulation gives a value of 60 nA. That means that the current registered when redox experiments are performed using nanointerdigitated electrodes is 15.6 times larger than the current registered with non-redox cycling process.

In contrast, when redox cycling simulation is performed for ten times larger IDEs, digits width of 1.5 μm and 3 μm pitch but the same active area (150 x 600 μm^2 and 25 nm thick metal), the concentration near the digits is much lower

158

than for nanometric IDEs. As there is a larger distance between digits, the molecules in between have a larger diffusion zone, and thus lower concentration gradients are present around the digits.

The current registered by redox cycling using IDEs ten times larger digits, pitch 3 μm, is 2089 nA for anode and 2205 nA for anode. In the case of non-redox cycling the current is 544 nA. Therefore, the signal obtained using microelectrodes gives a gain of 3.8 times.

Hence the gain obtained from redox cycling reducing ten times the dimensions of the digits and the gaps is more that four times larger.

Table 6-1. Comparison between current obtained from redox cycling and voltammetry using nano/micro electrodes. The gain obtained from each case is also shown.

		Nanoelectrodes (300 nm pitch)	Microelectrodes (3 μm pitch)
Redox cycling	Anode	942 nA	2089 nA
	Cathode	962 nA	2205 nA
Voltammetry	Anode	60 nA	544 nA
Gain		15.6	3.8

6.4   RESULTS AND DISCUSSION

In this section, the experimental procedure carried out for the detection of dopamine in presence of ascorbic acid is presented. In natural serum, both molecules appear together and have similar oxidation potentials. However, dopamine has a redox-couple, while ascorbic acid does not. Due to the clinical relevance of dopamine concentration it is important to obtain a selective detection. This process has been possible owing to the redox cycling technique, where current measured for redox species is substantially enhanced. As it will be seen, the current measured using redox cycling on a dopamine solution has been 17 times bigger than the one measured with standard voltammetry.

This section also describes the preliminary protocols performed before the characterization of the dopamine solution. First, the electrodes must be activated in order to remove any possible undesired material on the sensing area. Then, the correct operation of the IDEs has been demonstrated by the measurement of Ferricyanide, a well-known electroactive compound.

6.4.1 Activation of the n-IDEs

After several measurements of Ferricyanide and Dopamine, electrode fouling occurs, which partially or even totally block the electrode active area and thus negatively affect the electron transfer kinetics.

Fortunately, this situation is reversible. It can be overcome by the activation or cleaning of the electrode. The cleaning is performed by the immersion of the electrode in a 1 mM KNO_3 solution, and swept the voltage from -0.5 V to -1.5 V for 10 cycles. Under these conditions the water hydrolyzes and the H_2 bubbles mechanically remove the contaminating elements that may be attached to the electrode surface. However, this method could be too aggressive for the nanometric electrodes, as the high current flow that is generatedcould stress the metal structures and make them come off the substrates. To avoid this, the current passing through the working electrodes was limited to 100 nA. In Figure 6.19 it can be seen the difference on the recorded signal before and after the activation of the sensors.
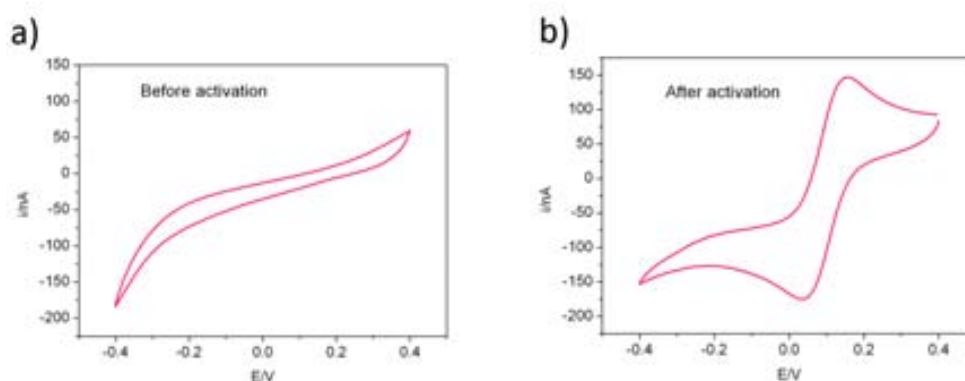
Figure 6.19 $Fe(CN)_6^{3-}$ 10^{-3} M voltammetry before and after activation. The activation was performed in KNO_3 10^{-3} M, the voltage was swept from 0.5 V to -1.5 V 10 times. The current was limited to 100 nA,

6.4.2 Electrochemical characterization of the IDEs

6.4.2.i *Measuring setup and electrodes*

Electrochemical measurements were performed using the configuration represented in Figure 6.9, where a counter electrode, one reference electrode and two working electrodes are used. The electrodes are connected to an external potentiostat (Metrohm, Autolab B.V.) using GPES software [19]. The holder and all the electrodes were placed inside the Faraday cage, extremely important to obtain clear signal and avoid noise.

The analyte solution was injected into the channels by means of a syringe with metallic needle, which was also used as counter electrode. As reference electrode an Ag wire was used. The wire was inserted in the exit hole of the channel, to be in contact with the solution. Finally the working electrodes were connected to the potentiostat using the spring-loaded pins of the holder, see Figure 6.20.
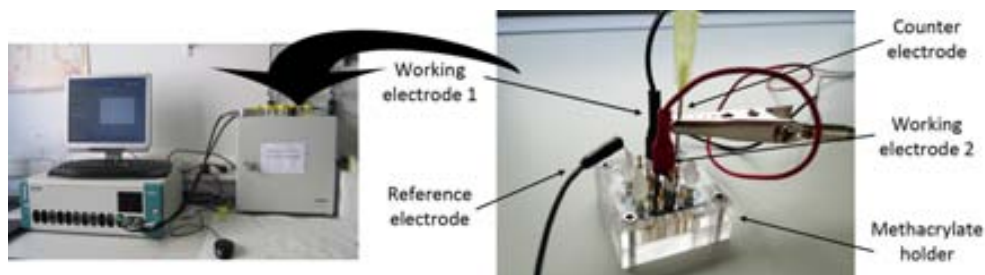
Figure 6.20. Picture of the set up used to measure the n-IDEs using methacrylate holder. a) Faraday cage and potentiostats. b) The holder with the connections for working, reference and counter electrodes.

The interdigitated electrodes used to perform these experiments have an active area of 600 x 150 μm^2 divided in three connected blocks (see Chapter 5), digits width of 150 nm and pitch 300 nm. They have large half-life, more than 300 measurements have been done with the same device.
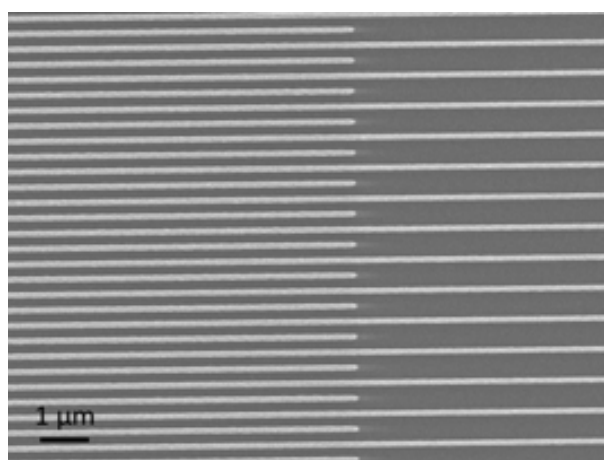
Figure 6.21. SEM image of the interdigitated electrodes used to perform Dopamine detection. a) Active area of the electrodes is 150 x 600 $\mu m2$ divided in three connected blocks. b) 150 nm width digits and gaps.

6.4.2.ii Characterization of nIDEs using Ferricyanide

Ferricyanide has been widely studied in electrochemistry because it performs an ideal redox-couple at E^0= 0.436 V [23,24]. It is usually employed to study the behavior and capability of the electrodes. Figure 6.22 shows that during the reduction of the Ferricyanide it absorbers one electron. In this work, the

Ferricyanide solutions were prepared in KNO_3 10^{-3} M, which played the roll of electrolyte.

$$[Fe(CN)_6]^{3-} \quad + e- \quad \rightleftharpoons \quad [Fe(CN)_6]^{4-}$$

Ferricyanide   Ferrocyanide
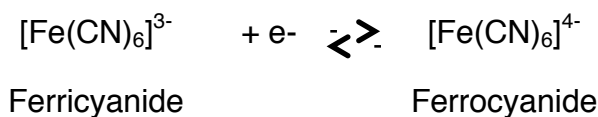
Figure 6.22 Reduction process from ferricyanide to ferrocyanide.

Voltammetry and redox cycling performed to ferricyanide solutions were done in the potential range between -0.5 V and 0.5 V, using a scan rate of 0.05 V/s and step potential 0.005 V. It is highly recommended to perform voltammetry of the studying specie to find the oxidation and reduction peak, so next electrochemical methods will be applied close from these potentials.

Figure 6.23a shows voltammogram of $K_3Fe(CN)_6$ 10^{-3} M in KNO_3 1 mM solution. It is observed that the oxidation peak appears at 0.15 V and the reduction peak at 0.3 V. These values are slightly different from the ones found in literature, when Ag/AgCl reference electrodes are used [25]. This is due to the fact that our reference electrode is an Ag wire, which causes a moderate shift of the potential to more negative values.
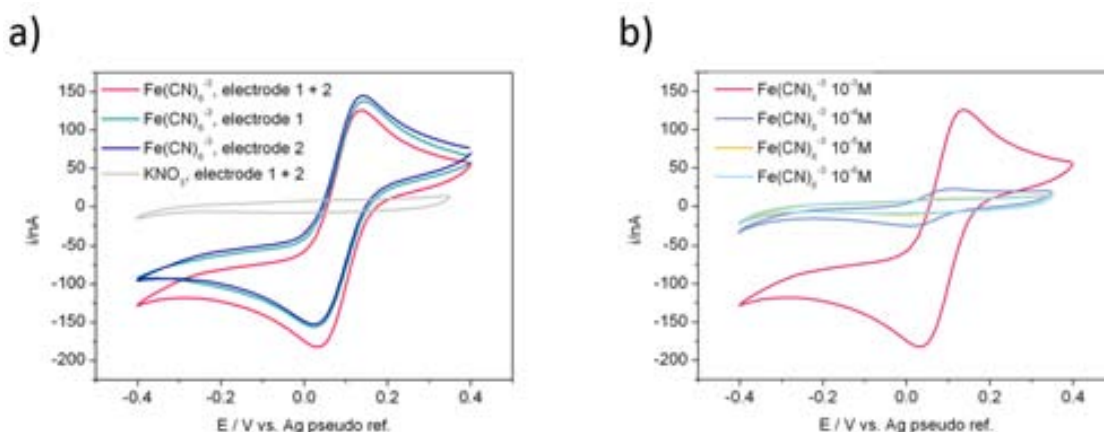
Figure 6.23. Voltammogram of a) Ferricyanide 10^{-3} M in KNO_3 1 mM performed to each of the electrodes separately and both together. b) Ferricyanide at difference concentration, in all the cases both electrodes of the sensor are externally shortcut.

The current intensity of the reduction peak recorded in Figure 6.23a is 150.3 nA and 153.8 nA, for the individual nIDEs, and 163 nA when the electrodes are short-circuited. The fact that the recorded current for the short-circuited electrodes is almost the same as for the individual electrodes, seems to be due to the overlap of the diffusion gradients. Therefore, if we measure a single electrode that takes up the same area as the total area taken by the nIDEs (digits and gaps included), it would produce the same results as the ones obtained with the nIDEs of this work.

The current intensity of a cyclic voltammetry in an electrochemical process, which is controlled by the diffusion of the electroactive molecule of the solution in the electrode-solution interface, when the electrochemical cell has a linear diffusion regime, can be calculated using the Randles-Sevcik's equation [26].

$$i_p = 0.4463 \, n F A C \left(\frac{n F v D}{R T}\right)^{1/2} \tag{6-1}$$

Where i_p is the intensity of the peak given in A, n the number of electron that are transferred in the equation, F is Faraday's constant, A the electrode area given in cm^2, C the concentration of the electroactive specie in the solution ($mol \cdot cm^{-3}$), v the sweep speed given in $cm^2 \cdot s^{-1}$ and T the temperature in K.

Assuming that the experiments have been done at 25 °C, the equation can be simplified as:

$$i_p = (2.687 \cdot 10^5) \, n^{3/2} A D^{1/2} C v^{1/2} \tag{6-2}$$

In order to verify this behavior, the theoretical current intensity was calculated using the assumptions mentioned in the previous paragraph. If we use Randles-Sevcik's equation (6-11), the theoretical current intensity is 145 nA (n=1, v=0.05 $V \cdot s^{-1}$, D=7.2·10^{-6} $cm^2 \cdot s^{-1}$ [27], A=0.09·10^{-4} cm^2, C=10^{-6} $mol \cdot cm^{-3}$). The estimated current value is of the same order of magnitude that the one registered for the nIDEs, as expected. In fact, slightly higher, but we have to keep in mind that the calculation have been performed considering that the active area is the same as the geometrical area, and we have not taken into account the electrode surface roughness. Actually, this equation is usually applied to calculate the electrochemical active area and thus the roughness of the electrode using the experimental peak current value.
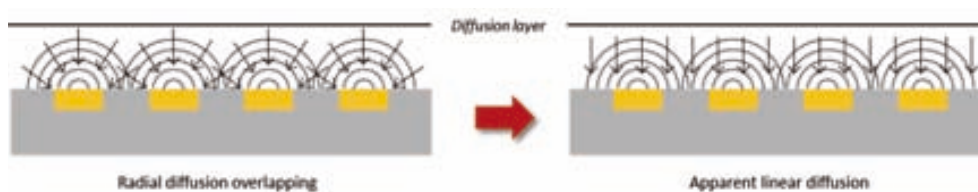
Figure 6.24. Diffusion layer diagram for nIDEs. Radial diffusion overlapping has the appearance of a linear diffusion layer.

Truly, an overlap of the radial current gradients of each digit occurs, which looks like a linear diffusion gradient, as it was explained above, see Figure 6.24.

Furthermore, Figure 6.23b shows the current registered for different concentrations of $Fe(CN)_6^{3-}$. It can be observed that the signal variation is significantly reduced for the smallest concentrations. The current measured for 10^{-5} M and 10^{-6} M is smaller than the capacitive charge, so the difference is rather appreciable.

Ferricyanide was also used to study the capability of the electrodes to perform redox cycling measurements. When voltammetry is performed, each molecule makes a single way from oxidation to reduction state and vice versa. In contrast, when redox cycling happens the molecules move from oxidation to reduction constantly, so the detected current extremely increases, two orders of magnitude in the case of Figure 6.25a. Figure 6.25b demonstrates that the registered current is proportional to the concentration of $Fe(CN)_6^{3-}$.
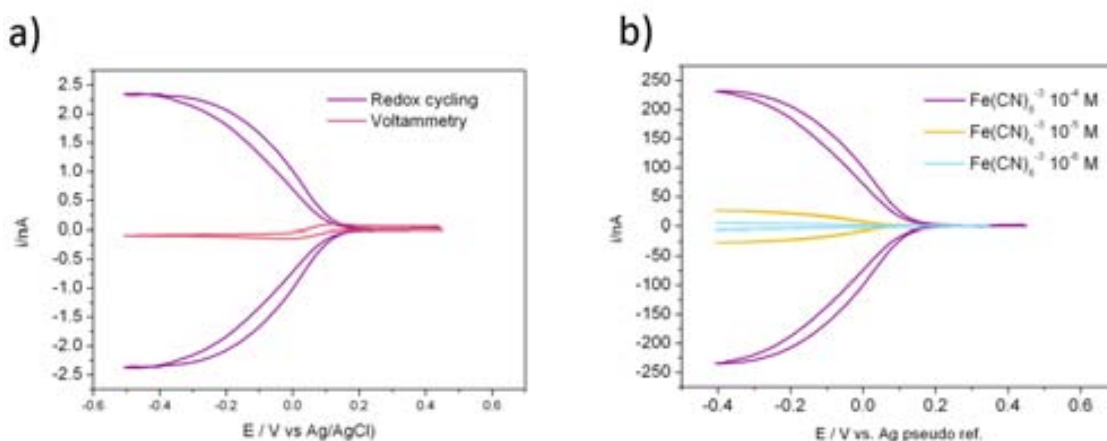
Figure 6.25. a) Comparison between measured current by means of voltammogram and redox cycling for $Fe(CN)_6^{3-}$ 10^{-4} M. b) Redox cycling at different concentrations of $Fe(CN)_6^{3-}$.

6.4.3 Dopamine selective detection by n-IDEs

The selectivity of the presented sensor has been demonstrated by the detection of dopamine in presence of ascorbic acid, which has a similar oxidation potential. For the next experiments, dopamine and ascorbic acid solution were prepared in 10 mM K_3PO_4. PO_4^{3-} will be used as electrolyte. In addition, it will keep constant the pH at 7.4, which is similar to the biological pH.

Figure 6.26a shows voltammograms of dopamine and ascorbic acid solutions, as well as both mixed. In this graph it can be seen that oxidation of dopamine occurs at 0.4 V and the reduction at 0.08 V using an Ag reference electrode. dopamine and ascorbic acid are complex organic molecules, therefore the obtained voltammograms do not show such well-defined oxidation and reduction peaks as ferricyanide. However, it can be appreciated that the oxidation peak of ascorbic acid is close to the dopamine one. When both molecules are mixed in the same solution, a single oxidation peak results, consequently it is impossible to distinguish the current intensity that corresponds to each molecule.
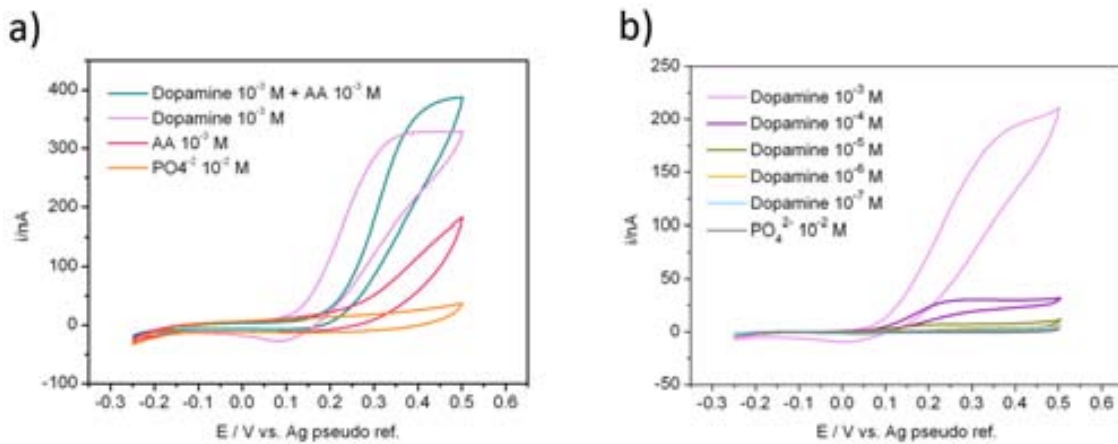
Figure 6.26 a) Comparison between voltammogram obtained for dopamine 10-3 M, ascorbic acid 10-3 M, phosphate 10-2 M and mixture of DA and AA 10-3 M each. b) Voltammogram of dopamine at different concentrations between 10-3 M and 10-7 M.

Redox cycling is an excellent technique to enhance the electrochemical signal obtained from a redox reversible couple. Since the molecule is oxidizing and reducing constantly from the anode to the cathode, the analyte concentration gradient in the vicinity of the electrodes become larger and the electrical signal increases. In Figure 6.27a the current obtained from redox cycling experiments of 10^{-4} M dopamine is compared with the voltammogram of the same solution. It is evidenced that when redox cycling is carried out the signal is 17 times larger.

Figure 6.27b shows the different current values registered for the redox cycling of a range of dopamine concentrations, from 10^{-7} M to 10^{-4} M.
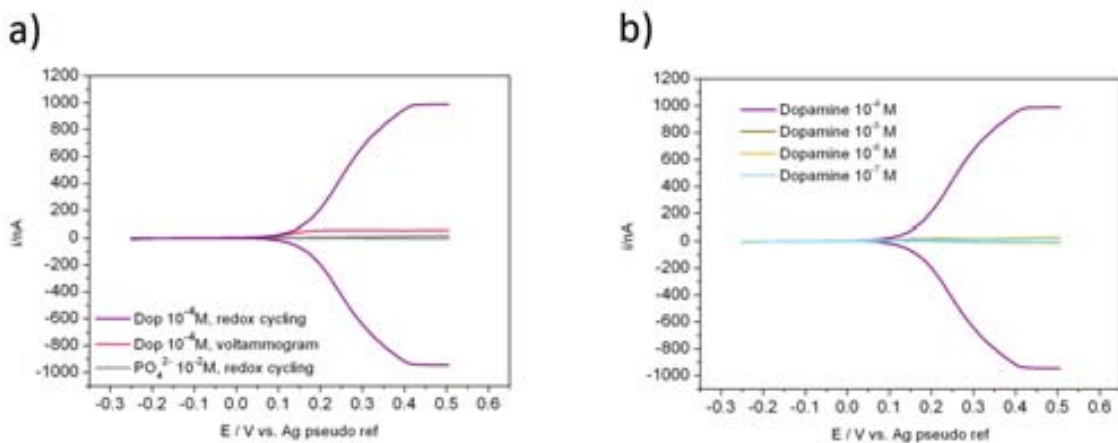
Figure 6.27. a) Comparison between the curve obtained from redox cycling and voltammogram of dopamine 10^{-4} M. the base signal of PO_4^{2-} can also be seen. b) Redox cycling curves of different concentration dopamine solutions, from 10^{-4} to 10^{-7} M.

For the selective detection of dopamine, it was mixed with ascorbic acid. The average ascorbic acid concentration in human serums is $0.7 \cdot 10^{-4}$ M [28]. In order to simulate a real setting, a 10^{-4} M excess of ascorbic acid was added to the dopamine solution. Dopamine concentration was varied from 10^{-4} M to 10^{-7}

M to calculate the detection limit of the sensor and calibrate it. Figure 6.28 clearly shows the redox cycling effect in dopamine (purple line), while only voltammogram effect is observed for ascorbic acid (red line). For the same concentration of both analytes, dopamine signal is 30 times higher due to the redox cycling process. When both analytes are together in the same solution (green line), redox curve is the same as dopamine solution's curve, this is because ascorbic acid does not contributes to the performed reduction reactions. In addition, oxidation curve is almost the same as only dopamine curve, but slightly enhanced due to the ascorbic acid contribution. For lower dopamine concentrations, Figure 6.28b, dopamine + ascorbic acid oxidation curves are higher in oxidation than in reductions, since ascorbic acid contributes in the oxidation curve, but not in reduction.
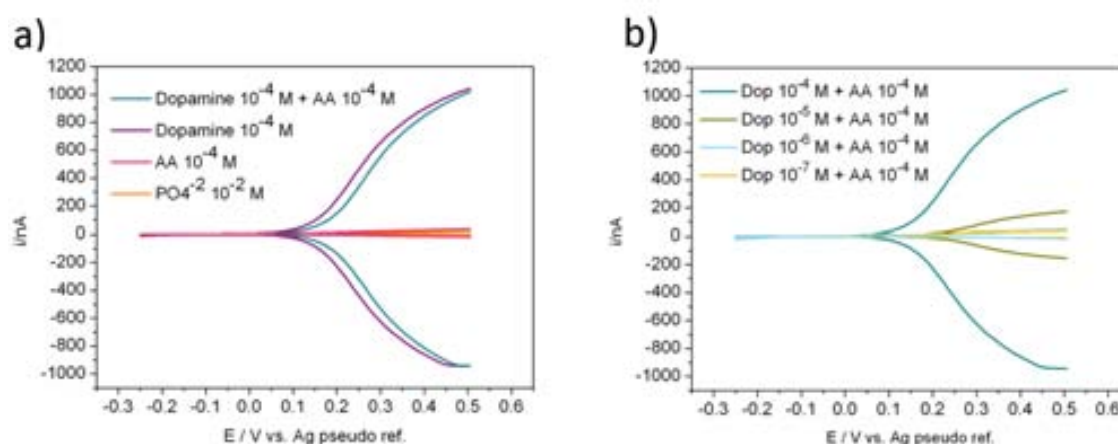
Figure 6.28. a) Redox cycling graph of dopamine 10^{-4} M, ascorbic acid 10^{-4} M, DA + AA 10^{-4} M and PO_4^{2-} 10^{-2} M. b) redox cycling of AA 10^{-4} M and DA with concentrations between 10^{-4} M and 10^{-7} M.

Calibration of dopamine redox cycling was performed in presence of ascorbic acid 10^{-4} M. Dopamine concentration varied from 10^{-7} to 10^{-4} M, Figure 6.29 represents the calibration curves obtained form reduction values. The calibration was repeated for four different batches of Dopamine solution. The concentration-current relation was linear in all the cases, but due to the degradation of the dopamine (it is oxidized along the time), the current value obtained in each case varies. Batch D was measured just after the preparation of each dilution, batch A some minutes later. Batch B and C were measured some hours later, first B and then C, which explains why the highest concentration were obtained for D batch and the lowest for C batch. The calibration plot, Figure 6.29, shows a linear tendency for concentrations below 0.1 mM. For that optimal range the detection limit of 0.62 μM was obtained.
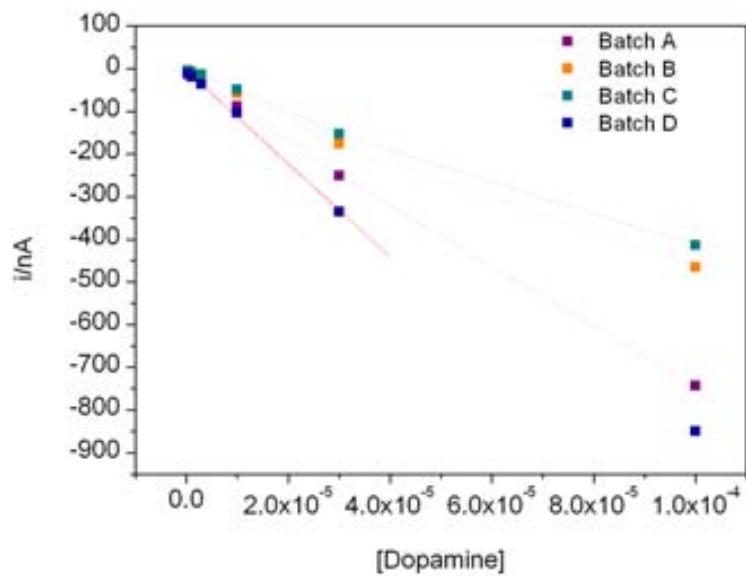
Figure 6.29. Calibration of dopamine from 10^{-7} M to 10^{-4} M in presence of ascorbic acid 10^{-4} M. The curve was structured from reduction values. Detection limit of o.62 μM was obtained, it was calculated from the linear regression of Batch D.

6.5   CONCLUSION OF CHAPTER 6

Usually ascorbic acid and dopamine appear at the same time in biological serum. As both of them have similar oxidation potentials, it is difficult to selectively detect dopamine in presence of ascorbic acid. However, dopamine is a reversible molecule, i.e. with capability to oxidize and reduce, while ascorbic acid is not. Therefore, redox cycling method was used to selectively detect dopamine in presence on ascorbic acid.

Redox cycling is performed by the separate polarization of two working electrodes. In the case of interdigitated electrodes each of the electrodes behaves as a working electrode, one of them is set at a fixed potential, while the other one continuously sweeps from E_1 to E_2. As the molecules move from one electrode to the nearest electrode, the diffusion of the molecules in the solution is reduced and the concentration gradient in the proximity of the electrodes increases. Consequently, the detected electrical signal is importantly enhanced, compared with the results obtained from standard voltammograms. When the gap between electrodes become smaller, as it is the case of our nanoelectrodes, shorter response time is obtained and this effect is intensified.

The relevance of having nanometric digits and gaps have been demonstrated by means of simulations performed using Comsol Multiphysics software. The gain obtained using redox cycling is more than four times bigger in the case of our 300 nm pitch electrodes, than in 10x larger electrodes.

Ferricyanide has been used to demonstrate the right operability of the electrodes. It has been experimentally and theoretically observed that there is an overlap of the radial diffusion layer and it seems to behave as a linear diffusion layers, thus our electrodes give the same signal as a single electrode with the same total area (digits and gaps).

Noticeably, redox cycling technique only works with redox-couples, i.e. dopamine, but not with molecules with one-direction oxidation, i.e. ascorbic acid. Thus, it is a suitable method for the selective detection of dopamine in presence of Ascorbic acid. When both molecules are in the same solution, dopamine signal will be enhanced, while ascorbic acid's not. Moreover, only dopamine's redox signal will be detected. This effect has been experimentally demonstrated, the signal obtained for dopamine redox cycling has been 30 times larger than for ascorbic acid an the detection limit of dopamine was 0.62 μM.

These experiments validate the correct operability of the nanointerdigitated electrodes for electrochemical detection. It has been demonstrate the improvements on redox cycling when the dimensions of the electrodes are reduced to the nanoscale.

REFERENCES CHARTER 6

1.   Aggarwal, A., Hu, M. & Fritsch, I. Detection of dopamine in the presence of excess ascorbic acid at physiological concentrations through redox cycling at an unmodified microelectrode array. *Anal Bioanal Chem* 405, 3859-3869, 2013).

2.   Obata, T. Dopamine efflux by MPTP and hydroxyl radical generation. *J Neural Transm* 109, 1159-1180, (2002).

3.   Wightman, R. M., May, L. J. & Michael, A. C. Detection of Dopamine Dynamics in the Brain. *Analytical Chemistry* 60, 769A-793A, (1988).

4.   Bibb, J. A. *et al.* Severe deficiencies in dopamine signaling in presymptomatic Huntington's disease mice. *Proceedings of the National Academy of Sciences* 97, 6809-6814, (2000).

5.   Phillips, P. E. M., Stuber, G. D., Heien, M. L. A. V., Wightman, R. M. & Carelli, R. M. Subsecond dopamine release promotes cocaine seeking. *Nature* 422, 614-618 (2003).

6.   Salahpour, A. *et al.* Increased amphetamine-induced hyperactivity and reward in mice overexpressing the dopamine transporter. *Proceedings of the National Academy of Sciences* 105, 4405-4410, (2008).

7.   Oleinick, A. *et al.* Cover Picture: Theoretical Investigation of Generator–Collector Microwell Arrays for Improving Electroanalytical Selectivity: Application to Selective Dopamine Detection in the Presence of Ascorbic Acid (ChemPhysChem 9/2013). *ChemPhysChem* 14, 1749-1749, (2013).

8.   Ensafi, A. A., Taei, M., Khayamian, T. & Arabzadeh, A. Highly selective determination of ascorbic acid, dopamine, and uric acid by differential pulse voltammetry using poly(sulfonazo III) modified glassy carbon electrode. *Sensors and Actuators B: Chemical* 147, 213-221, (2010).

9.   Breczko, J., Plonska-Brzezinska, M. E. & Echegoyen, L. Electrochemical oxidation and determination of dopamine in the presence of uric and ascorbic acids using a carbon nano-onion and poly(diallyldimethylammonium chloride) composite. *Electrochimica Acta* 72, 61-67, (2012).

10.   O'Neill, R. D. Microvoltammetric techniques and sensors for monitoring neurochemical dynamics in vivo. A review. *Analyst* 119, 767-779, (1994).

11.   Robinson, D. L., Hermans, A., Seipel, A. T. & Wightman, R. M. Monitoring rapid chemical communication in the brain. *Chemical reviews* 108, 2554-2584 (2008).

12.   Saila, U. K. *Kimika orokorra*. Vol. I - Chapter 13 (Universidad del Pais Vasco / Euskal Herriko Unibertsitatea, 1996).

13.   Zoski, C. G. *Handbook of electrochemistry.* (2007).

14.   Allen J. Bard, L. R. F. *Electrochemical methods: Fundamentals and applications.* (2001).

15. Stetter, J. R., Penrose, W. R. & Yao, S. Sensors, Chemical Sensors, Electrochemical Sensors, and ECS. *Journal of The Electrochemical Society* 150, S11-S16, (2003).

16. Wang, J. Glucose Biosensors: 40 Years of Advances and Challenges. *Electroanalysis* 13, 983-988 (2001).

17. Wang, Y., Xu, H., Zhang, J. & Li, G. Electrochemical Sensors for Clinic Analysis. *Sensors* 8, 2043-2081 (2008).

18. TanotoH *et al.* Greatly enhanced continuous-wave terahertz emission by nano-electrodes in a photoconductive photomixer. *Nat Photon* 6, 121-126, (2012).

19. Metrohm Autolab B.V. <http://www.metrohm.com>

20. Amado, N. G. *Desing and fabrication of miniaturised electroanalytical systems*, Universitat Autònoma de Barcelona, (2010).

21. Multiphysics, C. <http://www.comsol.com>

22. E. Colín-Orozco, S. C.-A. o., M. T. Ramírez-Silva, M. Romero-Romo, M. Palomar-Pardavé. On the Electrochemical Oxidation of Dopamine, Ascorbic Acid and Uric Acid onto a Bare Carbon Paste Electrode from a 0.1 M NaCl Aqueous Solution at pH 7. *Electrochemical science* 7, 6097-6105 (2012).

23. O'Reilly, J. E. Oxidation-reduction potential of the ferro-ferricyanide system in buffer solutions. *Biochimica et Biophysica Acta (BBA) - Bioenergetics* 292, 509-515, (1973).

24. Niranjana, E., Kumara Swamy, B. E., Raghavendra Naik, R., Sherigara, B. S. & Jayadevappa, H. Electrochemical investigations of potassium ferricyanide and dopamine by sodium dodecyl sulphate modified carbon paste electrode: A cyclic voltammetric study. *Journal of Electroanalytical Chemistry* 631, 1-9, (2009).

25. Xu, C., Cai, H., Xu, Q., He, P. & Fang, Y. Characterization of single-stranded DNA on chitosan-modified electrode and its application to the sequence-specific DNA detection. *Fresenius J Anal Chem* 369, 428-432, (2001).

26. Hultgren, V. M., Mariotti, A. W. A., Bond, A. M. & Wedd, A. G. Reference Potential Calibration and Voltammetry at Macrodisk Electrodes of Metallocene Derivatives in the Ionic Liquid [bmim][PF6]. *Analytical Chemistry* 74, 3151-3156, (2002).

27. Konopka, S. J. & McDuffie, B. Diffusion coefficients of ferri- and ferrocyanide ions in aqueous media, using twin-electrode thin-layer electrochemistry. *Analytical Chemistry* 42, 1741-1746, (1970).

28. Dhariwal, K. R., Hartzell, W. O. & Levine, M. Ascorbic acid and dehydroascorbic acid measurements in human plasma and serum. *The American journal of clinical nutrition* 54, 712-716 (1991).

Conclusions

This thesis presents the development of different nanofabrication methods to create new structures and devices. The work includes the design, fabrication and characterization of different approaches.

The first one is a simple and smart platform to contact single nanocrystals. It consists on the preparation of a nanocomposite compound of chemically synthesized nanocrystals and a highly isolating resist. When ultrathin layer of the nanocomposite is deposited on a substrate, and after several post-processes, the particles stays exposed to the surface, but at the same time electrically isolated. With the support of an AFM tip and gold micro/nanocontacts, characterization of the nanocrystals was performed. It was successfully demonstrated the reliability of the technology by preliminary electrical results, where it is clearly demonstrate that the particles were contacted. However, further work must be done for the better control of the particles distribution, and thus enhance the certainty that single nanocrystals have been contacted.
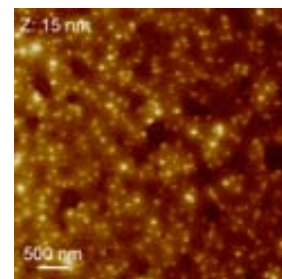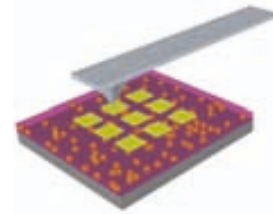
Moreover, complete processes of thermal and S&F UV nanoimprint lithography have been developed in this thesis, from the fabrication of the stamp, cross the imprint process itself to the post-processing. Nanoimprint has been used as lithography process to fabricate nanopatterns, but also for the structuration of functional polymers, such as PET, PTT or P(VDF-TrFE). Novel fabrication method based on stencil's hard mask concept and nanoimprint lithography has been developed for the fabrication of nanoparticles arrays and interdigitated nanoelectrodes. This method was first developed for S&F UV nanoimprint lithography at The Molecular Foundry, and then implemented in the CNM to perform the thermal NIL version.

This method made possible the preparation of high aspect ratio metallic nanoparticles arrays of different shapes, dimensions and materials. The specific relevance of these nanoparticles to be used as Local Focus Plasmonic Resonance sensors has been proved by their optical characterization. The absorbed and transmitted light was quantified for different particles and conditions. Besides, there is a wide range of other potential applications where these nanostructures can be useful.
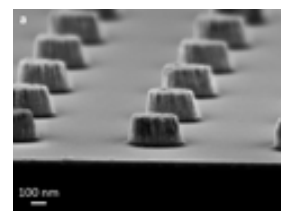
In addition, interdigitated nanoelectrodes were fabricated by means of thermal and S&F UV nanoimprint lithography. The application of the hard mask concept facilitated the lift-off process and allowed the deposition of thicker metal layers. Although this technology is an exceptional method for the fabrication of a vast variety of nanostructures, several improvements must be done for the reliable fabrication of interdigitated electrodes. These electrodes are composed of thousands of nanometric digits in a large area, and not even a single defect is allowed for the correct operation of the device. Defectivity is still the main drawback of the nanoimprint, therefore the yield of this type of devices was rather low.
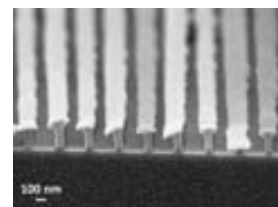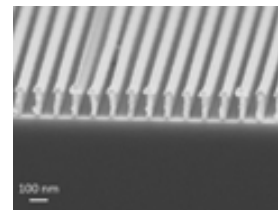
Interdigitated nanoelectrodes were also fabricated by e-beam lithography, which is a lower throughput and more expensive technique, but due to its high resolution and reliability it is usually applied to prepare prototypes. Improvement of the design was performed by the division of the digits in different blocks, in order to enable the isolation of damaged blocks. Two different packagings were used for the characterization of the devices as electrochemical sensors. The first one consisted of a compact PCB strip, which is frequently used for electronic devices. In order to overcome the drawbacks concerning the manipulation and wire bonding of the PCB's, a reusable methacrylate holder was designed. It covers the specific protection and connection requirements of the sensors. In the new packaging, the sensors are inside a channel, which gives protection to the digits, and the electrical connection is made directly by contact pins.
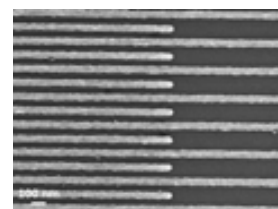
The operability of the interdigitated nanoelectrodes was demonstrated by the electrochemical characterization of ferricyanide, as standard molecule. In addition, the great capability of the sensors to selectively detect dopamine in presence of ascorbic acid by redox cycling was proved. Due to the reduced dimension of the gap between the digits, the selectivity respect standard voltammetry was improved 30 times.

In summary, this thesis demonstrates several methods that allow fabricating nanostructures and nanodevices with novel and enhanced functionalities. Moreover, these techniques can be further applied to different areas of nanotechnology.

Annexes

In the following annexes several processes performed during this work are explained. Due to the low technological contribution that provide to this thesis and also because they are repeated diverse times along the document, they have been collected in this section.

Annex 1. Lift-off

Lift-off is the process were the resist used as mask during lithography and subsequent metallization is removed, at the same time the excess of metal deposited on top of the resist is also eliminated, see Figure A30.
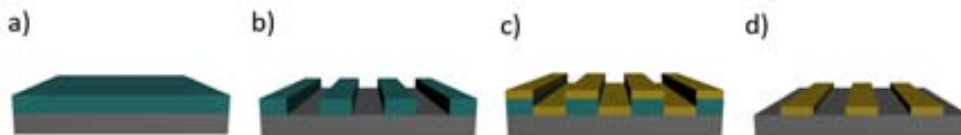
Figure A30. Typical lithography and lift-off process: a) resist deposition, b) lithography, c) metal deposition and d) lift-off process. During the lift-off the sample is immersed in acetone to solve the resist and as a result the metal above is removed.

The principal protocol used in this thesis is next one: the sample is dipped in acetone at 40 °C during 5 min, in order to soften the resist. Then the sample is shaked in ultrasonic bath during one minute (longer time can be applied if needed). When fragile patterns are manipulated, as shorter ultrasound time as possible must be applied, even a plastic piece can be placed under the beaker in order to buffer the ultrasound. In cases when the lift-off become complicate the sample is immersed in Stripper (Fujifilm) at 70 °C during 20 min, then rinsed in water and finally perform soft ultrasound process in acetone.

Annex 2. Positive resist photolithography

Photolithography is the process of transferring geometric patterns on a mask to the surface by the selective UV exposition of a resist.

First stage of the process followed during this thesis is the dehydration of the sample, it is performed in an over at 200 °C during 10 minutes. Then 1.2 μm of HIPR 6512 positive resist are deposited by spincoating. Next, the wafer is baked at 100 °C during 15 minutes to evaporate the solvent. Subsequently, the UV exposition is carried out in soft-contact during 9 s at 900 W/cm^2, using the aligner. In order to remove the exposed resist, it is developed during 30 s and rinsed in water to stop the reaction.

After a hardbake in an over at 115 °C during 10 min the resist is ready to be used as a mask in the future process, such as metallization, etching, doping…
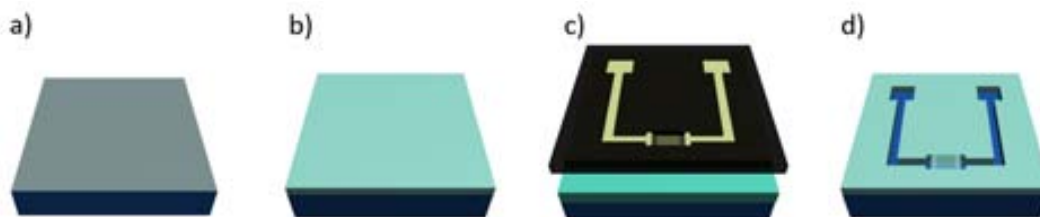
Figure A31. Photolithography process: a) Preparation of substrate, it must be baked to dehydrate. b) UV resist is deposited by spincoating. c) Optical lithograph is performed. d) Development and hardbake of the resist are carried out.

Annex 3. Silanization

In nanoimprint lithography the stamp and the resist are in physical contact, in order to avoid that the resist get stuck during the imprint process, the stamp is coated with an anti-sticking layer.

The silanes used in this thesis are the FTS13 and they were deposited by means of chemical vapor deposition.

Due to the fact that the silanes react with the OH groups on the surface, first of all the template is subjected to 3 minutes of ozone plasma to enhance the formation of OH groups. Then the template is exposed to FTS13 atmosphere in a vacuum over during one hour. The vacuum is used on the one hand to obtain a clean deposition of the product, but also to avoid the reaction of the FTS13 with the atmospheric water particles

Annex 4. Mesa-stamp fabrication

The mesa of the stamp is fabricated by means of optical lithography and wet etching. As substrate silicon wafers covered with 30 nm of SiO_2 have been used, the silicon oxide will be used as second mask during the wet etching.

As it can be seen in Figure A32 the first stage for the mesas exposition is the dehydration of the substrate, it is baked in the oven at 200 °C during 10 min. Then, 1.2 μm of positive resist HIPR 62:12 are spincoated. The resist is baked in the oven during 15 minutes at 100 °C. After, the exposition is performed using a glass and chromium mask, using 900 mW/cm^2 during 9 seconds. The resist is developed 30 s and rinsed 2 minutes in water to stop the reaction. Finally, the hard bake is carried out by baking the wafer at 150 °C during 10 min.
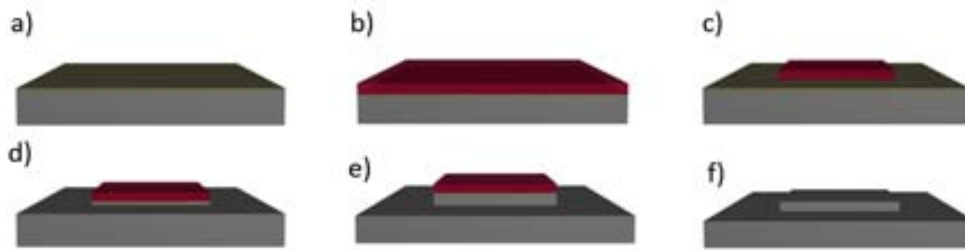
Figure A32. Fabrication process of mesa-stamp is sketched: a) Silicon substrate with 30 nm of SiO_2 in the surface. b) Positive photoresist is spincoated on the sample. c) UV exposition and development of the resist is performed. d) SiO_2 unprotected by the resist is etched. c) Si is etched. Photoresist and the SiO_2 are removed.

Once the resist is patterned, the wet etching of the silicon is performed in order to obtain the mesas, SiO_2 and resist are used as mask. First the SiO_2 is etched. Then the etching of the silicon is performed by using an isotropic mixture of HNO_3 (50 ml), HF (1 ml), H_2O (20 ml), during 55 seconds. The obtained mesa has a height of around 300 nm. Finally the positive resist is removed by acetone. In Figure A33 AFM image of the mesa's step can be seen.
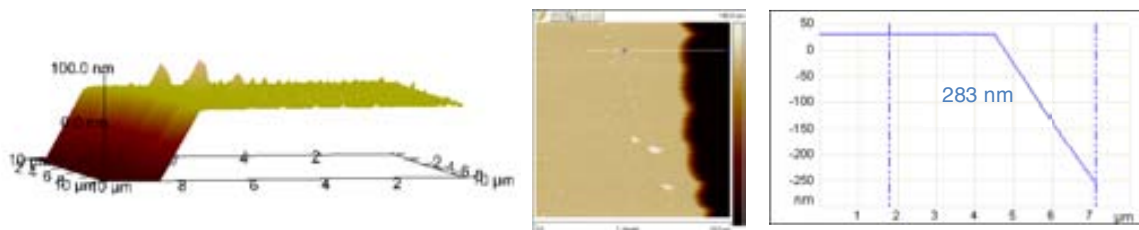
Figure A33. AFM image and profile of the mesa.

Note: the SiO_2 is used to reinforce the mask behavior of the resist. It has been seen that the resist is not totally waterproof and Si etcher penetrates, so non-homogeneous surface is obtained, example of that can be seen in Figure A34.
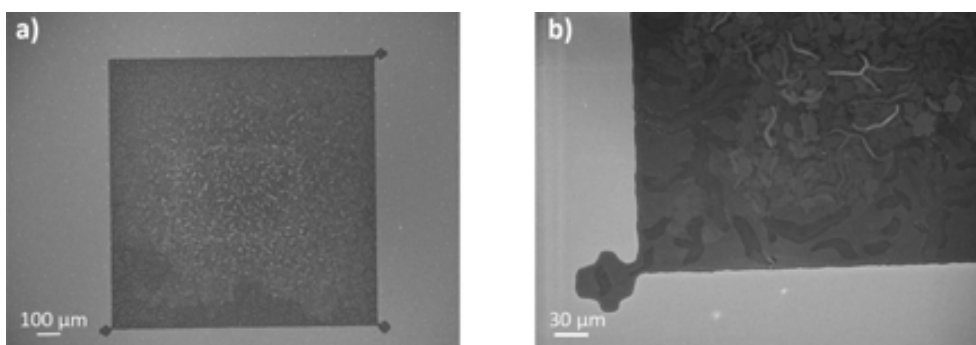
Figure A34. SEM image of the mesa fabricated without SiO_2 mask. In-homogeneities in the surface can be observed.

In this thesis the base of the mesa-stamps (which means the base + mesa) have been fabricated at wafer-scale, several stamps with mesas of different sizes have been prepared at the same time. As it was desired to hold stamps with alignment marks, first, they have been prepared by UV-lithography and lift-off previously to the mesas. The mask used to fabricate the alignment marks was named CNM 604-L1 and the one to expose the mesas CNM 604-L2.

The fabrication of the metallic alignment marks has been carried out in 4 inch wafers, coated with 30 nm of SiO_2. The photolithography was carried out on 1.2 μm of positive resist HIPR 62:12. After the patterning of the resist, 20 nm of Tungsten were deposited by sputtering, and by the subsequent lift-off the process was finished.

Then the fabrication of the mesas was developed following the steps explained at the begging of this annex. In Figure A35 the layout of the both masks is overlapped, in blue the design correspond to CNM 604-L1 is and the CNM 604-L2 in red.
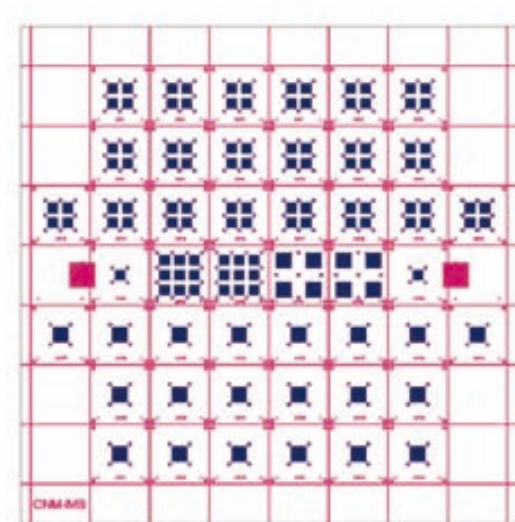
Figure A35. Overlapped of CNM 604-L1 (red) and CNM 604-L2 (blue) layouts. CNM 604-L1 is the mask aimed to fabricate the alignment marks and the CNM 604-L2 for the mesas.

Annex 5. SU8 thin layer deposition

SU8 is an epoxy based negative photoresist. During this thesis it was chosen to passivate the interdigitated electrodes due to its impermiavility, isolator and high resistivity characteristic. As thin layer of SU8 was needed, about 500 nm, SU8 2000.5 (MicroChem) was used. The protocol used to deposit and perform the lithography was the next one:

1. Dehydrate the substrate by placing it in an over at 200 °C during 15 minutes.

2. Spincoat the resist on the sample, spin coating recipe:

Step	Speed (rpm)	Time (s)	Acceleration (rpm·s^{-2})
1st	500	10	150
2nd	2000	30	150

3. Soft bake

4. Exposure in soft-contact during 12 s at 9 mW/cm^2, Figure A7

5. Post exposure bake, Figure A8.

6. Development of the resist in mrDev 600 (MicroChem) during 1 minute and 1 minute rinsing in isopropanol.

7. Hard bake, Figure A9.
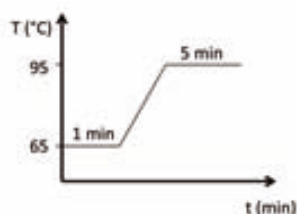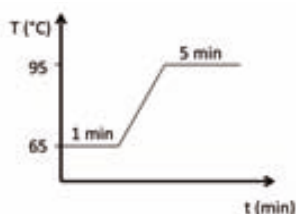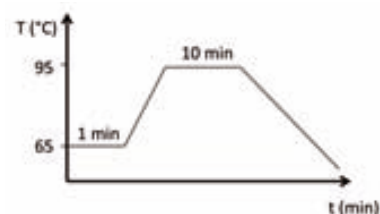
Figure A7   Figure A8   Figure A9

Annex 6. Fundamentals of electrochemistry

A brief introduction to basic electrochemistry principles is presented. For the sake of simplicity, this introduction has been limited to only the essential concepts.

6.5.1.i Redox-reactions

Electrochemistry is the branch of chemistry that studies the reactions where electrons are exchanged. When a species loses electrons it is called *oxidation*, when it gains electrons is called *reduction*. The combination of both phenomena is denominated as redox reaction.

$$O_{x_1} + n\,e^- \rightarrow R_{ed_1} \quad \text{REDUCTION} \tag{6-1}$$

$$\left(R_{ed_2} \rightarrow O_{x_2} + n\,e^- \right) \cdot n \quad \text{OXIDATION} \tag{6-2}$$

$$O_{x_1} + R_{ed_2} \rightarrow R_{ed_1} + O_{x_2} \quad \text{REDOX-REACTION} \tag{6-3}$$
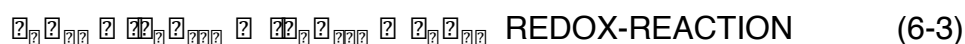
A_{ox} and B_{red} are the oxidized and reduced species, each of them have been reduced or oxidized, *n* is the number of electrodes that is exchanged. The species linked by a redox reaction are known as *redox-couple.*

In redox reaction, the electron transport is carried out by ions. Therefore, when a specie loses or gains an electron, there is another one that gains or loses it.

6.5.1.ii *Electrochemical potential*

Each of the oxidation or reduction reaction has its own electrochemical potential. The electrochemical potential ($\bar{\mu}$) of a redox-couple represents the oxidation or reduction capability of the couple in standard conditions and it is calculated by the sum of the potentials in a reaction, being n_i the number of electron exchanged:

$$\bar{\mu} = \sum_i n_i \, \bar{\mu}_i \qquad (6\text{-}4)$$

The potential of the reaction receives a negative sign for the products and a positive sign for the educts. The potential difference (E) is what drives the reaction. Electrochemical reaction happens when the sum of the potentials in a reaction is negative:

$$\Delta G = E = \sum_i n_i \bar{\mu}_i < 0 \qquad (6\text{-}5)$$

Assuming constant temperature and pressure, only chemical work and electrical work is allowed to perform. In that case, the electrochemical potential of the component *i* can be described as:

$$E_i = E_i^0 + RT \ln a_i + z_i F \varphi \qquad (6\text{-}6)$$

where E_i^0 is the standard potential of component *i* under standard conditions (T=25 °C, P=1 atm, and activity a_i=1). *RTlna$_i$,* is the change of chemical potential, when the component *i* is transferred from standard conditions into a system at temperature *T* where *i* has the activity a_i=1, and where *zFϕ* represents the electrical work with z_i as the charge of species *i*, *F* as Faraday's constant (F=96485 C) and *ϕ* as electrical potential phase. The activity a_i itself represents a corrected concentration.

6.5.1.iii *Electrode potential*

The electrochemical potential (E_{ep}) of a redox-couple cannot be measured in an absolute form. It can only be measured the potential difference. Therefore, it is necessary to compare the potential of a reaction (E^0) with a reference potential (E_{ref}), supplied by a reference electrode.

$$E_{ep} = E^0 - E_{ref} \qquad (6\text{-}7)$$

When an electrode is immersed in a solution, the ions of the solution have the tendency to approach the electrode to compensate the charge on the surface. During this process, in the interface between the electrode and the solution a diffusion layer is created, which establishes the potential difference, Figure A10. When all the species composing the redox-couple are in standard conditions, the potential difference is named *standard electrode-potential*. This potential is represented as E^0 and its value is always the same under standard conditions. Its value is a characteristic of the redox-couple, it represents the tendency of the couple to be oxidized or reduced and it will be fundamental in analytic applications.

Figure A10. The double electric layer established on the electrode surface and as a consequence, the created electrode potential.

Depending on the reference electrode used on the reaction, the current transport will be ionic or electronic:

🔹**Ionic electrodes:** this is the case when a metallic electrode is used, for instance cupper. If we are working with a $CuSO_4$ analyte in the solution, the electrode will be the reduced species, Cu^0, and the analyte the oxidized species, Cu^{+2}. The direction of the reaction will depend on the potential difference gradient. When the reaction reaches the equilibrium, it will stop. The reaction happens due to the ion exchange in the solution, this is why they are called ionic electrodes.

🔹**Electronic electrodes** are compounded of an inert metal, as platinum for instance. Thus the redox reaction takes place only on the analyte phase (ß), the inert metal will only exchange electrons.

- **Other reference electrodes:** many commercial electrodes are compounds of a metal electrode, nearly insoluble salt of this metal, and saturated solution containing one ionic species of the nearly insoluble salt. Some of the most common reference electrodes are the silver/silver chloride electrode (Ag/AgCl), the calomel electrode (Hg/Hg$_2$Cl$_2$), the mercury sulfate electrode (Hg/HgSO$_4$) and the mercury oxide electrode (Hg/HgO).

6.5.1.iv *Normal Hydrogen Electrode*

The reference Normal Hydrogen Electrode (NHE) was assumed as standard. In this electrode it is used [H$^+$]=1 and inert Pt as electrode. In 1953, IUPAC decided that the hydrogen-electrode standard consisted on an inert metal (Pt), which is immersed in an acid solution with unit activity of hydrated protons at 25 °C. Hydrogen gas is bubbled into the solution under the electrode with a standard pressure of 1 atm. Under equilibrium conditions the reaction can be described as:

$$\frac{1}{2}H^+_{(aq)} \leftrightarrow H^+_{(aq)} + e^-_{(NHE)} \qquad E^0_{\frac{1}{2}H_2/H^+} = 0V \qquad (6\text{-}8)$$
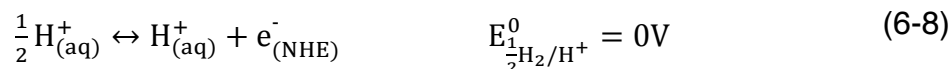
Therefore, in order to determine the standard potential of a redox-couple, the specie on the cathodic area, in standard conditions, can be determined by comparing with the reference electrode, NHE. For example:

$$E = E^0_{Cu^{2+}/Cu^0} - E^0_{H^+/H_{2(g)}} = E^0_{Cu^{2+}/Cu^0} \qquad (6\text{-}9)$$

The standard potentials of a certain redox couple can be found in extensive tables.

6.5.1.v *Nerst's equation*

Qualitative characterization of any interaction in a redox process is determined using Nerst's equation. This equation joins electrode potentials and the behavior of the species in the redox reaction.

$$E_{redox} = E^0_{redox} + \frac{RT}{zF}\ln\frac{a_{ox}}{a_{red}} \qquad (6\text{-}10)$$

being *a* the activity of the oxidized and reduced species, *z* charge of the species and *F* Faraday's constant (*F*=96485 C). As it can be deduced from equation 6-10, the potential imposed by the redox-couple not only depends on E^0, but also on the relation between the oxidized and reduced species. By this equation, the relation between the specie concentration and redox-potential has been defined.